Diss. ETH No. 25873

A deeper insight into LA-ICP-MS: exploring its challenges and extending its capabilities

A thesis submitted to attain the degree of

DOCTOR OF SCIENCES of ETH ZURICH

(Dr. sc. ETH Zurich)

Presented by

DEBORA BRIGITTE KÄSER

MSc Chemistry, ETH Zurich

Born on 13.04.1990

Citizen of Untersiggenthal (AG)

Accepted on the recommendation of

Prof. Dr. Detlef Günther, examiner

Prof. Dr. Thomas Lippert, co-examiner

Dr. Joachim Koch, co-examiner

2019

For Niki, Julian and Nino, who might wonder one day what I was doing during the times, I couldn't discover the world together with you...

Abstract

Over the past years, Laser Ablation - Inductively Coupled Plasma - Mass Spectrometry (LA-ICP-MS) has become a well-established technique for the direct and quantitative elemental analysis of main, major and trace analytes in solid samples. In LA-ICP-MS, sampling is performed by ablation of a solid specimen by impact of a pulsed laser. The sample is usually placed in an airtight ablation chamber and via a gas stream the LA-generated aerosol is transferred into the ICP, where it is vaporized, atomized, and ionized. Finally, the ions are recorded by a mass spectrometer, where they are separated according to their mass-to-charge ratio and subsequently counted.

Despite the fast developments towards high-speed, high-resolution elemental imaging by LA-ICP-MS and tackling of all the encountered pitfalls throughout many years of research, one of the biggest challenges still remains: the analysis is highly material dependent. Not only LA- but also ICP-related elemental fractionation, i.e. the difference between the measured composition of the ablated material and the actual bulk composition of the sample, render accurate quantification constantly demanding. Moreover, matrix-matched analysis, an often-employed strategy to overcome these limitations, may not always be appropriate, as has been discovered in the context of the first part of this thesis. We approached the question of matrix-matched analysis from a different point of view than normally done: the importance of the solid phase, e.g. glassy or powder, rather than a miss-match in the overall compositions of sample and reference was investigated. Due to the importance and natural abundance of silicates in rock-forming minerals, we concentrated on the analysis of silicates and report on elemental fractionation phenomena for the respective matrix elements. Their accurate quantification becomes essential when LA-ICP-MS is utilized as imaging technique, whereby so-called 100% mass normalization quantification approaches are typically applied.

Indeed, the nature of LA-ICP-MS turns characterization of the origin of elemental fractionation into a multi-dimensional problem. As a consequence, we investigated the effect of different parameters, such as wet plasma conditions, mass load or pulse duration on

the accuracy of the measurement. In addition, the LA-generated aerosol was studied using both SEM and an optical particle counter to obtain the aerosol morphology and the particle size distribution, respectively. Finally, an extensive comparison between different natural silicate reference materials processed into two different phases – glass and pressed nano-powders – was performed. These reference materials were based on various igneous (basalt, granite, diorite and gabbro) and metamorphic rocks (serpentinite). Using this series of different reference materials, we were able to compare the effect of matrix-matched and phase-matched analysis. In addition, these specific reference materials were used to quantify different mineral samples, such as Topaz (30 wt-% SiO_2), Wollastonite (50 wt-% SiO_2), Anorthite (60 wt-% SiO2), Clinochlore (30 wt-% SiO_2) and Clintonite (20 wt-% SiO_2). Overall, we discovered important elemental fractionation patterns for Si in silicate based samples, and were able to elucidate different origins thereof.

Most frequently, if LA-ICP-MS is used as elemental imaging technique, research would focus on the lateral dimensions. For example, the LA process by ns-LA can result in compositional changes in depth due to heat effects, and thereby render high-resolution analysis in depth challenging. However, by switching from ns-LA to ultrashort LA (i.e. femtosecond) such heat effects are generally mitigated and imaging in depth at increased resolution may become more manageable. A further, general prerequisite for high-resolution depth analysis is the presence of a homogenized laser beam profile. While in the case of ns-lasers a homogenized beam delivery set-up was already introduced in 1997, no versatile system was available for fs lasers. Hence the aim of the second part of this thesis was to develop and investigate an alternative strategy for homogenizing the laser beam profile for fs lasers. We studied the applicability of a pinhole imaging system and found well-defined craters in both non-conducting and conducting materials with diameters of 25 μm. In a next step, investigations interrogated the applicability of near (N)UV-fs-LA using this homogenization scheme for depth profile analysis of metal thin films by ICP-MS, specifically, for single layers of chromium (Cr) deposited on different substrates. By comparison of these measurements to simulated depth profiles for Gaussian and Super-Gaussian laser beam profiles, evidence for the latter on the sample surface was obtained. In addition, depth resolution data were specified according to ISO guidelines. The results indicated

a depth-dependent depth resolution for multi-layer samples ranging from < 50 nm for near-surface to > 100 nm further in the sample.

In summary, the presented thesis dealt with two key issues still inherent to state-of-the-art LA-ICP-MS measurements and its set-up: (1) selection of appropriate reference materials, with a specific focus on solid-phase sensitivity, in order to mitigate elemental fractionation, as well as, (2) beam profile homogenization in femtosecond (fs) laser ablation applications to allow for high-resolution depth profiling.

Zusammenfassung

Eine hohe Empfindlichkeit zur Messung von Ultraspurenelementen, sowie die Möglichkeit Isotopenverhältnisse zu bestimmen, haben dazu beigetragen, dass Induktiv gekoppelte Plasma – Massenspektrometrie (ICP-MS) heutzutage in vielen Bereichen der Wissenschaft Anwendung findet. Insbesondere im Bereich der Geologie wird ICP-MS mit Laserablation (LA) als Probennahemsysten als meist gebrauchte Methode beschrieben. Sie bietet die Möglichkeit, einen Feststoff direkt quantitativ und ortsaufgelöst zu analysieren. LA basiert auf dem Probenabtrag eines Feststoffes durch intensive Laserpulse. Die Probe befindet sich dabei in einer Probenkammer und mittels eines Gasstroms wird das abgetragene Material zur ICP-MS geführt. Im ICP wird die Probe dann verdampft, atomisiert und ionisiert. Die dabei enstandenen Ionen werden ins Massenspektrometer überführt, in welchem sie nach ihrem Masse-zu-Ladungsverhältnis (m/z) aufgetrennt und anschliessend detektiert werden.

Eine wiederkehrende Herausforderung in LA-ICP-MS ist die Elementfraktionierung. Sie beschreibt den Zusammensetzungsunterschied zwischen der Probe und dem Gemessenen durch die Materialabhängigkeit des Laserabtrages oder durch Vorgänge im Plasma. Diese Materialabhängigkeit macht eine akkurate Quantifizierung zu einer von Experiment zu Experiment unterschiedlichen Aufgabe. Im ersten Teil dieser Arbeit wird aufgezeigt, dass auch die typisch angewendete matrixangepasste Messstrategie nicht immer eine akkurate Quantifizierung erreicht. Deshalb wurde die matrixangepasste Analyse hinsichtlich dem Einfluss der Phase des Feststoffes, d.h. Glas oder Pulver, auf die Quantifizierung untersucht. Da Silikate das Grundgerüst vieler Erdgesteine sind, haben wir uns auf die Analyse der Matrixelemente solcher Proben konzentriert. In vielen Anwendungen, bei denen LA-ICP-MS als bildgebende Methode Anwendung findet, wird eine sogenannte 100% Massennormierungsmethode zur Quantifizierung verwendet. Daher ist es wichtig, die Matrixelemente akkurat zu bestimmen.
Die Art des Laserabtrages macht die Charakterisierung des Ursprungs der Elementfraktionierung zu einem multi-dimensionalen Problem. In dieser Arbeit wurden die Effekte verschiedenster Parameter auf die Richtigkeit der Matrixelemente untersucht. Zum Beispiel

wurde der Effekt der Probenmasse im ICP, der Feuchtikgeit im ICP, und der Pulslänge des Laserpulses untersucht. Desweiteren wurde das Aerosol aus der Laserablation mit Hilfe von Rasterelektronenspektroskopie charakterisiert und dessen Partikelverteilung gemessen. Eine umfangreiche Studie verschiedenster Referenzmaterialien, prozessiert in Glasphase und als Presslinge aus Nanopulvern, hat gezeigt, dass matrixangepasste Quantifizierungen nicht immer zu richtigen Resultaten führt. Darauf basierend, wurden dieselben Referenzmaterialien benutzt, um verschiedene Mineralproben, wie Topas (30 wt-% SiO_2), Wollastonit (50 wt-% SiO_2), Anorthit (60 wt-% SiO_2), Klinochlor (30 wt-% SiO_2) and Clintonit (20 wt-% SiO_2) zu quantifizieren, wobei der Effekt einer fehlerbehafteten Quantifizierung der Matrixelemente auf die Spurenelemente spezielle Beachtung fand. Diese Arbeit liefert daher wichtige Kenntnisse über das Auftreten von Elementfraktionierung bezüglich Silizium und zeigt die multi-dimensionalen Schwierigkeiten dieser Fraktionierung auf.

Neben eines lateral aufgelösten Bildes einer Probe kann man LA-ICP-MS auch nutzen um Informationen eines Feststoffes in der Tiefe zu gewinnen. Beispiele für solche Tiefenprofile sind Schichtprofile in Speichermedien oder bestimmte Mineralien. Um solche Strukturen zu charakterisieren braucht man eine empfindliche analytische Methode mit hoher Tiefenauflösung, wie dies der Fall ist für LA-ICP-MS. Durch konventionelle Lasersysteme in LA-ICP-MS kommt es durch den verhältnismässig langen Laserpuls zu Wärmetransport in der Probe. Dies führt zu Umverteilung im Material, wodurch die Zusammensetzung in der Tiefe verändert wird. Dies besonders bei leitenden Materialien, welche häufig in moderenen Technologien gebraucht werden. Wenn man von Nanosekunden- zu Femtosekundenpulsen wechselt, wird dieser Wärmetransport im Material minimiert. Zusätzlich braucht man für ein hochaufgelöstes Tiefenprofil ein homogenes Strahlprofil, welches einen gleichmässigen Abtrag des Materials erlaubt. Obwohl man im Zusammenhang mit Nanosekundenlasern seit 1997 bereits solch eine Homogenisierung verwirklicht hat, gibt es bis anhin keine Möglichkeit für Femtosekundenlaser im Bereich fs-LA-ICP-MS. Das Ziel des zweiten Teiles dieser Arbeit war deshalb einen homogenen Laserstrahl für Femtosekundenlaser zu erreichen. Dafür wurde das Prinzip der abbildenden Optik angewendet. Durch das Abbilden einer Lochblende in der Bildebene einer optischen Linse wurden gut definierte Krater mit flachem Kraterboden erzeugt. Anschliessend wurden die analytis-

chen Eigenschaften dieses Aufbaus ausgewertet. Dafür wurden verschiedene Proben mit genau definierten Schichtdicken gemessen. Die ersten Tiefenprofilmessungen von Chromschichten auf verschiedenen Substraten wurden mit simulierten Tiefenprofilen basierend auf Gauss und Super-Gauss Lasersintensitätsprofilen verglichen. Dabei wurde gezeigt, dass sich das gemessene Tiefenrofil dem simulierten Tiefenprofil mit einem Super-Gauss Laserintensitätsprofil annähert. Durch den bekannten Aufbau der gemessenen Proben und den scharfen Übergängen zwischen den Schichten konnte die Tiefenauflösung des Systems nach ISO Standard bestimmt werden. Dabei wurden Tiefenauflösungen in Abhängigkeit der Tiefe bestimmt, wobei für oberflächennahe Übergänge eine Auflösung von < 50 nm und für jene in tieferen Lagen eine Auflösung > 100 nm bestimmt wurden.

Zusammenfassend beschäftigt sich diese Arbeit mit zwei Schlüsselproblemen der modernen LA-ICP-MS bezüglich Quantifizierung und Aufbau. Zum einen der Auswahl der richtigen Referenzmaterialien, mit einem spezifischen Fokus auf die Festphasensensitivität, um Elementfraktionierung vorzubeugen. Zum Anderen mit der Homogenisierung von Laserstrahlen für Femtosekundenlaser für Laserablationsanwendungen um hochauflösende Tiefenprofile zu erreichen.

Acknowledgement

My eternal thanks goes to many people, without whom I would have not started, nor finished this challenge.

First, I would like to express my sincere gratitude to my advisor Prof. Dr. Detlef Günther, for the continuous support of my Ph.D. study and research, for his patience, motivation, and knowledge, he passed on. His guidance helped me in all the time of research and writing of this thesis. I am also very thankful for the possibilities to attend conferences and research groups around the world, where I had the chance to get to know many inspiring scientists. And I would like to thank Prof. Dr. Thomas Lippert and Dr. Joachim Koch for agreeing to co-referee my thesis.

I am also grateful to Joachim Koch for all the knowledge you passed on. For your supervision during the first important years, for showing me the laser technology and all the physical background I learned.

A special thanks goes to the whole current and past "Günther Group": Bodo, for all your support and confidence in me, Alex and Gunnar for the analytical and scientific support, Marcel for introducing me to the Günther family during my Master thesis, Lorenzo for being your-self, always willing to help and open for any kind of discussion. Jovana, Thomas V., Stefan, Kamyar and Lyndsey for being the G141 office team, sharing chocolate and coffee and not to forget the tea and of course for all your support. Mohammad and Christoph for bringing new energy into the group! And a big thank you to the 'Arbeitsbesprechungs'-Team Benito and Thomas for being warm-hearted and always there, with an open door, willing to help and listen. And of course a huge thank you to Nicole for all your help, support and encouragement throughout these four years. I also want to thank the former colleagues Daniel Fontaine, Steffen Allner, Olga Meili and Sabrina Gschwind.

A big thank you goes to the D-CHAB workshop team, especially Roland Mäder and Philippe Trüssel for all your support and amazing work.

A special gratitude goes to my students, who did a great job. It was so much fun to work with you, thank you, Marcel Müller and Christoph Neff.

The reviewers of my thesis chapters are much thanked for their suggestions and advises to help improve my thesis. Thank you very much: Nico Santschi, Christof Schneider, Laura Hendriks, Fabian Steinebach, Stefan Kradolfer, Christoph Neff, Nathan Baumli, Urs Käser.

My sincere thanks also goes to Christof Schneider, Michael Horisberger, Max Döbeli, Frank Krumeich, Eric Reusser, Christian Mathis, Aaron von Conta, Tran Trung Luu, Jorge Pisonero and Aline Fluri for all the analytical support with RBS, SEM, AFM and CM, all your scientific input and advise.

A special thank you also goes to Dieter Garbe-Schönberg and Samuel Müller for the collaboration concerning the Si fractionation, for all your support and scientific input. Visiting you in Kiel was not only scientifically, but also socially an important stay during my doctoral studies.

Deep gratitude has to be given to everyone who crossed my path and helped me over many different periods during my PhD studies. Especially, to the once greatest soccer team at Hönggerberg (Dani, Aaron, Seppi, Lyndsey, Jürgi, Fabianski, Chris, Granpa, Jouri), Olga Nazarenko and Ilia Moraz to cheer up the long lasting hours in the practicum and of course all the pep talks during many coffee breaks and lunches with Nico Santschi, Sebastian Schnoz, Oli Gröninger, Christian Marro, Fabian Brühning, Fabian Jähnig, Daniel Zindel, Micha Calvo, Jan Bloch and the famous Jahrestag, Lukas Langenegger. A big thank you goes to the VAC board for the great times and the fun we had together.

A special thank you goes to Corina Keller. Without you, the story at Hönggerberg would have never started. I will always remember our plan B. And I would also like to thank Iris Kalkman for your continuous support and friendship since our studies at ETH.

My eternal gratitude goes to Lyndsey Hendriks. Your help, support and encouragement throughout all the years. We started **together**, we now finish **together**! Without your daily support in all matters of life, I wouldn't have been able to tackle this challenge as I could. Thank you very much.

Furthermore, I cannot forget the help from the ladies Nicole, Lyndsey, Laura, Nora and Luzia. All the running hours over lunch time to get a free mind after hard working hours in the lab or office. All the trips and escape rooms we managed together. Thank you so much to all of you, for the continuous support with any kind of problem. We had

so much fun together. And not to forget the most important anecdotes: "Die Drei Die Immer Lachen", "Nur no eine!", "Chasch nid alles ha", "Bisch sicher, dass de Ballon nid zvill Luft drin hät!?"

And finally, last but no means least, I am eternally grateful to my family. Danke Mama und Papa, dass ihr immer hinter mir steht. Mich immer unterstützt und immer an mich glaubt. Die unzähligen Anrufe, bei welchen ihr mir immer zuhörten und mich zurück auf den Boden der Tatsachen holten. Tamara, du warst schon immer mein grosses Vorbild. Ohne deine Zuversicht wäre ich heute nie da, wo ich jetzt bin. Jan und Till, die besten kleinen grossen Brüder, die man sich vorstellen kann. Vielen Dank für eure Unterstützung. Und in der Reihe der Geschwister, natürlich auch ein riesiges Dankeschön an Nashi! Ohne deine Inputs wäre ich glaub so an manchen Matlabaufgaben gescheitert. Aber auch die Pep-talks während unseren Laufrunden haben mir immer geholfen. Oma, dass du mich in China besucht hast, einfach unvergässlich, vielen Dank! Danke Padrine für deine Unterstzützung! Und natürlich auch ein riesiges Dankeschön an Herrn Dr. Steinebach. Dich an meiner Seite zu haben, gab mir sehr viel Kraft. Mit dir zu lachen und das Leben zu geniessen! Danke, dass du immer an mich glaubst und für mich da bist.

Contents

Part I

Introduction

"The secret of getting ahead is getting started."

Mark Twain

New definitions and interpretation of *Analytical Chemistry* have been discussed as a competition in 1992 within the *Fresenius' Journal of Analytical Chemistry*. During this, the first prize was awarded to K. Cammann for the following definition:
"Analytical Chemistry is defined as the self-reliant, chemical sub-discipline which develops and delivers appropriate methods and tools to gain information on the composition and structure of matter, especially concerning type, number, energetic state and geometrical arrangement of atoms and molecules in general or within any given sample volume. Modern Analytical Chemistry can also be considered applied physical chemistry. In Analytical Chemistry, special techniques are used to transform measured chemical signals, derived mostly from specific interaction between matter and energy, into information and ordered knowledge. Thus this discipline succeeds in establishing exciting, new and unique possibilities which drastically expand our perception of the material world, by creating three-dimensional pictures of the true qualitative and quantitative chemical reality inside a material sample. Its magnificent cognitive power is also heavily used in the process of knowledge accumulation and theory formulation by a variety of other natural scientists." [1]

Nowadays, analytical chemistry is not only a key player for many natural scientists but also for society, e.g. regarding environment and technological advances. For instance in Earth Science, geologists seek to understand the formation of ore deposits. In addition, they explore new deposits in order to cover the continuing need of rare earth elements, which are currently used for many modern technologies. According to Cammann analytical chemists are confronted with four basic questions:[1] *What?, Where?, How much?, What arrangements, structure or form?* and their major role is to develop reliable meth-

ods and tools in order to find the true answers thereof. Hence, over the past few decades a tremendous increase in different methods and tools have been achieved. Starting from classical gravimetric and titrimetric analysis, which were addressing question of how much, especially in chemical branches, the possibility to study the molecular composition of biologically important liquids or the complex elemental composition of geological samples is nowadays possible.[2] **M**ass **S**pectrometry (MS) provides a substantive portion to characterize and identify compounds from molecular or atomic mass, in many fields of science. In areas of for example geology, forensic science, bioscience, and material science, the elemental information of a sample is important to determine purity, bioavailability, toxicity, and a host of other critical properties.[2–4] The dawn of mass spectrometers started in 1897, when J.J. Thomson discovered the electron. He reported for the first time the mass-to-charge ratio *(m/z)*,[5] as basis of all MS systems. Soon after his discovery the first MS was built,[5] and its initial contributions to science were the demonstration of isotopes, which stimulated the ongoing discussion about the structure of atom. Ever since the field of MS has expanded to its present-day size and the continuous development have resulted in a variety of hyphenated MS systems.

If a sample in solid phase is the target of the analysis, there are still many challenges. Most routine analysis are still bound to dissolutions or digestions of the solids in order to gain information about the different analytes and their concentrations. Such systems sometimes require intensive pre-treatments and can give rise to many error sources. Thus, recalling the example of ore deposits, where different rock types act as sample targets the analytes can only be extracted by digestions. Afterwards, they can for example be identified and quantified by liquid based **S**olution **N**ebulization **I**nductively **C**oupled **P**lasma-**M**ass **S**pectrometry (SN-ICP-MS). SN-ICP-MS has become one of the most important analytical methods to investigate trace-elemental composition in many different areas, such as geology, forensics science, health, bioscience, nanotechnology, material science, industrial process control or semi-conductor industry.

It was only in 1985 when Gray *et al.* introduced **L**aser **A**blation-**I**nductively **C**oupled **P**lasma-**M**ass **S**pectrometry (LA-ICP-MS),[6] which opened up the possibility for direct solid analysis, retaining the advantages of ICP-MS as fast, multi-elemental method with low limits of detection and the capability for isotopic discrimination. In this method,

high-energy pulsed laser systems are focused on a sample surface and are used as the direct solid sampling tool. Since its discovery, LA-ICP-MS is a rapidly developing method and plays an important role in advancing knowledge in Earth Science, especially with respect to micro-geochemistry and mineral formation. Recalling the example of ore deposits, LA-ICP-MS has a long history for understanding and exploring their formation. Already at the end of the last century LA-ICP-MS was used to measure the element concentrations in fluid inclusions.[7,8] Hereby, one of the key features of LA-ICP-MS for spatially resolved analysis of solid samples was exploited. Development of *fast-washout* LA cells [1] [9] and in particular the combination thereof with newly developed ICP-TOFMS systems[10] have pushed the capabilities of LA-ICP-MS forward and nowadays high-resolution elemental imaging has emerged as a promising method for the determination of major, minor and trace elements in solid samples.[11,12] Contrary to fast-evolving high-resolution multi-elemental imaging by LA-ICP-MS, a remaining challenge is the matrix dependency of the LA process. Owing to the fact, that LA is being the sampling tool in LA-ICP-MS, understanding the LA process is pivotal in order to obtain high accuracy and extend the capabilities of LA-ICP-MS.

Working principles of LA-ICP-MS

In LA-ICP-MS the analytes are directly sampled from the solid surface by a pulsed laser beam of short laser pulses. The LA-generated aerosol containing all the analytes is transported into the ICP, where the aerosol is digested, i.e. vaporized, atomized, and ionized. The ions are extracted into the MS, in which they are separated by their mass-to-charge ratios and finally counted by specific detection systems. Generally, in LA-ICP-MS the MS response is recorded as intensity *vs.* time, i.e. transient signal. The basic set-up is displayed in Figure I.0.1 and can be separated into three different parts, which will be discussed in more detail in the following sections:

[1] The washout time of a LA cell is generally determined by the time a single LA pulse takes to decrease to a specific value of its peak maximum of its transient signal and is related to the aerosol dispersion within the transport system between the LA site and the ICP.

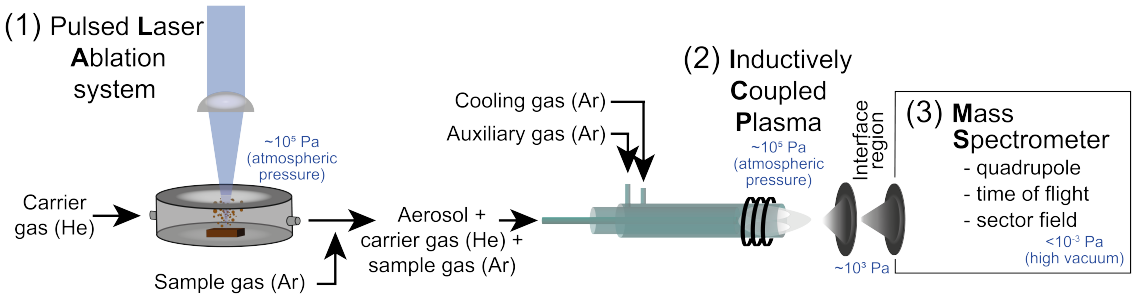

Figure I.0.1: Schematic set-up of **L**aser **A**blation - **I**nductively **C**oupled **P**lasma - **M**ass **S**pectrometry.

1. **Pulsed laser ablation system**

   The pulsed lasers (**L**ight **A**mplification by **S**timulated **E**mission of **R**adiation) commonly applied in LA-ICP-MS can be separated by their pulse duration into nanosecond (ns) and femtosecond (fs) laser systems. When a high energy laser pulse (above 10^9 J/cm^2) is focused onto a sample surface, material is removed. This material removal is called laser ablation (LA) and can be described by four sequential phases (for more details on the LA process see part II, chapter 2 and part III, chapter 6):[13]

   (a) Energy absorption of the incoming laser pulse by the electrons of the sample.[14]

   (b) Energy transfer from electrons by radiative and non-radiative transition processes. [2]

   (c) Ejection of particles (i.e. atoms, molecules and ions) from the sample surface due to energy absorption and transfer within the sample.

   (d) Formation and expansion of a dense plume of neutral and ionized gas of *ejecta* (i.e. hot plasma).

   The ejected particles form the so-called LA-generated aerosol are the information carrier of the sample's composition. In LA-ICP-MS the sample is placed in an air-tide LA ablation chamber, which is flooded by a carrier gas to transport the LA-generated aerosol to the ICP. However, LA does not always result in accurate quantification, mainly due to laser-induced,[16] and ICP-induced fractionation effects.[17] Concerning the LA-site, its material dependency on one side and a number of laser parame-

[2] Radiative transitions: energy emission by photons – Non-radiative transitions: energy transfer from excited electrons in form of phonons, which are associated with lattice vibrations of solids.[15]

ters on the other side highly influence the chemical composition and particle size distribution (PSD) of the LA-generated aerosol.[18] Indeed, depending on the laser pulse duration (i.e. ns or fs),[16,19] wavelength,[20–22] energy density,[23–26] repetition rate,[26–28] spot size,[26] type of carrier gas,[29] and laser beam profile,[30,31] as well as the sample type[32,33] the formed particles can greatly vary in their morphology and chemical composition. Generally, it was shown that by the choice of an adequate laser system such fractionation effects could be minimized.[34] On the other side, by matrix matched analysis and appropriate calibration strategies such effects could be cancelled out and accurate quantification of various different samples was possible.[35–37]

2. **Inductively coupled plasma – ICP**

After the material is ablated, the LA-generated aerosol is transported to the ICP – where gas-phase ions are generate and being analysed later on within the MS. As schematically shown in Figure I.0.1 the ICP is generated in a horizontally aligned torch. The general set-up of an ICP torch was first developed by Reed in 1961[38] and in its simplest form contains three concentric quartz tubes. The central channel is used to guide the sample to the argon plasma. In LA-ICP-MS this gas stream consists of a mixture of He and Ar which carries the LA-generated aerosol, while in SN-ICP-MS only an Ar gas stream carries a fine aerosol of analyte containing droplets. The middle channel directs the main Ar gas stream for the generation of the plasma. To prevent the quartz tubes from melting, the outer tube is used as cooling channel. As depicted in Figure I.0.1 a water-cooled induction coil (usually a hollow copper-coil) is wrapped three times around the outer quartz tube. This coil delivers an oscillating current (between 27 and 41 MHz) to the torch and therefore generates a magnetic field around it, which is needed to sustain the plasma. The oscillating field in the coil is powered by a radio frequency (RF) generator and the plasma is started by a Tesla spark, which introduces free electrons. Such seed electrons can collide with Ar gas atoms and ionize them, which in turn releases more electrons. The generated ions and electrons interact with the oscillating field, and hence are accelerated and can collide with other Ar atoms to generate further ions or atoms by ion-electron recombination. At some point an equilibrium between ion-

ization and recombination is reached and a stable plasma is formed, which on its net scale is neutral. As a result of these collisions the plasma is heated up to temperatures of 7'500 K.[39]

This intense heat in the plasma leads to the decomposition of the introduced sample aerosol and causes excitation of atoms. Thus initially, the ICP torch was applied in the field of spectrochemical analysis in e.g. optical emission spectroscopy.[40,41] However, the enormous heat not only excites the atoms, it also leads to efficient positive ionization, hence in 1980 Houk *et al.* coupled the ICP torch as an ion source to mass spectrometry.[42] By applying the Saha-Eggert equation,[43] considering a plasma temperature of 7500 K and an electron density of 10^{15} cm^{-3}, the degree of ionization for different elements can be calculated and result in efficiencies between $6 \cdot 10^{-6}$% for neon up to nearly 100% for sodium.[43] Furthermore, most of the elements in the periodic table, classified by geochemistry as *lithophiles* or *siderophiles* are efficiently ionized (> 90%), whereas the class of *chalcophiles* show lower degrees of ionization.

3. **Mass analyzers – MS**

After formation of the ions within the ICP torch, they will be extracted through a so-called interface region (see Figure II.3.2) and eventually transferred into the MS. This interface consists of two cones (diameter $0.7 - 1.2$ mm), which provide a stepwise reduction of the pressure, from atmospheric pressure in the ICP torch down to a pressure below 10^{-3} Pa in the MS region. The first cone (sampler cone) extracts the ions directly from the plasma while the second cone (skimmer cone) is the entrance to the MS. After the skimmer cone, the cloud of ions and electrons experiences a *space charge* effect.[44] Ion lenses are introduced behind the skimmer cone in order to reshape and stabilize the divergent ion beam. Due to the transmission of neutrals, ions, electrons and photons, the mass analyzer and detector systems are usually placed off axis from the incoming analyte beam. This way the unwanted particles are removed and only the positively charged ions are guided through the mass analyzer units and finally reach the detector.

Nowadays, many different mass analyzers in combination with ICP as ion source exist. Their basic separation techniques include magnetic fields, electromagnetic

fields, time of flight and radio-frequency electric fields.[45] Even though they all make use of static or dynamic and/or magnetic fields, each of these mass analyzers are based on different principles, resulting in unique properties. Generally, in scanning analyzers, ions are successively transmitted and only after one cycle the scan is restarted. In the case of quasi-simultaneous transmission, such as time of flight[10] and distance of flight,[46] all ions of an ion cloud are simultaneously extracted into a field free region, where they are separated by their velocities and successively detected. The mass resolution R is defined as the ratio of m/z, at which the ion of interest is detected, to the mass difference Δm needed to resolve it from the neighbouring m/z with a valley definition of 10% (see equation (1)).

$$R = \frac{m}{\Delta m} \tag{1}$$

The techniques used here are summarized in Table I.0.1 and discussed in more detail within the following sections.

Table I.0.1: Characteristics of mass analyzers for LA-ICP-MS.[18]

Mass analyzer	Separation technique	Mass resolution	Ion Sampling	Detector range
Quadrupole	radio-frequency field	<350	continuous	10^9
Sector-field				
- low resolution	magnetic field	300	continuous	10^{12} (with FC*)
- medium resolution	magnetic field	4000	continuous	10^{12} (with FC*)
- high resolution	magnetic field	10'000	continuous	10^{12} (with FC*)
TOF	time of flight	>4000	pulsed	10^6

FC - Faraday Cup, see paragraph 3.4

3.1 Quadrupole mass analyzer

The principle of quadrupole (q) mass analyzers is the flight path stability of different ions in an alternating radio-frequency field. qMSs consist of four parallel and equidistant rods. The ions are introduced into the MS along the z-axis and enter the region between these four rods at a specific kinetic energy. An alternating current (AC) and a direct current (DC) are applied to these rods. Through one pair of opposite rods a positive DC potential, whereas through the other pair a negative DC potential is applied. Indeed, low mass ions are mostly affected by the AC potential,

while high mass ions are heavily affected by the DC potential. For example, if the pair of rods with negative potential are considered, the high mass ions are mostly attracted towards the rods and eventually strike the electrodes, while low mass ions respond to the AC current and are focused towards the middle of the four rods. Finally, depending on the introduced AC/DC potentials, ions with specific *m/z* hold a stable trajectory between the rods and are able to travel along the z-axis towards the detector. Mathematically, this process is described by the Mathieu equations (2)-(4), which were already developed around 1870 to describe the motion of vibrating membranes and are nowadays widely used to explain the motion of ions trapped in quadrupole fields.[47]

$$\frac{\delta^2 u}{\delta \xi^2} + u \cdot \left(a_u - 2 \cdot q_u \cdot cos(2\xi)\right) = 0 \tag{2}$$

Here, u stands for coordination x or y, ξ the dimensionless time, defined as $\xi = \omega \cdot T/2$ and ω the frequency of the alternating current. The stability parameters a_u and q_u are the dimensionless DC and AC amplitudes, respectively:

$$a_u = \frac{-8 \cdot e \cdot U}{m \cdot {r_0}^2 \cdot \omega^2} \tag{3}$$

and

$$q_u = \frac{4 \cdot e \cdot V_0}{m \cdot {r_0}^2 \cdot \omega^2} \tag{4}$$

With e being the electronic charge, V_0 the electronic zero-to-peak RF storing potential, U the applied DC potential, m, the mass of the ion and $\omega/(2 \cdot \pi)$, r_0 the effective radius of the quadrupole field. Finally, plotting a_u versus q_u results in a stable oscillation zone for ions with a defined mass-to-charge ratio.[45]

Nowadays, quadrupole mass analyzers have become the most common MS types. They comprise several advantages such as no requirement for very high vacuum, and their relatively fast and simple operation for high-throughput analysis. In addition such MS systems are rather cheap. Their disadvantages include low transmittance, a low *m/z* cut-off, and low mass resolution (generally one mass unit). Indeed, most qMS are not able to resolve prominent interferences (see Table I.0.2), which in return can make the determination of ultra-trace elements challenging.

Table I.0.2: Examples for common interferences in ICP-MS, which cannot be resolved by qMS systems. In many cases, an alternative isotope is listed.

Analyte	Interference	Required R	Possible alternative	Type
$^{27}Al^+$	$^{12}C^{15}N^+$	1454	–	polyatomic
$^{28}Si^+$	$^{14}N_2^+$	958	–	polyatomic
$^{52}Cr^+$	$^{40}Ar^{12}C^+$	2375	$^{53}Cr^+$	polyatomic
$^{54}Fe^+$	$^{54}Cr^+$	73890	$^{57}Fe^+$	isobaric
$^{56}Fe^+$	$^{40}Ar^{16}O^+$	2502	$^{57}Fe^+$	polyatomic
$^{58}Fe^+$	$^{40}Ar^{18}O^+$	2479	$^{57}Fe^+$	polyatomic
$^{63}Cu^+$	$^{40}Ar^{23}Na^+$	2790	$^{65}Cu^+$	polyatomic
$^{69}Ga^+$	$^{138}Ba^{++}$	2549	$^{61}Ga^+$	isobaric

3.2 Sector-field mass analyzer

Sector-field (sf) mass analyzer are in comparison to qMS, very sensitive systems, due to a higher extraction voltage, and can reach much higher resolutions up to $R = 10'000$.[4,48] The separation is based on the m/z dependent flight path in a magnetic field, oriented normal to the ion flight path. This way, the ions follow a circular trajectory, according to the Lorentz force and the m/z dependent flight path can be described by the following formula:

$$\frac{m}{z} = \frac{B^2 \cdot r^2 \cdot e}{2 \cdot V} \tag{5}$$

The kinetic energy of the ions is introduced by an acceleration voltage in the beginning and given by the potential V, while B is the strength of the applied magnetic field. The ions reaching the magnetic field possess a high velocity spread, resulting in a peak broadening. Hence, by combining the magnetic sector with an electrostatic analyzer (ESA) the ions are refocused and their velocity spread is compensated for. The magnetic sector and ESA can be arranged in both ways – First the ESA then the magnet, which is called the Mattauch-Herzog geometry, while the other way around is called the Nier-Johnson geometry.[3] The mass resolution can be modified by the diameters of entrance and exit slits before and after the mass analyzer systems. For higher resolution, the width is minimized. This in return also decreases

the ion transmission and results in less overall sensitivity.[4] In the case of sfMS not only sequential detection is possible, but also simultaneous detection possibilities exist in combination with multicollector ICP-MS.[49]

3.3 Time of flight (TOF) mass analyzer

The separation of ions by TOF mass analyzers is based on the fundamental principle of the direct relation between the kinetic energy of an ion and its mass and velocity. By introducing the same kinetic energy on a population of ions, their velocities will depend on their masses. These ions can then be separated in the time domain. After the initially imposed kinetic energy the ions fly in a field-free region (i.e. flight tube) and eventually reach the detector. The time dependency of the m/z is described by the following formula:

$$\frac{m}{z} = \frac{2 \cdot e \cdot V \cdot t^2}{L^2} \tag{6}$$

With $e \cdot V$ the energy, t the time and L the length of the flight tube. [3]

3.4 Detection systems

At the end of each mass analyzer, the ions reach a detector. The detection of the ions can for example be accomplished by direct charge measurements with a conducting electrode, i.e. Faraday detector.[52] In this system the current (I) from the charged species, striking the detector is equal to the number of ions (n) multiplied by the unit charges on each ion (z) and the fundamental charge (e):

$$I = e \cdot z \cdot n \tag{7}$$

The ion beams leaving the MS produce currents in the subfemto- to nanoampere range ($1\ fA = 6242\ ion/s$) and hence electronic amplification by 10^9-10^{13} need to be applied in order to convert the current into a voltage, which can be used to read the signal. Such Faraday cups (FC) are currently employed in isotope ratio mass spectrometers due to their high stability. In such systems, multiple FCs are placed in parallel.[52] Secondary electron multipliers (SEM) with discrete dynodes are nowadays the most common ion detection system for quadrupole MS systems. If ions

[3] ICP-TOFMS in combination with LA allows the detection of single LA pulses.[50,51] Due to the quasi-simultaneous detection capabilities and the high time resolution short transient signals arising from single LA pulses, high-resolution high-speed multielemental images can be obtained.[50,51]

strike the first conversion dynode of this system, secondary electrons are emitted. All subsequent dynodes generate an electron cascade and hence the incident of a single ion can be multiplyed by a factor of 10^6 or more.[52] This factor depends on the composition of the individual dynode surface, the acceleration per stage, the number of dynodes and the bias current circuit design. Concerning low signal intensities ($< 2 \cdot 10^6$ $ions/s$) the ions are measured in *pulse* counting mode. For higher signals the raw secondary electron current is directly processed in the *analog* counting mode.[52] This way, high dynamic detector ranges can be reached (see Table I.0.1). Overall, depending on the detection system which are incorporated different dynamic detector ranges are reached (see Table I.0.1). Besides such discrete dynode systems, secondary electrons can also be produced through a voltage across an insulating surface, this example of SEM variation are called multichannel plate detectors (MCP). Such detectors are used for TOFMS systems, where precise arrival times and narrow pulse widths, to allow fast signal processing, are required.[52]

Thesis outline

My dissertation research was devoted to the fundamental question of the LA process in combination with LA-ICP-MS. More specifically, two questions were addressed, namely the material dependent quantification bias obtained for silicate based samples and the usage of fs-laser systems for depth profile analysis by fs-LA-ICP-MS. After the first introductory part (**part I**), the content of this thesis is divided in the two above mentioned topic parts, which contents will be described here below.

Part II, which spans chapter 1 to 5, was driven by the ongoing challenges related to the nature of the LA process, in particular being highly material dependent. The first two chapters deal with the fundamentals of LA and the term elemental fractionation, which is responsible for constant recurring quantification errors obtained in LA-ICP-MS. Owing to the fact that LA-ICP-MS is widely used in Earth Science research, elemental fractionation on silicate based samples was of focus and the origins of this phenomena were addressed. An overview of all performed experiments is given in chapter 3 and material details are outlined. Chapters 4 and 5 deal with the results, including details on different calibration strategies applied in LA-ICP-MS. Their limitations will be outlined and the obtained sources of the elemental fractionation of Si highlighted.

The research efforts in **part III** deal with improving depth profile analysis by femtosecond (fs) laser beam shaping and covers chapter 6 to 8. Chapter 6 introduces the importance of depth profile analysis in many modern technologies and describes the key points to achieve high depth-resolution when LA-ICP-MS is applied. Chapter 7 and 8 highlight the progressive nature of this research: the first provides preliminary results and presents challenges related to fs-laser beam shaping, while the second addresses the analytical outcome with respect to depth resolution according to the ISO guidelines. A significant portion of this part has been published in Käser et al.[53,54]

Part II

Insights into the challenges regarding the quantification of geological silicate samples by state-of-the-art LA-ICP-MS

"When faced with a challenge, look for a way, not a way out."

David Weatherford

Chapter 1

Introduction

The upper continental crust, being the most accessible part of the Earth, has long been the target of geochemical investigations.[55] The most abundant elements in the Earth crust range from Oxygen, over Silicon to metals, like Iron, Calcium, Aluminium, Titanium, Manganese, and Magnesium (see Figure II.1.1). Due to the high abundance of Silicon, most rock types are based on silicate phases. For this reason, research in geology, including studies about the origin and differentiation of the Earth as well as the investigation of new ore deposits, involve the analysis of silicate based minerals. LA-ICP-MS is an important and very powerful analytical technique commonly applied to unravel the elemental and isotopic composition of such rock samples. The two key components to this success are (i) the possibility for the direct analysis of solid samples and hence the circumvention of digestion based analysis and (ii) the ability to quantify matrix and trace elemental composition during one course of analyses.

Due to non-stoichiometric effects, labelled elemental fractionation[23,56–60] (see part II, chapter 2 for more details) suitable standard reference materials (SRMs) are pivotal to evaluate the analytical accuracy of LA-ICP-MS. Indeed, such elemental fractionation make quantification one of the major challenges to date. Many research groups have investigated the importance of the calibration standards, and nowadays so-called matrix matched analysis is highly recommended.[35,37,61] Indeed, it has been shown that in cases, where the matrix composition of a given sample and the calibration material are matched, quantifi-

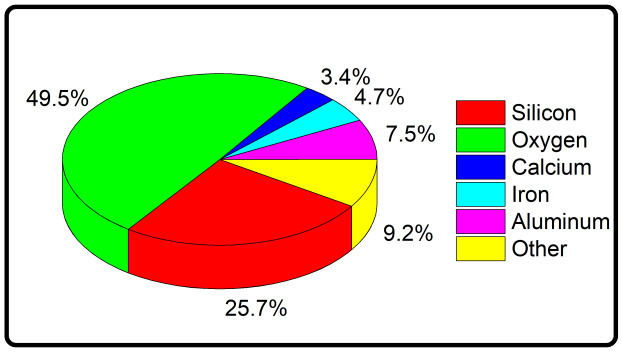

Figure II.1.1: Composition of Earth crust.

cation is most accurate.[35,37,61] The glass series of NIST SRM 61x (x = 0/2/4) have been the most commonly applied calibration materials in LA-ICP-MS.[62,63] Even though, these standards were intended for quality control and only about 100 kg have been produced in the 1970s,[64] they have since then been used in many different applications and determination of accepted values for other SRMs.[65–70] However, geologically relevant elements such as Ti, Fe and Mg are only present in low mass fractions and hence the natural abundances of these elements are typically not matched. Consequently, the NIST SRM 61x series is not well suited for the quantification of minerals,[71] and therefore more adequate SRMs are needed. Besides the required variety of SRMs, they also need to be homogeneous in the micrometer-scale regime. Indeed, due to evolutions towards high-spatial resolution analysis extremely homogeneous SRMs became very important. Nowadays, different approaches have been applied in order to produce such homogeneous SRMs. On one side, the U.S. Geological Survey employed a strategy which is similar to the production pathway used for NIST SRM 61x series.[72] In here, a powdered material is melted in a high-temperature furnace and then flash-cooled to prevent crystallization. This way glass-like materials are formed. However, similar to the challenges encountered during the production of the NIST SRM 61x series, they suffer from losses of volatile elements (e.g. Au, Ag, Ru, Tl). In another approach, synthetic sulfide standards are produced.[73] However, the production of homogeneous synthetic minerals is very difficult with respect to trace element composition. In addition to the manufacturing of glasses and minerals, pressed powder tablets have garnered more and more interest.[74,75] Garbe-Schöberg & Müller introduced the pro-

duction of pressed nano-powders without the usage of binders [1] allowing the production of many different SRMs with the possibility to add internal standards or isotopic spikes.[74] In the context of such a variety of different SRMs nowadays available, we reconsidered the term matrix-matched analysis and investigated the influence of the phase (i.e. glass phase, mineral phase, pressed powder) in comparison to matrix-matched analysis. In here, we focused on the elemental fractionation regarding the most abundant elements of the Earth crust, accessible by LA-ICP-MS. In addition, elemental fractionation processes in LA-ICP-MS with respect to the matrix elements of naturally occurring rock samples was explored and the influence of different quantification approaches was assessed.

[1] The general idea, when adding a binder, is to obtain compact and mechanically stable pellets, resistant for LA. However, adding a binder contains the risk of contaminating the SRM.

"In theory, there is no difference between theory and practice. In practice, there is."

Richard Feynman

Chapter 2

Theoretical background

2.1 Elemental fractionation

As already touched upon when explaining the working principles of LA-ICP-MS, analysis by LA-ICP-MS are often subject to quantification uncertainties due to so-called elemental fractionation.[23,56–60] It is generally referred to differences between the measured composition of the ablated material and the bulk sample and can be caused at three different stages within LA-ICP-MS systems: (1) The LA process, (2) the transportation of the LA-generated particles and (3) ICP-related processes. In order to understand the laser-induced elemental fractionation effects and the partly resulting ICP-related fractionation, the LA process itself and the formation of the particles need to be explained in more detail.

2.1.1 Theoretical background of LA

As described in part I, the deposition of optical energy into a sample is mediated by the sample's electrons.[76] Within the chain of the LA process, the first step therefore is the elevation of electrons to a conducting state.[76] The success of this elevation is highly material dependent and determined by the laser pulse duration. [1] Once the electrons are excited, the system relaxes to its equilibrium state. The involved relaxation chain and the characteristic time scales are:[77]

[1] For further details see Part III, chapter 6.

- 10^{-13} s – free electron heating and thermalization
- 10^{-12} s – hot electron gas cooling and energy transfer to the lattice
- 10^{-11} s – thermal diffusion into the bulk material
- $> 10^{-10}$ s – thermal melting and ablation

At this point, the difference between ns-LA and fs-LA needs to be emphasized: In the case of fs-LA the pulse already stops before the energy is being transferred to the lattice and therefore, thermal diffusion into the bulk material is reduced, whereas for ns-LA the pulse duration exceeds the lattice heating time and hence the thermal wave propagates into the sample, leading to a relatively large layer of melted material and heat affected zones.[78] [2] In both cases, the results of the relaxation processes are the ejection of a dense plume of neutrals and ionized gas.[13] The fundamental mechanisms controlling the removal of material by LA, however, are still being controversially discussed.[13,19,32,33,76]

According to Miotello & Kelly, there are three thermal processes which may result in material ejection upon laser heating, including (i) vaporization, (ii) normal boiling, and (iii) explosive boiling.[79]

LA by **vaporization**, including *sublimation* and *evaporation*, is considered when the temperature rise is directly followed by ejection of material from the surface.[79,80] It was calculated, that within 1 ns much less then a monolayer of material could be vaporized, if the vaporization velocities for different metals are considered as function of their boiling temperatures.[79] As a result, the contribution by vaporization is too slow to be responsible for the formation of particles using ns or fs lasers.[79]

On the other side, **normal boiling** as discussed by Miotello & Kelly involves heterogeneous nucleation at the boiling temperatures of the material.[79] This process predicts the formation of vapour bubbles, initiated by a variety of disturbances (e.g. gas or solid impurities, defects). An important obstacle to this mechanism is the fact, that these bubbles need to diffuse towards the surface, where they can escape. This motion, however, is very slow and hence can only be responsible for material removal if the pulse duration is long enough ($t_{pulse} > 1$ ns) and the energy density is sufficient. Therefore this mechanism

[2] Further details are described in Part III, chapter 6.

cannot be responsible for the material loss in fs-LA.[79]

The third process predicted by Miotello & Kelly is by excessive overheating, due to the high temperatures reached in both cases of ns- and fs-LA.[79] It assumes a phase explosion (**explosive boiling**), due to homogeneous nucleation. The excessive heating of the liquid leads to a thermodynamically critical temperature in a short period of time. It follows that this very hot region near the surface breaks down into vapour and liquid droplets.[79,81]

Bulgakova *et al.* also predicted the LA mechanism by ultrashort pulsed lasers as a result of **Coulomb explosion**, in the case of dielectric materials.[82] Upon irradiation of the surface, surface electron are being separated from their nuclei, resulting in charged surface regions. A strong electrostatic repulsion force causes an explosion of matter outwards.[82]

Within the next step of the LA process, the ejected matter forms a hot plasma above the surface,[13] which expands in space. LA in combination with ICP-MS is commonly performed under a gas stream used to transport the ablated material towards the ICP. Under these conditions, the plasma expansion can be described by the point-blast model published by Arnold *et al.*[83] and applied by Margetic *et al.*[77] for fs-LA. It assumes a gas with a constant heat capacity and density, in which huge amounts of energy are applied to a small volume in a very narrow time interval. Hereby the plume acts as a piston – the ambient gas is compressed and heated. An external shock wave propagating outwards is formed. At the same time, within the contact region, the molecules of the plasma plume collide with the ambient gas molecules or atoms and are reflected. This way an internal shock wave is formed, which propagates inwards. This results in a homogenization of the plume.[77,83] However, this model fails for high laser energy densities with respect to the LA threshold and laser pulse durations longer than the formation of the shock wave. In those cases, the use of the laser-supported detonation would be more appropriate to describe the plume expansion.[77,84] In this model plasma shielding is taken into account, which occurs, if the plasma absorbs the laser energy and hence, the laser energy which reaches the surface is reduced.[84]

Research on particle morphology, composition and size distribution of ns- and fs-LA-generated aerosol have been used to differentiate between different LA mechanisms.[19,32,33,85] In addition, material ejection was studied by shadowgraphy,[86,87] visualized by laser-induced light scattering,[88] and further predicted by modelling,[57] in order to follow the

formation mechanism of the particles and to better understand the influence of various parameters, such as laser energy density, wavelength, pulse duration, beam profile and repetition rate, in combination with LA as analytical tool. Understanding and being able to control the particle size distribution (PSD) might minimize elemental fractionation.[57] Up until now, elemental fractionation is still considered as being the major challenge regarding accurate quantification in LA-ICP-MS. Aforementioned three stages, where elemental fractionation can occur, will therefore be discussed in more detail in the following sections (2.1.2 - 2.1.4) and are summarized in Figure II.2.1.

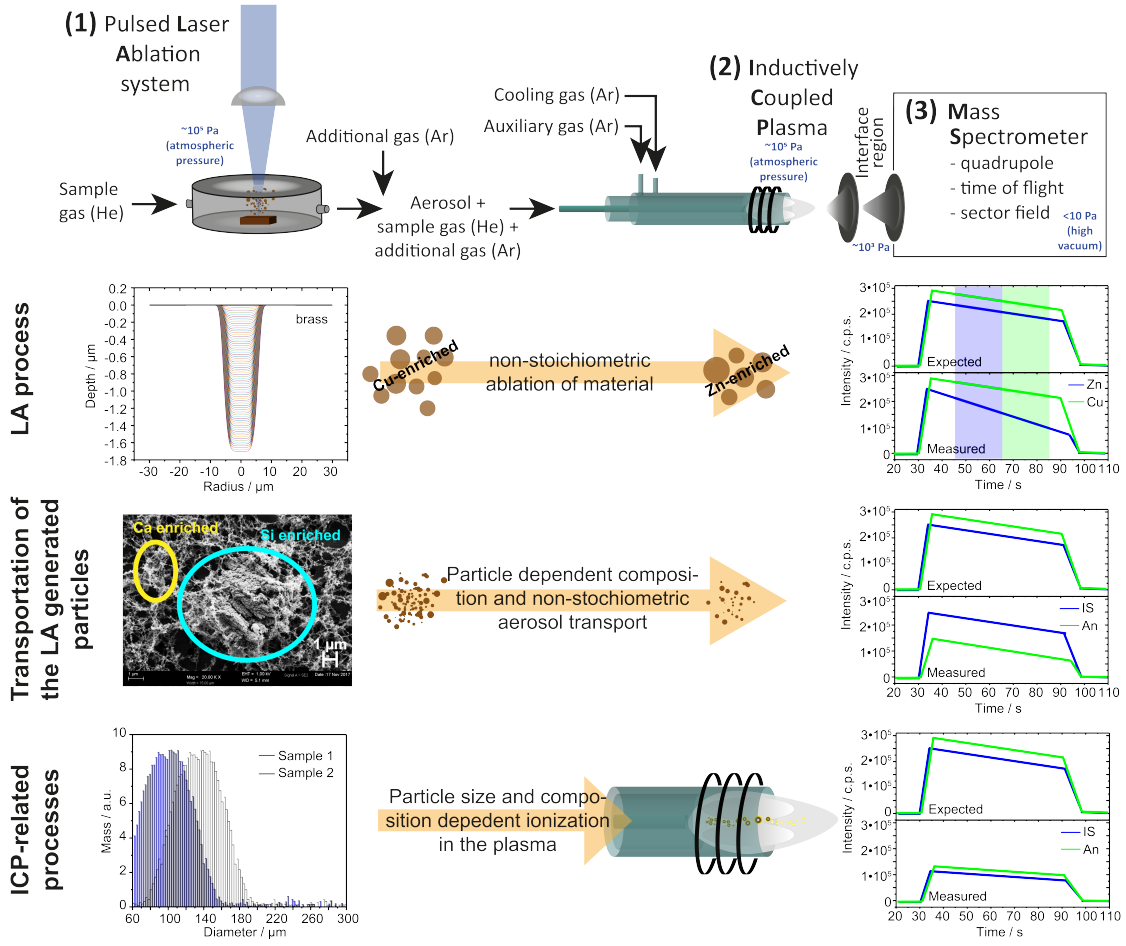

Figure II.2.1: Overview over elemental fractionation mechanisms. **LA process:** Enrichment or depletion of certain elements in the formed aerosol. **Transportation of the LA-generated aerosol:** Particle loss along the aerosol transportation system. **ICP-related processes:** Incomplete particle decomposition, diffusion loss or matrix dependent intensity loss.

2.1.2 Elemental fractionation induced by the LA process

The composition of the sampled material can either be enriched or depleted in certain elements,[19,89] due to the different physical properties of the elements ablated (i.e. boiling points, melting points, masses, volatilities, ionization potentials, condensation temperatures, ionic radii, field strengths).[59,87,90] Indeed, it has been shown that volatile siderophile/chalcophile elements, such as Zn and Pb, tend to evaporate more quickly and can therefore diffuse out of the sample more easily compared to less volatile elements.[32,37] Volatile elements can evaporate more easily within the first LA pulse and could therefore be depleted regarding the following LA pulses (as indicated in Figure II.2.1). This depletion will increase with increasing number of LA pulses on the same LA spot and the sample composition at the LA site and/or the particles may profoundly differ from the original one. For instance Glaus *et al.* reported on significant changes of the Cu/Zn ratios along the course of the analysis by ns-LA.[32] In addition, also particle-size dependent Cu/Zn ratios after ablation of brass were obtained. It was found that independent of the pulse duration (i.e. ns and fs) smaller particles were enriched in Zn while larger particles showed higher Cu contents.[32] However, in case of fs-LA, the overall stoichiometry of the fs-LA-generated aerosol agreed with the stoichiometry of the bulk sample, which was not the case for ns-LA.[19] Hence, in this example concerning fs-LA, if no other fractionation would occur, neither along the transportation nor within the ICP, no elemental fractionation within the final analysis would be obtained.

2.1.3 Elemental fractionation induced by non-stoichiometric aerosol transport

After the particles have been formed, they are transported to the ICP. As already touched on above, a broad range of particle sizes can be produced during LA[19,85,91] and in addition, also the composition has been reported to be size dependent.[32,33] Hence, regarding the transportation of the aerosol, a selective particle deposition, either by diffusion, gravitational settling and/or by inertial forces directly on the sample surface or within the transport tubing,[19] can result in transport-induced elemental fractionation.[92] Indeed, if e.g. brass is analyzed and the overall composition of the aerosol shows the same stoichiometry as the bulk, larger particles can be enriched in Cu while smaller particles are

enriched in Zn, as found in ref.[32] In this example, the larger particles may settle down due to gravitational forces, and hence the overall stoichiometry of the aerosol reaching the ICP has changed compared to the bulk, leading to a transport-induced elemental fractionation. This would result in an overall lower signal intensity for Cu (see Figure II.2.1). Consequently, such transport-induced elemental fractionation is reduced, if a narrow monomodal PSD is obtained. Koch *et al.* demonstrated a positive effect on the PSD when He was applied as carrier gas.[19,91] In addition, non-stoichiometric aerosol transport was found to be minimized to 2% if distances below 1 m between the LA site and the ICP were present.[19] Finally, transport efficiencies were found to exceed values of 90% and hence may only have a minimal effect on the overall elemental fractionation.[19]

2.1.4 Elemental fractionation induced by ICP-related processes

Given the LA-generated aerosol, all individual particles reaching the plasma need to be transformed into ions in order to obtain the elemental and/or isotopic composition thereof. Thereby, the degree of ionization of a single particle greatly depends on its size, composition and the time it remains in the plasma. With the beginning of this century not only LA-related elemental fractionation, but also ICP-related processes have been demonstrated to significantly contribute to the overall elemental fractionation.[93–95] In fact, a composition-dependent penetration depth of the particles/aerosol has been observed,[96] which affects the location in the plasma where vaporization, atomization and ionization occurs. Additionally, by studying mono-disperse micro-droplets with varying diameter but same analyte concentrations differences in detection efficiencies have been shown.[97] According to Niemax[97] the detection efficiency is better for bigger droplets, if complete ionization of the analyte at the position of the sampler cone is apparent. This is due to reduced diffusion of the ion cloud in front of the sampler.[97] If this principle is translated to dry aerosol particles, for example produced by LA,[95,97] decreased detection efficiencies are obtained, due to the immediate start of evaporation of the particle in the plasma, because of absence of water and water vapour.[97]

The challenge with a LA-generated aerosol is the broad PSD compared to a rather monodisperse aerosol obtained by traditional SN-ICP-MS, as well as the particle dependent composition. Generally, bigger particles, i.e. higher analyte masses, compared to smaller

particles require more energy for atomization. Therefore, the atomization process will last longer downstream of the ICP. This can result in incomplete vaporization of large particles and hence cause elemental fractionation.[95] Indeed, images of incomplete vaporization have first been reported by Aeschliman *et al.*[95] – After LA of pressed pellets made of Yttrium oxide, high-speed photography revealed that bigger particles could pass through the plasma intact. Further research by Kuhn *et al.*[98] revealed only complete vaporization for particles in the range of 90-150 nm, while more recent research by Koch & Günther[92] assumes complete evaporation of all particles below 200 nm. Overall, non-representative sampling of ions from the plasma, in combination with the particle size, results in ICP-induced fractionation and in addition, also mass-load dependent ionization efficiencies have been revealed.[59]

2.2 Quantification in LA-ICP-MS

In LA-ICP-MS, concentrations of the sample target can only be determined by comparing the signal intensities of the sample with the ones of a well-characterized standard reference material (SRM). Therefore, elemental fractionation always needs to be considered relatively, between the SRM and the sample target. With this respect, three theoretical aspects of elemental fractionation can be assumed:

1. Elemental fractionation between SRM and sample occur to the same extend
2. Elemental fractionation between SRM and sample are different
3. No elemental fractionation for the SRM is obtained, while for the sample elemental fractionation occurs, or vice versa.

In the first case, the effect of the elemental fractionation between SRM and the sample cancel each other out and accurate quantification is possible. In the second case, elemental fractionation will make accurate quantification demanding. The same holds true for the last case, if elemental fractionation only occurs in one of the two, quantification becomes challenging. Elemental fractionation in all cases can refer to only one element of interest or to all of them.
Concerning the third case, according to Koch & Günther,[88] elemental fractionation during

the course of analysis can be acceptable, if the different contributions from the LA process, the transport and the ICP-related fractionation compensate for each other, in a way that the overall fractionation cancels out to unity, as described in the following equation:

$$\frac{I_{An\,a,measured}}{I_{An\,b,measured}} = \frac{I_{An\,a,theoretical}}{I_{An\,b,theoretical}} \cdot \underbrace{F_{Laser} \cdot F_{Transport} \cdot F_{ICP}}_{F_{tot}} \tag{2.1}$$

With $I_{An,measured}$ and $I_{An,theoretical}$ the measured and theoretical responses, respectively and F_{Laser}, $F_{Transport}$ and F_{ICP} the respective contributions of each fractionation source. At the end, simple calibration strategies allowing for direct calibration using the sensitivity of the SRM (see equation (2.2)) are challenging.

$$S_{An,SRM} = \frac{I_{An,SRM}}{C_{An,SRM}} \tag{2.2}$$

With $I_{An,SRM}$ and $C_{An,SRM}$ being the intensity and concentration, respectively, of the analyte of interest in the SRM.

Only in case one and in addition having stable operating conditions (i.e. constant laser energies, no oscillations in the ICP) during the analysis a direct calibration using equation (2.2) is possible. It also requires the LA up-take rate between the SRM and the sample target being equal, i.e. the amount of material being removed per LA pulse needs to be the same between the SRM and the sample.

In order to correct for such differences in LA up-take rates and oscillating operating conditions (i.e. Laser energy and ICP ocsillations) different quantification strategies were developed (for details see section 2.2.1).[99,100] Moreover, occurrence of elemental fractionation requires so-called matrix-matched analysis. It has been reported that if the SRM and the sample target have similar matrix compositions, elemental fractionation between SRM and the sample cancel each other out and render accurate quantification possible. Nowadays, research not only focuses on understanding and ways to minimize elemental fractionation, [3] but also the development of newer and more adequate SRMs is tackled.[74] Even though, during the past few years non-matrix-matched calibration was successfully demonstrated for fs-LA-ICP-MS,[16,61,101] in most applications, matrix-matched analyses

[3] Minimizing elemental fractionation with high impact on analytical capabilities of LA-ICP-MS was for example shown by the application of fs-LA,[61] homogenization of the laser beam profile in the case of ns-LA,[25] or the switch of the laser wavelength to deep UV ($\lambda = 193\,nm$) in the case of ns-LA.[85]

is still pivotal.[102] The application of an adequate laser system (pulse duration and wavelength) and optimization of the laser ablation parameters (spot size and energy density) is crucial for the quantitative chemical analysis using LA-ICP-MS. The *golden rules* developed by Pisonero *et al.*[34,103] suggest to use laser wavelengths of 193 nm for the ablation of non-conducting materials and lasers with a pulse duration below 1 ps for the analysis of conducting materials. Furthermore, the ablation in He is strongly advised and nowadays state-of-the-art: it greatly increases the analyte signal intensities and reduces the deposition of ablated material onto the sample surface compared to Ar.[29,104]

2.2.1 Quantification using an internal standard

The general idea of the quantification strategy described by Longerich *et al.*[99] is the application of internal standardization. This concept is adapted from solution based anaysis, in which a well-known concentration of an internal standard (IS) is added to the solution in order to monitor instrumental drifts and other possible variations. The challenge in direct solid analysis is that the samples composition cannot be modified, i.e. the addition of an IS is impossible. However, if the concentration of at least one element within the sample is known, prior to LA-ICP-MS, it can serve as IS and sensitivity variations can therefore be corrected (see equation (2.3)). In addition to instrumental drifts (i.e. laser energy and ICP oscillations), the IS also corrects for differences in LA up-take rates. Ideally, the IS is homogeneously distributed within the samples and a main constituent thereof. It is either determined independently by a second analytical method (e.g. *EPMA*[4]) or calculated from the stoichiometric formula.

$$S_{An,Sample} = \underbrace{\frac{I_{An,SRM}}{C_{An,SRM}}}_{\substack{Sensitivity \\ SRM}} \cdot \underbrace{\frac{C_{IS,SRM}}{I_{IS,SRM}} \frac{I_{IS,Sample}}{C_{IS,Sample}}}_{\substack{Correction\,term \\ internal\,standard}} \tag{2.3}$$

From equation (2.3), the concentration of the analyte in the sample can be determined according to equation (2.4). The basis of this calculation is a *two-point-calibration.* [5]

$$C_{An,Sample} = \frac{I_{An,Sample}}{S_{An,Sample}} \tag{2.4}$$

[4] Electron Probe Micro Analysis.

[5] Calibration between $P_1(0,0)$ and $P_2(C_{An,SRM}, I_{An,SRM})$.

Here, $C_{An,Sample}$ denotes the concentration of the analyte within the sample, $I_{An,Sample}$ the background corrected intensity and $S_{An,Sample}$ the corrected sensitivity according to equation (2.3).

For further illustration, the effect of the IS on the concentration of SiO_2 is demonstrated in Figure II.2.2. Indeed, the red data point in Figure II.2.2a denotes the uncorrected $S_{An,SRM}$. In this case, the measured intensity of the sample (green) would result in 2/3 of the expected SiO_2 concentration. However, if the sensitivity $S_{An,SRM}$ is corrected by the IS according to equation 2.3 the calibration results in the expected concentration (blue).

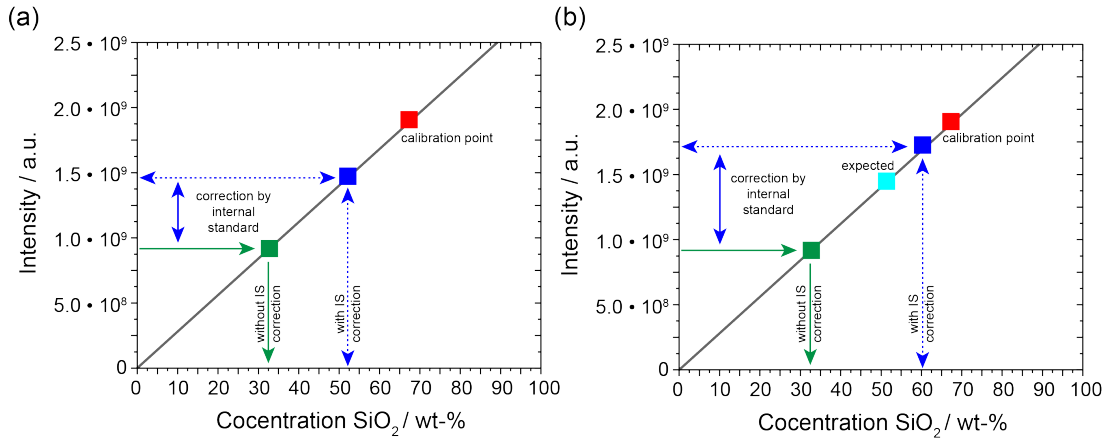

Figure II.2.2: Overview of the quantification strategies in LA-ICP-MS using an IS for the determination of SiO_2. ■ represents $I_{An,Sample}$, hence the measured intensity, without correction by IS, ■ is $I_{An,SRM}$ and therefore, the calibration point, and ■ is $I_{An,Sample,corr}$, so the measured intensity, using the correction term for the internal standardization (see equation (2.3)). In case (a) the obtained concentration using the correction by IS, results in the expected value. In case (b), ■ represents the expected concentration. Here, the correction by the internal standard leads to an overestimation of the concentration.

The application of a single or multiple different IS has been crucial for the development of the technique and in many examples it allows non matrix-matched analysis.[105–109] By far the most commonly applied SRM in LA-ICP-MS are the reference material series of NIST (i.e. NIST SRM 61x, x=0/2/4), which have a matrix unlike almost all naturally occurring geological materials.[110] The major challenge of this approach is the assumption that all analytes within the sample and SRM behave the same as the chosen IS. If this is not the

case, the determined concentration is biased. For instance, in Figure 2.3b, the correction by the IS does not lead to an accurate determination of the SiO_2 concentration, which can be caused by elemental fractionation. Understanding and extracting the origin of this bias is not straightforward. One measure to estimate the degree of elemental fractionation is the calculation of the so-called fractionation index (equation (2.5)), described by Fryer *et al.*.[56] It has been observed, that for elements such as Cu, Zn, Cd, Ag, Sb, Tl and Pb a relative elemental fractionation to Ca, used as IS, occurs as the LA progresses deeper into the sample.[56]

$$FI = \underbrace{\frac{I_{IS,Sample,1}}{I_{An,Sample,1}}}_{\substack{1^{st}\,half\,of\\ transient\,signal}} \cdot \underbrace{\frac{I_{An,Sample,2}}{I_{IS,Sample,2}}}_{\substack{2^{nd}\,half\,of\\ transient\,signal}} \tag{2.5}$$

The fractionation index, which has been extensively used in the literature, is an indicator for possible effects over time.[59,93]

In addition to the calibration strategy described above, the limits of detection (LODs) in LA-ICP-MS are usually calculated according to the following equation (2.6).[99] This formula takes the distribution of the mean of the number of measurements ($N_{background}$ and N_{Signal}) into account.

$$LOD_{An} = \frac{3 \cdot \sigma_{background}}{S_{An}} \cdot \sqrt{\frac{1}{N_{background}} + \frac{1}{N_{Signal}}} \tag{2.6}$$

With $\sigma_{background}$ the standard deviation of the instrumental background measurements, S_{An} the sensitivity of each analyte, $N_{background}$ the number of data points acquired for the instrumental background and N_{Signal} the number of data points used for calculating the ion signal intensity.

This calculation assumes a normal distribution of the background and may not always be adequate.[111] A normal distribution may be considered if the background signal is 70 counts per acquisition, while in cases, where the background signals are close to zero, assuming a normal distribution of the background typically leads to underestimation of the LOD.[18]

2.2.2 100-% mass normalization quantification approach

An alternative quantification approach is based on a 100-% mass normalization scheme.[62,100,112,113] The concept of this approach is that all elements of a sample are measured and their determined concentrations are corrected to result in 100 wt-%. One prerequisite to this concept is that one needs to know the sample type and its components in order to be able to correct for non-measurable components, such as non-metals. For example, when analyzing silicates, oxygen is one of the main components, but cannot be measured by ICP-MS. Thus, it is assumed that all components are present in their most common oxides. In addition, concentrations of components, such as H_2O, which cannot be measured should be as low as possible in their concentration. In 2008, Liu *et al.*[100] modified the initial approach[62,112] so that all concentrations of the analytes in the sample are first calculated according to a simple *two-point-calibration* described in equation (2.7) and only later is the sum normalized to 100 wt-% oxides. This concept results in a so-called ablation yield correction factor (AYCF) described in equation (2.8).

$$C_{An,Sample} = \frac{I_{An,Sample}}{I_{An,SRM}} \cdot C_{An,SRM} \tag{2.7}$$

$$AYCF = \frac{100}{\sum_{j=1}^{N} C_{j,Sample}} \tag{2.8}$$

Whereby j runs from analyte number 1 to N – the number of all analytes within the sample.

$$C_{An,Sample,corr} = AYCF \cdot \frac{I_{An,Sample}}{I_{An,SRM}} \cdot C_{An,SRM} \tag{2.9}$$

The corrected concentration of the analyte in the sample can be calculated according to equation (2.9). This approach to the 100-% mass normalization has been successfully applied to quantify anhydrous silicate minerals,[100] carbonates,[114] and glass silicates.[62] It is nowadays widely applied when LA-ICP-MS is used as imaging tool for geological samples.[50,51] This way, LA-ICP-MS can be used as a *stand-alone* method, "without prior quantitative knowledge of the chemistry of the sample",[110] gained by either an independent analysis or determined from known stoichiometry. Especially in combination with ICP-TOFMS systems, the use of a phase-specific 100-% mass normalization quantification strategy seemed to perform adequately.[115] The major analytical drawback of this approach is the implicit requirement that *all* elements present in significant concentrations are known

and accurately determined.

Going back in history, research either focused on the elemental fractionation occurring for the trace elements investigated,[56] or the quest for ideal ISs,[100,116] to circumvent the effect of elemental fractionation. However, when a 100-% mass normalization approach is applied, the accurate determination of all matrix elements must be guaranteed. Since most of the studies reported in the literature have been founded on Ca or single internal standards, the knowledge of the accuracy of the entire matrix quantification approach has not been available and forced the studies reported in the following chapters and our aim was to turn attention towards elemental fractionation obtained for matrix elements.

"Amateurs sit and wait for inspiration, the rest of us just get up and go to work"

Stephen King

Chapter 3

Experimental

3.1 Studies of elemental fractionation processes in LA-ICP-MS

The studies were channelled to gain insight into elemental fractionation processes and their effect on the accuracy of various different standard reference materials (SRM) and minerals. The focus was set on the importance of the solid phase, e.g. glassy or pressed nano-powder [1], rather than a miss-match in the overall compositions of sample and external standard. In general, the studies were performed on USGS BHVO2-G/BHVO-2P and BIR-1G/BIR-1P, and NIST SRM 610 reference materials (except section 3.1.3). [2] They are the three most often used SRMs for LA-ICP-MS analysis and well-characterized according to the literature.[68,117,118] Regarding BHVO-2P & BHVO-2G and BIR-1P & BIR-1G matrix matched analysis is fulfilled, while their phases are considered to be different: BHVO-2**G** and BIR-1**G** in glass phase, and BHVO-2**P** and BIR-1**P** in finely ground mineral/rock phase. The third type of SRM was a synthetic glass standard, in this case

[1] Provided by D. Garbe-Schöngerb & S. Müller produced according to ref. [74]

[2] In here, USGS stands for *U.S. Geological Survey* and NIST for *National Institute of Standards and Technology*. Throughout this part II, **G** and **P** behind each SRM are used to differentiate between the two phases: **G** = glass phase and **P** = pressed nano-powder.

a different matrix composition was present. The elemental fractionation studies can be separated into 4 different parts, which will be outlined in the following:

- **Investigation of LA up-take rates and LA-generated aerosol**

  The goal was to depict similarities and differences of the LA-generated aerosol (composition and morphology) and the LA process between SRMs of different solid phases, i.e. glass phase and pressed nano-powder phase. The LA up-take rate was assessed by evaluation of the crater depth using confocal microscopy (CM) and the morphology and composition of the LA-generated aerosol by scanning electron microscopy coupled to energy dispersive x-ray spectroscopy (SEM-EDX).

- **Investigation of elemental fractionation under different LA-ICP-MS conditions**

  In these experiments, the effect of different LA-ICP-MS parameters, including the LA-generated aerosol mass load in the ICP and *wet* plasma conditions, on the accuracy were investigated and compared to the experimental results at standard conditions. The goal was to highlight possible ICP-related origins of elemental fractionation.

- **Matrix-matched and non-matrix matched analysis of standard reference materials and mineral samples, focusing on the importance of the solid phase**

  In this section, an extensive comparison between different synthetic and natural silicate SRMs again processed into two different phases - pressed nano-powders and glass - was performed. In the first part, the accuracies, sensitivities and fractionation indices of these different SRMs were evaluated. In the second part, the different SRMs were used to quantify a variety of mineral samples (see Table II.3.5). They were selected to cover a range of 17 - 60 wt-% SiO_2. The goal of this section was to assess the overall accuracy obtained for different mineral samples and to investigate sample characteristics, which may help to predict an accurate choice of external standard for different minerals.

- **The effect of the pulse duration on elemental fractionation**

  In the last section the influence of the pulse duration on the elemental fractionation

and the overall accuracy regarding matrix elements was addressed. With respect to the pulse duration, higher accuracy for non-matrix matched analysis, due to lower elemental fractionation, in case of fs-LA was expected.

Experimental details about the different parts will be described in the following subsections (3.1.1-3.1.4), material details will be addressed in section 3.2 and data processing and measurement work-flow will be given in section 3.3.

3.1.1 Investigation of LA up-take rates and LA-generated aerosol

3.1.1.1 LA up-take rate investigated by Confocal Microscopy (CM)

The LA up-take rates of BHVO-2P and BHVO-2G were compared. Therefore 1, 5, 10 and 30 LA pulses at a spot size of 60 μm, 1 Hz LA frequency and two different laser energy densities of 5 J/cm^2 and 15 J/cm^2 were applied on both samples, using a ns-LA system (ArF Excimer ns-laser, GeoLas Q, Lambda Physics, Göttingen, Germany). The crater morphology and depth was assessed using CM [3] (PluNeox, Sensofar, Barcelona, Spain) at 50 fold magnification.

3.1.1.2 Particle size distribution (PSD) of LA-generated aerosol investigated by an Optical Particle Counter (OPC)

The PSD of the LA-generated aerosol of BIR-1P/G, BHVO-2P/G, and NIST SRM 610 after ns-LA (ArF Excimer ns-laser, GeoLas Q, Lambda Physics, Göttingen, Germany) equipped with a single volume LA cell was investigated using an optical particle counter (OPC) (Ultra High Sensitivity Aerosol Spectrometer, Droplet Measurement Technologies, Longmont, USA). The schematic set-up is depicted in Figure II.3.1. Particle sizes from 60 to 1000 nm in 99 equidistant bins were measured. To obtain acceptable particle counts, a dilution system for sub-micrometer aerosol (MD19 1i, Matter Engineering AG, Wohlen, Switzerland) was incorporated. The connection of these two systems was completed using a Y-junction and the spectrometer influx pump was set to higher gas flow rates than the chosen dilution gas flow. This way, no particles were lost but rather ambient air was sampled. The gas flow rates, dilution settings and LA parameters can be found in Table II.3.1. All measurements were repeated 3 times and finally averaged.

[3] Further details on the working principles of CM can be found in Part III, chapter 6.

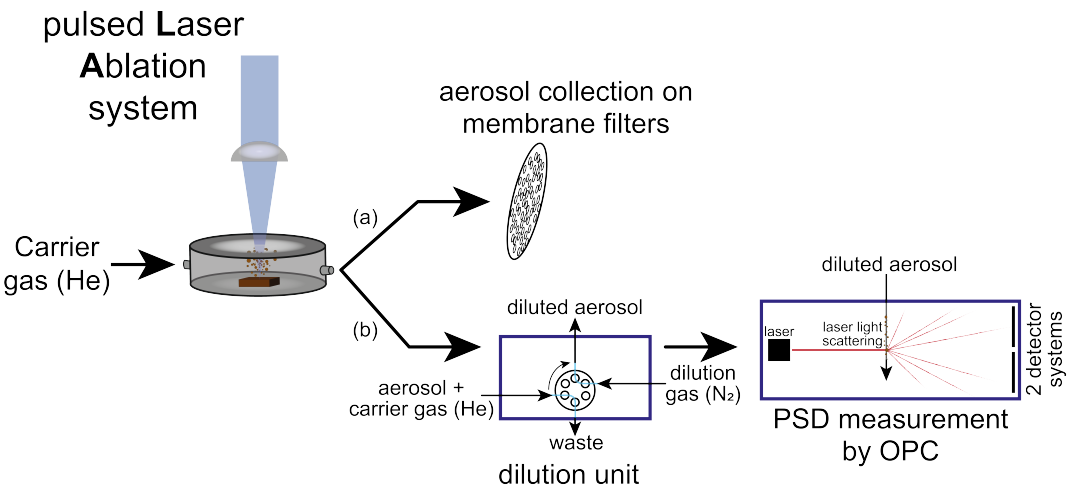

Figure II.3.1: Schematic set-up for LA-generated aerosol studies. (a) The LA-generated aerosol was directly collected on membrane filters after the LA cell. (b) The LA-generated aerosol was guided through a dilution unit before the PSD thereof was determined using an OPC system.

Table II.3.1: LA and OPC parameters for the PSD measurements. Generally, for smaller dilution settings a higher value of the dilution wheel speed is required. Exact dilution factors were neglected – only relative values were compared.

LA parameters	
Laser wavelength	193 nm
Laser energy density	15 J/cm^2
Laser spot size	60 μm
LA frequency	10 Hz
Number of LA pulses	$\approx$ 600 LA pulses
LA cell	single volume ablation cell (V=20 cm^3)
OPC parameters	
Carrier gas flow (He)	0.6 L/min
Dilution gas (N2)	0.13 L/min
OPC pump gas flow	0.05 L/min
Dilution wheel speed	3

3.1.1.3 Particle morphology and composition of LA-generated aerosol investigated by Secondary Electron Microscopy (SEM) - Energy-Dispersive X-ray Spectroscopy (EDX)

The particle morphology and composition of the LA-generated aerosol of BHVO-2P and BHVO-2G using a ns-LA system (ArF Excimer ns-laser, GeoLas Q, Lambda Physics, Göttingen, Germany) equipped with a single volume LA cell were investigated. The aerosol was collected on IsoporeTM membrane filters (0.4 μm pore size, HTTP, Merck Millipore Ltd., Cork, Ireland). In the next step, the aerosol collected on filters was examined by SEM (LEO 1530 Gemini, Carl Zeiss AG, Oberkochen, Germany). [4] In addition, the elemental compositions of individual particles of BHVO-2G with sizes exceeding several microns were investigated using SEM-EDX (FEI Quanta 200F, Thermo Fisher Scientific, Hillsboro (OR), USA). The applied LA parameters, in combination with aerosol morphology studies are shown in Table II.3.2.

Table II.3.2: LA parameters for aerosol collection on membrane filters.

LA parameters	
Laser wavelength	193 nm
Laser energy density	15 J/cm^2
Laser spot size	60 μm
LA frequency	10 Hz
Number of LA pulses	$\approx$ 600 LA pulses
LA cell	single volume ablation cell (V=20 cm^3)
Carrier gas flow (He)	0.5 L/min

[4] Further details on the working principles of SEM can be found in Part III, chapter 6.

3.1.2 Investigation of elemental fractionation under different LA-ICP-MS conditions

The experiments to investigate the elemental fractionation under different LA-ICP-MS conditions were performed using a ns-LA system (ArF Excimer ns-laser, GeoLas Q, Lambda Physics, Göttingen, Germany) equipped with a single volume LA cell and coupled to an ICP-sfMS (Element 2, Thermo Finnigan, Bremen, Germany). The system was optimized according to the optimization protocol described in section 3.3. In addition, lens voltages were adjusted on $^{40}Ar^{16}O$ and ^{56}Fe aiming for medium resolution ($R \approx 4000$). The general operating conditions are listed in Table II.3.3.

3.1.2.1 Elemental fractionation of matrix elements in standard mode

Initial studies were conducted on BIR-1P/G, BHVO-2P/G, and NIST SRM 610 to examine accuracy and elemental fractionation, with respect to the matrix elements. In here, all 5 different SRMs were used as external standard to measure the respective other 4 SRMs, using ^{42}Ca as IS.

3.1.2.2 LA-generated aerosol mass load effect in ICP

In this part, the effect of the mass load[59] by various LA spot sizes (24 μm, 60 μm, 120 μm) was investigated. NIST SRM 610 was used as external calibration standard and ^{42}Ca as IS to evaluate the accuracy of BVHO-2G and BHVO-2P. Mass load effects were determined on *element-to-Al* ratios of the background corrected mean intensities and furthermore, sensitivities changes and fractionation indices were calculated for all three SRMs (NIST SRM 610, BHVO-2G, BHVO-2P).

3.1.2.3 Elemental fractionation under *wet* plasma conditions

O'Conner *et al.*,[119] Wälle *at al.*,[120] and Flamigni *et al.*[121] showed that through addition of H_2O to the dry LA-generated aerosol into the plasma the sensitivity can be increased and also improved quantification abilities were reported. Flamigni *et al.*[121] hypothesized that a matching of analyte-to-material dependent points of vaporization in the ICP could be responsible for the improved accuracy, which was obtained under these conditions. A

shortening of the steep temperature jump along the ICP axis, due to better heat conduction in the presence of gaseous water and higher ion density, which enables a more efficient coupling to the RF field, was assumed. The authors of ref.[121] describe that the varying melting points of different species are reached over a much shorter distance and hence leading to local matching vaporization points in the ICP and conclude that the relative portion of fractionation originating from the ICP might be estimated under these conditions. The effect of such *wet* plasma conditions on the accuracy of the matrix elements in matrix and non-matrix matched analysis, sensitivity changes and fractionation indices were assessed on BHVO-2G/P, BIR-1G/P and NIST SRM 610. For this purpose, the sampling gas was mixed with humid Ar, as presented in Figure II.3.2a and measurements at relative Ar humidity of the total sample gas between 0% to 73% were investigated. In order to obtain highest sensitivity the z-position of the torch was adjusted for each humidity setting; the distance between ICP load coil and sampler orifice had to be reduced. The relative humidity of the total sample gas was measured off-line prior to the measurements using a humidity sensor (DHT44 (RHT05), MaxDetect Technology CO, Ltd, China) connected to an in-house built adapter.[122] For quantification BHVO-2G was used as external standard and ^{42}Ca as IS.

3.1.3 Matrix-matched and non-matrix matched analysis of standard reference materials and mineral samples, focusing on the importance of the solid phase

The studies in this section were carried out with a ns-LA system (ArF Excimer ns-laser, GeoLas Q, Lambda Physics, Göttingen, Germany) coupled to an ICP-qMS (Agilent 7900, Agilent Technology, Tokyo, Japan). The system was again optimized according to the optimization protocol described in section 3.3. In here, a Zurich-type large volume LA cell was used.[123] The general operating parameters for the ICP-MS can be found in Table II.3.3. In addition, H_2 was applied as additional gas II as depicted in Figure II.3.2b and hence increased sensitivity was expected.[124,125] In this section the focus was not on the LA-ICP-MS parameters, but rather on the different materials investigated, therefore detailed description of the materials will follow in section 3.2.

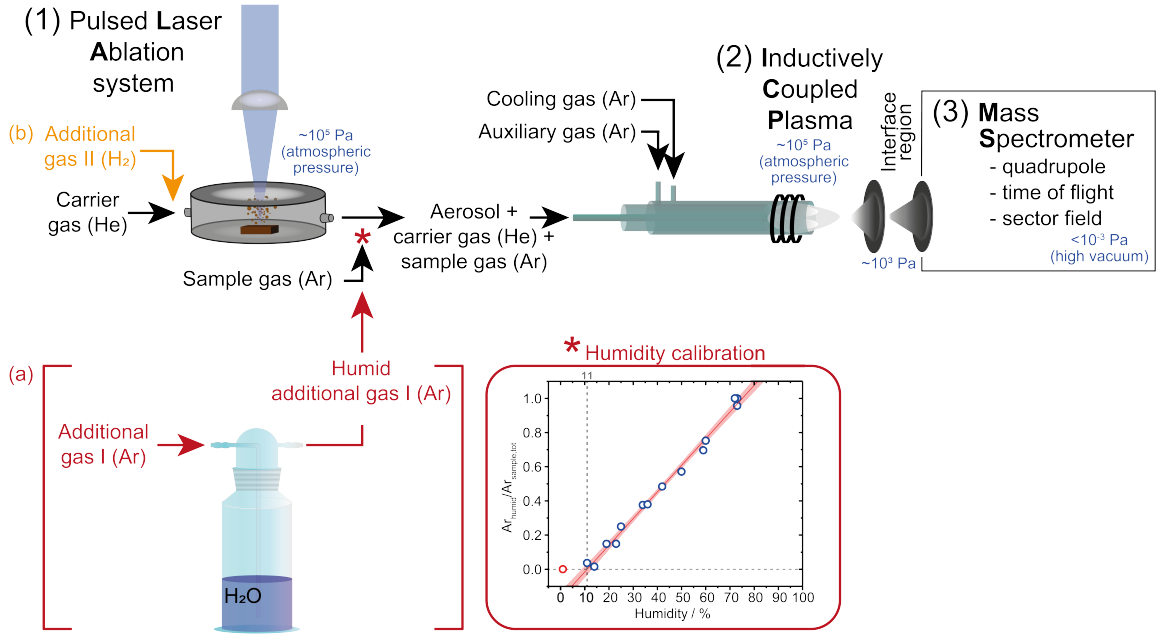

Figure II.3.2: Schematic representation of the LA-ICP-MS experimental set-up. The standard arrangement is displayed in black. By addition of a humidified Ar sample gas flow (additional gas I) in case (a), *wet* plasma conditions were studied. By changing the ratios between the additional gas I and the sample gas the relative humidity was adjusted. As can be extracted from the humidity calibration, relative addition of the humid Ar gas flow resulted in relative humidity between 11% to maximally 73% for the total sample gas. In order to improve sensitivity H_2 (additional gas II) was added before the LA cell for all studies regarding section 3.1.3, as displayed in (b).

3.1.3.1 Standard reference materials with different solid phases

Sensitivities and fractionation indices for a variety of different SRMs were evaluated. Accuracy was further determined, using BHVO-2G as external standard and in addition, different quantification approaches were compared.

3.1.3.2 Matrix- matched versus non-matrix matched analysis of mineral samples

Selected SRMs were used as external standards for quantification of different minerals (see Table II.3.5). This way, matrix-matched and non-matrix matched analysis was performed, while in addition the effect of the solid phase of the SRM on the accuracy could be highlighted. The reference method to investigate the accuracy was EPMA (see section

3.2). In addition, the effect of 100-% mass normalization quantification strategy was investigated and its effect on the rare earth elements (REE) and the chondrite-normalized pattern was explored. [5]

3.1.4 The effect of the pulse duration on elemental fractionation

3.1.4.1 Effect of pulse duration on accuracy

To explore the laser pulse duration on the accuracy and fractionation a pharos fs-laser system (Excite Pharos, Teledyne CETAC Technologies, USA) was coupled to an ICP-qMS (Elan 6100 DRC^{plus}, Perkin Elmer, Sciex, Canada). The operating conditions are listed in Table II.3.3. This study was performed on BHVO-2G/P, BIR-1G/P, NIST SRM 610, which were quantified against each other, using ^{42}Ca as IS.
Garcia *et al.*[24] and Dikawar *et al.*[26] proposed a dependency of the elemental fractionation in fs-LA on the ionization potential of the elements. A tendency of elements with lower ionization potential for preferential ablation in multi-element samples was highlighted.[24] Here, we addressed this question of preferential ablation concerning the matrix elements of BIR-1G/P and NIST SRM 610. Thus, pulse by pulse resolved measurements were conducted. Therefore, the pharos fs-laser system was coupled to an ICP-TOFMS (*icp*TOF, TOFWERK AG, Thun, Switzerland). The TOFMS signals of each SRM were integrated over each LA pulse by the trapezoidal rule of Matlab R2016b (MathWorks, Massachusetts, USA). To determine the pulse beginning and ending a threshold was applied, which was evaluated by summing the ion count of all m/z of interest and subsequently calculating the threshold from 3 to 5 times of the mean background. Each integrated pulse was background corrected and abundance normalized. Finally, quantification was performed for each LA pulse for NIST SRM 610 and BIR-1P, using BIR-1G as external standard and ^{27}Al as IS.

[5] "The REE comprise fourteen naturally occurring elements with extremely similar chemical properties." [126] They are important constituents in geology to reveal fundamental information on the 'cosmic abundances'. [126] In this context, the chondrite pattern was determined as the concentration of the REE in chondrites. Chondrites are the most primitive meteorites found on Earth. [127] Further geological interpretations of the chondrite-normalized pattern of the analyzed minerals exceed the goal of this thesis. Only the effect of the quantification strategy on the pattern was evaluated.

Table II.3.3: Operating conditions for different LA-ICP-MS measurements. In cases where multiple values are listed the parameters in **bold** highlight the standard conditions applied. Concerning the gas flows, they were adjusted on a daily basis in order to obtain highest sensitivity and performance. For the measurements performed using Elan 6100 DRC^{plus}, Element 2 and *icp*TOF MS He (99.999%, PanGas AG, Dagmarsellen, Switzerland) and Ar (99.996%, PanGas AG, Dagmarsellen, Switzerland) were used. For the measurements performed using Agilent 7900 He (99.999%, Linde AG, Hamburg, Germany), Ar (99.996%, Linde AG, Hamburg, Germany) and H_2 (99.999%, Linde AG, Hamburg, Germany) were used.

LA parameters				
	ArF Excimer ns-laser		Yb:KGW fs-laser	
Laser wavelength	193 nm		206 nm	
Laser energy density	10 - 15 J/cm^2		2.5 J/cm^2	
LA spot diameter	24 μm, **60 μm**, 120 μm		55 μm	
LA frequency	8 / 10 Hz		1 & 10 Hz	
LA cell	Zurich-type large volume LA cell[123] / single volume LA cell (V=20 cm^3)		HelEx Cell	
ICP-MS parameters				
	Elan 6100 DRC^{plus}	Element 2	Agilent 7900	*icp*TOF MS
Plasma Power	1510 W	1350 W	1500 W	1550 W
Auxiliary gas flow (Ar)	0.8 L/min	0.6 - 0.95 L/min	0.7 L/min	0.97 L/min
Cooling gas flow (Ar)	16.5 L/min	17.0 L/min	17.0 L/min	17 L/min
Sample gas flow (Ar)	0.97 L/min	0.9 - 1.3 L/min	0.68 L/min	0.9 L/min
Carrier gas flow (He)	1 L/min	0.8 L/min	1 L/min	0.9-1 L/min
Additional gas I (humid Ar)	-	**0%**, 14%, 28%, 73%	-	-
Additional gas flow II (H_2)	-	-	0.014 L/min	-
Dwell time	**10 ms** for all isotopes investigated	**9 ms** for 8 isotopes* over one pass of 0.8 s	**12 ms**: ^{23}Na, ^{27}Al, ^{29}Si, ^{43}Ca, ^{44}Ca, ^{47}Ti, ^{55}Mn, ^{57}Fe **2 ms**: ^{24}Mg, ^{56}Fe	TOF time resolution: **1.5 ms**
Isotopes investigated: ^{23}Na*, ^{24}Mg*, ^{27}Al*, ^{29}Si*, ^{42}Ca*, ^{43}Ca, ^{44}Ca, ^{47}Ti*, ^{55}Mn*, ^{56}Fe*, ^{57}Fe ^{139}La, ^{140}Ce, ^{141}Pr, ^{146}Nd, ^{147}Sm, ^{153}Eu, ^{157}Gd, ^{159}Tb, ^{163}Dy, ^{165}Ho, ^{166}Er, ^{169}Tm, ^{172}Yb, ^{175}Lu				

3.2 Materials and characterization of glass, pressed nano-powder and mineral samples

3.2.1 Standard reference materials

All natural SRMs investigated based on various igneous (basalt, granite, diorite and gabbro) and metamorphic (serpentinite) rocks (see Table II.3.4), were both processed into pressed nano-powder SRMs and glass phase and provided by D. Garbe-Schönberg and S. Müller from the University of Kiel. According to Garbe-Schönberg & S. Müller,[74] the pressed nano-powder SRMs were made from the respective certified reference powders. By applying wet-milling protocols in aqueous suspension using a planetary ball mill and agate tool, undiluted nano-particulate pressed powder tablets were manufactured.[74] The possibility of contamination during milling and powder pressing was assessed by reference measurements of the milled nano-powder compared to the original powder using XRF (i.e. X-ray Fluorescence). [6] Indeed, the XRF measurements showed a mean difference between the two powders of maximally 5% (see Figure II.3.3). The only exception was MgO in the case of AC-EP, for which a 3 times lower concentration in the case of the original powder was obtained. However, this can be explained by the low concentration of MgO in AC-EP. In Figure II.3.3 a comparison of the measured and the reference values from Govindaraju[117] for AC-EP, DR-NP, JGb-2P, UB-NP, BIR-1P and the GeoRem database (preferred values,[110]) for BHVO-2P, is displayed. In order to correct for the loss of ignition (LOI, due to the digestion into lithium tetraborate pellets) of the XRF measurements, the values were normalized to the reference concentration of either CaO or Al_2O_3. Generally, light elements such as Na, Mg, Si and Al are very challenging to measure by XRF and show high LODs. The obtained data of the pressed nano-powders give no rise for contamination in the case of BHVO-2P and JGb-2P. Concerning AC-EP, problems were encountered for

[6] Contamination from the milling balls could lead to addition of Si, due to the used glass / agate milling tools. According to Garbe-Schönberg & Müller Zn and Pb contamination from sample handling during the wet-milling procedure were obtained.[74] No other contamination was reported. For XRF measurements, the powders were transferred into lithium tetraborate pellets with a dilution factor of 6. The measurements were performed by Stefan Jung according to ref.[128] using PanAnalytical MagixPro X-ray instrument (Malvern Panalytical, Malvern, United Kingdom).

MnO, MgO and CaO, which may be explained by their low concentrations. UB-NP is a highly depleted serpentinite sample with high water content. The deviations for TiO_2, Al_2O_3 and MnO could again be explained by too low concentrations. Concerning BIR-1P, i.e. the nano-powder, a high deviation for the SiO_2 can be seen in Figure II.3.3 a and b. This could be attributed to a contamination of SiO_2. At this point, the measured XRF values for BIR-1P were used as reference for all further measurements, while for the other pressed nano-powder pellets the respective reference values from Govindaraju were used.[117]

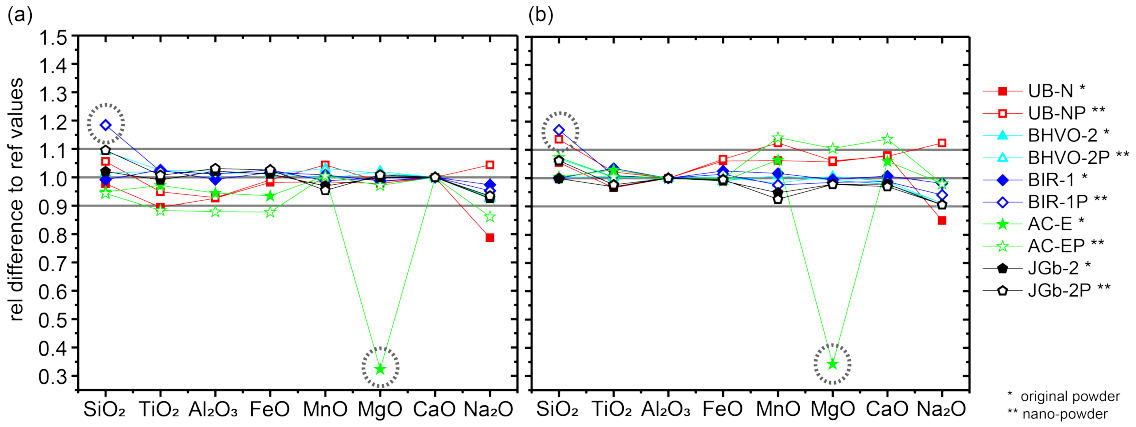

Figure II.3.3: Relative difference to reference values from Govindaraju.[117] The values were normalized to the reference concentration of CaO and Al_2O_3 in (a) and (b), respectively.

Regarding the SRMs in glass phase, ACE-G, DRN-G, JGb1-G, JGb-2G and UB-NG were produced from the original CRM in powder form by Iridium-Strip Heater as reported by Stoll *et al.*[129] and BHVO-2G and BIR-1G were certified reference materials from USGSG. An overview of all reference values used can be found in Table II.3.4.

3.2.2 Mineral samples

The investigated minerals provided by E. Reusser from ETH Zurich were mounted on epoxy resin. Reference measurements were performed by EPMA at the University of Kiel and the obtained concentrations are listed in Table II.3.4. Further colour, crystallographic and compositional details of the different minerals are depicted in Figure II.3.4, however, no geological details will be addressed throughout this thesis.

Table II.3.4: Matrix composition of the SRMs investigated. SRMs highlighted in the same color represent groups of either basalt, granite, diorite, gabbro, serpentinite or synthetic glasses from top to bottom. **P** and **G** indicate SRMs processed into pressed nano-powders and glasses, respectively. BHVO-2G/P & BIR-1G/P are USGS standards, JGb-1G/P & JGb-2G/P are from *Geological Survey of Japan, 1-1-3 Higashi, Tsukuba, Ibaraki 305-0046, Japan*, AC-EG/P, DR-NGP & UB-NG/P are CRPG standards. [7] All values are given in wt-%.

	SiO_2	CaO	Al_2O_3	TiO_2	FeO	MnO	Na_2O	MgO
BHVO-2P# origin: Kilauea Hawaii, Halemaumau crater	49.6	11.4	13.44	2.731	11.15	0.169	2.219	7.257
BHVO-2G# origin: Kilauea Hawaii, Halemaumau crater	49.3	11.4	13.6	2.79	11.3	0.17	2.4	7.13
BIR-1P* origin: 12 km east of Reykjavik (Iceland)	52.2	12.2	14.4	0.9	9.6	0.2	1.5	8.9
BIR-1G# origin: 12 km east of Reykjavik (Iceland)	47.5	13.3	15.5	1.04	10.4	0.19	1.85	9.4
ACE-P/G** origin: Ailsa Craig island in the firth of Clyde, SW Scotland	68.7	0.35	14.29	0.11	2.20	0.06	6.54	0.01
DR-NP/G** origin: Neuntelstein,Massif du Champ du Feu (Vosges), France	52.85	7.05	17.52	1.09	8.75	0.22	2.99	4.4
JGb-1P/G** origin: Utsushigatake, Funehiki-machi, Fukushima Prefecture	43.44	11.98	17.66	1.62	13.68	0.17	1.23	7.83
JGb-2P/G** origin: Tsukuba-san leucogabbro, Tsukuba tunnel No 2	46.68	14.2	23.32	0.58	6.186	0.127	0.92	6.24
UB-NP/G** origin: Col de Bagenelles (Vosges), France	39.43	1.2	2.9	0.11	7.52	0.12	0.1	35.21
NIST SRM 610#	69.7	11.4	1.95	0.076	0.059	0.057	13.4	0.072
NIST SRM 612#	72.1	11.9	2.03	0.0073	0.0066	0.0050	13.7	0.0113

Values extracted from GeoRem database, preferred values.[110]

* Measured mean values of pressed nano-powder from XRF measurements, normalized to 100 wt-%.

** Values extracted from Govindaraju.[117]

[7] **CRPG**: Centre de Recherches Petrographiques et Geochimiques, CNRS, B.P. 20, Vandoeuvre-lès-Nancy Cedex 54501, France.

Table II.3.5: Matrix elemental composition of the investigated mineral samples. All values are given in wt-% and determined using EPMA. [8] The values in brackets represent the standard deviation.

	SiO_2	CaO	Al_2O_3	TiO_2	FeO	MnO	Na_2O	MgO
Anorthite	59.90 (0.46)	6.76 (0.28)	25.00 (0.25)	0.026 (0.011)	0.051 (0.011)	0.032 (0.004)	7.94 (0.15)	0.029 (0.009)
Clinochlore a *	33.75 (0.06)	0.013 (0.002)	12.97 (0.07)	0.036 (0.014)	5.75 (0.07)	0.077 (0.003)	0.026 (0.011)	33.78 (0.11)
Clinochlore c **	33.85 (0.08)	0.016 (0.010)	13.03 (0.13)	0.031 (0.007)	5.42 (0.05)	0.074 (0.004)	0.015 (0.004)	34.09 (0.12)
Clintonite	17.96 (0.23)	13.01 (0.05)	40.79 (0.24)	0.106 (0.011)	2.09 (0.08)	0.034 (0.006)	0.10 (0.02)	20.93 (0.10)
Topaz	33.26 (0.06)	0.011(0.004)	54.83 (0.04)	0.033(0.002)	0.037 (0.007)	0.019 (0.004)	0.016 (0.003)	0.024 (0.030)
Wollastonite	51.72 (0.17)	48.04 (0.06)	0.144 (0.013)	0.038 (0.010)	0.117 (0.012)	0.051 (0.008)	0.021 (0.005)	0.324 (0.012)

* Crystallographic axis $a \rightarrow$ axis within one layer.

** Crystallographic axis $c \rightarrow$ axis perpendicular to the layers.

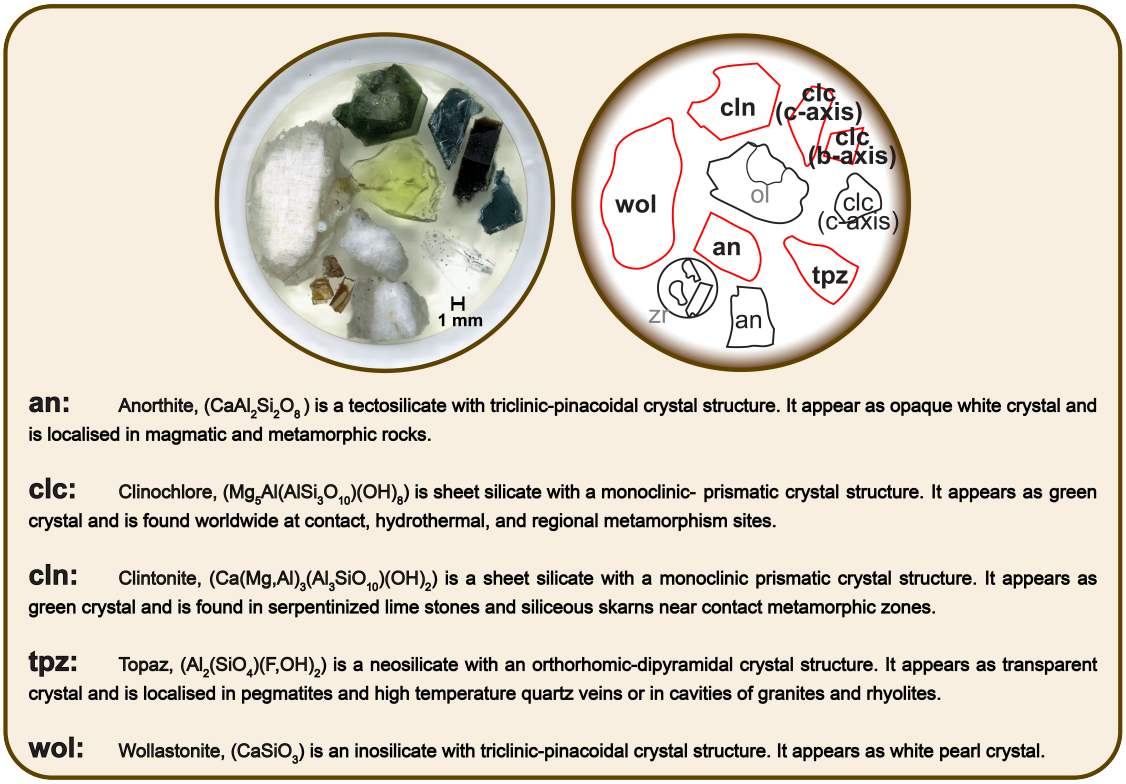

Figure II.3.4: Basic information about the minerals investigated. Information were extracted from the database *webminerals.com.*[130]

[8] 10 individual reference measurements were performed on EPMA (JEOL JXA 8900 R EMP, JEOL USA, Peabody, MA, USA.) by Peter Appel at University of Kiel, Germany, provided by S. Müller and D. Garbe-Schönberg. The acceleration voltage was 15kV, 15 s counting time and the spot size 1-2 μm.

3.3 Optimization, data processing and quantification schemes

The general work-flow for all LA-ICP-MS measurement sequences and subsequent data analysis performed in part II are summarized in Figure II.3.5. LA-ICP-MS performance was evaluated for every measurement day and ICP-MS conditions were optimized on NIST SRM 610 for highest signal intensity over the whole mass range (commonly on ^{7}Li, ^{27}Al, ^{140}Ce, ^{232}Th, ^{238}U), robust plasma conditions, i.e. $Th/U = 1$, and low oxide rates ($ThO/Th < 0.5\%$). Each measurement sequence was composed of $2-3$ independent measurements of an SRM, used as external calibrant, followed by ≥ 2 independent measurements of the target sample and finally enclosed by another $2-3$ independent measurements of the same SRM. The analyses of the SRM was repeated on a regular basis (approx. every two hours), in cases several sample targets were investigated. The bracketing SRM measurements were not only used for external calibration, but also to further obtain and correct for instrumental drifts. The time dependence was approximated by a linear correlation between the different SRM measurements for each element of interest (see Figure II.3.5). Concerning data analysis, the transient signal of each measurement was carefully evaluated – signal considered as most representative for the sample and SRM (e.g., free of spikes, surface contamination, etc.) were determined. Thereafter, the mean value of this evaluated ablation signal was calculated and background corrected. The instrumental background signals were obtained from measurements of the *gas blank*, acquired immediately before the initiating ablation (see Figure II.3.5 left side). After the drift correction of the background corrected signal intensities of the external standard, either of the two different quantification strategies (i.e. internal standardization or 100-% mass normalization, see part II, chapter 1) was applied to provide the bulk concentrations of each analyte measured. The sensitivities were determined from mean background corrected intensities, divided by the expected concentration of the SRM and the fractionation indices were calculated according to equation (2.5), described in part II, chapter 2. Regarding the fractionation indices, depending on the sample and LA system used, different time intervals were addressed. However, the intervals as well as the IS coincided with the intervals and IS used for quantification. All data reduction, sensitivity and fractionation calculations as well as quantification for elemental analysis, were carried out using Matlab

R2016b (MathWorks, Massachusetts, USA). The processed data were plotted with OriginPro 8.6 (OriginLab Corporation, Northampton, England) or Matlab R2016b and all compiled figures were assembled in Adobe Illustrator (Adobe Systems, California, USA).

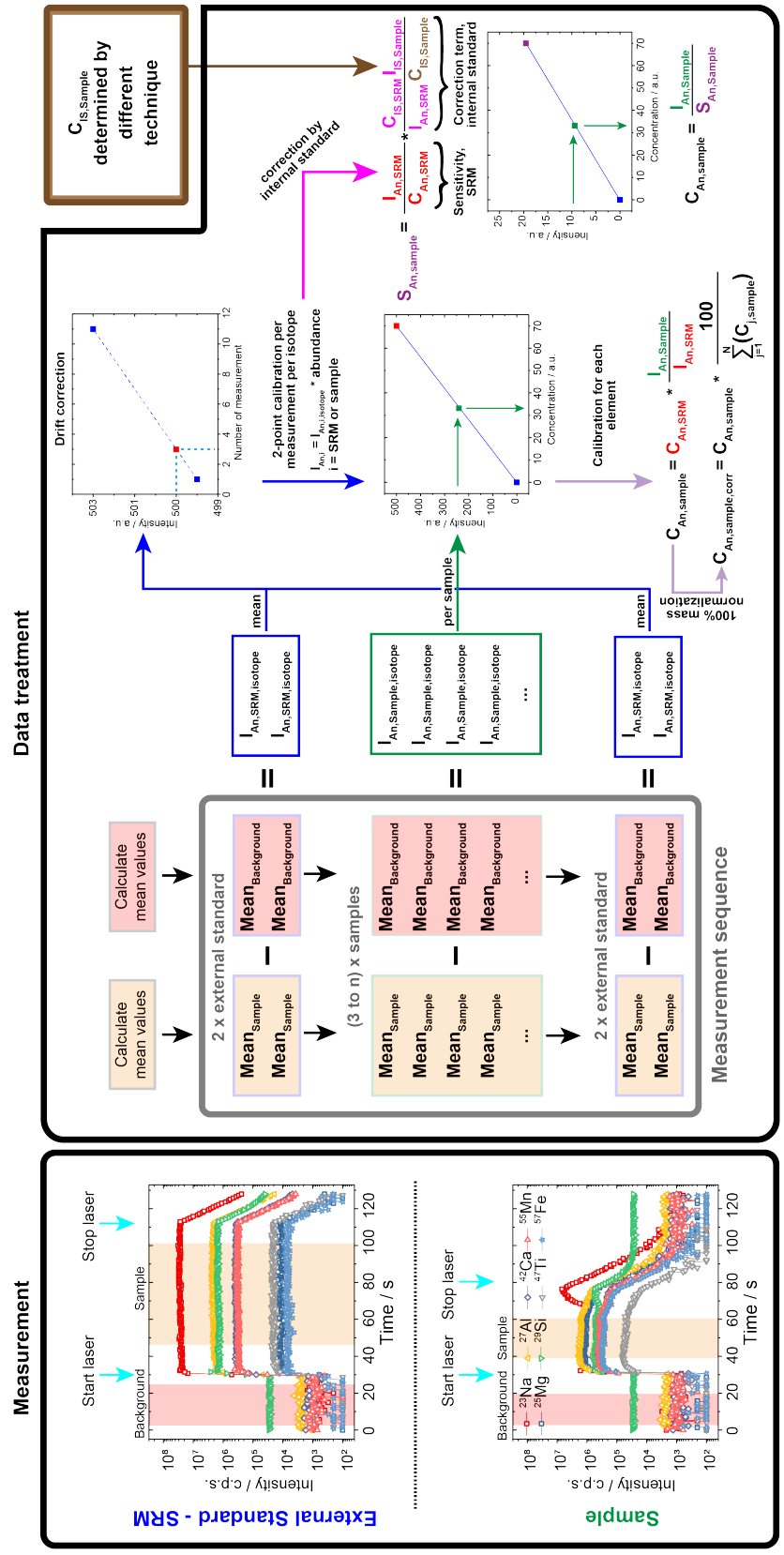

Figure II.3.5: Left: Transient signals of two different measurements (SRM and Sample). In the case of the sample a thin-section of a clinopyroxene was measured. The increase in ^{23}Na indicates the glass substrate and hence only the stable signal before is averaged (orange region). **Right:** Overview of the work-flow of a typical LA-ICP-MS measurement sequence. For each measurement, the stable time trace is assessed, as indicated on the left, averaged and background corrected. After performing a drift correction by the SRM measurement in the beginning and at the end of the measurement sequence, either of the two quantification strategies was applied.

"Don't give up on your dreams, keep on sleeping."

Albert Einstein

Chapter 4

Results and Discussion

4.1 Studies of elemental fractionation processes in LA-ICP-MS

In order to discuss the relevance and implications of the experiments described in part II, chapter 3, section 3.1, one must first understand the problem at hand: the recurrent inaccuracy of Si in LA-ICP-MS measurements of silicates. Therefore, the first experimental results presented, will be the ones measured using standard conditions (see subsection 3.1.2.1).

To this respect, BHVO-2G and BHVO-2P as well as BIR-1G and BIR-1P were studied. Both pairs represented examples of the same matrix composition, however they were present in different phases. In addition, NIST SRM 610 as non-matrix matched standard was analysed. The accuracy of the matrix elements was evaluated by comparing the measured concentrations with the reference values (see Table II.3.4), as shown in Figure II.4.1. Recalling the term matrix-matched analysis as strategy to obtain high accuracy, more accurate results for the two pairs of basalts were expected, while strictly speaking NIST SRM 610 should not allow for accurate quantification of the basalt SRMs, as Mg, Fe, Ti and Mn are only present in low element concentrations.

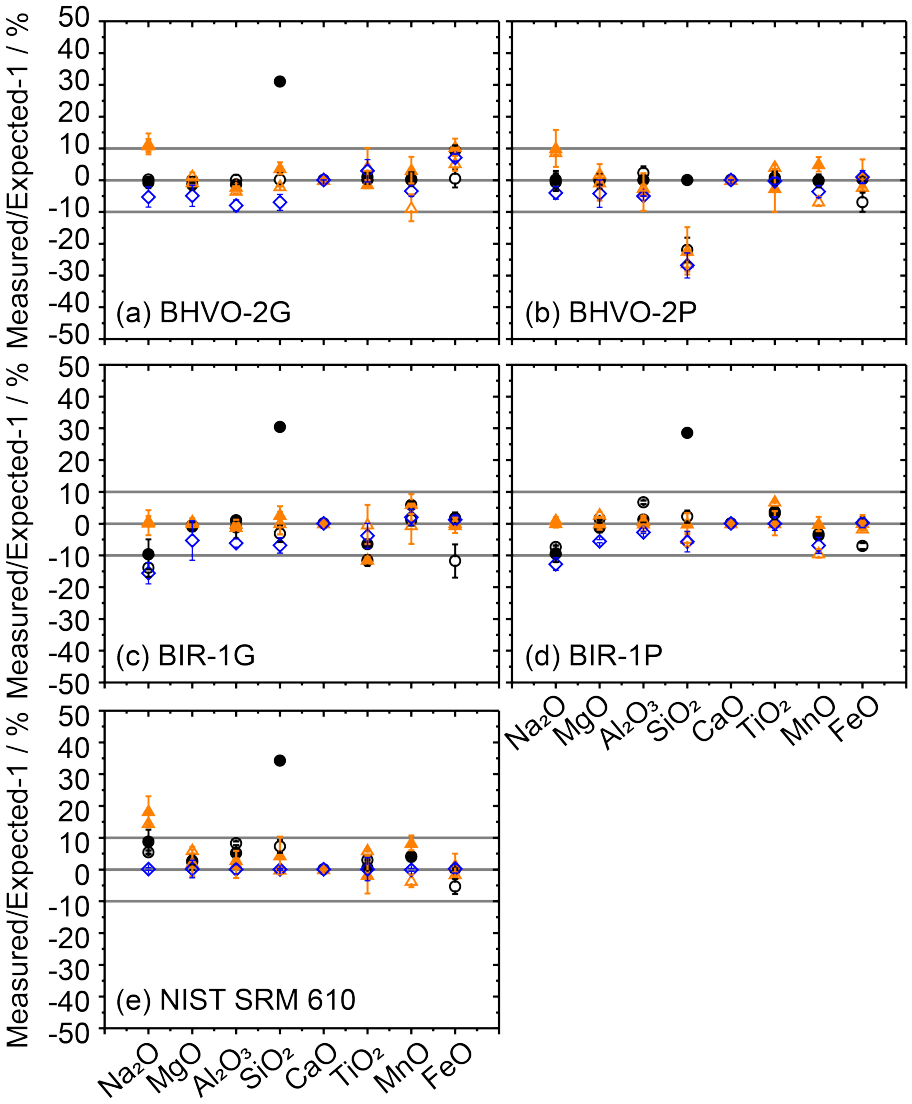

Figure II.4.1: Accuracy of matrix elements of 5 different SRMs. To investigate the effect of matrix matched analysis (a) BHVO-2G, (b) BHVO-2P, (c) BIR-1G, (d) BIR-1P and (e) NIST SRM 610 were used as external standard, respectively. Concerning BHVO-2G & BHVO-2P, and BIR-1G & BIR-1P complete matrix matched analysis was apparent. In all cases, quantification using ^{42}Ca as IS was performed. The measured oxide concentrations for each of the matrix elements of BHVO-2G (○), BHVO-2P (●), BIR-1G (△), BIR-1P (▲), and NIST SRM 610 (◇) were compared with the expected values thereof (i.e. reference values, see part II, chapter 3). The error bars represent the standard deviations from two individual measurements.

Concerning case (a) and (b) in Figure II.3.4 for which the same matrix was used as external calibrant (i.e. BHVO-2G/P), the same pattern was obtained for all elements and SRMs investigated, except for Si. The SiO_2 concentration in the pressed nano-powder (i.e.

BHVO-2P) was overestimated by more than 20% in case (a), where BHVO-2G was used as external calibrant. While on the other side, the SiO_2 concentrations for all SRMs were underestimated, when BHVO-2P was used as calibration material.

As a first explanation, this may indicate a phase dependency of the accuracy of Si. However, contradictory to this explanation was the result for BIR-1P, another pressed nanopowder. BIR-1P showed the same tendency as BHVO-2G and BIR-1G, which in terms of matrix-matched analysis was expected. In support of this observation of matrix-matching were the measurements in case (c) and (d), when using BIR-1G and P, respectively, as external calibrant. Here again, the same matrix composition for both SRMs was present and the same pattern within the uncertainties of the measurements was obtained.

Concerning the last case (e), where NIST SRM 610 was employed as external calibration material, the same trend for BIR-1G & BIR-1P and BHVO-2G & BHVO-2P as two pairs of same matrix composition was hypothesized. However, the accuracy obtained for BHVO-2P concerning Si turned this expectation upside down. Si was again over estimated by more than 20% and the pattern resembled the ones in case (a), (c) and (d).

To which extend the combination of phase and matrix composition was involved in the troubles encountered to quantify Si accurately was not clear at this point. Within the following three sections different approaches will be outlined, which were used to investigate the possible origins and to gain knowledge about the elemental fractionation leading to such inaccuracies of Si in relation with matrix composition and solid phase of the samples. The results of the experiments described earlier (subsection 3.1.2) will be depicted in detail.

4.2 Investigation of LA up-take rates and LA-generated aerosol

The first step concerning the elemental analysis by LA-ICP-MS is the sampling by LA and as described in part II, chapter 2 LA-induced elemental fractionation can occur already here, due to the material dependent LA process. It can result in particle-size dependent elemental compositions and material dependent particle size distributions. Therefore, these first studies were conducted to describe differences between the LA process of glasses ver-

sus pressed nano-powders and to gain insight into the morphology and composition of the LA-generated aerosol.

Starting with the general occurrence of these two solid phases, on one side glass is a solid amorphous bulk material and on the other side, pressed nano-powders are small particles of either crystal minerals or amorphous material or even a mix of these two, which are pressed into a pellet. The small particles are assumed to adhere due to Coulomb electrostatic and Van der Waals forces.[74,131] Concerning the nature of these two phases, differences in LA processes are anticipated. For bulk materials, such as the glass SRMs, the LA process would expectedly follow the process for ns-LA described in part II chapter 2. The absorbed energy is transferred from the electrons to the lattice and leads to material ejection. In the case of BHVO-2G and BIR-1G, dark opaque glass SRMs were present (see Figure II.4.3b). A high density of absorbing colour centres are available, resulting in good coupling of the laser energy into the sample target. On the other side, already from the appearance of the pressed nano-powder (see Figure II.4.3a) a different absorption behaviour was expected. Research on the absorption behaviour of nanoparticles showed a size dependency thereof in the case of for example TiO_2 nanoparticles.[132] In addition to the absorption change, it was also reported that LA of pressed powders leads to fusion of the particles and hence different LA behaviour over time was obtained.[133]

4.2.1 LA up-take rate investigated by Confocal Microscopy (CM)

The LA up-take rates of BHVO-2G and BHVO-2P were investigated by CM at two different energy densities (see Figure II.4.2) and revealed higher LA up-take rates for BHVO-2P for both energy densities. Generally, the higher LA up-take rate in case of the pressed nano-powder is a result of a different LA behaviour.

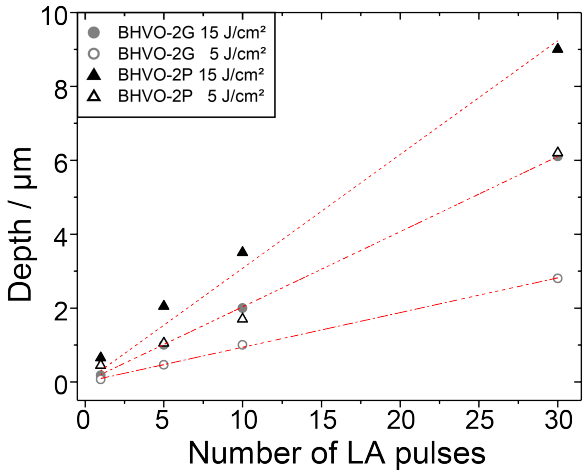

Figure II.4.2: LA up-take rate of BHVO-2G and BHVO-2P after 1, 5, 10 and 30 LA pulses at two different energy densities (5 J/cm^2 and 15 J/cm^2) evaluated by CM.

Following this difference between the LA up-take rates, one might expect higher signal intensities in case of BHVO-2P, if parameters like aerosol transport, PSD and ICP related processes are similar. However, in the case of pressed nano-powders a lower material packing density is expected and therefore, if the LA up-take rates would coincide, lower sensitivities would be the result. In Figure II.4.8(a),(b) and II.4.15 the abundance normalized sensitivities for a variety of different SRMs present in glass phase and as pressed nano-powders are compared. And indeed, a general trend for lower sensitivities for the pressed nano-powder SRMs, compared to their counter part in glass phase were obtained. At this point it was not clear whether this was due to the expected lower material density of the pressed nano-powders or whether it was a result of the LA-generated aerosol PSD, the aerosol transport efficiency, or a combination of all three.

Furthermore, the CM measurements of BHVO-2G and BHVO-2P presented in Figure II.4.3 show a rough surface not only at the crater rim but also on the bottom for the pressed nano-powder compared to its counter part in glass phase.

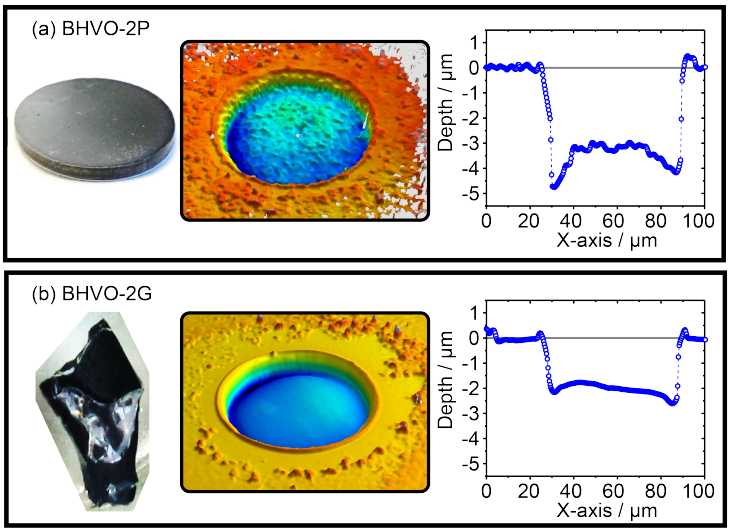

Figure II.4.3: Confocal micrograph of LA produced craters after 10 LA pulses at 15 J/cm^2 of (a) BHVO-2P and (b) BHVO-2G. The extracted profiles reveal higher LA up-take rates in the case of BHVO-2P compared to BHVO-2G. Neglecting the edge effects on the crater bottom outsides, a mean crater depth of 3 μm and 2 μm for BHVO-2P and for BHVO-2G, respectively were obtained.

4.2.2 Particle size distribution of LA-generated aerosol investigated by an Optical Particle Counter

The particle size distribution (PSD) of BHVO-2G/P, BIR-1G/P and NIST SRM 610 are compared in Figure II.4.4. Concerning particles < 200 nm only minimal differences between the 5 different samples were obtained. Indeed the majority of particles were smaller than 150 nm, which fall below the critical diameter of particles being completely ionized within the ICP.[?] However, a zoom-in on the particles > 250 nm revealed the formation of larger particles for all 3 glass SRMs (i.e. BHVO-2G, BIR-2G and NIST SRM 610). Such bimodal distributions in the case of NIST SRM 610 has already been reported.[85] The properties of these large particles may lead to elemental fractionation. Indeed, it is most likely that, if such large particles reach the ICP, they are not completely ionized. Hence, either if their composition deviates from the bulk material (i.e. LA-induced elemental fractionation) or preferential ionization within the ICP (i.e. ICP-related elemental fractionation) of certain elements contained in these particles occurs elemental fractionation will be obtained. These large particles in the range of $250 - 600$ nm may be formed either by agglomeration of primary particles generated by vapour condensation or

they may have a spherical nature and be the result of liquid droplet ejection.[134] However, from the PSD, the morphology of the particles is not revealed.

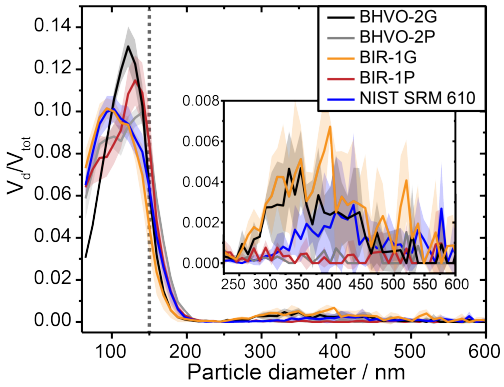

Figure II.4.4: Particle size distribution of BHVO-2G, BHVO-2P, BIR-1G, BIR-1P and NIST SRM 610. The particle diameters were stored in 99 equidistant bins. The volume of each particle (V_d) was approximated assuming spherical particles. Adding up the total of ablated particles multiplied by their respective volume resulted in the total volume (V_{tot}.

4.2.3 Particle morphology and composition of LA-generated aerosol investigated by Secondary Electron Microscopy (SEM) - Energy-Dispersive X-ray Spectroscopy (EDX)

In the next step the aerosol morphology of BHVO-2G and BHVO-2P was investigated using SEM. As shown in Figure II.4.5 in both cases agglomeration of particles was obtained. The agglomeration of particles may not only be caused during particle formation and secondary processes but may also be filter-induced.[134] By careful observation of the particle morphology for BHVO-2G, particles and/or particle agglomerates >10 μm were found (see Figure II.4.5a).

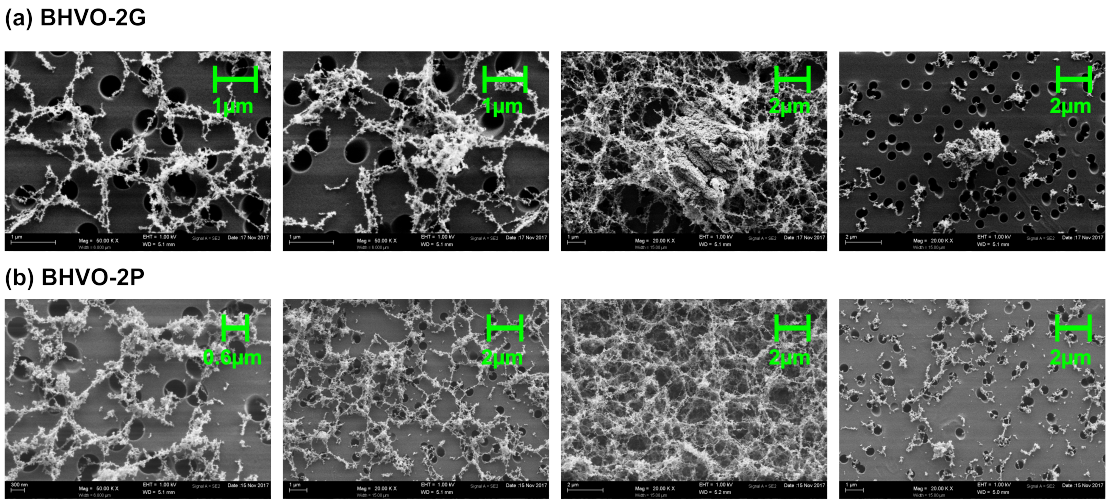

Figure II.4.5: SEM micrograph of the LA-generated aerosol of (a) BHVO-2G and (b) BHVO-2P on membrane filters. For both sample types large networks of agglomerates were obtained. In addition, concerning BHVO-2G large particles > 10 μm were found. The black shadows are the pores of the membrane filter.

These large particles ($> 10\,\mu$m) in case of BHVO-2G were further investigated. Thereby 2 different types of particle morphologies were observed: *elongated* and *round* particles (see Figure II.4.6). The evaluation of the composition of such particles, using EDX [1] revealed a particle morphology dependent composition by normalizing the measured concentrations to the CaO concentration of the bulk material. Elongated particles showed lower SiO_2 concentrations, compared to the *round* shaped particles. Recalling the difficulties to quantify SiO_2 accurately, this is a strong evidence for the elemental fractionation of Si during the LA process of BHVO-2G.
At this point it cannot be explained to which extend such a particle morphology dependent composition influences the overall elemental fractionation.

[1] Energy dispersive X-ray spectroscopy

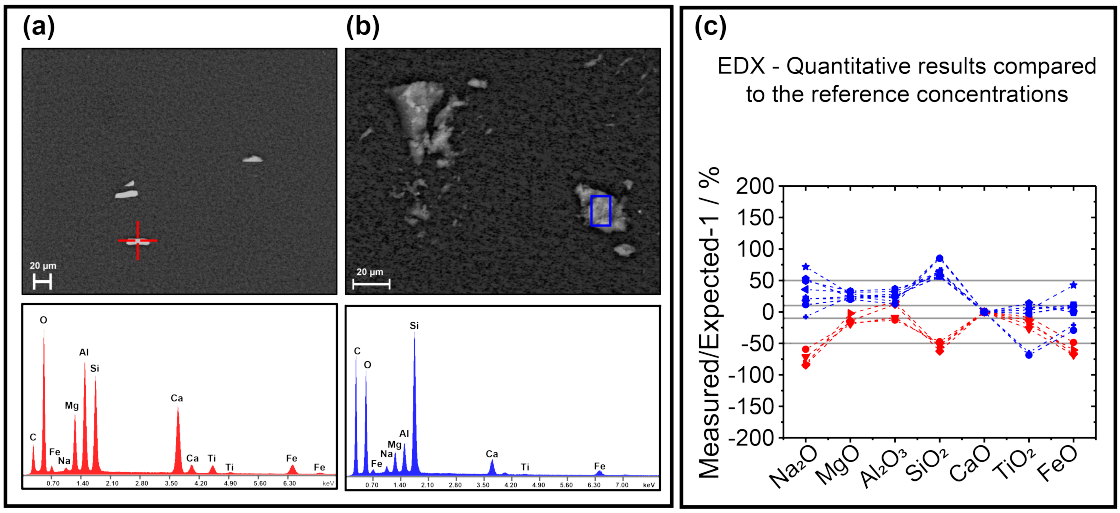

Figure II.4.6: SEM-EDX measurements of individual LA-generated particles of BHVO-2G. All investigated particles were > 10 μm. Two types of particle morphologies were found: (a) elongated and (b) round. (c) EDX measurements of 12 individual particles revealed different compositions, depending on the form of the particles.

4.3 Investigation of elemental fractionation under different LA-ICP-MS conditions

In addition to the observed differences between the SRMs in glass phase and pressed nanopowder concerning the LA up-take rates, PSDs and aerosol composition, also ICP-related elemental fractionation might occur and cause the recurring inaccuracies for Si during LA-ICP-MS measurements. In the second studies different LA-ICP-MS conditions were applied, in order to gain more insight into such ICP-related elemental fractionation.

4.3.1 LA-generated aerosol mass load effect in ICP

The observed differences in LA up-take rate may result in different aerosol mass being transported to the ICP, inducing mass load effects within the ICP.[59] To investigate the occurrence of such a mass load effect, BHVO-2G, BHVO-2P and NIST SRM 610 were measured at three different LA spot sizes, i.e. 24 μm, 60 μm, 120 μm, and constant laser energy density. In Figure II.4.7 the transient signals are presented and are as expected: decreasing intensities for smaller spot sizes by steady background and LA-induced signal

are revealed. Furthermore, Figure II.4.8 presents the abundance normalized sensitivities for BHVO-2G, BHVO-2P and NIST SRM 610. The bulk diagrams indicate the abundance normalized sensitivity at 60 μm. In reference to this and assuming a constant LA up-take rate at the three different LA spot sizes, the expected sensitivity decrease and increase for 24 μm and 120 μm, respectively, were calculated and compared with the measured sensitivities (see Figure II.4.8). In all cases, the obtained abundance normalized sensitivities for crater diameters of 24 μm fall about 25% below the expected values. One reason for this could be a less efficient material transport from the crater to the ICP.[22,135] When comparing the transient signals at 24 μm crater diameter with the other two cases (see Figure II.4.7), a faster decrease of the signal intensity was obtained. Additionally, if a constant LA up-take rate of 3 μm/10 LA pulses (see Figure II.4.3a) in case of BHVO-2P was applied to calculate the crater depth after 60 s signal (i.e. 600 LA pulses) an aspect ratio of 7.5/1 of the crater depth/diameter would be present. According to Mank & Mason,[135] such high aspect ratios may lead to increasing elemental fractionation and indeed the fractionation indices in Figure II.4.9 support this assumption. They were calculated according to equation (2.5) using ^{42}Ca as IS. While high fractionation indices at low LA spot sizes were obtained, only minimal deviations were determined for increasing LA spot sizes. Hu *et al.* observed the same effect for low LA spot sizes.[136] According to Hergenröder a melting zone around the vaporized volume can be a source for non-congruent (i.e. fractionated) evaporation and hydrodynamic sputtering (see part II, chapter 3). Hence, higher fractionation at lower LA spot sizes may be explained by more pronounced heat diffusion due to changes of the surface-to-volume ratio, i.e. increased melting zones, in comparison to the total ablated volume.[76]

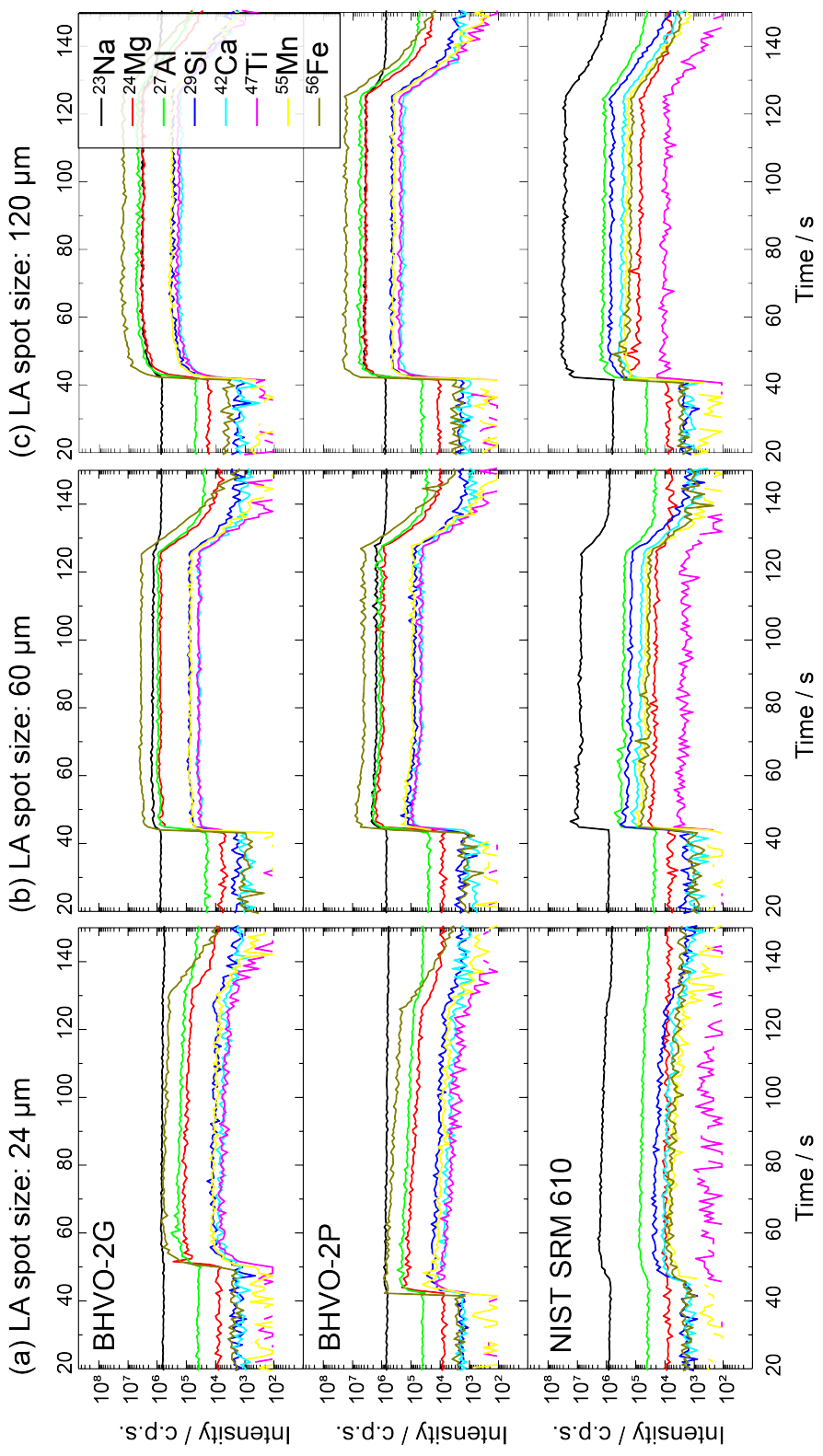

Figure II.4.7: Transient signal at different LA spot sizes: (a) 24 μm, (b) 60 μm and (c) 120 μm in diameter for the isotopes measured of BHVO-2G, BHVO-2P and NIST SRM 610.

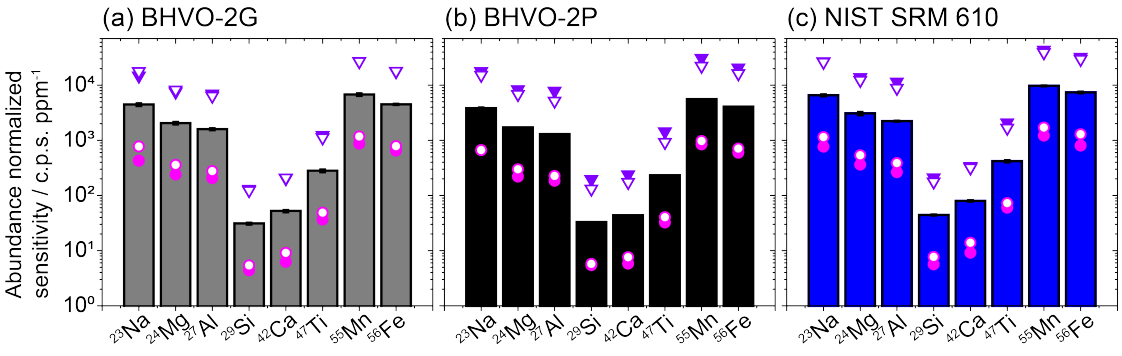

Figure II.4.8: Abundance normalized sensitivities of the measured isotopes in the different SRMs (i.e. (a) BHVO-2G, (b) BHVO-2P, (c) NIST SRM 610) at a LA spot size of 60 μm. The filled pink (●) and purple (▼) data points represent the measured sensitivities in case of 24 μm and 120 μm LA spot size, respectively. The empty data points (○ & ▽) indicate the expected sensitivities with respect to the sensitivities obtained at LA spot size of 60 μm. The error bars represent the standard deviations from two individual measurements.

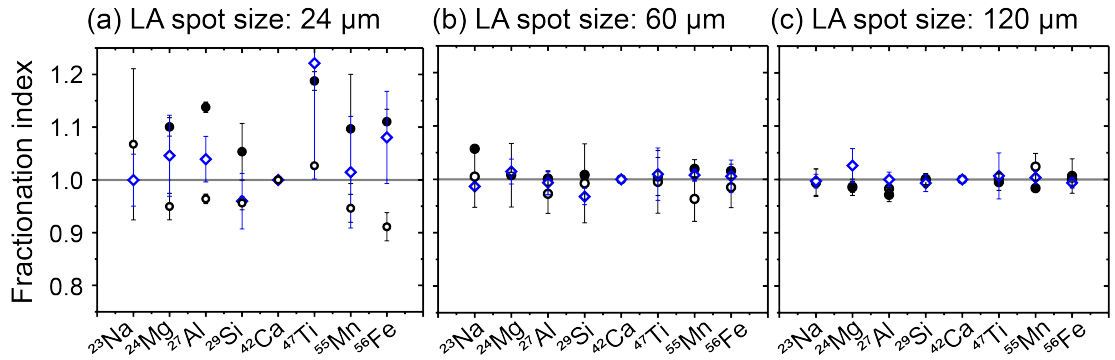

Figure II.4.9: Fractionation index obtained for BHVO-2G (○), BHVO-2P (●) and NIST SRM 610 (◇) at different LA spot sizes (i.e. (a) 24 μm, (b) 60 μm, (c) 120 μm), calculated after equation (2.5) using ^{42}Ca as IS. The error bars indicate the standard deviations from two individual measurements.

The measured sensitivity increase at LA spot size of 120 μm coincides with the expected values in case of BHVO-2G. For NIST SRM 610, an average of 10% sensitivity increase compared to the calculated values was determined. Concerning the pressed nanopowder pellet BHVO-2P over 30% sensitivity increase compared to the calculated values was achieved. Whether these deviations between the measured and the expected sensitivities were due to mass load effects were assessed in the following.

The measurements at the three different LA spot sizes were used to investigate the mass

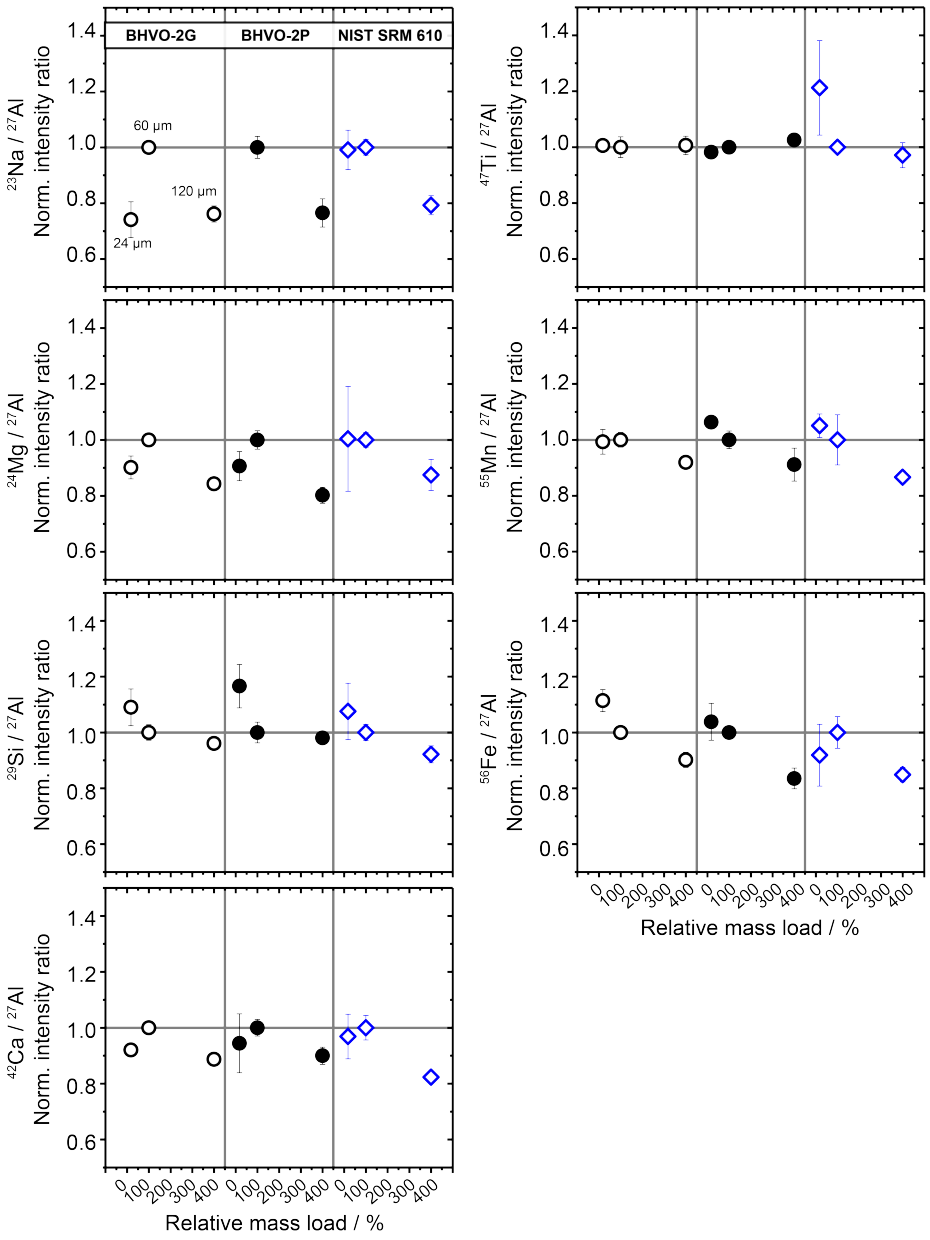

Figure II.4.10: Element/Al mean intensity ratios for different SRMs (i.e. BHVO-2G (○), BHVO-2P (●), NIST SRM 610 (◇)) at different LA spot sizes. The measured ratios were normalized to the LA spot size of 60 μm. The x-axis indicates the relative mass load with respect to the mass load at 60 μm LA spot size. The error bars represent the standard deviations from two individual measurements.

load effect as described by Kroslakova & Günther.[59] In Figure II.4.10 the background corrected mean intensity ratio of the element-to-Al ratio were compared for each of the samples. The calculated ratios were normalized to the measured ratio at 60 μm crater

diameter. In the case of BHVO-2P, the ratio of Na/Al at 24 μm crater diameter was not determined, as the LA signal of ^{23}Na was not distinguishable from the gas blank. The element-to-Al ratios at high mass load all tend to decrease, which agrees with the observations by Kroslakova & Günther.[59] Such intensity decrease may indicate a mass load effect for higher LA spot sizes. Highlighting the Si-to-Al ratio no significant difference between the pressed nano-powder and the counter part SRM in glass phase was revealed. Because the same trend was observed, the mass load effect at this point did not explain the obtained elemental fractionation for Si.

Finally, the determined accuracy for BHVO-2G and BHVO-2P presented in Figure II.4.11 reflect the high fractionation indices at low spot sizes (i.e. 24 μm). The use of NIST SRM 610 as non-matrix matched external standard for BHVO-2G and BHVO-2P affects the accuracy, especially for smaller spot sizes. Such NIST SRM 61x specific Si fractionation was already described by Hu *et al.* in 2011.[136]

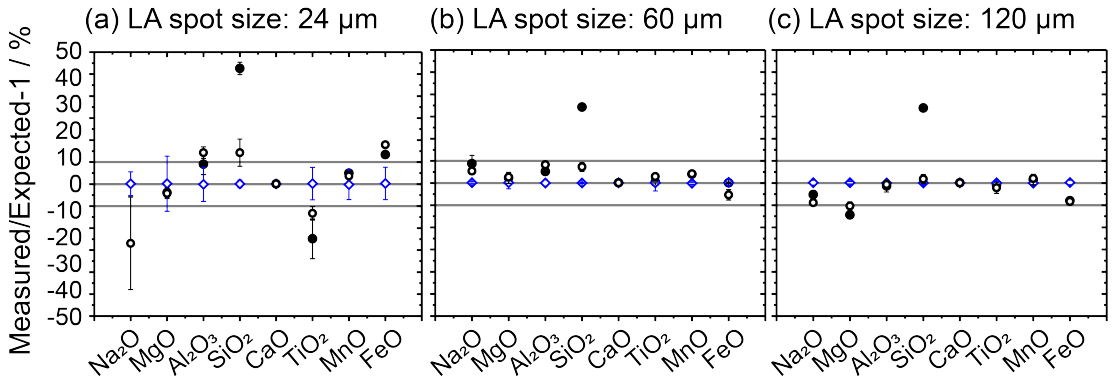

Figure II.4.11: Accuracy obtained for BHVO-2G (○) and BHVO-2P (●) using NIST SRM 610 (◇) as external standard and ^{42}Ca as IS at different LA spot sizes (i.e. (a) 24 μm, (b) 60 μm, (c) 120 μm). The measured concentrations for each of the matrix elements were compared with the expected values thereof (i.e. reference values, see part II, chapter 3). The error bars represent the standard deviations from two individual measurements.

4.3.2 Elemental fractionation under *wet* plasma conditions

One approach to obtain ICP-related elemental fractionation proposed is the addition of humid Ar into the ICP.[121] As described in part II, chapter 3, this way, a shortening of the steep temperature jump along the ICP axis was obtained,[121] and the melting points from various species are reached within a shorter distance along the ICP.

In the first step, the abundance normalized sensitivities measured for BHVO-2G & BHVO-2P, BIR-1G & BIR-1P, and NIST SRM 610 were compared at different humidity settings with respect to *dry* conditions (see Figure II.4.12). For all SRMs the highest sensitivity gain was obtained for ^{29}Si compared to the other elements investigated.

Assuming the aerosol particles entering the plasma in oxide form, several processes are involved to eventually form the ions. Besides evaporation, atomization and ionization, the breaking of oxide bonds and/or the oxide evaporation will take place. According to the first law of thermodynamic, it does not matter which of the processes involved occurs first, meaning whether the oxide bonds will break first, before the particles are vaporized or the other way around. Due to the addition of H_2O the formation of hydroxides may be promoted. Metal-hydroxide bonds tend to dissociate at lower temperatures and may therefore mediate the dissociation process of the particles. Furthermore, the addition of water has shown to serve as buffer against matrix effects and the molecular dissociation products thereof (O_2, H_2) foster the energy transfer from the outer region of the plasma to the central part and therefore cause increased thermal conductivity and heat transfer.[119] This processes may also have caused the required change in z-position towards the sampler cone (see part II, chapter 3). Comparing the trend obtained for all different humidity settings and samples, with the thermodynamic constants displayed in Figure II.4.12 a correlation between the sensitivity increase and the element-oxide bond, as well as the evaporation enthalpy for the elements was revealed. Concerning the nature of the particles, this may give an indication on the rate limiting step during the particle digestion. However this is only speculative and further research, i.e. experiments and modelling, would need to be done. Important in the context of this thesis was the high effect on the sensitivity of Si, which indicated an ICP-induced fractionation of Si. Following the assumption of Flamigni *et al.*,[121] the steep temperature increase applying *wet* plasma conditions and the resulting sensitivity increase of Si, may indicate a more efficient bond breaking between Si-O and

vaporization of Si, compared to *dry* conditions. Furthermore, the highest increase for ^{27}Al, ^{29}Si and ^{47}Ti were obtained at 14% humidity, while for all other elements, 73% humidity lead to maximal sensitivity gain. This may be related to the evaporation enthalpy of the elements. If the water content is high, higher local cooling is present.

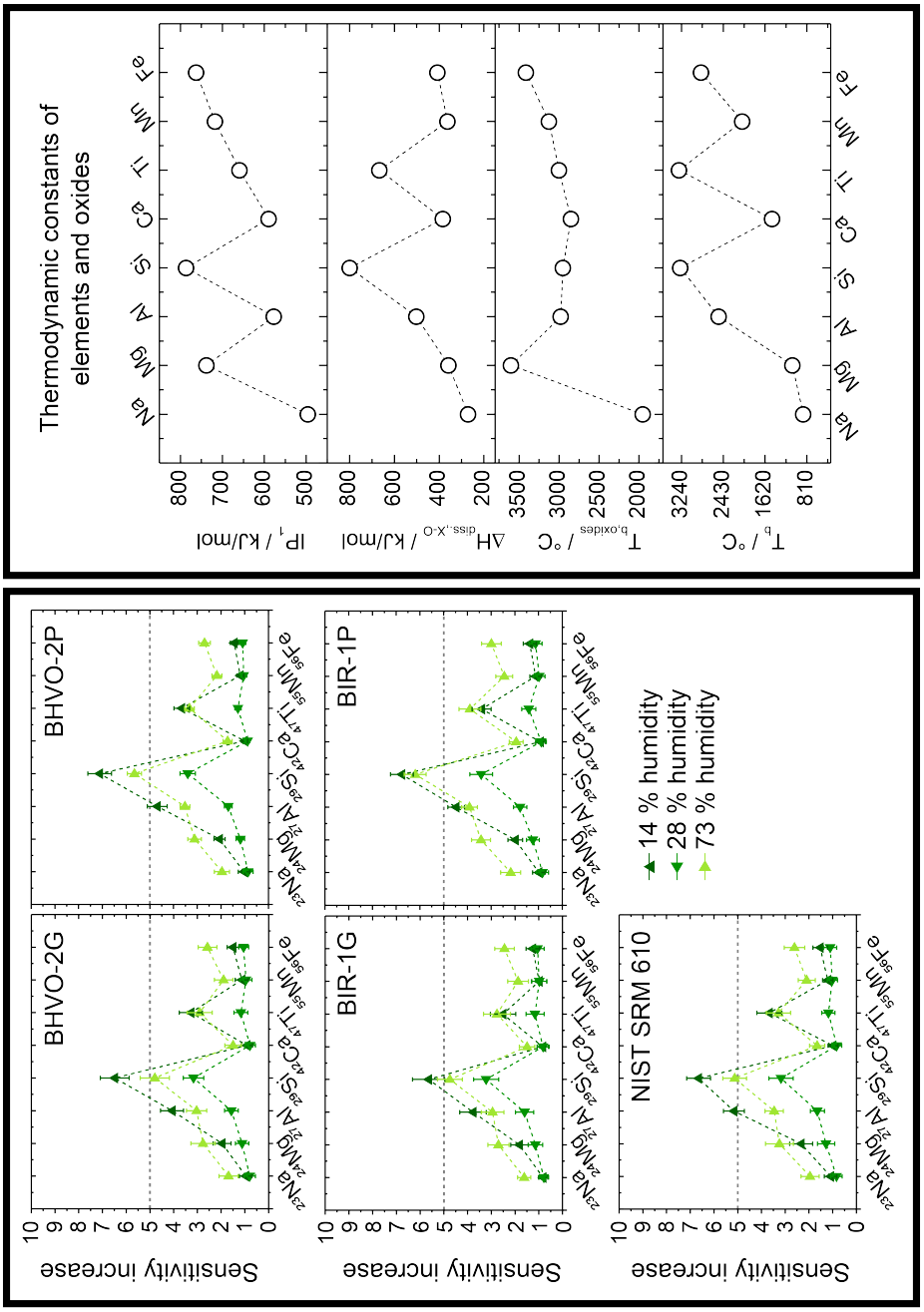

Figure II.4.12: Left The obtained sensitivity increase for different SRMs (i.e. BHVO-2G, BHVO-2P, BIR-1G, BIR-1P, NIST SRM 610) at different humidity settings of the sample gas (14% (▲), 28% (▼), 73% (▲)). The values were normalized to the standard conditions, when using *dry* sample gas. On the **right** thermodynamic constants for the elements investigated are shown. The dashed lines have no physical meaning, they are to guide the reader. From top to bottom it goes over the ionization potential of the elements, the dissociation enthalpy of the element-oxide bond to the boiling temperature of the stable oxide forms of the elements (Na_2O, MgO, Al_2O_3, SiO_2, CaO, TiO_2, MnO, FeO) and finally to the element boiling temperature. All values are taken from ref.[137]

In Figure II.4.13 the effect of the humidity on the fractionation indices is presented. High fractionation was observed for all elements at humidity settings of 14%.
In the last step, the accuracy at different humidity settings was evaluated. BHVO-2G was used as external calibrant and ^{42}Ca as IS. The obtained concentrations were compared with the reference values, as shown in Figure II.4.14. An increase in accuracy could not be confirmed.

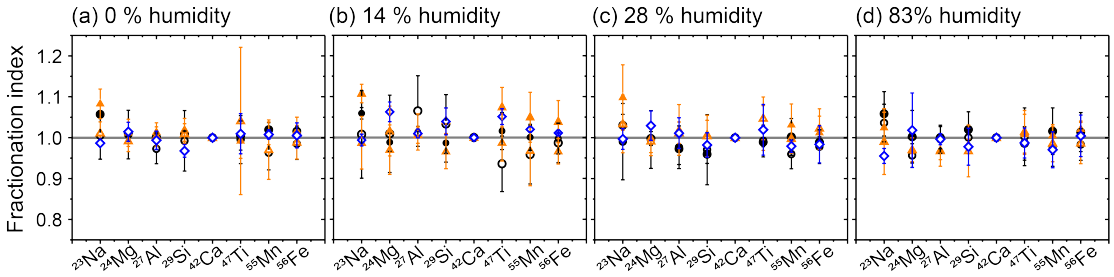

Figure II.4.13: Fractionation index obtained for BHVO-2G (○), BHVO-2P (●), BIR-1G (△), BIR-1P (▲)and NIST SRM 610 (◇) at different humidity settings of the sample gas (i.e. (a) 0%, (b) 14%, (c) 28%, (d) 73%), calculated after equation (2.5) using ^{42}Ca as IS. The error bars indicate the standard deviations from two individual measurements.

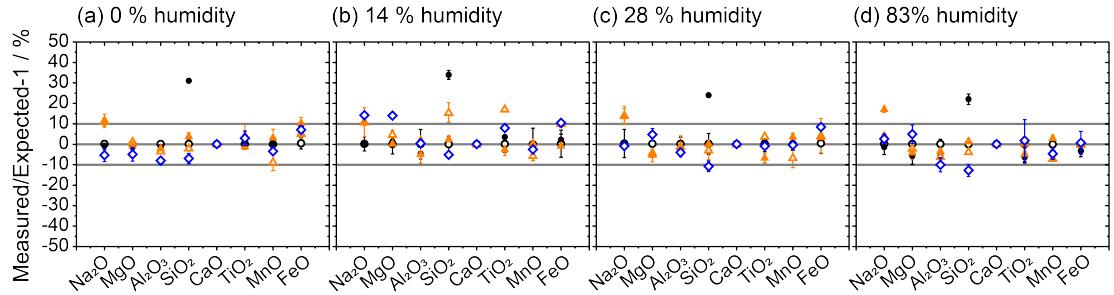

Figure II.4.14: Accuracy obtained for BHVO-2P (●), BIR-1G (△), BIR-1P (▲), and NIST SRM 610 (◇) using BHVO-2G (○) as external standard and ^{42}Ca as IS at different humidity settings of the sample gas (i.e. (a) 0%, (b) 14%, (c) 28%, (d) 73%). The measured oxide concentrations for each of the matrix elements were compared with the expected values thereof (i.e. reference values, see part II, chapter 3).

4.4 Studies of the effect of matrix matched and non-matrix matched analysis on elemental fractionation

After exploring the particle morphology, particle composition, particle size distribution, mass load effect and effect of *wet* plasma conditions indications towards Si fractionation were obtained. However, the same trends were present for all different samples investigated and eventually resulted in similar accuracy pattern when compared to Figure II.4.1 at standard conditions. In this section the question of the influence of different material properties and characteristics on the accuracy of Si was explored. Therefore 15 different SRMs were compared to each other and in addition used as external standards for quantification of various mineral samples. The aim was to evaluate possible material properties, allowing to predict appropriate external standards to facilitate accurate quantification of the matrix elements. Furthermore, different quantification approaches were applied and their outcome on the accuracy was compared.

4.4.1 Standard reference materials with different solid phases

The different SRMs can be separated into pairs of same matrix composition but different phase (glass (**G**) and pressed nano-powder (**P**)), except NIST SRM 612, which was only present in glass phase. Figure II.4.15 revealed higher sensitivities for almost all glass standards. Two exception were UB-NG/P and BHVO-2G/P, for which higher sensitivities for the pressed nano-powder phase in the case of ^{29}Si was obtained. Concerning UB-NG and UB-NP in general higher sensitivities were obtained, when compared to other natural rock SRMs. Indeed, the sensitivity for UB-NG and UB-NP were similar to synthetic glass NIST SRM 612. For AC-EG and AC-EP significant differences in sensitivity for ^{24}Mg was observed. As already obtained during the XRF measurements in part II, chapter 3, Figure II.3.3 MgO was 70% below the expected reference value in case of the original powder. In respect to this, AC-EG and AC-EP may not be suitable to quantify MgO.

In Figure II.4.16 the fractionation indices for all 15 SRMs are displayed. No significant fractionation throughout the LA process into the samples was revealed. Only in the case of AC-EG and AC-EP more scattered results were obtained. The transient signal of AC-EG showed distinct patterns, in the case of ^{47}Ti, which could explain the high fractionation

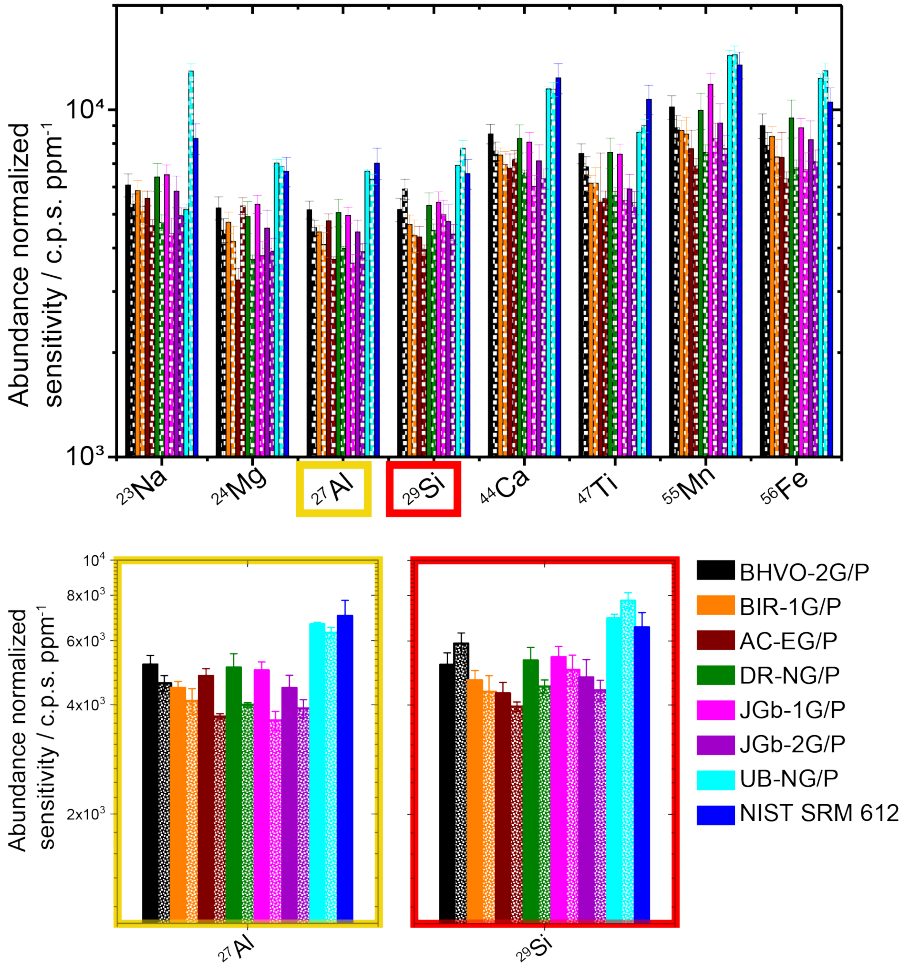

Figure II.4.15: Measured abundance normalized sensitivities for fifteen different SRMs. The isotope labels indicate the measured isotopes. Except NIST SRM 612, all of the SRMs can be separated into pairs. Each pair had the same matrix composition but a different phase, i.e. glass and pressed nano-powder. The filled bars indicate all SRMs in glass phase, while the bars with patterns show the sensitivities for the pressed nano-powder SRMs. A tendency for higher sensitivities for the SRMs in glass phase was observed, as indicated in the zoom-in on ^{27}Al and ^{29}Si. Two exceptions were BHVO-2G/P and UB-NG/P, in the case of ^{29}Si, for which higher sensitivities for the pressed nano-powder SRMs were obtained. The error bars represent the standard deviations from 5 individual measurements.

(see Figure II.4.16). Generally, this may indicate heterogeneity of Ti within AC-EG. On the contrary, for AC-EP no patterns were observed during the transient signal acquisition.

Concerning Figure II.4.17 and II.4.18 the accuracy for all different SRMs was studied, using BHVO-2G as external standard while otherwise different calibration strategies were

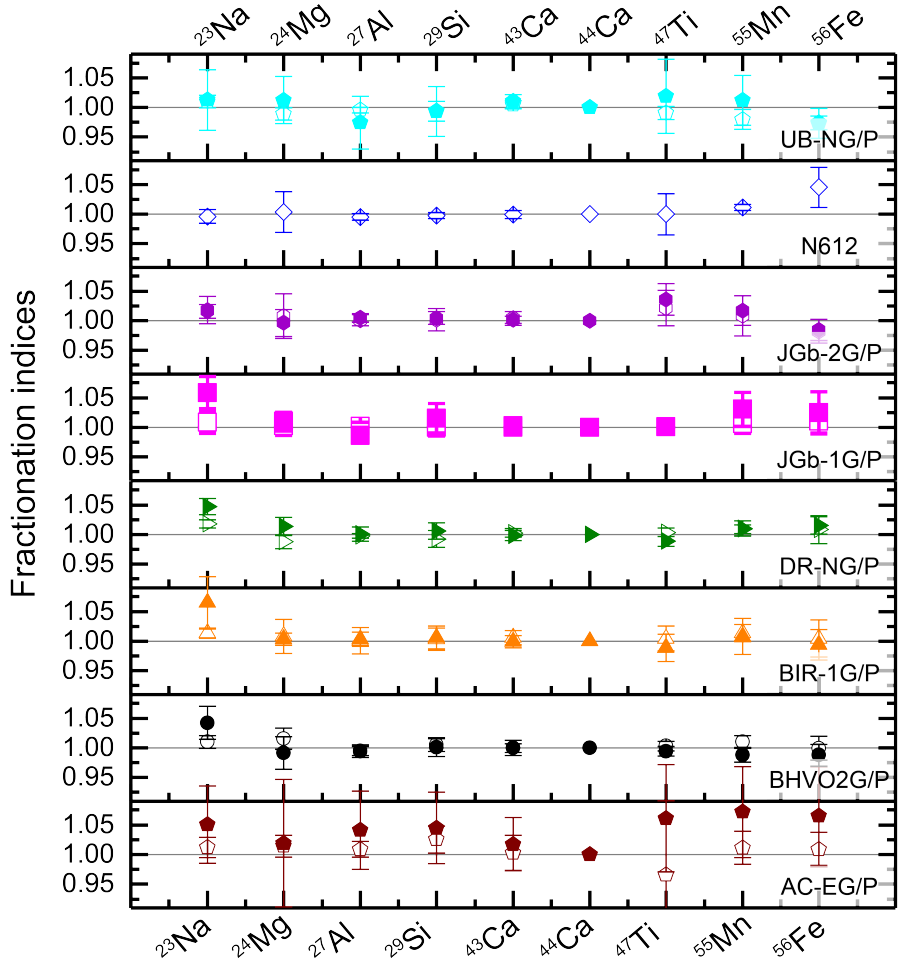

Figure II.4.16: Fractionation indices for the different SRMs. The filled and empty data points represent the values for the pressed nano-powder and the glass SRMs, respectively. For the calculation of the fractionation indices, ^{44}Ca was used as IS. The error bars represent the standard deviations from 5 individual measurements.

employed. In Figure II.4.17 internal standardization using either ^{44}Ca for (a) and (b) or ^{27}Al for (c) and (d) as IS were utilized and in Figure II.4.17 the 100-% mass normalization approach was applied. In both figures, the filled data points depicted on the left graphs show the deviations of the measured concentrations from the reference values (see Table II.3.4) concerning all pressed nano-powder SRMs, while on the right graphs the results for their counter parts in glass phase are presented as empty data points.

Regarding Figure II.4.17 the determined accuracies when using either ^{44}Ca or ^{27}Al as IS were compared. In a first step, the effect on the accuracies for the pressed nano-powder

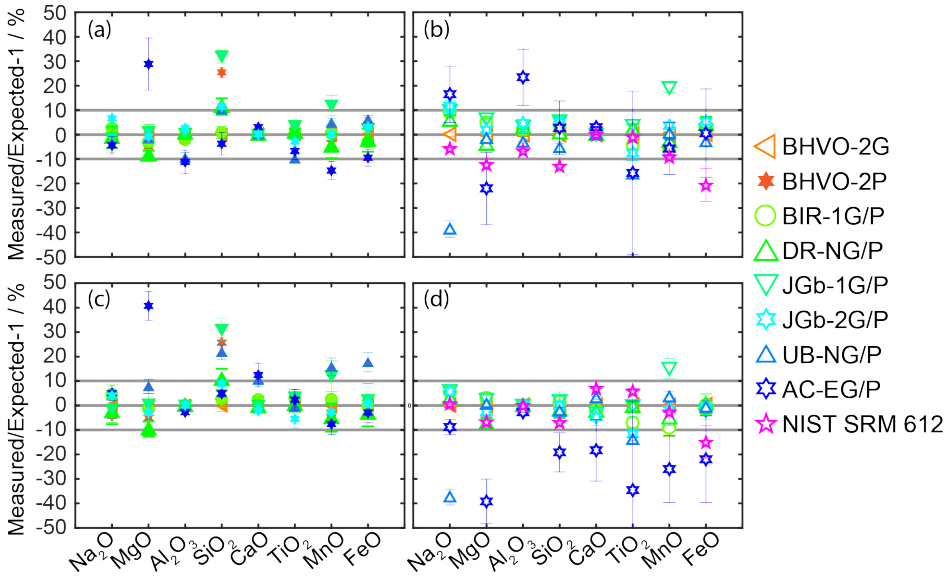

Figure II.4.17: Accuracy for all different SRMs, with respect to the reference values from [117]. In all cases BHVO-2G was used as external standard and ^{44}Ca or ^{27}Al as IS for (a) & (b) and (b) & (d), respectively. For better overview, the SRMs in pressed nano-powder and glass phase were separated into the left and right plots, respectively.

applying different ISs will be discussed while in the second step the discussion concerning the accuracies obtained for the SRMs in glass phase will be in focus.

Figure II.4.17 (a) and (c): As a first approximation no significant difference between the determined accuracies when using different IS was revealed. Concerning the accuracy obtained for Al_2O_3, when using ^{44}Ca as IS, deviations in the range of ±3% were obtained and hence if the IS is changed to ^{27}Al, the same pattern was expected. Two exceptions were UB-NP and AC-EP. In both cases, Al_2O_3 was underestimated by approximately 10%. Therefore, changing the IS to Al shifted the pattern upwards. Overall, higher accuracy was obtained when using ^{27}Al as IS, in the case of AC-EP and opposite for UB-NP. A reason for this outcome could be the low concentration of CaO in AC-EP. Highlighting the accuracy of SiO_2, BHVO-2P and JGb-1P was overestimated by over 20%. Furthermore, JGb-2P, DRN-P and UB-NP showed deviations in the range of 10%. A tendency for higher accuracies was observed for SRMs with higher SiO_2 concentrations.

Figure II.4.17 (b) and (d): Recalling the outcome of the section 4.1 and 4.3, higher accuracies for SRMs in glass phase were expected, especially concerning SiO_2. Indeed,

Figure II.4.17b illustrates accuracies in the range of ±10%, if AC-EG and NIST SRM 612 are excluded. A minimal, anticipated pattern shift when changing the IS from ^{44}Ca to ^{27}Al was observed. However, highlighting the outliers in case of UB-NG and JGb-1G, deviations over 20% were revealed for Na_2O and MnO, respectively. Concerning NIST SRM 612, higher accuracy was obtained, using ^{27}Al as IS, when compared to ^{44}Ca. The opposite trend was revealed for AC-EG. This contradicts the result obtained for AC-EP, where higher accuracy was determined, when using ^{27}Al as IS. Hence, the statement of Ca being not an ideal IS for AC-EG/P, because of its low concentrations has to be reconsidered. In case of AC-EG and AC-EP already the accuracy pattern obtained during the analysis of the original versus the milled nano-powder (see Figure II.3.3, part II, chapter 3) high deviations from the reference values of Gonvindaraju were observed.[117] This might explain the deviations obtained during the LA-ICP-MS analysis to some extend. However, almost two times higher deviations and an opposite trend was observed. This requests that during LA-ICP-MS other parameters may play an important role and the deviations cannot only be attributed to possible contaminations during preparation of the pressed nano-powders.

Figure II.4.18 illustrates the accuracy obtained, when a 100-% mass normalization approach was applied. The meaning of top and bottom row will be explained in the following. When applying a 100-% mass normalization approach, four different observations can be outlined:

1. Figure II.4.18b case JGb-1G: If the quantification of all matrix elements is accurate, also the weight normalization approach results in high accuracy.

2. Figure II.4.18a case JGb-1P: If the concentration of a matrix element, such as SiO_2, is affected by elemental fractionation, which results in inaccurate quantification, a 100-% mass normalization affects all elements and the accuracy pattern is compressed.

3. Comparing Figure II.4.18a and c or b and d, with respect to UB-NP and UB-NG, respectively, a clear shift from top to bottom is illustrated. Within these graphs, the effect of the water content is revealed. In case a and b, the relatively high water

content of UB-NG/P of ∼ 11% was considered and hence the mass was normalized to 89%. If the water content is neglected within the normalization process, or other major constituents, which may not have been determined nor included, low accuracy for all matrix elements was detected (see Figure II.4.18c and d).

4. The last case concerns AC-EG in Figure II.4.18b. Generally, if low accuracies for matrix elements are present, the mass normalization approach leads to an averaging resulting in an overall higher accuracy, when compared to the application of an inappropriate IS (compare to Figure II.4.17d).

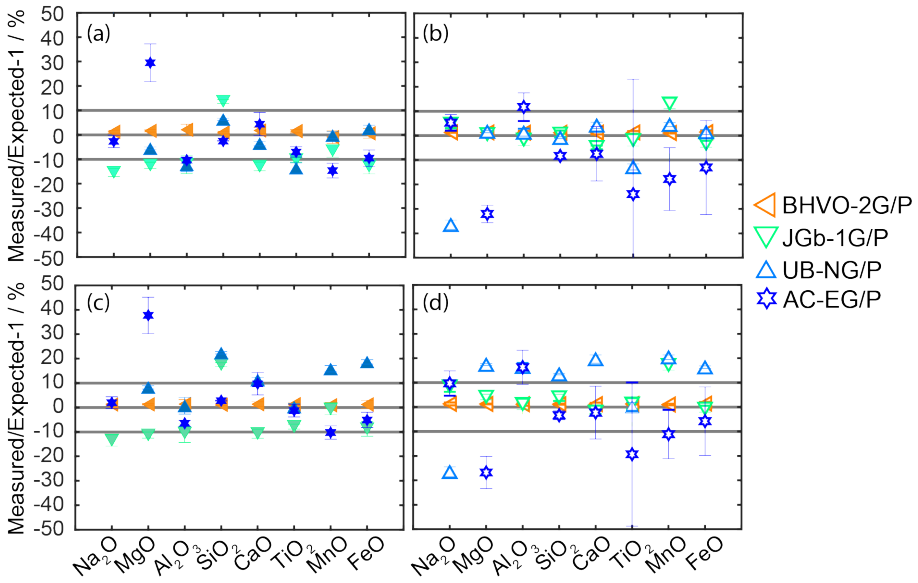

Figure II.4.18: The effect of 100-% mass normalization on the accuracy on a selection of SRMs. Again BHVO-2G was used as external standard and the SRMs in pressed nano-powder and glass phase are separated into left and right plots, respectively. For (a) and (b) the determined oxide concentration according to equation were normalized to 100%, while for (c) and (d) the water contents of the SRMs were considered further.

Overall, concerning matrix-matched versus non-matrix matched analysis no clear trend can be concluded. When taking the solid phase of the SRM into account, however, a tendency towards overestimation of the SiO_2 concentration in the pressed nano-powders was obtained. One might think, that the pressed nano-powders were contaminated during their production leading to higher SiO_2 concentrations within the pressed nano-powder SRMs.

However, contradictory to this are the results obtained for AC-EP/G and NIST SRM 612, for which a deviation with opposite trend was observed. In addition, contaminations over 20% regarding SiO_2 are very unlikely, as such high abrasion during milling are highly debatable. [2] In conclusion, the deviations obtained for the pressed nano-powder SRMs may be attributed to distinct elemental fractionation for Si, already obtained in section 4.1 to 4.3. At this point no sample characteristic/composition leading to the difficulty of analysing Si accurately could be evaluated.

4.4.2 Matrix- matched versus non-matrix matched analysis of mineral samples

In a next step, a selection of the above studied SRMs was used to quantify different minerals. The aim was to follow the hypothesis of a phase dependent elemental fractionation of Si and to find out whether pressed nano-powder SRMs may lead to more accurate results for the SiO_2 determination in minerals, when compared to these SRM in glass phase. Therefore, each of the SRM was once used as external standard. If not otherwise noted, for quantification either ^{44}Ca or ^{27}Al, as IS as well as 100-% mass normalization was applied for each of the mineral samples. Concerning the different figures in this subsection the aforementioned quantification approaches are arranged from left to right in the above described sequence. In all plots, the accuracy of the LA-ICP-MS measurements were evaluated by comparison of the measured concentrations with EPMA measurements of the minerals (see part II, chapter 3).

Overall, the results obtained for the 5 different minerals investigated will be separated into three blocks. In the first block the three minerals **Clintonite, Wollastonite, and Topaz** are summarized as examples for non-matrix matched analysis. In the second block **Anorthite** will be discussed. In this case, many different SRMs show a similar matrix-composition to the mineral and therefore matrix-matched analysis was facilitated. In the last block the accuracy obtained for **Clinochlore** as example of stacked silicate mineral will be outlined. Due to its composition, UB-NG & UB-NP were the two SRMs with similar matrix.

[2] Pers. Commun. with D. Garbe-Schönberg and S. Müller.

Non-matrix matched analysis of Clintonite, Wollastonite, and Topaz

Clintonite, Wollastonite, and Topaz show very different elemental composition (see Figure II.4.19). In Figure II.4.19 a high variation in accuracy over the different samples and elements was detected. The deviations generally obtained for MgO, when using AC-EG/P as external standard and for Na_2O, when using UB-NG/P as external standard might be due the inaccuracies obtained in subsection 4.4.1. Excluding these values, the same *cluster* pattern in all three minerals was revealed. This so-called *cluster spread* (i.e. overall precision when comparing different external standards) for all elements was between $10 - 20\%$, except for SiO_2. In this case the relative differences to the reference values were spread over 40% depending on the SRM used for all three minerals. As an example for such *cluster spread* let us look at Clintonite, when using ^{44}Ca as IS. In here, a *cluster spread* of $\approx 10\%$ for MgO was observed. Nevertheless, the accuracy when compared to the EPMA results was between 11 to 21%.

In the following the three different minerals will be discussed in more detail, with respect to the obtained accuracy and matrix composition (see Figure II.4.19).

Clintonite: Regarding the different quantification approaches highest accuracy was obtained, when ^{27}Al was used as IS, especially when employing JGb-2P and UB-NP as external standards. This again translates to the pattern obtained for the 100-% mass normalization.

Wollastonite: Using ^{27}Al as IS does not seem appropriate, due to its low concentration. Indeed, CaO as major constituent in Wollastonite was overestimated by more than 20% for all SRMs. Due to the composition of Wollastonite, external standards which result in high accuracy for SiO_2 and CaO also lead to highest accuracy applying the 100-% mass normalization approach. AC-EG, AC-EP, DR-NG and UB-NG were the most appropriate external standards.

Topaz: In Topaz, Al_2O_3 and SiO_2 are the major constituents, therefore quantification using ^{44}Ca as IS is not recommended. However, here the effect on Al_2O_3 using ^{44}Ca as IS is not as significant as in the case of Wollastonite, when using the minor constituent ^{27}Al as IS. After all, many different external standards, allow for accurate quantification.

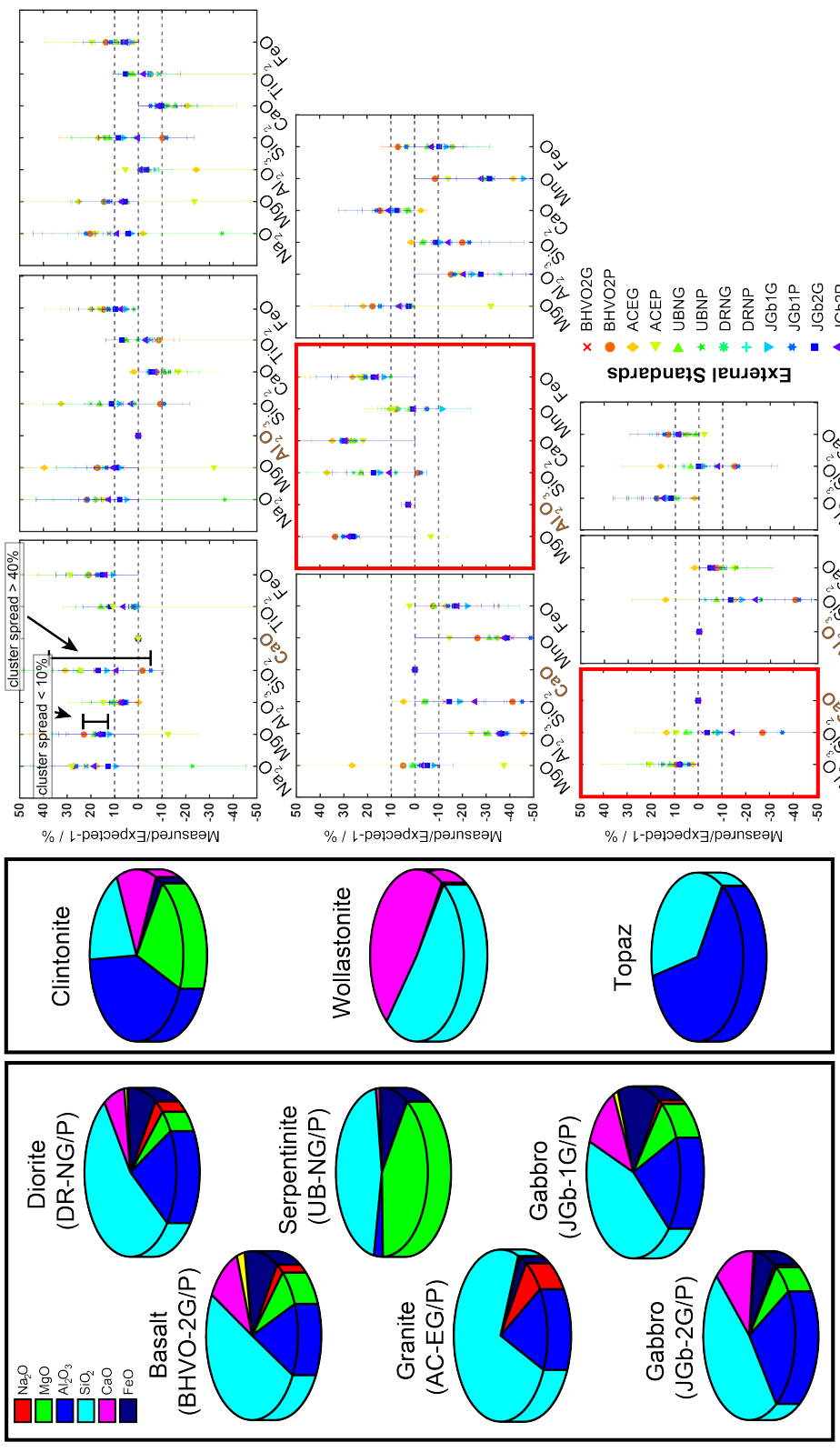

Figure II.4.19: Accuracies obtained for three different minerals (i.e. Clintonite, Wollastonite, Topaz), calculated by comparison with the reference values from EPMA measurements (see part II, chapter 3). On the **left** side, the matrix composition of the different minerals and external standards are revealed. On the **right** side, the deviations from the EMPA measurements are presented. Here from **left** to **right** different quantification approaches were applied: ^{44}Ca as IS, ^{27}Al as IS, 100-% mass normalization. The framed plots in red highlight the results, when unfavoured IS were applied. The error bars represent the standard deviations of 5 individual measurements.

Even though no perfect matrix-matched analysis was possible for these three minerals, in all cases three or more external standards lead to accurate results, concerning the main constituents. Furthermore, in some cases, SRMs in pressed nano-powder phase and in other cases SRMs in glass phase or even both types revealed high accuracy. It follows, that neither the matrix composition, nor the phase alone helps to predict, which SRM will allow for accurate quantification concerning these three minerals.

Matrix matched analysis of Anorthite

Concerning Anorthite, all SRMs investigated had a very similar matrix composition, except UB-NG/P. Figure II.4.20a provides a first overview, where all SRMs were used as external standard. Generally high accuracy and the same clustering as in Figure II.4.19 was revealed. Concerning the argument of matrix-matched analysis, these results were as expected. If two specific cases of matrix (i.e. DR-NG/P) and non-matrix matched (UB-NG/P) analysis were extracted (see Figure II.4.20b), no clear indication for higher accuracy concerning matrix-matched analysis were observed. What appeared to be more important was the phase of the SRM used as external standard. [3]

[3]Concerning the 100-% mass normalization, lower accuracy for UB-NG/P were obtained, due to the difficulty of quantifying Na_2O accurately using these SRMs (see Figure II.4.17)

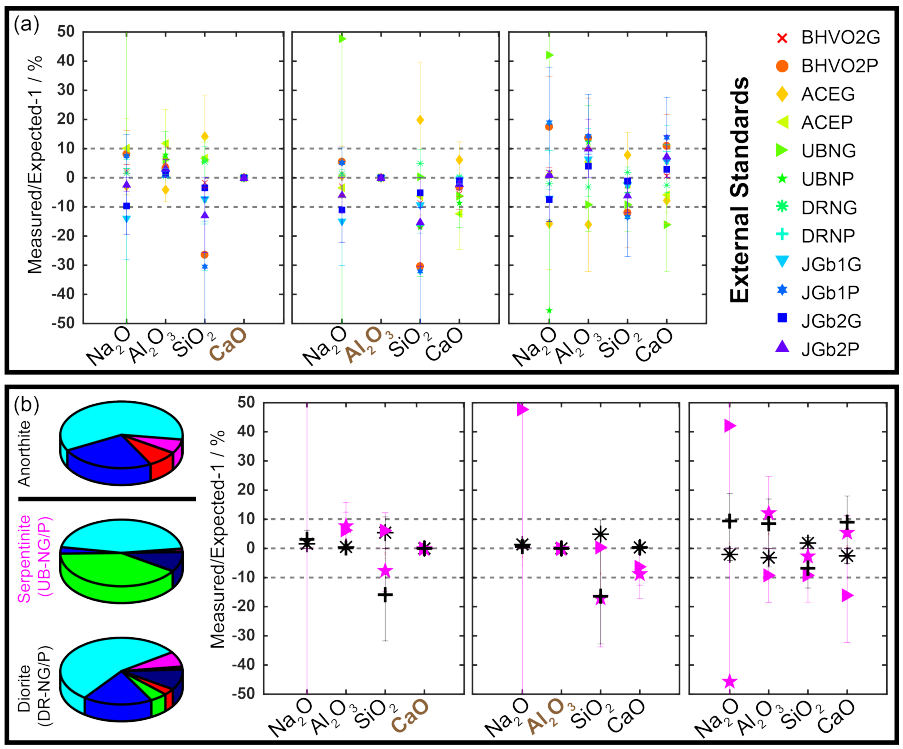

Figure II.4.20: Accuracy obtained for Anorthite, again calculated by comparison with the reference values from EPMA measurements (see part II, chapter 3). On **top**, the results for all SRMs are presented. Again the plots show the results for different quantification approaches - from left to right, using ^{44}Ca as IS, ^{27}Al as IS, 100-% mass normalization. On the **bottom** only the results using UB-NG/P and DR-NG/P as external standard are displayed. The error bars represent the standard deviations of 5 individual measurements.

Non-matrix matched analysis of Clinochlore, a stacked silicate mineral

In Figure II.4.21a an overview of the accuracy obtained for Clinochlore using all different SRMs as external standards is provided. Due to the very low CaO concentration in Clinochlore, the results using ^{44}Ca as IS are not shown – extremely low accuracy (i.e. $>$ 20% deviation from EPMA measurements) for all major elements was obtained. For better comparison, the determined accuracies using the same two SRMs as in the case of Anorthite were extracted (see Figure II.4.21b) and indeed the same trend as obtained for Anorthite was revealed. Despite the different matrix-composition of DR-NG/P and the mineral high accuracy was achieved. The results for Clinochlore were supporting the hypothesis of the phase being more important than the matrix composition of the SRM.

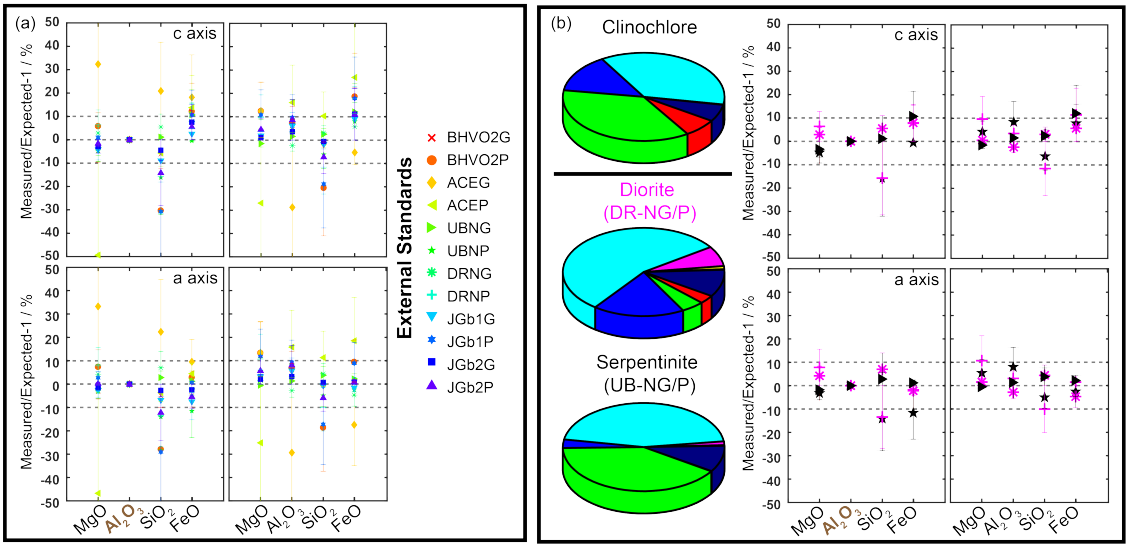

Figure II.4.21: Accuracy obtained for Clinochlore, again calculated by comparison with the reference values from EPMA measurements (see part II, chapter 3). On the **left** side, the results for all SRMs are presented. The plots show the results for different quantification approaches - from left to right, ^{27}Al as IS, 100-% mass normalization. Here the difference between drilling into the sample along the c-axis and a-xis of the mineral are deployed. On the **right** only the results using UB-NG/P and DR-NG/P as external standard are displayed. The error bars represent the standard deviations of 5 individual measurements.

4.4.2.1 Effect of different quantification approaches on the Rare Earth Elements of Wollastonite

Aiming for LA-ICP-MS as *stand-alone* method means a so-called 100-% mass normalization approach needs to be applicable for the minerals of interest. Therefore, as seen throughout several examples above, the accuracy of the major constituents of a sample are pivotal. In some cases, the 100-% mass normalization approach also results in an averging of erroneous concentrations, and therefore may lead to an overall higher accuracy. However, knowledge about H_2O or other unmeasurable species within the sample need to be known prior to quantification. Finally, what is most interesting to e.g. discover and characterize new ore deposits or to investigate the formation processes of mountain chains, are the rare earth elements (REE). Indeed, the chondrite pattern of a mineral reflects the cumulative effects of all fractionations undergone by the material since its origin. [4] [126]

[4] For the explanation of chondrite patterns see part II, chapter 3. Note that fractionation here does not relate to the term elemental fractionation in combination with LA-ICP-MS.

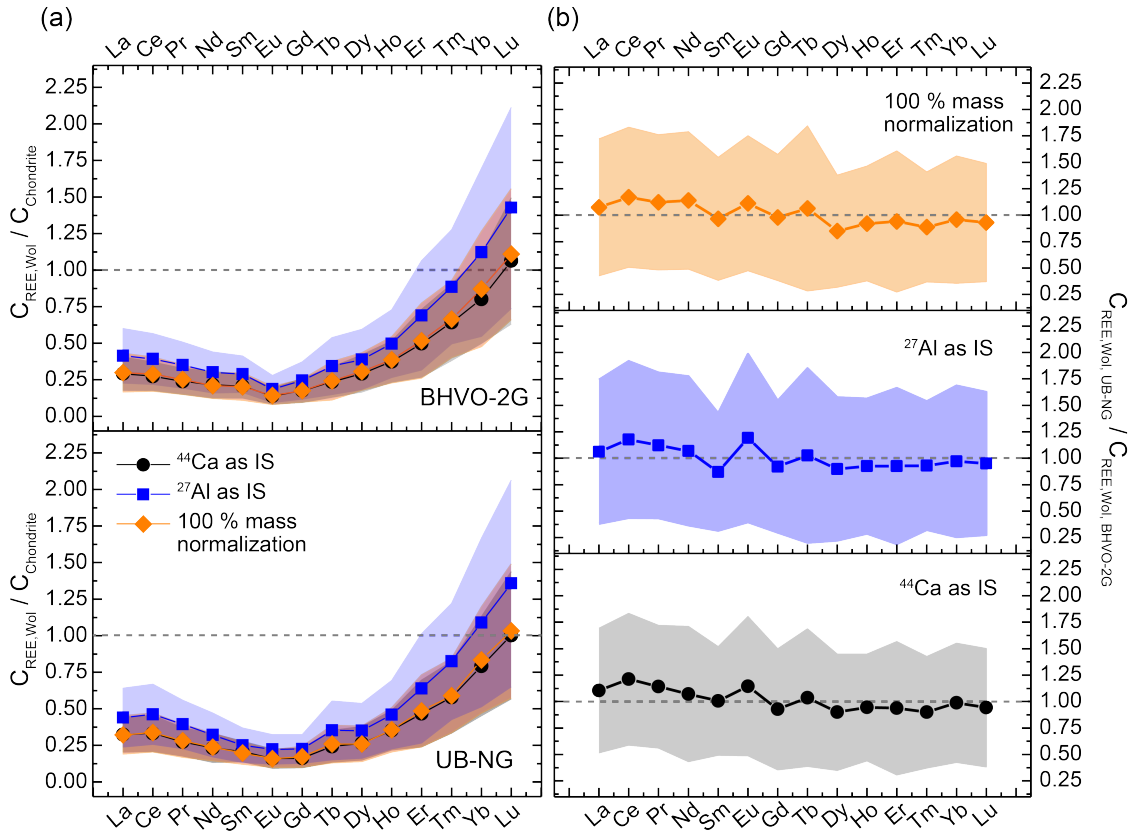

Figure II.4.22: Chondrite pattern for Wollastonite calculated using the chondrite values from ref. [138] (a) The differences applying different quantification strategies are revealed for two different external standards (i.e. BHVO-2G, UB-NG). (b) The difference between the two external standards (i.e. BHVO-2G/UB-NG) is illustrated. The shaded areas represent the standard deviations of 5 individual measurements.

Due to the importance of the REE in geology, the effect of the different quantification strategies and different SRMs on the REE and respective chondrite pattern were investigated. In Figure II.4.22 these effects with respect to Wollastonite are presented. Concerning Figure II.4.22a, the chondrite patterns obtained applying different quantification strategies and SRMs are deployed. Only a minimal difference between the different chondrite patterns was revealed. However, the ratios (i.e. $C_{REE,Wol}/C_{Chondrite}$) were shifted, depending on the quantification approach applied. Expectedly, the chondrite pattern obtained using ^{44}Ca as IS and applying the 100-% mass normalization were aligned. To investigate the effect of the SRM on the chondrite pattern the patterns determined using either BHVO-2G or UB-NG were compared in Figure II.4.22b and indeed only a mini-

mal trend was revealed. Using UB-NG as external standard resulted in higher values for the REE from La to Eu (except Nd). However, these differences were only minor, when compared to the precision of the measurements. Finally, a dependency of the measured concentration of the REE on the quantification strategy applied became apparent. Nevertheless, the chondrite pattern stayed constant within the precision of the measurements independent on the external standard and quantification strategy.

4.5 Investigating the effect of the pulse duration on elemental fractionation

Different studies have proposed the possibility for non-matrix matched analysis using fs-LA.[101,139] Higher accuracy and less LA-induced elemental fractionation was reported.[140] The aim of this section was to find out, whether higher accuracy for Si can be obtained, when switching from ns-LA to fs-LA in case of silicate samples.

For this purpose, the two pairs of basalt SRMs (i.e. BHOV-2G/P and BIR-1G/P) present in two different phases as well as NIST SRM 610 were studied. Firstly, the sensitivities between the different SRMs were evaluated (see Figure II.4.23). The pattern obtained hereby was similar to the pattern displayed in Figure II.4.15. The abundance normalized sensitivities for the SRMs in pressed nano-powder phase were lower, when compared to their respective counter part in glass phase. However, the absolute values are approximately one order of magnitude lower than the sensitivity obtained for ns-LA-ICP-MS.

In Figure II.4.24 the calculated fractionation indices for all five SRMs are illustrated. Directly comparing the fractionation indices obtained with the ones for ns-LA at a similar spot size (here 55 μm, for ns-LA 60 μm, see Figure II.4.13a), higher fractionation for Mg, Si, and Mn in case of fs-LA was revealed. Indeed already Diwakar *et al.* reported elemental fractionation of Si using fs-LA.[26]

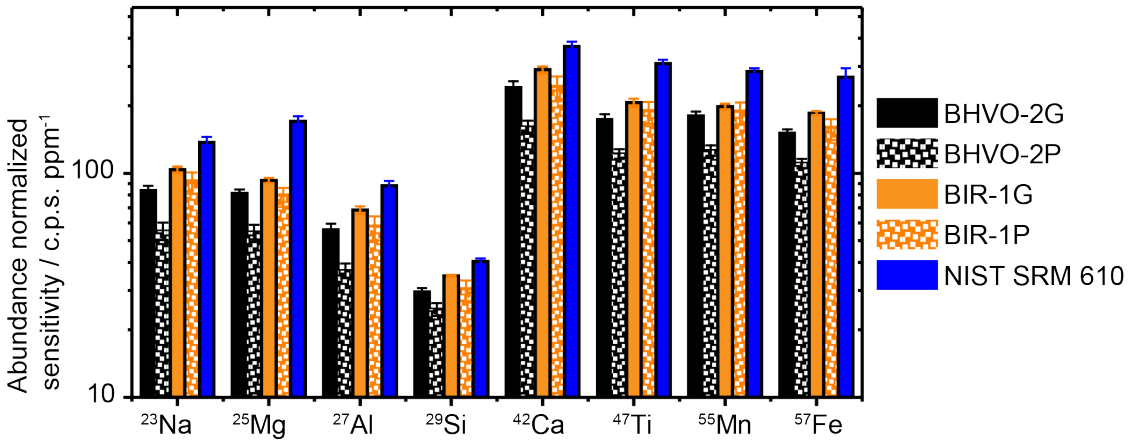

Figure II.4.23: Abundance normalized sensitivities for BHVO-2G/P, BIR-1G/P and NIST SRM 610 in case of fs-LA-ICP-qMS. Higher values for the SRMs in glass phase were obtained, compared to the respective SRMs in pressed nano-powder phase. The error bars represent the standard deviations from two individual measurements.

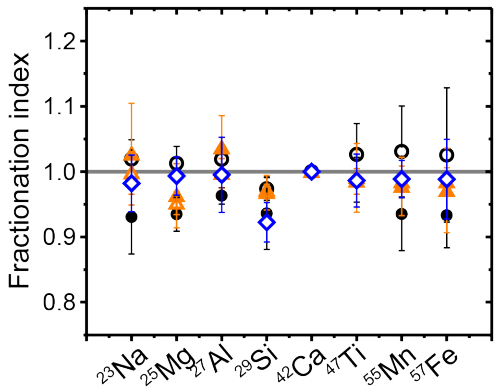

Figure II.4.24: Fractionation indices for BHVO-2G (○), BHVO-2P (●), BIR-1G (△), BIR-1P (▲), and NIST SRM 610 (◇) in case of fs-LA-ICP-qMS. It was calculated according to equation (2.5), using ^{42}Ca as IS. The error bars represent the standard deviations from two individual measurements.

In conclusion, the overall accuracy obtained when using fs-LA was affected (see Figure II.4.25). Generally, higher deviations for non-matrix matched analysis were obtained, especially for elements which were lower in the NIST SRM 610 when compared to the

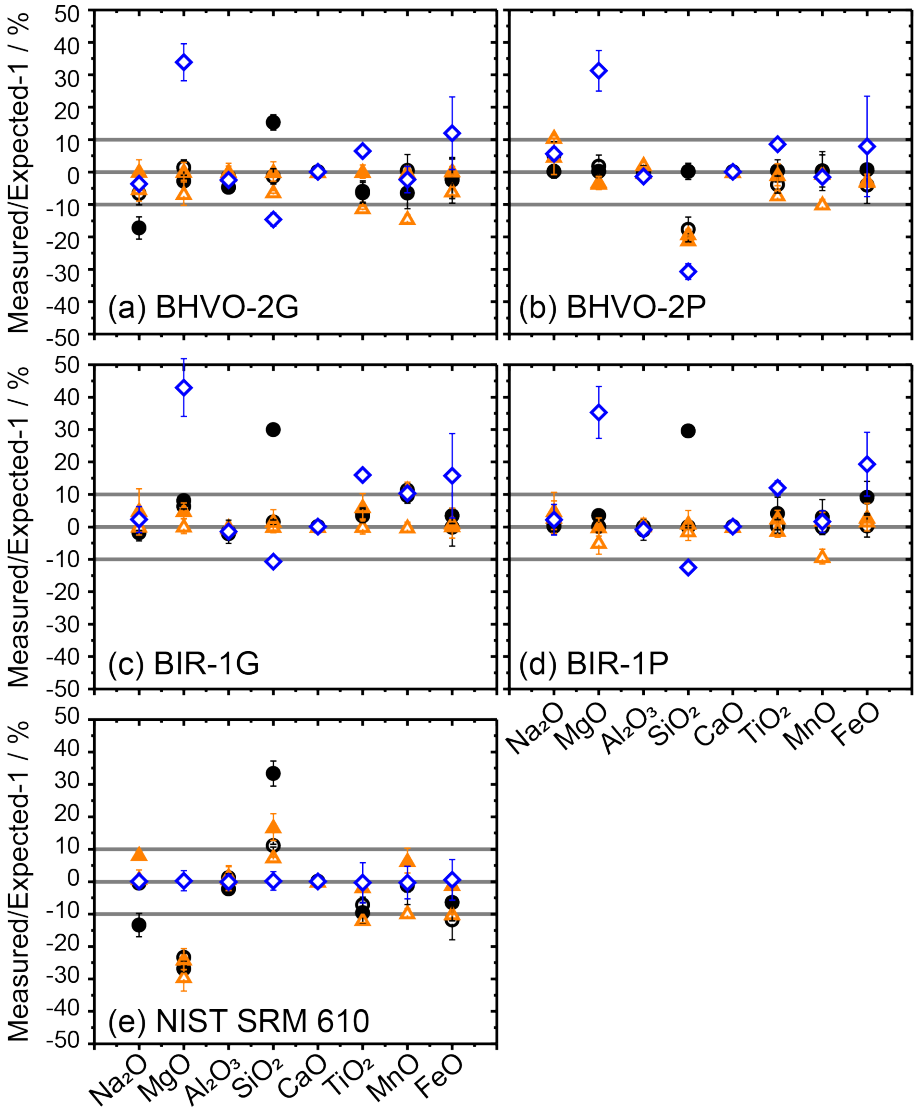

Figure II.4.25: Accuracy obtained for BHVO-2G (○), BHVO-2P (●), BIR-1G (△), BIR-1P (▲), and NIST SRM 610 (◇). In (a) BHVO-2G, (b) BHVO-2P, (c) BIR-1G, (d) BIR-1P, and (e) NIST SRM 610 were used as external standard, respectively. In all cases, internal standardization, using ^{42}Ca as IS was performed. The determined oxide concentrations for each of the matrix elements were compared with the expected values thereof (i.e. reference values, see part II, chapter 3). The error bars represent the standard deviations from two individual measurements.

basalt SRMs (e.g. FeO and MgO) This might have lead to the lower accuracy obtained thereof, when using NIST SRM 610 as external standard for the basalt SRMs. As expected, the opposite deviation was obtained, when using the basalt SRMs for NIST SRM 610 as sample. Recalling Figure II.4.1 deviations over 20% for Si in BHVO-2P, using BHVO-

2G as external standard were obtained. Switching from ns-LA to fs-LA minimized this deviations to approximately 15%. However, this was only obtained in case of matrix matched analysis between BHVO-2G and BHVO-2P.

4.5.1 Pulse by pulse resolved analysis

Due to the change in pulse duration, also the LA process alters (for more details see part II, chapter 2 and part III, chapter 6) and reduced heat affected zones are expected.[14] In addition, Stoian *et al.* and Bulgakova *et al.* investigated the initial process by LA with fs laser pulses.[82,141] They show experimental and theoretical evidence for Coulomb explosion during fs-LA of dielectrics.[82,141] In dependence of their findings, Garcia *et al.* suggested a correlation between preferential elemental ablation and the ionization energies of the elements.[24]

To this respect, the obtained elemental fractionation in fs-LA (see Figure II.4.24) in combination with preferential elemental ablation will be discussed regarding BIR-1G, BIR-1P and NIST SRM 610. Therefore, as pulse by pulse resolved analysis was performed.

In Figure II.4.26 the time trace, i.e. the transient signal, of BIR-1G, NIST SRM 610 and BIR-1P are illustrated. A selection of the time trace for ^{27}Al and ^{29}Si are presented. Comparing the structure of the transient signal between the three SRMs in Figure II.4.26a distinct differences were observed. While for BIR-1G a *slow* LA uptake occurred, NIST SRM 610 and BIR-1P were undergoing a *fast* LA uptake rate, which resulted in the higher peak intensities for the first 10 to 60 LA pulses.

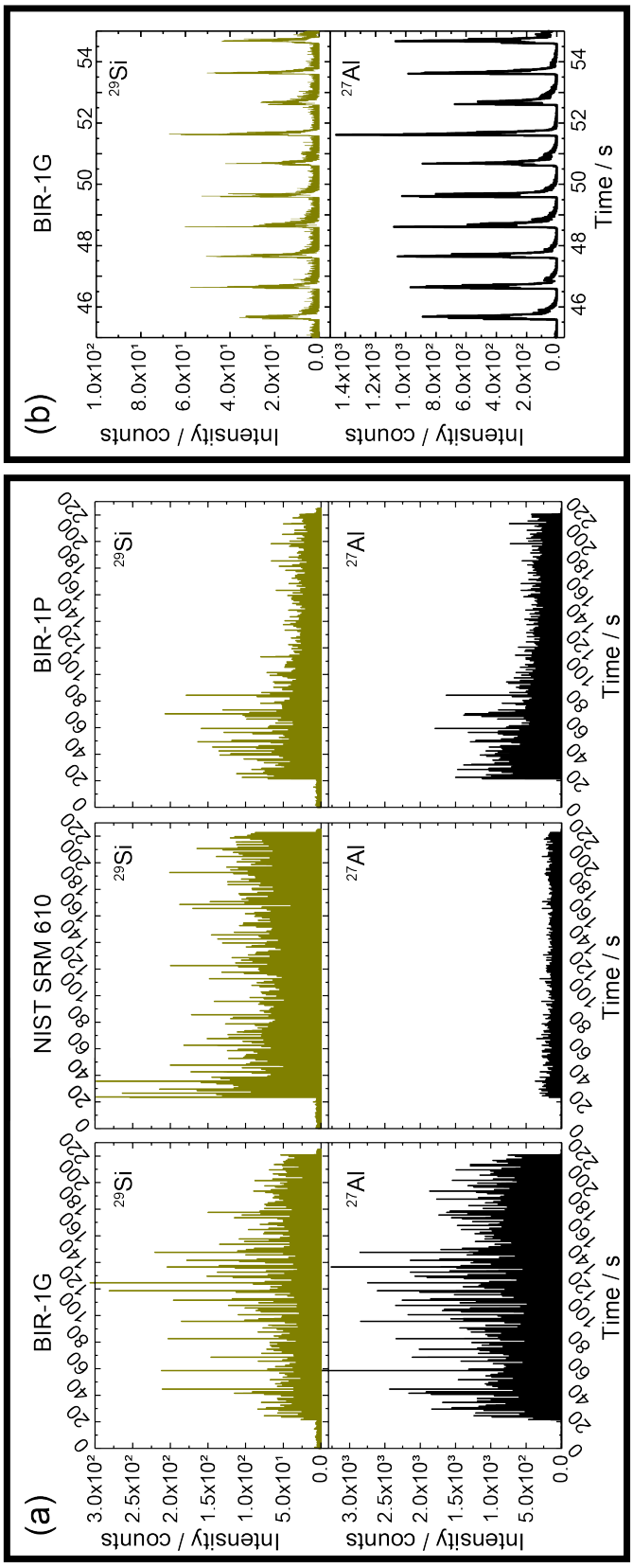

Figure II.4.26: (a) Time-trace of fs-LA-ICP-TOFMS signal of BIR-1G, NIST SRM 610 and BIR-2P over 200 LA pulses of ^{29}Si and ^{27}Al. The wash-out time of approximately 0.6 s at 55 μm spot size allowed a LA frequency of 1 Hz, in order to obtain a pulse by pulse separated spectrum. (b) Zoom-in on the transient signal of BIR-1G.

In Figure II.4.27 the intensity ratio between ^{29}Si and ^{27}Al for all three samples (i.e. NIST SRM 610, BIR-1G, BIR-1P) are displayed. Overall a more stable intensity ratio for NIST SRM 610 compared to BIR-1G and BIR-1P was revealed. However in the case of BIR-1P the elements investigated showed the same structure within the fluctuations of the intensity ratio, already from the first LA pulse. Concerning NIST SRM 610 and BIR-1G, only after $1-3$ LA pulses, a steady signal ratio between ^{27}Al and ^{29}Si was observed. While the intensity ratio concerning NIST SRM 610 started with a higher value before the levelling, the opposite trend was revealed for BIR-1G.

The ionization potential of Al is 578 kJ/mol and therefore approximately 200 kJ/mol lower then for Si (i.e. 787 kJ/mol). According to Garcia *et al.* a preferential LA of Al compared to Si would be expected. In contradiction to this was the obtained trend for NIST SRM 610, where an initial higher signal for Si was revealed, when compared to Al. Note that even though preferential LA of elements with higher ionization potential is proposed, the effect on the LA-generated aerosol, i.e. the information carrier in LA-ICP-MS, is not clear. Moreover, another explanation for the obtained effect could also be the PSD. Guillong *et.al.* already described in 2002 a crater depth dependent particle size distribution and showed, that larger particles were formed during the first LA pulses.[93]

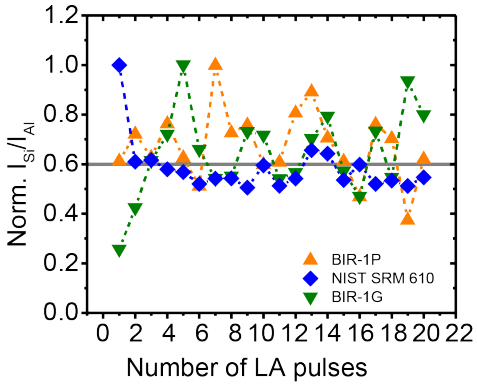

Figure II.4.27: The intensity ratios for each SRM (i.e. BIR-1P, NIST SRM 610, BIR-1G) between ^{29}Si and ^{27}Al. For the intensity, each pulse was integrated over time, then background corrected and abundance normalized. The grey line at 0.6 has no meaning, it is to help the reader for pattern recognition.

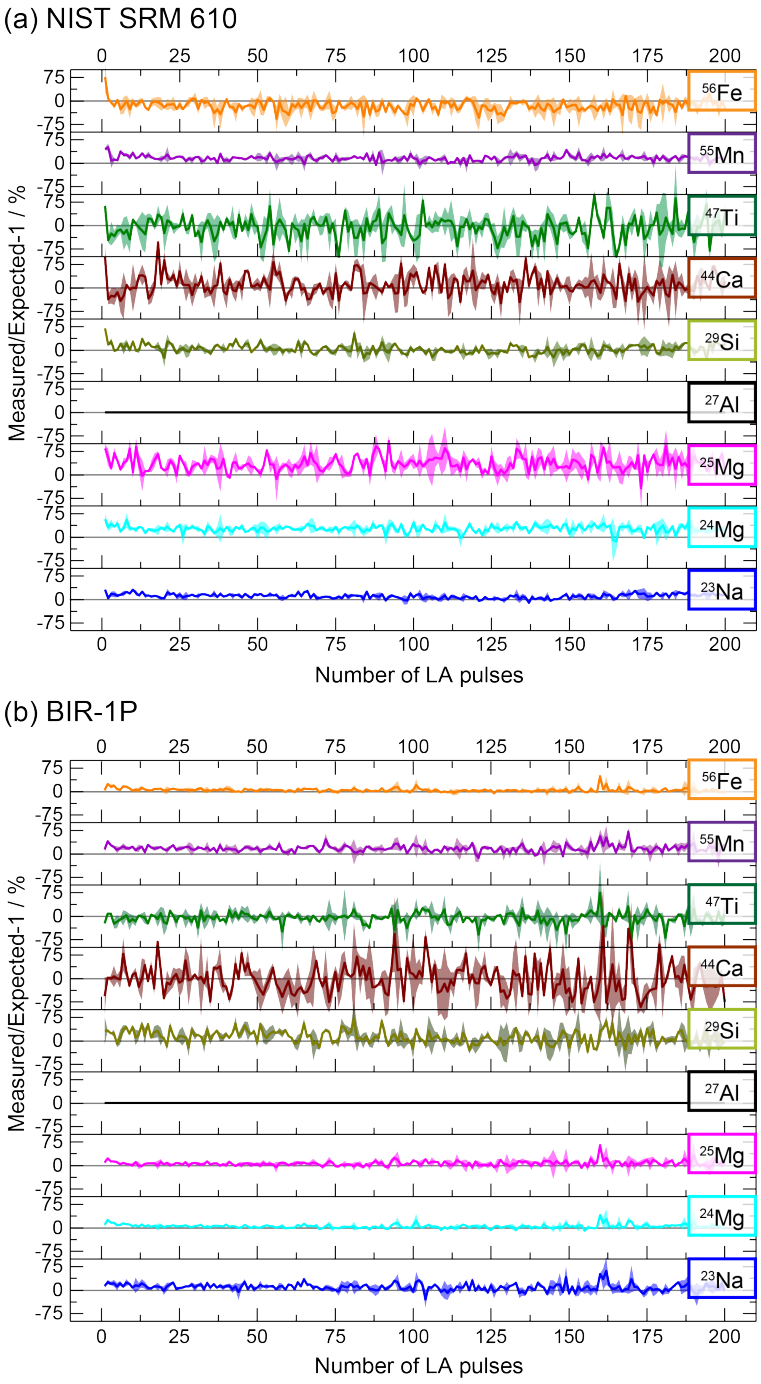

Figure II.4.28: Accuracy obtained for 200 subsequent LA pulses for (a) NIST SRM 610 and (b) BIR-1P. For quantification BIR-1G was used as external standards and ^{27}Al as IS. The determined concentrations were compared with the reference value of the respective SRM in order to calculate the accuracy. The shaded areas represent the standard deviations from two individual measurements.

In Figure II.4.28 the determined accuracies per LA pulse, using BIR-1G as external standard and ^{27}Al as IS are illustrated. The described effect of the initially low signal intensity for Al in case of BIR-1G is reflected within the accuracy pattern (see Figure II.4.28a) of BIR-1P. Generally, lower precision in case of NIST SRM 610 were determined for elements present at ppm-level (i.e. MgO, TiO_2, and FeO, exception was MnO).[24,26]
Finally, the mean accuracy over 200 LA pulses was calculated (see Figure II.4.29). Concerning SiO_2 an overestimation of approximately $5 - 10\%$ was revealed for both samples. Note that the initial 200 LA pulses were analysed in this experiments, while the integration windows for bulk analysis are commonly set after the first 100 to 200 LA pulses. Performing bulk analysis, typically a stable signal is only obtained after several LA pulses.

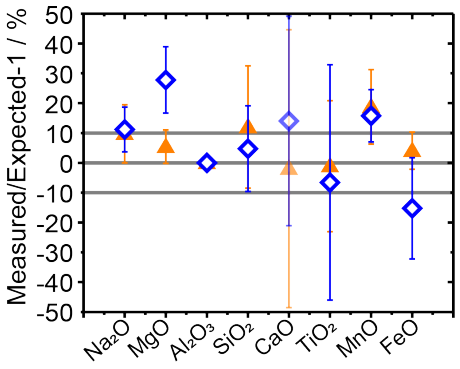

Figure II.4.29: Accuracy obtained from the mean over all 200 LA pulses for BIR-1P (▲), and NIST SRM 610 (◇), using BIR-1G as external standard and ^{27}Al as IS. The error bars represent the overall standard deviations, which were calculated from the two individual measurements per sample and the pulse by pulse deviations over each measurements by error propagation.

"Be curious, not judgemental."

Walt Whitman

Chapter 5

Conclusion and Outlook

In summary, exploring the particle morphology and composition, PSD, mass load effect and effect of *wet* plasma conditions revealed fractionation of Si within silicate based samples. Not only Si enrichment in big particles from LA generated aerosol in case of BHVO-2G was obtained, but also a significant effect of *wet* plasma conditions on the sensitivity of Si was presented. Even though a mass load effect for high LA spot sizes was illustrated, no trend for certain matrices or phases was discovered. Exploring a variety of different SRMs and minerals supported the proposed elemental fractionation of Si in silicate based samples, which has already been particularly addressed by Yuan *et al.* in 2011.[142]

In conclusion, we were not able to extract a single parameter to explain the Si fractionation obtained. Changing the investigated parameters listed above the accuracy could not be improved below 10% for all SRMs. The precision of the analysis including the effect of elemental fractionation was reproducible for the different parameters for certain groups of samples, namely the SRMs in glass phase. On the other side, based on our results the pressed nano-powder SRMs did not show a consistent elemental fractionation concerning Si between each other. Only some pressed nano-powder SRMs, i.e. AC-EP and BIR-1P, exhibited similar behaviour as the group of glass phase SRMs. Moreover, due to the material specific and phase dependent elemental fractionation, a prediction about appropriate external standard for different minerals remained difficult. Even if erroneous concentrations of matrix elements impact the concentrations of all constituents when a 100% mass

normalization is employed the nature of this normalization might still facilitate an overall higher accuracy.

Future studies should therefore focus on the characterization of the LA process of the pressed nano-powders and in particular the LA-generated aerosol. Further investigation of the involved processes during the LA-generated aerosol digestion in the plasma might unravel the elemental fractionation obtained.

Part III

The importance of the third dimension – Depth profile analysis

"It is impossible to imagine a four-dimensional space. I personally find it hard enough to visualize a three-dimensional space!"

Stephen Hawking

Chapter 6

Introduction

This work is published in part as "D. Käser, L. Hendriks, J. Koch, D. Günther, Depth profile analyses with sub 100-nm depth resolution of a metal thin film by femtosecond - laser ablation - inductively coupled plasma - time-of-flight mass spectrometry, Spectrochimica Acta: Part B, 149 (2018), 176-183."[53] *Reproduced with permission from Elsevier.*

Depth-dependent compositions and structures are also of high interest in many modern technologies. Metal, semiconductor and oxide thin films of thicknesses in the micro- and nanometer range have become fundamental building blocks for the fabrication of surface-engineered materials and/or coatings with user defined functionalities. Composition, thickness, number of layers and/or the periodicity may be adjusted to control the physical or chemical properties of the material, and thus, allow adjustment of the material properties. The controlled fabrication of such thin films and the fundamental understanding of their various functionalities require reliable and detailed chemical and structural analysis. Of particular interest is the lateral and depth resolved composition to verify the materials homogeneity in particular with respect to surfaces and interfaces.[143,144] The depth resolution as characteristic figure of merit to describe the precision and accuracy of such depth profiling methods is crucial and can be evaluated by the specific broadening of a sharp interface.[145,146] For example, systems with alternating layers of different materials can serve as model targets to evaluate the characteristic depth dependent resolutions.

6.1 Different analytical techniques for depth profile analysis

Nowadays, many different analytical techniques are used to identify the chemical structure and composition of such nanoscale layers. Among these techniques, we can differentiate between techniques capable of characterizing chemical bonding and elemental composition as well as techniques used for surface imaging and topological studies. In some applications the chemical bonding and crystallinity of the thin layers are evaluated using for example X-ray diffraction (XRD), Fourier transform infrared (FTIR), Raman scattering or X-ray photoelectron spectroscopy (XPS) analysis.[147–149] A combination of these different techniques reveal different crystallinity between or within the layers.[148,149] Furthermore, imaging techniques such as atomic force or transmission and scanning electron microscopy (AFM, TEM, SEM) are applied to examine the surface topography of thin films.[147,148] In some applications the elemental composition is investigated as it delivers relevant information that is unavailable from topography, crystallinity or chemical structure studies. In this context, analytical techniques based on X-ray, electron or ion detection are commonly applied. X-ray based techniques such as energy- or wavelength-dispersive X-ray fluorescence spectroscopy (EDX and WDX) provide knowledge about the spatial distribution of matrix elements.[147,150] EDX is usually combined with scanning electron microscopy to provide a fast analysis of cross-sectional specimen.[151] Although, the limits of detection (LODs), especially for light elements, are not sufficient to detect trace elements, different analytical techniques combined with sputtering processes may be applied. One advantage of these sputtering based techniques is the tunable sputtering rates for fast or slow removal rates in order to improve depth resolution.[151] For example, electron detection based techniques, such as Auger electron spectroscopy (AES) or XPS exhibit good lateral and depth resolution in the range of μm and a few nm, respectively.[152] Concerning these techniques, the sputtering process though is only applied to expose the region of interest layer by layer. On the other side, secondary ion mass spectrometry (SIMS) directly analyzes the sputtered material. Its depth resolution can go down to the nm-range with detection limits as low as ng/g.[103,153] Glow-discharge – time of flight – mass spectrometry (GD-TOFMS) is another technique used for high resolution depth profile analyses of thin films giving resolutions below 40 nm.[154] During the past few years also laser ablation (LA)

assisted methods have gained more importance concerning depth profile analysis, such as LA ionization mass spectrometry (LIMS), whose reported depth resolutions go down to the nm-range.[155]

6.1.1 Working principles of different analytical tools for depth profiling

In order to investigate the depth-dependent elemental composition of a sample usually different complementary analytical techniques are applied.[156,157] The most common techniques are presented in Table III.6.1.

All of these methods can be applied on any type of material (insulators, semiconductors, metals), however, the materials have to be stable in vacuum. RBS is a non-destructive method, unlike AES, XPS and SIMS, in which the material is removed by using an ion beam, while for GD-MS the material is removed by low energy ions produced by a glow discharge. Such sputtering techniques damage the sample at the probed sites. The maximal depth of analysis ranges from 0.1 μm up to 100 μm, depending on the analytical method. In the case of GD-MS and SIMS, the sputtered ions can be analysed by various different mass analysers (qMS, sfMS, TOFMS). In both cases, the most promising results for depth profile analysis are obtained by TOF mass analysers, due to the quasi-simultaneous detection and fast sampling possibilities. The underlying principles of these methods are summarized in the following section and represented in Figure III.6.1.

Table III.6.1: Comparison of the main characteristics of different surface-analysis and in depth analytical methods, adapted from ref. [158]

	AES	XPS	RBS	SIMS	GD-MS*
Excitation probe	Electrons	Photons (XR)	Ions	Ions	Ions
Emission / Detection	Electrons	Electrons	Electrons	Ions (m/z)	Ions (m/z)
Sputtering	Ion beam	Ion beam	No	Ion beam	DC/RF
	< 10 keV	< 10 keV		< 10 keV	< 50 eV
Atom mixing	Yes	Yes	No	Yes	No
Crater effect	No	No	No	Yes (-)	Yes (++)
Max. Depth analysis (nm)	10^3	100	$5 \cdot 10^3$	$5 \cdot 10^3$	$> 10^5$
Depth Resolution (nm)	$0.5 - 2.5$	$0.5 - 2.5$	5	$0.5 - 2.5$	< 5
Lateral Resolution (nm)	10	10^2	10^5	10	10^6
Chemical bond information	Yes (+)	Yes (++)	No	Yes (+)	No
Detection Limit (μg/g)	10^3	10^3	10^3	10^{-1} - 10	1
Elemental range	$Z > 2$	$Z > 2$	$Z > 2$	All	All
Calibration Method	Easy	Easy	Standard free	Complex	Complex
Vacuum at sample site (mbar)	10^{-10}	10^{-10}	10^{-6}	10^{-10}	10^{-2}
Acquisition time	Moderate	Slow	Moderate	Slow	Very fast

** Values taken from ref.* [154,159]

6.1.1.1 Auger electron spectroscopy – AES

AES is a spectroscopic method which is based on the Auger effect. Through bombardment of the sample by an electron beam of some eV up to 50 keV core state electrons can be removed. Thereby an electron hole is formed. The core hole can be filled by an electron from a higher level and due to the conservation of energy another electron must be ejected. This ejected electron is called Auger electron and its specific energy can be associated to its parent atom and is in the range of 0.02-1 keV.[160] In this sense, the sample will not be visibly damaged. Since the maximal escape depth for these electrons is only a few atomic layers, AES is commonly coupled with sputtering techniques in order to measure a depth profile. This combination is called AES sputter profiling.[161]

6.1.1.2 X-ray photoelectron spectroscopy – XPS

According to Watts *et al.*,[160] in XPS a core electron is removed by X-ray photons of energy $h\nu$. The kinetic energy (E_k) of the removed electrons is measured. The kinetic energy itself is dependent on the photon energy and the X-rays applied and is therefore not an intrinsic material property. To investigate the specific binding energy (E_B) and hence to identify the parent element and atomic energy level the relationship between three parameters involved in the XPS experiment is used:

$$E_B = h\nu - E_k - W \tag{6.1}$$

with W the work function of the electron. The emitted and measured photoelectron generates like AES an electron hole. The same way like in AES the escape depth for these electrons is only a few atomic layers and hence XPS is usually coupled with sputtering in order to measure a depth profile.

6.1.1.3 Secondary Ion Mass Spectrometry – SIMS

In SIMS the surface of interest is bombarded with a beam of accelerated ions. By collision with surface atoms, these ions transfer enough energy to sputter the surface atoms into the vacuum. These so-called secondary ions can be positively or negatively charged and are measured by a mass spectrometer. The bombarding ions are typically either single

atoms such as Cs, Ga, Bi or C_{60}-buckyballs or other cluster ions.[162] The sputtered ions can directly be analysed by different mass analysers.

6.1.1.4 Rutherford Backscattering Spectroscopy – RBS

In the case of RBS an MeV ion beam is directed onto the sample surface. These ions, usually $^4He^+$ ions, continuously lose energy to electrons of the sample material until they are stopped at a depth of several micrometers. Some of them are elastically scattered by the atomic nuclei of the sample and can be detected under backscattering angles. The collisional loss depends on the ratio of the projectile mass to the mass of the sample atoms and is characteristic for each isotopic mass. Therefore the composition of the sample can be determined by a simple energy measurement of the backscattered He. The continuous energy loss of the ions on their path through the material allows to establish a depth profile of elemental concentrations at the same time. One of the biggest advantages of RBS is its quantitativeness since the elastic scattering cross-sections are known with an accuracy of better than 1 % and do not depend on the matrix composition. The technique is essentially non-destructive and the maximum depth of analysis is several μm.[163]

6.1.1.5 Glow-Discharge Mass Spectrometry – GD-MS

In GD-MS, ions are produced through a glow-discharge. The cathode (+), usually being the sample, and anode (−) are in contact with one another by a discharge gas (typically Ar, at 0.13 - 13 mbar) and through the application of sufficiently high voltages between them a breakdown of the discharge gas is reached. As a consequence of the potential difference (250 - 2000 V) between cathode and anode, the positively charged ions are accelerated towards the cathode. The impinging ions transfer their energy onto the target surface. This way atomic or ionic populations are directly ejected from the sample surface. The sputtered ions can then directly be analysed by MS.[164] Using traditional dc-GD-sources only conducting materials can be probed, whereas with rf-GD-MS also non-conducting targets are accessible.[165]

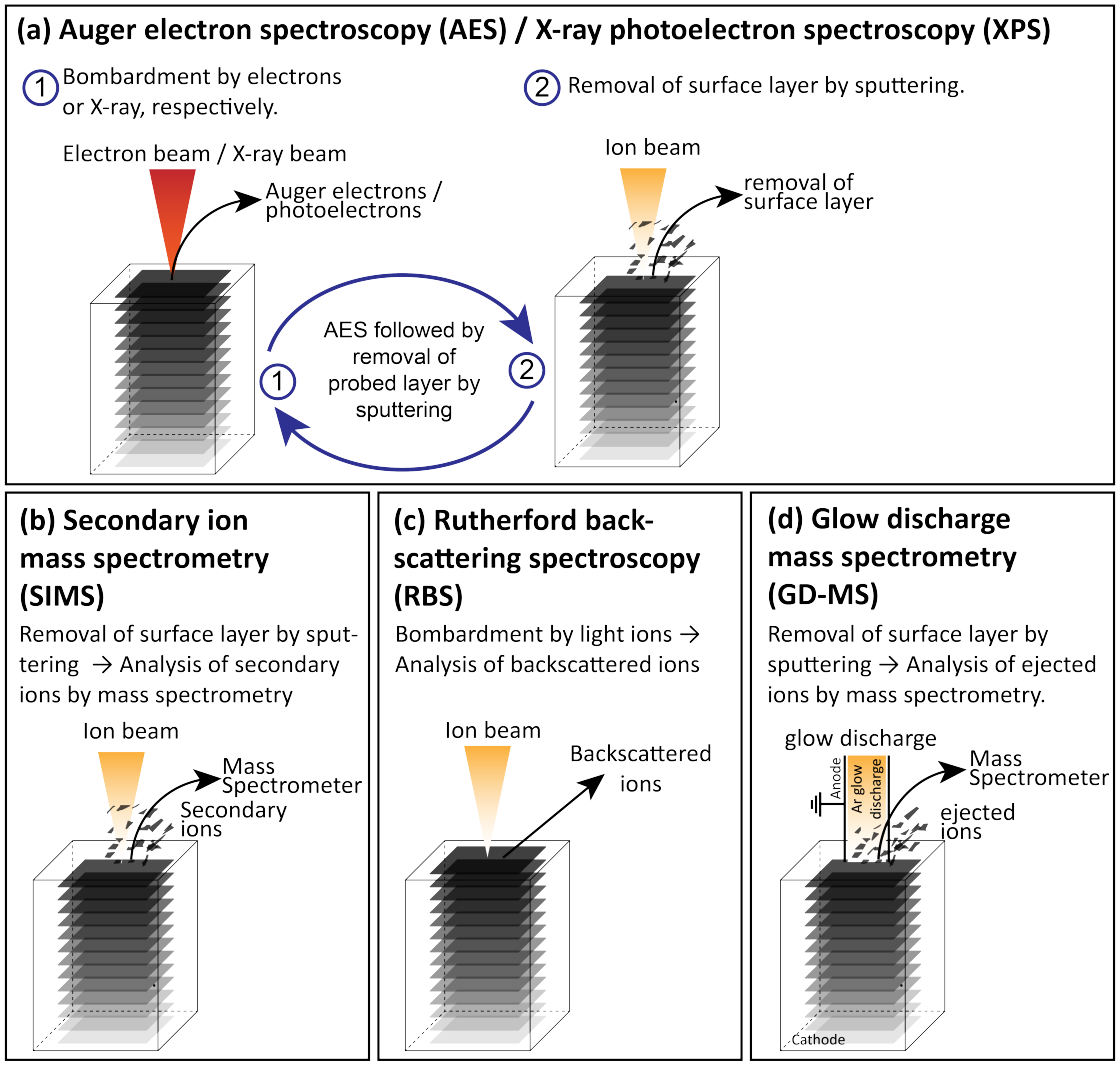

Figure III.6.1: Analysis of a surface layer by (a) AES and XPS, respectively (to be able to analyze layers further down in the sample, the surface layer is removed by sputtering), (b) SIMS, (c), RBS (d) and GD-MS.

6.2 LA-ICP-MS for depth profile analysis

The potential of LA-ICP-MS for depth profile analysis has already been investigated throughout various studies.[30,34,166,167] Its major advantages lie within the low LODs (g/g – ng/g),[103] and hence the possibility to reveal concentrations of trace elements. Additionally, an adjustable lateral resolution in the range of 100 μm to as low as 1 μm can be achieved. Furthermore, the LA cell is operated at atmospheric pressure which results in fast throughput and finally, depth resolutions below 300 nm have already been reported.[30,34,166–168]

6.2.1 Basic principle of LA-ICP-MS for depth profiling

When LA-ICP-MS is used to probe a sample in depth, a pulsed laser with constant frequency is aimed at the same area. The frequency is adjusted to the given conditions of the LA cell (i.e. wash-out time) in such a way, that the transient signal of each LA pulse can be fully separated from another (see Figure III.6.2a). This way, mixing of aerosol originating from subsequent LA pulses is suppressed. By decreasing the wash-out time the total acquisition time also decreases, while the signal to noise ratio (S/N) increases.[11] Indeed, due to the short time period, less noise is integrated and e.g. for a 10 μm spot size absolute detection limits of 60 attogramms for ^{238}U have been reported.[50] Additionally, by fast aerosol transport the instantaneous concentration of an analyte within the ICP increases and hence sensitivities (cps/ppm) are improved.[169]

In Figure III.6.2, the elemental composition of e.g. the first laser pulse corresponds to the average composition of the volume of the solid that has been ablated in this very first pulse. In order to obtain the depth profile of a specific sample, the aerosol composition of each LA pulse is evaluated independently. The transient peak of each LA pulse is integrated over time and by different quantification strategies the composition per laser pulse can be determined.[170] Finally, to obtain the depth profile for different elements the depth of the crater after each LA pulse needs to be evaluated according to the LA up-take rate. [1] In the idealized example in Figure III.6.2, the depth profile of layer type A, which

[1] The LA up-take rate can be determined by for example CM analysis of the crater depth after each LA pulse, decoupled from the LA-ICP-MS measurements. In order to reconstruct the depth profile directly the possibility for an on-line monitoring of the crater depth would be beneficial (see part IV, chapter 9).

may be a single element or any type of material different from layer type B, shows an ideal step function. The depth resolution of an analytical method is shown by an eventual broadening of such a sharp interface in the measured profile and vice versa. Indeed, if such a sharp interface is probed, the depth resolution can be determined by the evaluation of the measured profile. This process will be explained in detail in part III, chapter 8.

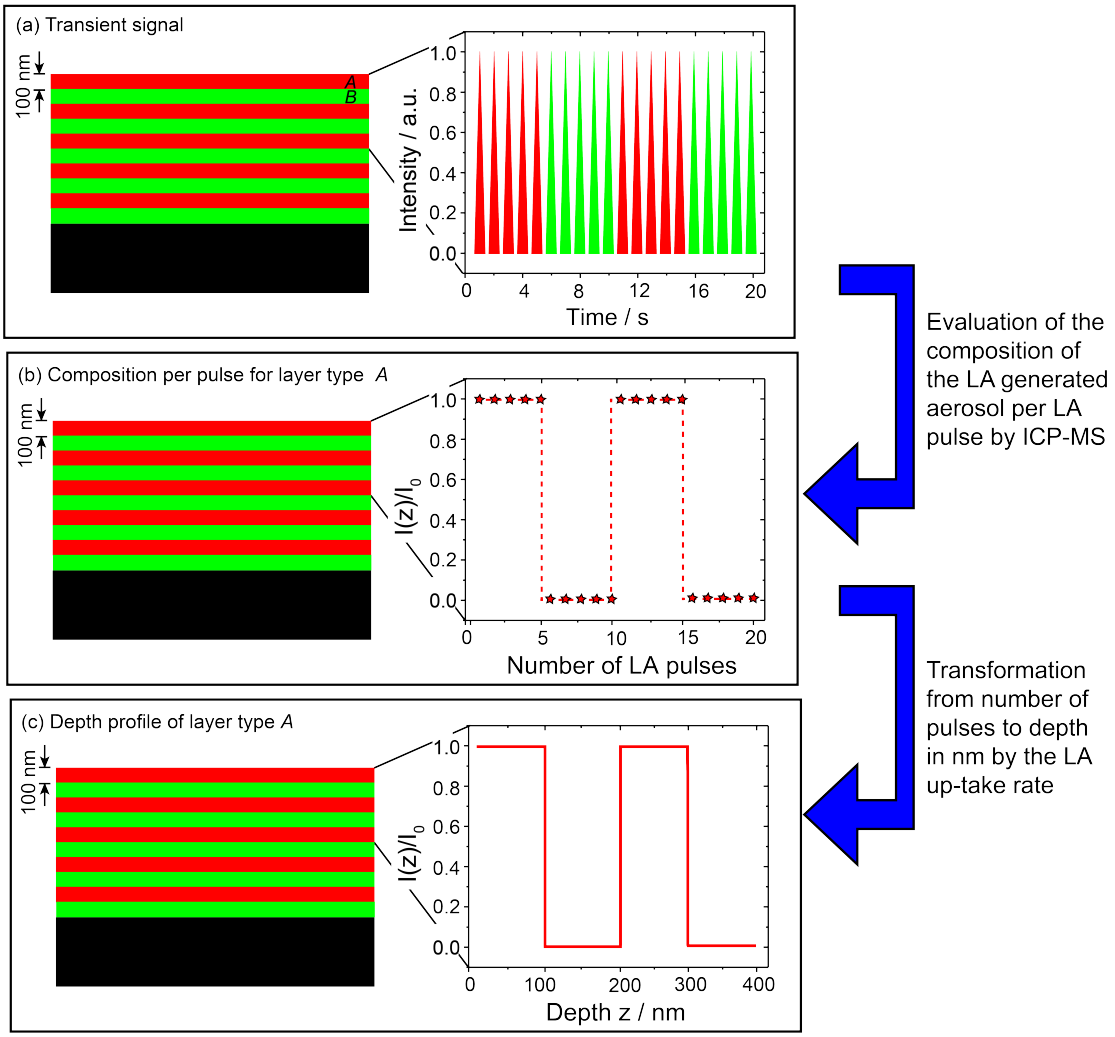

Figure III.6.2: (a) Transient signal in an idealized case. Integration and normalization per laser ablation pulse results in the real depth profile of the measured sample. In this model, the evaluation of the composition and the crater depth of each LA pulse result in a pulse profile (b). Finally, the determination of the crater depth after each LA pulse, by the specific LA up-take rate, the depth profile in (c) is obtained.

6.2.2 Prerequisites for a high depth resolution by LA-ICP-MS

In LA-ICP-MS different parameters and processes significantly contribute to the ultimate achievable depth resolution. If again the example in Figure III.6.2 is considered, the LA up-take rate, i.e. the amount of material which is removed per laser pulse, can be recognized as the dominant parameter which influences the resolution. Indeed, in an extreme case, if the LA up-take rate was as high as to remove all layers simultaneously in one LA pulse, the layered structure of this target would not be detectable. Gratifyingly, the laser ablation up-take can be tuned by modifying the applied energy density on the sample surface. If the laser energy directed at a constant area is decreased, generally, lower LA up-take rates result.[60,171] Hence, the LA up-take is preferably as small as possible in order to obtain the highest achievable depth resolution. However, the energy cannot be decreased arbitrarily due to the so-called LA threshold. This LA threshold determines the minimal amount of energy density required for LA to occur. Overall, since LA is based on the interaction of the incoming laser beam with the material surface, the LA threshold is highly dependent on the material properties, the laser wavelength and the laser pulse duration.[172–174]

Recalling the discussion from *part I and II*; the first step for LA to occur is the absorption of a significant amount of laser energy, which may proceed by single- or multi-photon processes.[172] Generally, the band structure of the material determines the dominant absorption process. In the case of metals, the Fermi level is situated in the middle of an electron band and thus the single-photon absorption of low-to-moderate-energy photons is possible. For semiconductors and insulators, the Fermi level is located between the valence and conduction bands. Hence, only photons which exceed this specific energy can result in single-photon absorption. However, two processes still allow the elevation of electrons from the valence band to the conduction band, even if the single-photon energy is too low. These two processes consist of the electron avalanche ionization and the strong multi-photon absorption/ionization.[172] Avalanche processes can occur if electrons, at e.g. defect sites are elevated into the conduction band by single-photon absorption. Such electrons (also called seed electrons) can further absorb single-photons, whereby their kinetic energy is increased. The collision of such electrons with bound electrons then leads to avalanche ionization. Additionally, when the laser intensity is very high ($> 10^{12}$ W/cm^2),

as in the case of fs-lasers, bound electrons can be ionized by multi-photon absorption. At long laser pulse durations (i.e. ns) such multi-photon ionizations are negligible and the LA of insulators and semiconductors is dominated by avalanche ionization.[175]
When comparing the LA thresholds of insulators and semiconductors with the LA thresholds of metals, as a first approximation, higher values are apparent.[173] In addition, in the case of ns-LA generally higher LA thresholds for insulators and semiconductors compared to metals are observed. This can be explained by the fact that the LA of insulators and semiconductors requires the generation of seed electrons within the first step, while in the case of linear absorption during the LA of metals such seed electrons are not required.[175] The relative contributions of multi photon and avalanche ionization are still debated.[176–179] However, in both cases (fs-LA and ns-LA) the absorption and hence the initial step of LA is highly dependent on the photon energy and therefore a lower wavelength (increasing photon energy) results in lower LA thresholds. An overview of the dominant processes related to the different material types and lasers can be found in Table III.6.2.[173]

Table III.6.2: Overview of dominating absorption processes related to the material and laser type according to ref.[172,173,175]

	ns-LA	fs-LA
Metals	single photon absorption	single & multi photon absorption
Semiconductors	avalanche ionization	avalanche ionization & multi photon absorption
Insulators	avalanche ionization	avalanche ionization & multi photon absorption

Inherently not only the LA threshold can vary with different laser parameters and material properties, but also the ablated mass. Indeed, the LA up-take rate is tightly connected with the LA threshold and follows the same principles. The LA up-take rate can only be considered as the ultimate depth resolution in LA-ICP-MS if other effects, such as heat diffusion and crater morphology are negligible. Significant discrepancies between LA up-take rates and depth resolutions have been observed. One of the main reasons for this was found to be a non-uniform laser radiation delivered to the LA site.[30,170] The effect of heat diffusion within the sample and the imposed intensity distribution of the delivered

laser radiation are discussed in the following sections.

6.2.2.1 Heat diffusion

After absorption of the incoming laser intensity by electrons, the energy is transferred by radiative and/or non-radiative relaxation processes within the material (see part I and part II, chapter 2). The absorbed laser energy leads to thermalization of the electronic subsystems and subsequently to an energy transfer to the lattice. Through this process, energy is lost by the electron heat transport into the target. Assuming the thermalization of the electronic subsystem to be much faster than the energy transfer to the lattice, the temperature of each subsystem can be described individually (T_e and T_i) and the energy transfer into the target can be calculated by a one-dimensional, two-temperature diffusion model:[78]

$$C_e \frac{\partial T_e}{\partial t} = -\frac{\partial Q(z)}{\partial z} - \gamma\big(T_e - T_i\big) + S \tag{6.2}$$

$$C_i \frac{\partial T_i}{\partial t} = -\gamma\big(T_e - T_i\big) \tag{6.3}$$

$$Q(z) = -k_e \frac{\partial T_e}{\partial z} \tag{6.4}$$

$$S = I(t) A \alpha e^{\alpha z} \tag{6.5}$$

with C_i and C_e the heat capacities of the electron and the lattice subsystems, respectively, γ the parameter characterizing the electron-lattice coupling, z the direction perpendicular to the surface, $Q(z)$ the heat flux, k_e the electron thermal conductivity, S the laser heating source term, $I(t)$ the laser intensity, $A = 1-R$ the surface transmissivity and α the material absorption coefficient.[78] [2]

This model is only fulfilled for ultra-short laser pulses. In this case, the pulse duration τ_L is much shorter than the electron cooling time τ_e and the lattice heating time τ_i, ($\tau_L \ll \tau_e \ll \tau_i$).[78] This way, the pulse and therefore the laser heating source term ends before the energy is transported to the lattice subsystem. On the other side for ns laser pulses, the pulse duration is much longer than the electron cooling time and the lattice heating time ($\tau_e \ll \tau_i \ll \tau_L$). Hence, the electronic and lattice subsystem have time to equilibrate before the laser heating source term ends (see part I). The two-temperature

[2] For details regarding the solution of this two-temperature diffusion model see appendix A.

diffusion model reduces to:[78]

$$C_i \frac{\partial T}{\partial t} = -\frac{\partial}{\partial z}\left(k_0 \cdot \frac{\partial T}{\partial z}\right) + S \tag{6.6}$$

The significant pulse width difference between ns and fs lasers result in different heat diffusion processes. In the case of fs-lasers the heat penetration depth is dependent on the electron thermal diffusivity along the time interval of the laser ablation for low energy densities.[78] In the case of ns-lasers the heat penetration depth is determined by the heat diffusion coefficient of the target.[14] For ns-LA the heat penetrations depth can lead to large heat-affected zones and reduced ablation efficiencies. Additionally, the heating of the sample to a melt phase can be detrimental for LA-ICP-MS due to preferential vaporization. The heating can also lead to elemental migration within the bulk material and therefore distort the original elemental distribution in depth, which is critical for depth profile analysis.

6.2.2.2 Crater shape induced by the laser intensity distribution

According to St-Onge the crater depth at specific positions can be described by the following equation:[170]

$$D(r) = Y_i \cdot F(r) \tag{6.7}$$

with Y_i the LA up-take rate of material type i, and $F(r)$ the laser energy density profile. Indeed, it is exactly this energy density profile which determines the crater shape. If a laser hits a flat surface, the crater shape is directly proportional to the laser energy density distribution. In theory, all subsequent laser pulses irradiate a larger area of material. Since the total energy is constant, the average energy density would become smaller and $F(r)$ would change with each laser pulse. However, St-Onge has shown, that for small aspect ratios between crater radius and depth ($r/R_0 \leq 0.2$), $D(r)$ can be approximated by equation (6.7) and hence $F(r)$ stays constant.[170]

Laser beam profiles commonly occur with a Gaussian optical intensity profile. If such profiles are imaged onto a sample surface, conical craters are formed due to stronger ablation in the central part of the crater as indicated in Figure III.6.3a.[170] This example clearly shows, that even though the laser drills through the first layer (type A) within the first pulse, there would still be a significant contribution from layer type A to the second

pulse. Hence, the ablated volume of the second laser pulse would contain material from layer type A and B. In order to minimize this contribution, a flat-top laser energy density profile is required.

In a general expression (equation (6.8)) St-Onge describes the laser energy density profile for a Super-Gaussian.[170] In here, the value of α determines the form of the Super-Gaussian: For $\alpha = 2$, $F(r)$ is Gaussian and for $\alpha \to \infty$, $F(r)$ is a flat-top.

$$F(r) = F(0) \cdot exp\left[- \left(\frac{r}{R} \right)^{\alpha} \right] \tag{6.8}$$

$$F(0) = \frac{1}{\Gamma\left(1 + \frac{2}{\alpha}\right)} \cdot \frac{E}{\pi R^2} \tag{6.9}$$

with $F(0) = E/\left(\pi R^2\right)$ the energy density at the centre of the beam (r=0), R the beam waist radius and Γ the gamma function. Already for $\alpha = 8$ the crater shape significantly differs from a Gaussian shape as depicted in Figure III.6.3b. The amount of material removed from layer type A within the second laser pulse is reduced by a factor of 2.5 as compared to a Gaussian profile, with the overall contribution from layer type A still in the range of 12% as calculated based on the crater area. Hence only for $\alpha \to \infty$ and, if each laser pulse ablates a perfectly cylindrical volume, the contribution of the top layers are eliminated. Indeed, in such an ideal case, a mixing of different layers would only occur if one laser pulse was to directly remove material from two different layers and hence mixing would only appear within a single laser pulse. In this ideal scenario the depth resolution is not limited by the crater shape but rather by the LA up-take rate. The goal for high-resolution depth profile analysis by LA-ICP-MS is to use a flat-top energy density profile at the sample surface.

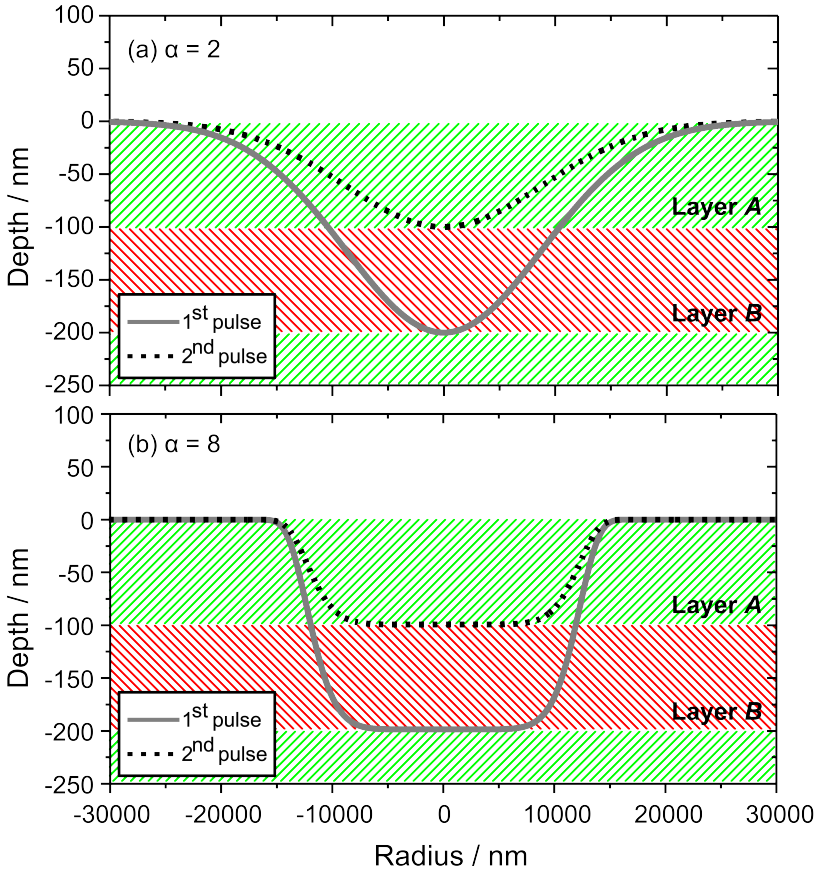

Figure III.6.3: Crater evolution after two laser pulses for (a) Gaussian beam and (b) Super-Gaussian beam profile. According to St-Onge the laser energy density profile can be described by equation (6.8).[170]

"The efficiency of a group working together is directly related to the homogeneity of the work they are performing"

Luther Gulick

Chapter 7

Homogenization of laser beam profiles

This work is published in part as "D. Käser, L. Hendriks, J. Koch, D. Günther, Depth profile analyses with sub 100-nm depth resolution of a metal thin film by femtosecond - laser ablation - inductively coupled plasma - time-of-flight mass spectrometry, Spectrochimica Acta: Part B, 149 (2018), 176-183."[53] Reproduced with permission from Elsevier.
& "D. Käser, L. Hendriks, J. Koch, D. Günther, Corrigendum to "Depth profile analyses with sub 100-nm depth resolution of a metal thin film by femtosecond - laser ablation - inductively coupled plasma - time-of-flight mass spectrometry" Spectrochimica Acta Part B: Atomic Spectroscopy 149 (2018) 176–183, Spectrochimica Acta: Part B, 149 (2018), 322."[54] Reproduced with permission from Elsevier.

7.1 Homogenization of laser radiation in ns-LA-ICP-MS

A flat-top energy density profile for state-of-the-art UV-ns-LA systems was already achieved in 1997, whereby complex beam shaping by an imaging multiaperture beam integrator is performed.[25,180] Generally, such imaging beam integrators consist of two lenslet arrays

and a primary lens. The first lenslet array breaks up the input beam into smaller beamlets and focuses them onto the second lenslet array, which is placed at a distance f, the focal length of the first lenslet array. The second lenslet array together with the primary lens forms the image of the first lenslet array on a target plane.[180] In the case of ns-LA systems this target plane is located together with a field lens at the plane of a masking aperture.[25] This aperture in turn consists of round holes to allow different LA spot sizes at the sample surface. At the end, a Schwarzschild objective is used to image this aperture onto the sample surface. With such a mirror objective a high numerical aperture [1] is obtained and hence high image resolutions can be achieved. Due to the arrangement of such Schwarzschild objectives the inner maximum of the initial beam profile has to be transferred to the outer region. To do so, a set of two prisms is used right in the beginning, before the homogenization by the imaging beam integrator is performed. To eventually observe the sample surface through the central mirror of the Schwarzschild objective, a microscope equipped with a camera on top is used.[25]

With this set-up only 1% of the initial energy of the laser reaches the sample surface. However, in the case of ns-lasers, a high energy output still results in high energy densities at the sample surface (up to $20\,J/cm^2$). Furthermore, independent of the spot size constant energy densities are present and highly reproducible craters with steep walls and flat bottoms for various spot sizes (4μm to 200 μm) are achieved.[25]

7.2 Homogenization of laser radiation in fs-LA-ICP-MS

The extremely high peak irradiance of up to 10^{14} W/cm^2 of fs-lasers renders the adaption of the projection assemblies used for ns-LA extremely challenging. Multiaperture beam integrators, as described above, with a high number of intermediate foci are usually avoided – they can lead to plasma formation, self-focusing, and filamentation of the laser beam, which significantly affect the quality of the produced image[181] and eventually lead to unwanted crater morphologies.[139] In general for fs lasers, the number of optical elements should be minimized, since they can result in laser pulse distortions, such as laser pulse stretching.[182,183] This can be detrimental for LA, because only if the laser pulse duration

[1] The numerical aperture is defined as $NA = n \cdot sin(\Theta)$ with n the refractive index and Θ the maximal half angle of the incoming laser beam.

is < 1000 fs, it is shorter than the energy transport from the electronic subsystem to the lattice and hence heat diffusion is minimized (for more details see part III, chapter 7).
To better cope with such distortions we made use of an alternative optical beam processing strategy which allows the build-up of fully homogenized radiation fields at the objective's image plane for fs-laser systems. Its concept is based on pinhole imaging. The schematic set-up is shown in Figure III.7.1a. Here, a pinhole with a diameter q is imaged by an objective lens (with focal length f) in its image plane at a distance i. This concept follows the well-known lens law (equation (7.1)).

$$\frac{1}{f} = \frac{1}{o} + \frac{1}{i} \tag{7.1}$$

with o the distance of the pinhole to the objective lens, f the focal length of the lens and i the distance between the lens and its image plane. According to this the size of the image and therefore the spot-size of the LA crater in the image plane, can be calculated by equation (7.2).

$$q_I = \underbrace{\frac{f}{o-f}}_{magnification} \cdot q \tag{7.2}$$

with q_I the size of the pinhole in the image plane. Depending on the magnification smaller spot sizes can be obtained with increasing distance o.
In fact, if the distance o is very large and the pinhole diameter q very small, pinhole imaging can be described by two consecutive Fourier transforms as indicated in Figure III.7.2. Details about this Fourier optical description of the imaging process will be discussed in the following section.

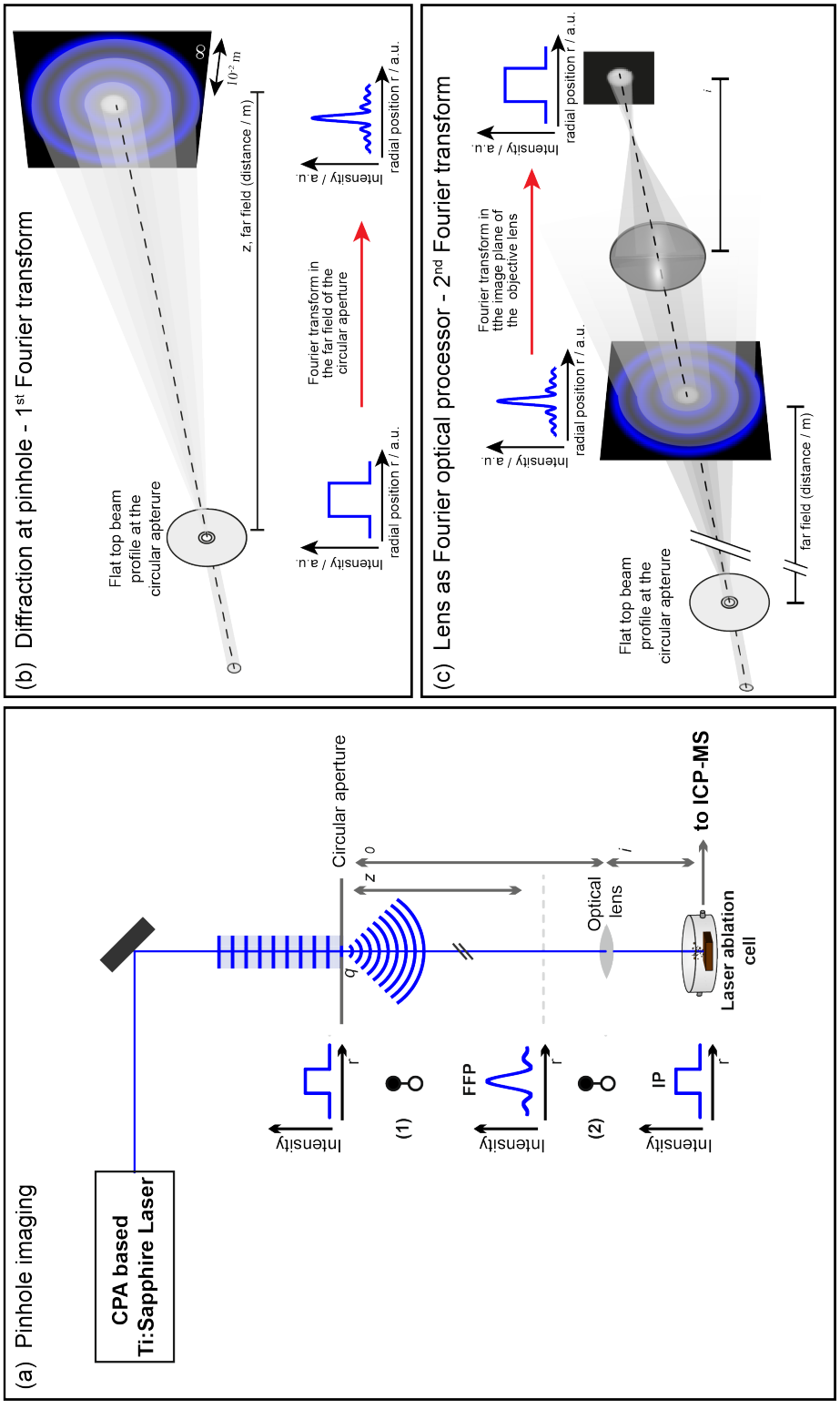

Figure III.7.1: (a) Schematic of the pinhole imaging for fs-LA systems, with q being the diameter of the pinhole, o the distance to the objective lens, i the distance to the image plane. The set-up can also be described by two Fourier transforms: (b) The diffraction in the far field of the a pinhole resulting in an Airy disk pattern. This diffraction is described by the Fraunhofer integral – the first Fourier transform. (c) The objective lens acting as Fourier optical processor. This way, the Airy disk pattern in the far field is re-transformed into a flat-top beam profile.

7.2.1 Pinhole imaging by objective lens – Description by two consecutive Fourier optical transforms

Generally, if a plane wave propagates through an aperture, it gets diffracted.[184] Diffraction was defined by Sommerfeld as "any deviation of light rays from rectilinear paths which cannot be interpreted as reflection or refraction." and hence occurs if a light wave is confined on its lateral extent for example by a pinhole.[184] In this case, the degree of diffraction highly depends on the diameter of the pinhole and the wavelength. Only if the wavelength is of the order of the pinhole diameter or the distance between the pinhole and the target plane is very high, diffraction becomes appreciable.[184] In the case of an incoming plane wave, the complex theory of diffraction can be approximated by the Fraunhofer diffraction integral (7.3) in the far field of the pinhole.

$$u(\alpha,\beta,z_0) = -\frac{i\cdot n\cdot z_0}{\lambda\cdot {l_0}^2}\cdot exp\Big[i\,k\,l_0\Big]\cdot\iint_A u_0(x',y',0)\cdot exp\Big[-\frac{2\pi\,i\,n}{\lambda}(\alpha x'+\beta y')\Big]\,dx'\,dy' \tag{7.3}$$

which is fulfilled if:

$$\frac{nq^2}{4\lambda z_0} \ll 1 \tag{7.4}$$

with q the diameter of the aperture, λ the wavelength of the incoming laser beam, $l_0 := \sqrt{x^2+y^2+{z_0}^2} \gg q$ the position in the far field, z_0 the distance to the aperture and n the refractive index. According to this approximation, the complex amplitude ($u(\alpha,\beta,z_0)$, describing the incoming light wave) in the far field corresponds to its Fourier transform at $z=0$. Due to the radial symmetry in case of a circular pinhole the Fourier transform can be described by the Hankel transform in radial coordinates (equation (7.5)):

$$H(q) = 2\pi\int_0^\infty r\cdot f(r)\cdot J_0\big(2\pi qr\big)\,dr \tag{7.5}$$

$$f(r)^2 = I_0\cdot c\cdot\big(\frac{J_1(q)}{q}\big)^2 \tag{7.6}$$

$$c = const.,\ x = r\cos(\alpha),\ y = r \cdot \sin(\alpha),\ r = \sqrt{x^2 + y^2},$$
$$u = q \cdot \cos\phi,\ v = q \cdot \sin\phi,\ q = \sqrt{u^2 + v^2} \tag{7.7}$$

$$J_0 = \frac{1}{2\pi i} \cdot \int_0^{2\pi} exp\big(2\pi i r q \cos\alpha\big)\, d\alpha \tag{7.8}$$

$$J_1 = \frac{1}{2\pi i} \cdot \int_0^{2\pi} exp\big(ir\cos(\alpha)\big) \cdot exp\big(i\alpha\big)\, d\alpha \tag{7.9}$$

with $f(r)$ the function being Fourier transformed and J_0 and J_1 the Bessel functions of first kind of zero and first order, respectively.

Finally, a radially symmetric flat-top beam profile is present at $z = 0$, due to the pinhole. Its Fourier transform in the far field is a $sinc(x)$-like function and the obtained diffraction pattern in the far field of a circular pinhole is the well-known Airy disk pattern, shown in Figure III.7.1b. After this first Fourier transform from a flat-top beam profile into an Airy disk pattern, the objective lens acts as a Fourier optical processor.[184] Hence the Airy disk will get re-transformed by the objective lens back into a flat-top beam profile in the image plane of the lens (see Figure III.7.1c).

7.2.2 Performance of the pinhole imaging concept

In the following sections the performance of such pinhole imaging systems was tested in order to obtain homogeneous removal by fs-LA. In a first step the importance of the sample position and the *depth of focus* were evaluated, while in the second step the crater morphology and hence the effect of the imposed beam profile on different sample materials was investigated.

7.2.2.1 Experimental

Optical set-up of fs-laser homogenization scheme

The fs-laser system used was a Ti:Sapphire chirped laser pulse amplification (CPA) fs-laser (Mira Legend, Coherent Inc., Santa Clara, CA, USA). Its fundamental wavelength was 800 nm and the output energy in the range of 3.8 mJ. The laser pulse duration was determined to be between 150 fs up to 200 fs. (For details on pulse duration measurements see appendix B.) Due to the aforementioned effect of a shorter laser wavelength on the LA

threshold it was frequency doubled by a second-harmonics generation (SHG) crystal. This way the system was operated at a wavelength of 400 nm. In Figure III.7.2 the detailed optical set-up is shown.

Before the laser beam was processed to form a flat-top energy distribution on the sample surface as described above, it was filtered in order to remove random noise. This was done using a pinhole with a diameter $\sim$ 1 mm about 2000 mm in front of the SHG crystal. Together with the second pinhole, low frequency noise was removed. [2] Before the laser beam was frequency doubled by the SHG crystal it was spatially reduced through the telescope by a factor of two in order to increase the conversion efficiency. After this, the beam was truncated by the second pinhole which was then imaged on the sample surface.

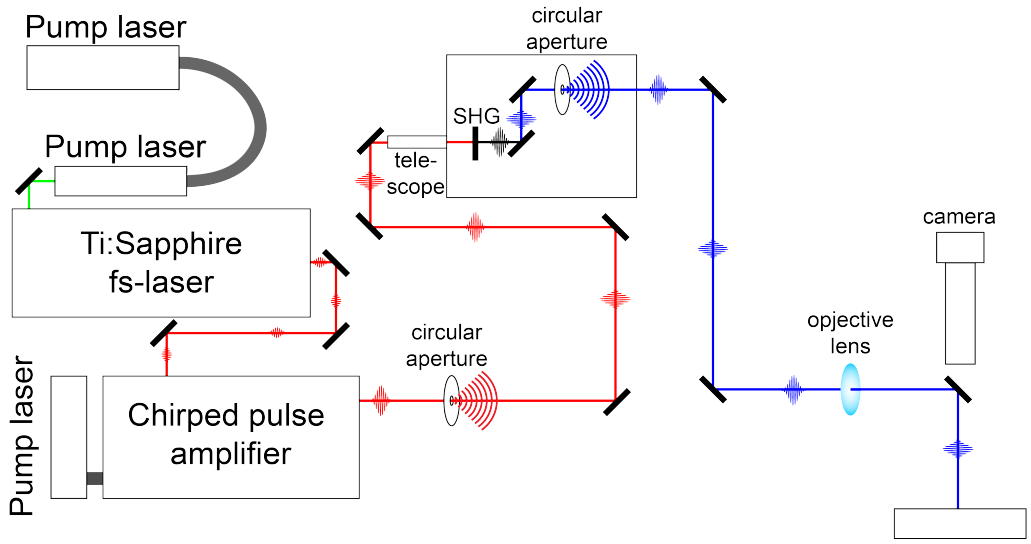

Figure III.7.2: Schematic of optical set-up. The distance between the first circular aperture and the second was approximately 2000 mm. The telescope had a magnification of two. Through the SHG the primary wavelength of 800 nm was frequency doubled. A 1500 mm beam path was between the second circular aperture and the objective lens.

In order to be able to observe the sample through a camera focusing was initiated beforehand. The observation was placed from above and the beam was guided by a thin

[2] By forming an Airy disk in the far field of the first pinhole, the beam is Fourier transformed and the low frequency noise is spatially located away from the center of the output beam.

mirror onto the sample surface. This way, the image plane i had to be in the range of $100\,mm$. Furthermore, also the focal length f was preferably in the same range. If the focal length would be located too close to the thin mirror, damage thereof would occur, the same would happen if it would be too close to the thin window of the LA cell. To reduce spherical aberration a best form lens with either $f = 75$ mm or $f = 100$ mm was used.

In order to allow a spot size in the range of 0.025 mm and still have a reasonable energy density at the sample surface, the diameter of the pinhole was between 0.4 mm to 0.7 mm positioned 1500 mm before the focusing lens with $i \approx 107$ mm. The maximal energy transported to the sample surface was in the range of $20\,\mu$ J corresponding to energy densities of ≈ 5 J/cm^2. The overall energy loss can be attributed to the first circular aperture ($\approx 80\%$), the telescope ($\approx 30\%$), the SHG ($\approx 60\%$) and the second pinhole ($\approx 80\%$). In addition, minimal loss also occurs at the mirrors and the the objective lens. Overall, the high energy loss may seem undesirable, however, as mentioned above intermediate focal planes could lead to air breakdown. In the presented set-up, the energy travelling through the focal plane of the objective lens was extremely low and consequently no distortion was expected.

Finally, due to the large distance between the pinhole to be imaged and the objective lens the Fraunhofer integral is fulfilled and the imaging set-up can be described by two Fourier optical transforms. Indeed, measurements of the beam profile just before the objective lens showed the expected Airy disk pattern (see Figure III.7.3).

Furthermore, we were able to simulate the beam profile in the image plane (see Figure III.7.4). Only if the Fourier transform of the Airy disk can be performed from infinity, a perfect flat-top beam profile is obtained. Due to the finite size of the objective lens and the beam divergence the transform will only be performed until a finite distance. Indeed, if a pinhole with $q = 0.5$ mm was used, the first minimum of the Airy disk was displaced by 1.83 mm from the central maximum, according to equation (7.10).

$$\begin{aligned} y &= o \cdot \frac{m \cdot \lambda}{q \cdot 2} \\ with \quad m_{minima} &= \frac{zeros\,of\,J_1(x)}{\pi} \end{aligned} \tag{7.10}$$

with $J_1(x)$ the Bessel function of first kind. In this case, the Airy disk will only be Fourier transformed up until the 7^{th} minima. In which case the simulations in Figure III.7.4 show

a nearly flat-top beam profile.

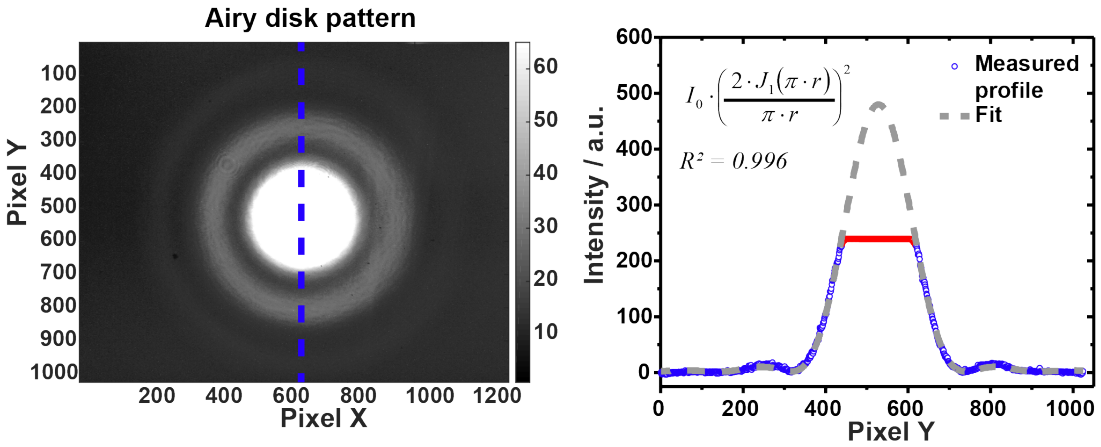

Figure III.7.3: Measured beam profile in front of the lens using a 0.7 mm pinhole. The central part was overexposed in order to see the second maximum of the Airy disk pattern.

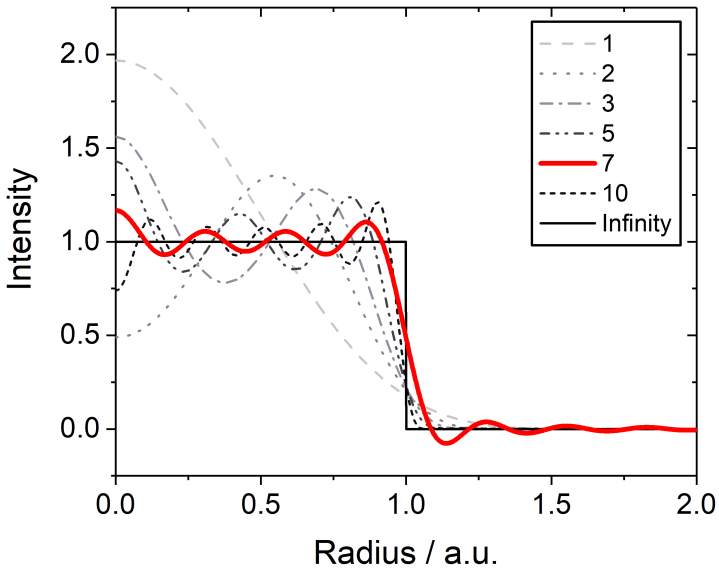

Figure III.7.4: Simulation of intensity profile for a different number of minima which are Fourier transformed by the optical lens.

Assessing the sample position

In order to determine the image plane, crater morphologies at different z-positions were evaluated. Position x showing craters with a flat bottom were assumed to be the position

where the image plane was aligned with the sample surface. By changing the position of the sample in the z-direction the image plane was either above, below or aligned with the sample surface.

To evaluate the *depth of focus*, i.e. the range within which the study of the crater morphology showed flat bottoms and steep walls, a 0.5 mm circular aperture and an objective lens with $f = 75\,mm$ were used. This way an energy density of approximately 3.8 J/cm^2 was applied. These studies were performed on a borosilicate glass (Schott Schweiz AG, St. Gallen, Switzerland). For more details, regarding the properties of the sample, see Table III.7.1.

Assessing different types of materials

The effect of the homogenized laser intensity distribution on different materials was assessed ($SrTiO_3$ (Crys Tec GmbH Kristalltechnologie, Berlin, Germany) and Ni/Cr multilayer system (NIST SRM 2135c)). A 0.4 mm circular aperture and an objective lens with $f = 100\,mm$ were used. This way energy densities in the range of 1 J/cm^2 were applied. Different energy densities were obtained by either reducing the energy by decreasing the conversion efficiency of the SHG in the case of $SrTiO_3$ or by the introduction of a filter system along the beam path resulting in lower energies transported to the sample surface (Cr / Ni multilayer sample).

Overview of the sample properties

The samples are listed in Table III.7.1 and were either amorphous or crystalline materials, and insulating or conducting.

Table III.7.1: Properties of materials investigated.

Material	Type	Structure	layer depth
Borosilicate glass	insulator	amorphous	bulk
$SrTiO_3$	insulator *	crystalline	bulk
Cr / Ni	conducting	crystalline	Alternating Cr/Ni layers
(NIST SRM 2135c)			(5 x 57 nm Cr / 4 x 56 nm Ni)

* If $SrTiO_3$ looses oxygen, the material becomes conducting.

Microscopy techniques

The laser intensity profile at the sample surface was studied by characterizing the crater morphology. To do so, four different imaging techniques were applied. Their basic set-ups are shown in Figure III.7.5 and will be explained in the following:

1. **Optical microscopy (OM).**[185] The light source (a tungsten-halogen bulb) is positioned in a reflective housing. Via a collector lens, the light is guided through a beamsplitter mirror. For illumination of the sample, the light is focused onto the sample surface by an objective. The reflected light from the sample re-enters the objective and by a series of lenses in the objective, the sample is magnified. The light travels back through the beamsplitter into a photosensitive camera. In the case of OM the light source emits white light and hence the resolution is limited to $R = 200$ nm, according to the Rayleigh criterion (equation (7.11)).

$$sin(\Theta_R) = 1.22 \cdot \frac{\lambda}{d} \tag{7.11}$$

2. **Confocal microsopy (CM).**[186] The light source in CM are different LED light sources from red to blue and white. According to the Rayleigh criterion resolutions $R_{vertical} < 3$ nm and $R_{spatial} = 170$ nm for $\lambda = 460$ nm are achievable. [3] In addition, a low depth of field is possible due to the monochromatic light and hence, it can be focused on a single point within a defined focal plane. Thereby, light noise from other planes of different depth can be eliminated through the confocal pinholes. By scanning plane by plane a three dimensional image can be reconstructed and the crater depth can be evaluated. However, angles in-depth $> 42°$ cannot be resolved [3], due to the reflection properties. Furthermore, increased surface roughness and reduced reflectivity on the crater bottom render profiling by CM challenging and may lead to artefacts.

3. **Atomic force microscopy (AFM).**[187] This technique is based on the interaction of a very small tip with the sample surface. The tip is mounted on a cantilever and scanned across the surface. Depending on the morphology of the sample surface and the interaction the tip is bent out of its equilibrium state. Through a laser

[3] According to the specifications of Plu neox, Sensofar, Barcelona, Spain.

beam reflected from the cantilever surface the movement of the tip along the sample surface can be monitored. This way resolutions in the order of $R \leq nm$ can be achieved depending on the morphology of the tip. However, this technique is limited in its maximal measurable depth to 14 μm [4] due to the geometrical arrangement of the cantilever. Using AFM not only fine structures on the surface of a sample can be imaged, but also the depth of the craters can be evaluated.

4. **Scanning electron microscopy (SEM).**[188] In SEM an electron beam is focused onto the sample surface. This way, the electrons interact with the sample and produce secondary and back-scattered electrons (SE & BSE). SE originate from surface near regions while BSE come from deeper regions of the sample. Detecting either the SE or BSE different information can be extracted and finally SEM can be used to study surface structures at very high resolutions. By using electrons instead of light to image a sample surface, the resolution can be increased due to the short wavelength of electrons ($R \leq 1\,nm$). In SEM, the sample is placed in a vacuum chamber in order to be able to bombard it with electrons.

[4] According to the specifications of NaioAFM, Nanosurf, Futuro Liestal, Switzerland.

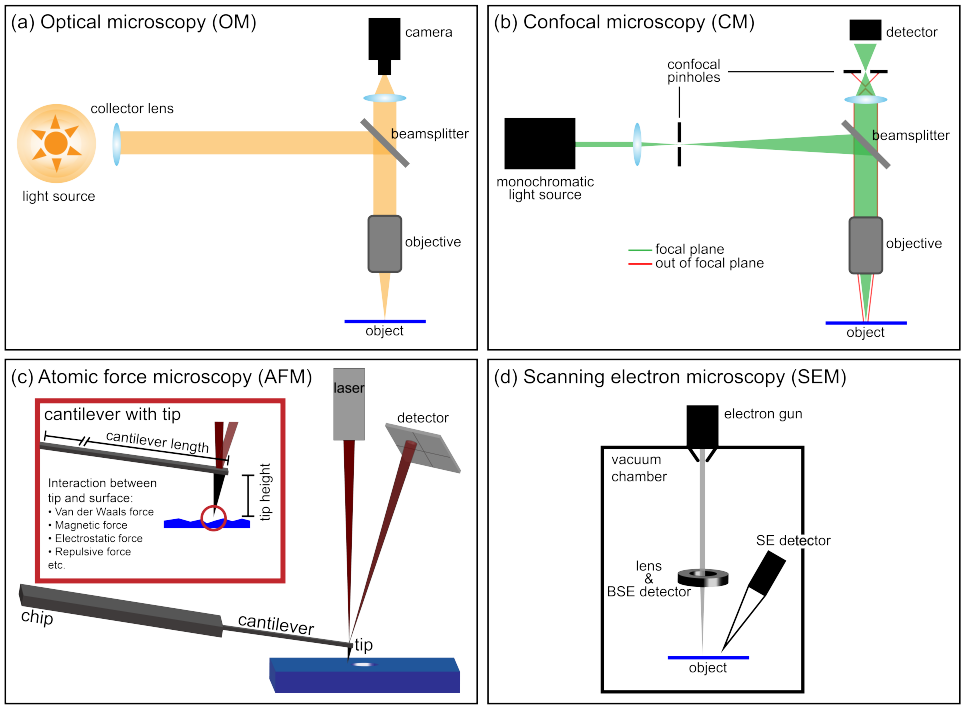

Figure III.7.5: Schematic of (a) optical microscopy, (b) confocal microscopy, (c) atomic force microscopy and (d) scanning electron microscopy.

Data evaluation of SEM, AFM and CM measurements, in terms of surface roughness and 2D FFT analysis, as well as profile extraction, were performed using the free software Gwyddion.[189] For 2D FFT analysis, the default Hanning windowing in Gwyddion was used. Regarding SEM micrographs, the obtained amplitudes of the 2D FFT analysis cannot be interpreted, since SEM does not contain height information. All processed data were plotted with OriginPro 8.6 (OriginLab Corporation, Northampton, England) and all compiled figures were assembled in Adobe Illustrator (Adobe Systems, California, USA).

7.2.2.2 Results and discussion

Assessing the sample position

Several studies on the position dependence of the crater morphology revealed a very small range throughout which the formed craters showed flat bottoms and steep walls. Indeed, position movements in the z-direction in the range of some 10s of μm resulted in a drastic change of crater morphology (see Figure III.7.6) and hence a very narrow *depth of focus*.

As shown in Figure III.7.7, if the sample was placed below the image plane ($-40\,\mu m$), the crater bottom did not appear to be flat in the OM image for 25 and 50 LA pulses. In case the sample was placed above the image plane ($+40\,\mu m$), the crater bottom after 25 LA pulses seemed to be rather flat, while after 50 LA pulses, odd morphologies started to appear in the central part of the crater bottom.

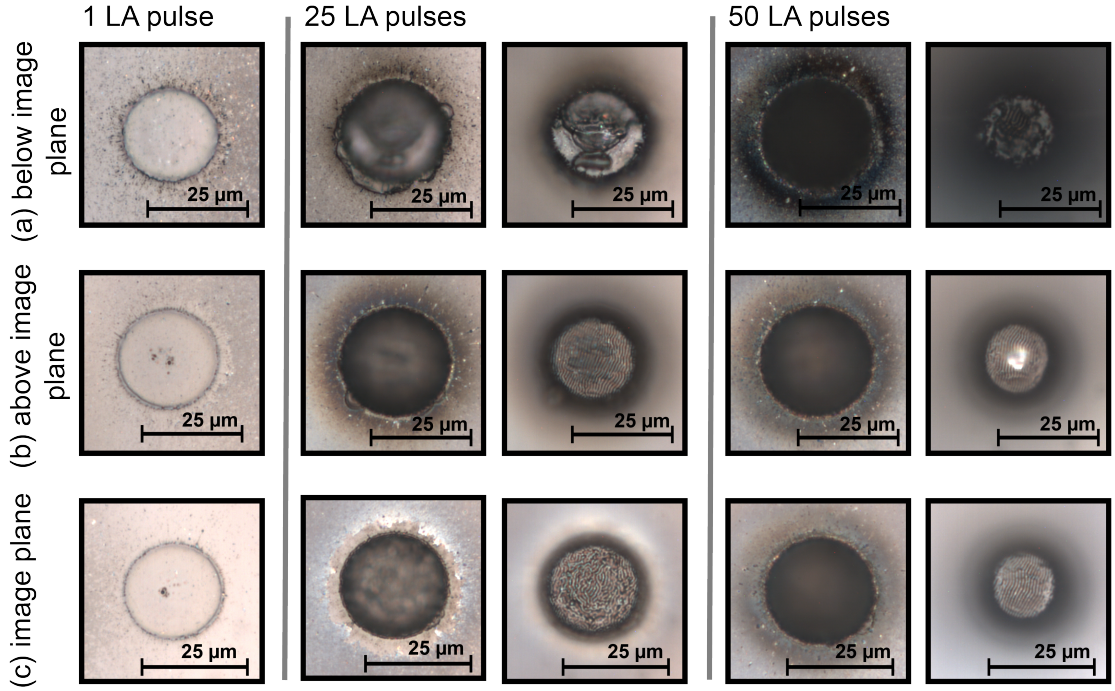

Figure III.7.6: Morphology study of LA induced crater after 1, 25 and 50 LA pulses. The sample was positioned below the image plane (a), above the image plane (b) and at the image plane (c).

By exploring the morphology of the craters formed in the image plane in more detail by AFM measurements, an elevation in the central part of the sample became apparent (see Figure III.7.7). Indeed height differences between minimum and maximum on the crater bottom of 0.2 mum after 1 LA pulse and 1.35 mum after 25 LA pulses were revealed. In the case of one LA pulse, this resulted in 57% height difference to the total depth of the crater, while after 25 pulses it decreased to 33%. With increasing number of LA pulses, the elevation in the central part of the crater bottom had a smaller effect on the total depth of the crater. Assuming this elevation on the crater bottom measured after the first LA pulse would multiply with each subsequent LA pulse, then the height difference on the bottom

with respect to the total depth of the crater would increase. Since this was not observed, one could assume that the effects leading to the elevation in the central part start to level out. Generally, the origin of this elevation could be due to remaining inhomogeneities in the laser beam profile at the sample surface and/or a result of imperfect alignment of the sample position. [5]

Furthermore, the slope of the craters were approximated according to the radius difference between the crater bottom and the rim and the depth of the crater (see Figure III.7.6). [6] This way slopes of $\alpha_{1\,LA\,pulse} = 82°$ and $\alpha_{25\,LA\,pulse} = 40°$ were calculated. With an increasing number of LA pulses the slope decreases and hence the crater wall gets steeper. The depth after one LA pulse is only in the range 1.5% of the spot size and the deviation from a cylindrical crater morphology plays only a minor role within further ICP-MS analysis. Indeed, in this case, the amount of material missing from the outer part of this a circular truncated conical crater is only in the range of 7%.

fs-LA induced surface roughness

In Figure III.7.7b characteristic fs-LA induced surface roughness, also called laser-induced periodic surface structures (LIPSS) or ripples, was revealed on the crater bottom. Bonse *et al.* described two different types of LIPSS.[190] On one side, low-spatial-frequency LIPSS (LSFL) show periods close to the wavelength of the laser ($\lambda \approx \Lambda_{LSFL}$), on the other side high-spatial-frequency LIPSS (HSFL) have been obtained with frequencies significantly smaller than the laser wavelength ($\lambda/2 > \Lambda_{HSFL}$).

[5] Please note, it is not clear whether the sample at this position was placed at the real image plane.

[6] The slope can be approximated by $\alpha = tan^{-1}((r_1 - r_2)/z)$ with z being the depth, r_1 the radius of the crater rim and r_2 the radius at the crater bottom. If $r_1 = r_2$ then $\alpha = 0$ and hence a cylindrical crater is apparent.

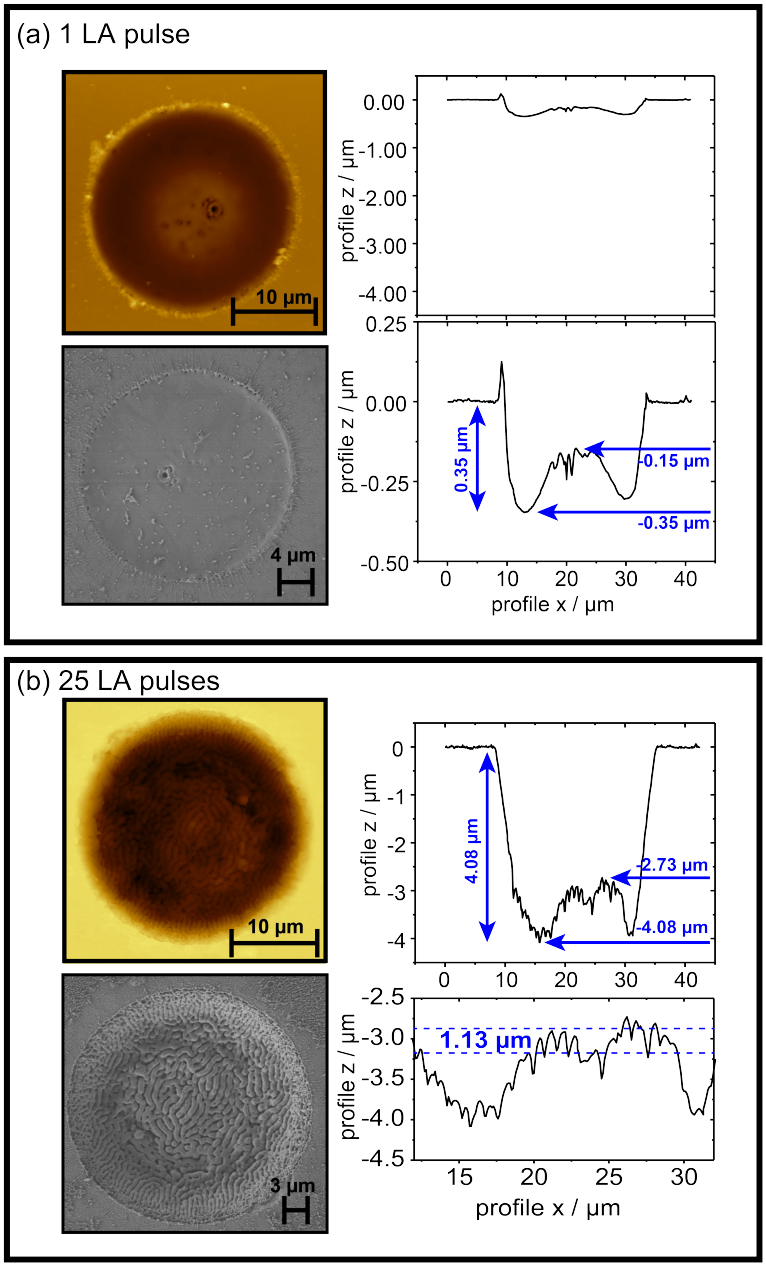

Figure III.7.7: Morphology study of LA induced crater on borosilicate glass after (a) 1 LA pulse and (b) 25 LA pulses. In case of 1 LA pulse (a), the crater depth at its deepest point is 0.35 μm. In case (b), after 25 LA pulses, the crater depth at its deepest point is 4.08 μm.

The assumed building mechanism of LSFL is the interaction of the incident laser beam with a surface electromagnetic wave generated at a rough surface.[190,191] In the case of metals and semiconductors with high absorbance, such LSFL are found to be perpendicular to the beam polarization. Considering dielectrics the periodicity of the LSFL was reported to be either close to λ or close to λ/n, with n being the refractive index of the dielectric material.[192] The orientation of the LSFL in the case of dielectrics was found either perpendicular[193] or parallel[194] to the polarization of the incoming beam. On the other side the mechanism controlling the generation of HSFL is controversially discussed in the literature. Second-harmonics generation,[193,195] involvement of specific types of plasmon modes[196,197] or self-organization[194] have been proposed as mechanisms. Such HSFL were predominantly obtained for transparent materials and the orientations were found to be either perpendicular[193] or parallel[198] to the polarization.[190]

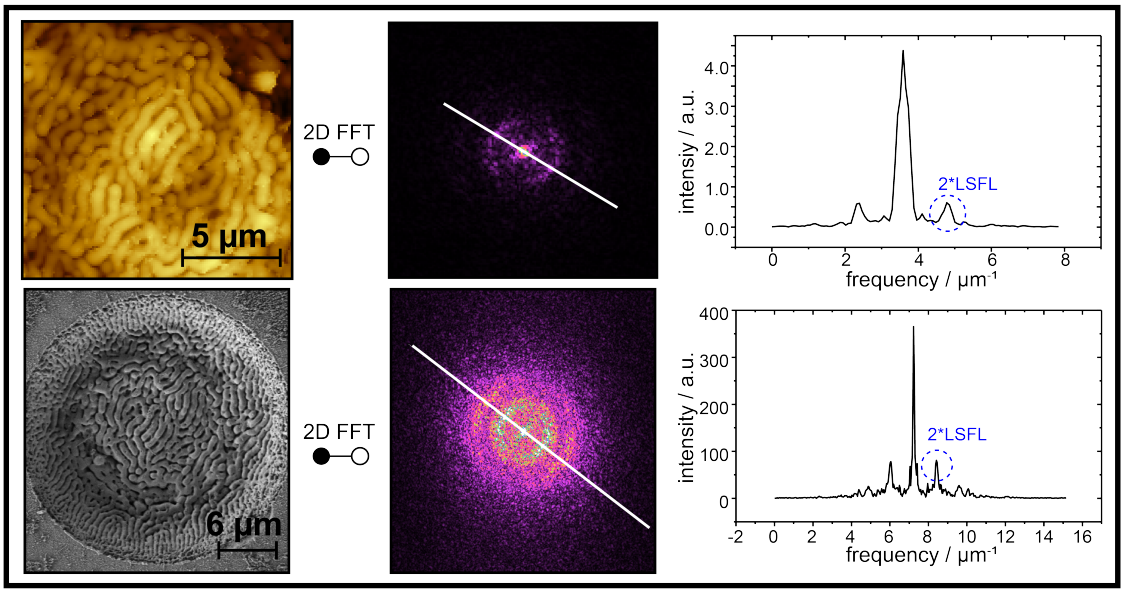

Figure III.7.8: LIPSS study after 25 LA pulses. The top row shows a cut of the measured AFM (see Figure III.7.7b). The 2D FFT analysis thereof resulted in $\Lambda_{2*LSFL} = 0.8\,\mu m$. The bottom row is a cut from the SEM micrograph (see Figure III.7.7b). The obtained LIPSS period of the 2D FFT analysis was again $\Lambda_{2*LSFL} = 0.8\,\mu m$.

Different experimental parameters have been examined to influence the generation of these LIPSS. Not only the wavelength λ but also the beam polarization, number of LA pulses

and the laser energy density influence the structure of these LIPSS.[190]

The period extracted from the AFM and SEM measurements in Figure III.7.8 was determined to be $\Lambda_{LSFL} = 0.8\,\mu m$ by 2D FFT analysis and shows double the value of the LSFL expected.[190] Note, that at this point, it is not clear why such low frequency LIPPS were generated, with half the frequency of the expected LSFL. The RMS roughness [7] of the crater bottom was calculated to be $0.3\,\mu$m according to the AFM measurement. In conclusion, the overall roughness induced by the LIPSS formation on the crater bottom is approximately four times lower than the height difference between the minimum and maximum depth of the crater.

Assessing different types of materials

Besides borosilicate glass used to study the dependence of the sample position, the effects of the flat-top beam profile on $SrTiO_3$ and a Cr/Ni multilayer sample were investigated. For each of the sample, the optical set-up was carefully adjusted and the image plane was evaluated according to the crater morphology as described in section 7.2.1.2.

The morphology study on the **$SrTiO_3$** wafer showed craters with steep walls and flat bottoms (Figure III.7.9). The slope was in the range of $\alpha_{1\,LA\,pulse} = 85°$ after one LA pulse and reduced to $\alpha_{10\,LA\,pulse} = 53°$ after 10 LA pulses (Figure III.7.9). The LA uptake rate extracted from the CM measurements was approximately $0.1\,\mu$m / LA pulse. As shown in Figure III.7.9b again LIPSS were formed on the crater bottom. Their period was determined to be $\Lambda_{LSFL} = 0.2\,\mu$m and hence followed the theory discussed by Bonse *et al.*[190] Compared to the morphology study of the craters formed on the borosilicate glass sample, no elevations in central part of the craters were present. This may be due to perfect alignment of the z-position of the sample with respect to the image plane.

[7] RMS roughness is the root mean square of the profile height deviations from the mean.

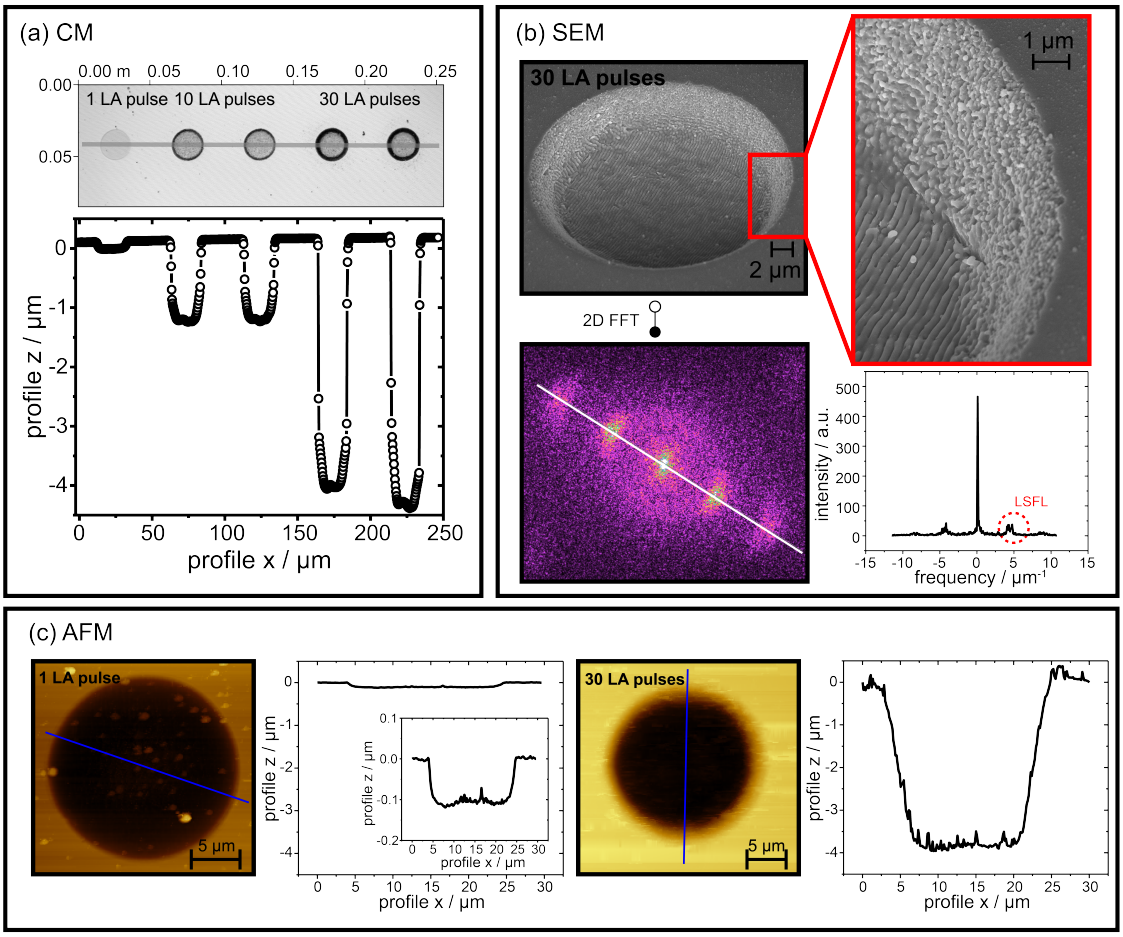

Figure III.7.9: Sample $SrTiO_3$ showing nice cylindrical crater by (a) CM, (b) SEM and (c) AFM morphology studies. The 2D FFT analysis of the SEM micrograph results in $\Lambda_{LSFL} = 0.2\mu m$.

The third material investigated was a **metal** sample (NIST SRM 2135c). This sample consisted of 9 alternating layers of Cr and Ni on a Si wafer. Each of the layers had a certified thickness of 57 nm for Cr and 56 nm for Ni. Due to these thin layers, already after 25 LA pulses the Si wafer was reached (see also part III, chapter 8). For this sample, the crater morphologies at three different energy densities were investigated. In the case of an energy density $\leq$ 1 J/cm^2 periodic LIPSS were found after 5 LA pulses (Figure III.7.10a). According to the 2D FFT analysis of this SEM micrograph the period of the LIPPS was determined to be $\Lambda_{LSFS} = 0.3$ μm. However, after 25 LA pulses no periodic surface structures but rather irregular fingers were found (see Figure III.7.10b).

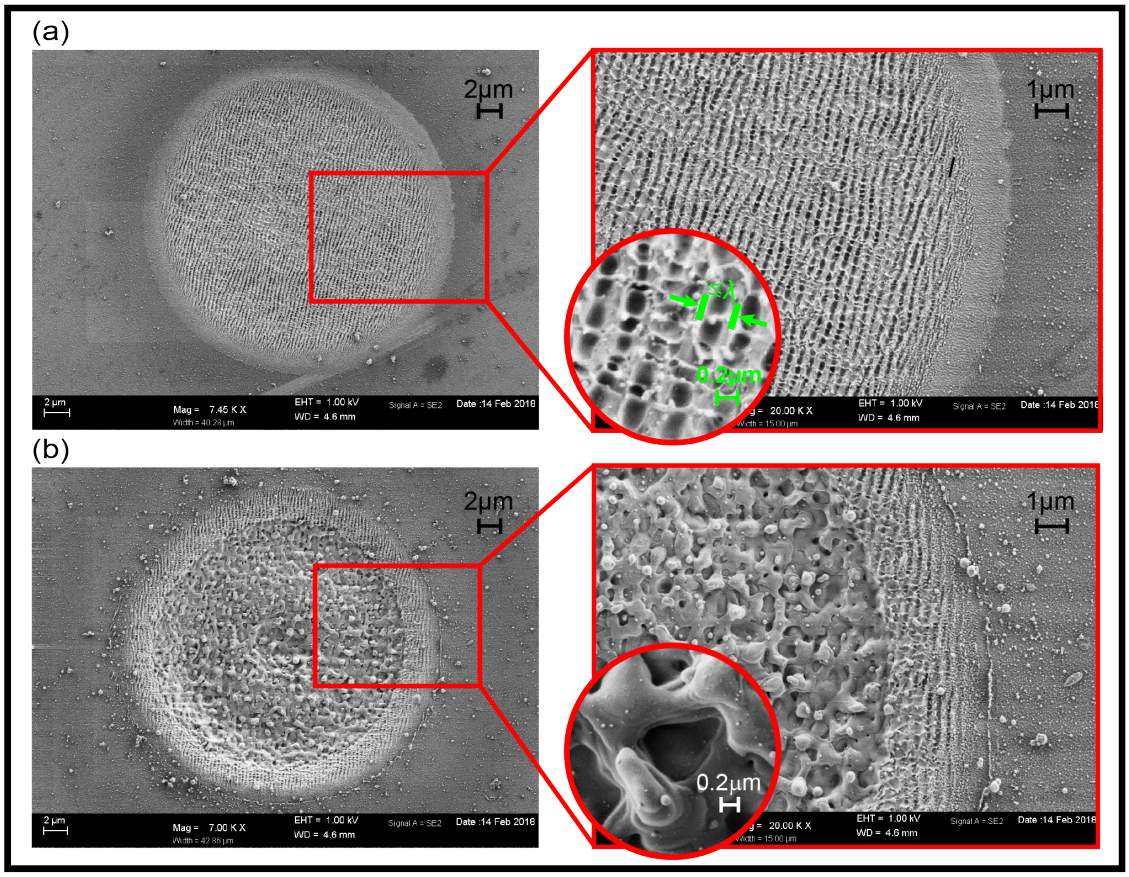

Figure III.7.10: SEM micrographs of craters on NIST SRM 2135c after (a) 5 and (b) 25 LA pulses, generated at a laser energy density of $\leqq 1$ J/cm^2. The crater morphology reveals the characteristic ripple formation on the crater bottom, i.e. the induced roughness through the LA process. The periodicity of the ripples in (a) are just below the laser wavelength. The arrows not only indicate the grating distance, but also the direction of the polarity. In (b), additionally, a cumulative effect of remaining heterogeneities of the laser intensity profile is apparent.

In addition the effect of a lower energy density well below 1 J/cm^2 on the crater morphology was studied (see Figure III.7.13). The LIPSS analysis after 20 LA pulses resulted in $\Lambda_{LSFS} = 0.35\,\mu$m. A closer look on the LIPSS structure showed a main direction of the waves. In addition less pronounced waves perpendicular to the main LIPSS were present. According to the 2D FFT analysis thereof, the same periodicity was obtained (Figure III.7.12). In conclusion, the low laser energy density resulted in perpendicular as well as parallel oriented LIPPS. However, the direction of the polarization was not determined and therefore it was not clear whether the main waves were perpendicular or parallel.

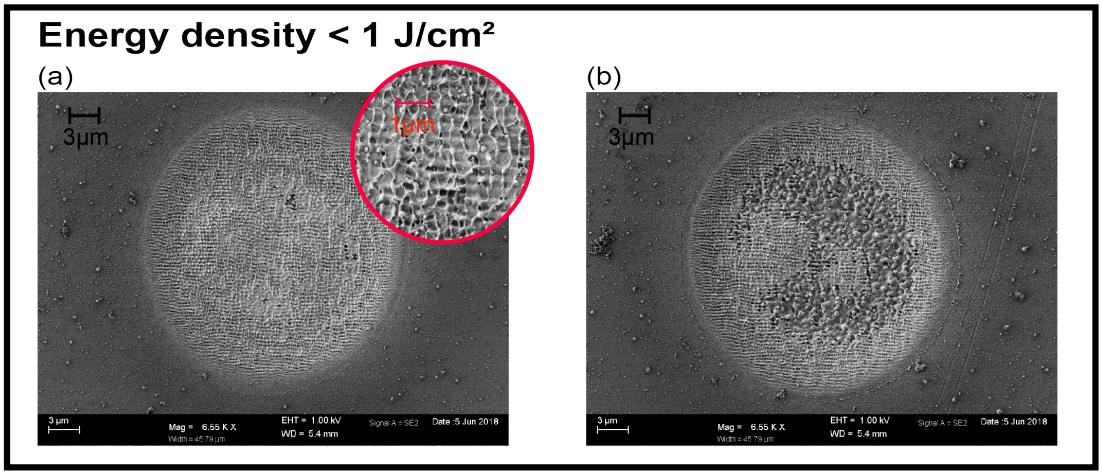

Figure III.7.11: SEM micrographs of craters on NIST SRM 2135c after (a) 20 and (b) 25 LA pulses. In case (b) the Si waver starts to appear, while a remaining layer of Ni/Cr is still present, shown by the fine structured area, similar to (a).

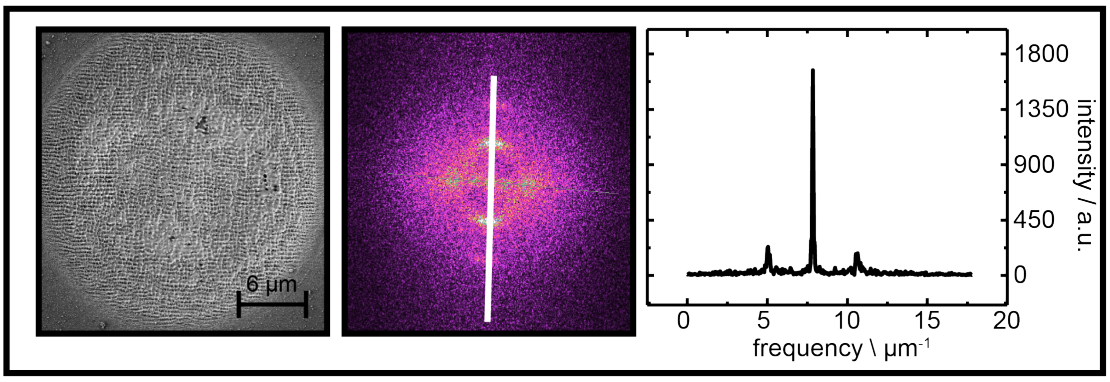

Figure III.7.12: 2D FFT analysis of the micrograph of the crater after 20 LA pulses on NIST SRM 2135c applying an energy density < 1 J/cm^2.

Furthermore, the crater morphology after 25 LA pulses applying an energy density well below 1 J/cm^2 reveals the transition between well-oriented LIPSS and unstructured surface roughness, as already found in Figure III.7.10b. By evaluation of the LA up-take rates determined by ICP-MS analysis, the transition region between the Si wafer and the remaining Cr/Ni layers was reached after 25 LA pulses. If we follow the LIPPS pattern observed after 20 LA pulses, we could assume that the well-oriented LIPPS showed the

Cr/Ni layers, while the non-periodic surface structures most probably displayed the Si wafer. Applying higher energy densities (>1 J/cm^2, see Figure III.7.13) on the sample surface, LA induced surface roughness was already found after 1 LA pulse, however no clear structure could be identified. Similar structures were revealed after 5 LA pulses. Considering the crater morphology after 10 LA pulses, some LIPSS were obtained at the edge of the craters. The periodicity was determined to be $\Lambda_{LIPSS} = 0.4\,\mu$m and follow the theory for LSFL.[190] In addition, molten and re-solidified material was identified, which could be explained by the higher energy density within this experiment.

Finally, the different energy densities applied on the metal target revealed the expected energy density dependence of the LIPSS formation. Indeed, only for energy densities >1 J/cm^2 molten and re-solidified areas were obtained and in addition, the LIPSS only appeared after 10 LA pulses on the crater rim, which may be again due to the higher energy density. However, one must know that even if in all three cases a constant energy density is focused onto the sample surface, the actual energy density on the sample may change rapidly with each LA pulse due to the prompt surface area increase induced by the LIPSS formation.

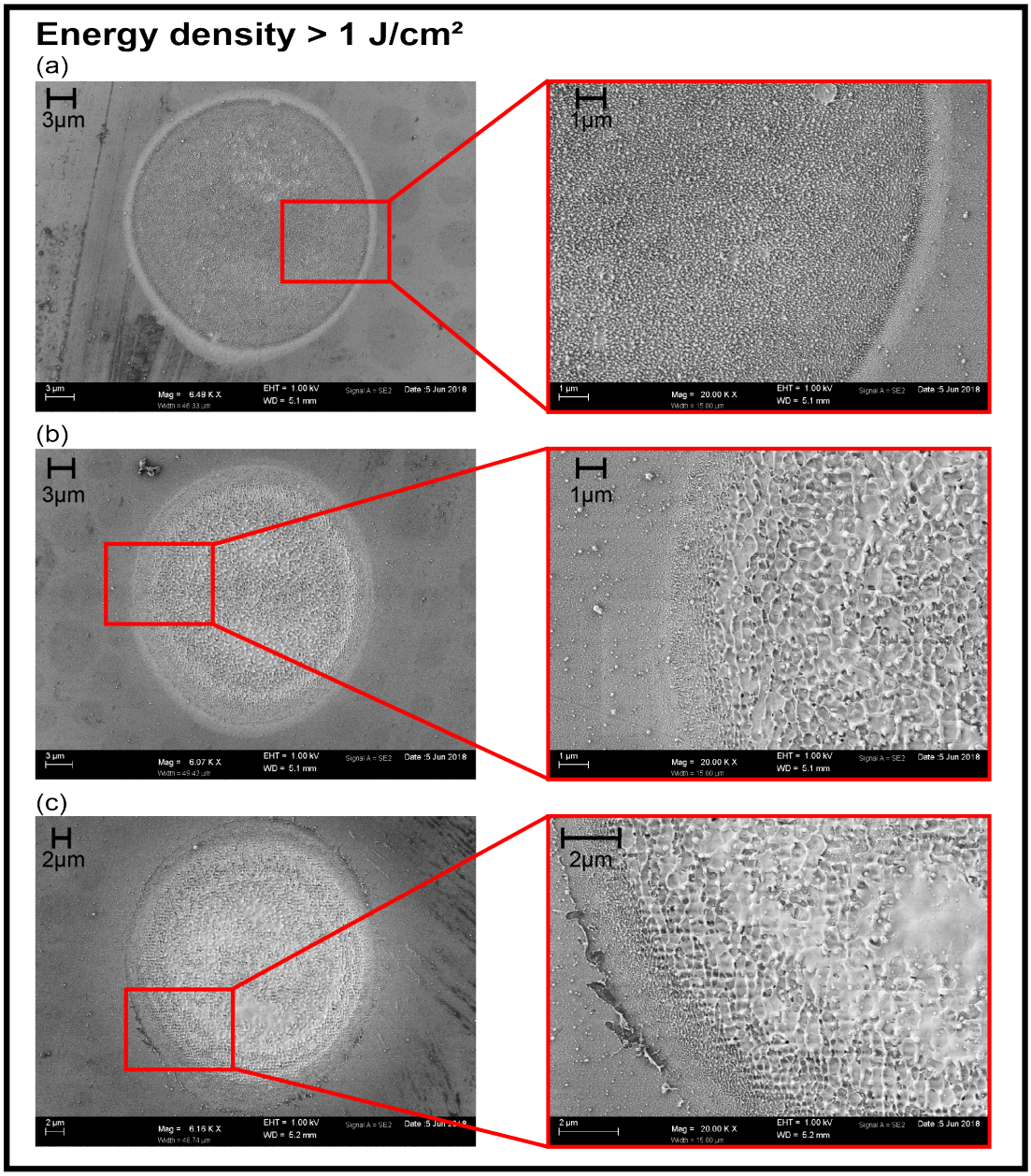

Figure III.7.13: SEM micrographs of craters on NIST SRM 2135c after (a) 1, (b) 5 and (c) 10 LA pulses, respectively, generated at a laser energy density >1 J/cm ^{2}.

7.2.2.3 Conclusion

In conclusion, LA induced surface roughness was obtained for all three samples (borosilicate glass, $SrTiO_3$, Cr/Ni multilayer sample). The determined periodicities were in the

range of the applied wavelength ($\lambda = 400$ nm) and followed the theory for LSFL. Furthermore, the dimensions of the LA induced surface roughness were found to be smaller then the inhomogeneities in the laser beam profile on the sample surface for the borosilicate glass sample. The evaluation of the slopes of the craters showed decreasing values for higher number of LA pulses – The craters converge towards cylindrical structures. Due to the narrow *depth of focus*, the most challenging parameter to obtain the desired crater morphology was the determination of the image plane. It was only after careful adjustment of the z-position of the sample that craters with flat bottoms were obtained. The presented results raise the question of how the beam profile affects the ICP-MS signal response which will be followed up next.

"Healey's First Law Of Holes: When in one, stop digging."

Denis Haeley

Chapter 8

Depth resolution determination

This work is published in part as "D. Käser, L. Hendriks, J. Koch, D. Günther, Depth profile analyses with sub 100-nm depth resolution of a metal thin film by femtosecond - laser ablation - inductively coupled plasma - time-of-flight mass spectrometry, Spectrochimica Acta: Part B, 149 (2018), 176-183."[53] Reproduced with permission from Elsevier.
& "D. Käser, L. Hendriks, J. Koch, D. Günther, Corrigendum to "Depth profile analyses with sub 100-nm depth resolution of a metal thin film by femtosecond - laser ablation - inductively coupled plasma - time-of-flight mass spectrometry" Spectrochimica Acta Part B: Atomic Spectroscopy 149 (2018) 176–183, Spectrochimica Acta: Part B, 149 (2018), 322."[54] Reproduced with permission from Elsevier.

8.1 Theoretical background

Depth resolution is an important figure of merit as it defines a characteristic distance below which the in depth composition of a sample cannot be resolved. As an example adapted from Hofmann,[199] a depth resolution of 20 nm in practice represents a distance within which the elemental distribution of A and B (e.g. Cr and Ni) cannot attributed to a specific pattern. In the particular case of A and B, both being quantified as 50% of the total mass, it cannot be distinguished within this 20 nm range whether the region consists of a bilayer of 10 nm of each or whether it is a single layer containing 50 weight-% of A

and 50 weight-% of *B*. Hence, lower values of the depth resolution indicate an improved depth resolution.

In the case of fs-LA-ICP-MS or LIMS different concepts for the evaluation of the depth resolution have been investigated. For example, according to Plotnikov et al. the maximum slope of the tangent within an interface region can be used to quantify the depth resolution.[200] When profiling a sharp interface, a characteristic blurring thereof (i.e. profile degradation) can occur. Hence, the specific time required to obtain the maximal signal by means of the maximal slope multiplied by the LA up-take rate can be used to determine the depth resolution. Furthermore, the depth resolution has also been set equal to the LA up-take rate or approximated by the accurate identification of an embedded single layer and hence set equal to the thickness thereof.[155,166] However, the definition of the depth resolution as accepted by the International Organization for Standardization (ISO) refers to *the depth range over which a signal intensity increases or decreases by a specified amount, when profiling an ideally sharp interface between two media. By convention, a measure of the depth resolution is often taken to be the distance over which the signal intensity changes from 16% to 84% of the full change between the respective plateau values of the two media.*[201] Despite a phenomenological understanding of this definition by simple measurement prescription, it can also be translated back from a physical definition. Indeed, a measured profile can be described by a convolution of the 'true' profile with an instrument response function, i.e. the depth resolution function (DRF). In this case, the physical meaning of the definition by ISO is based on a Gaussian shaped DRF. For instance, as adapted from Hofmann[145] and described in Fig. III.8.1a, if the 'true' depth profile of e.g. layer *A* is a step function and is convoluted with a Gaussian shaped DRF, then the measured profile can be described by an error-like function. The positions in depth of 84% and 16%, respectively of the initial intensity value of *A* each correspond to the standard deviation ω of the Gaussian DRF. Hence, the depth resolution can be defined as 2ω, and directly be extracted from the formula, as indicated in Fig. III.8.1.

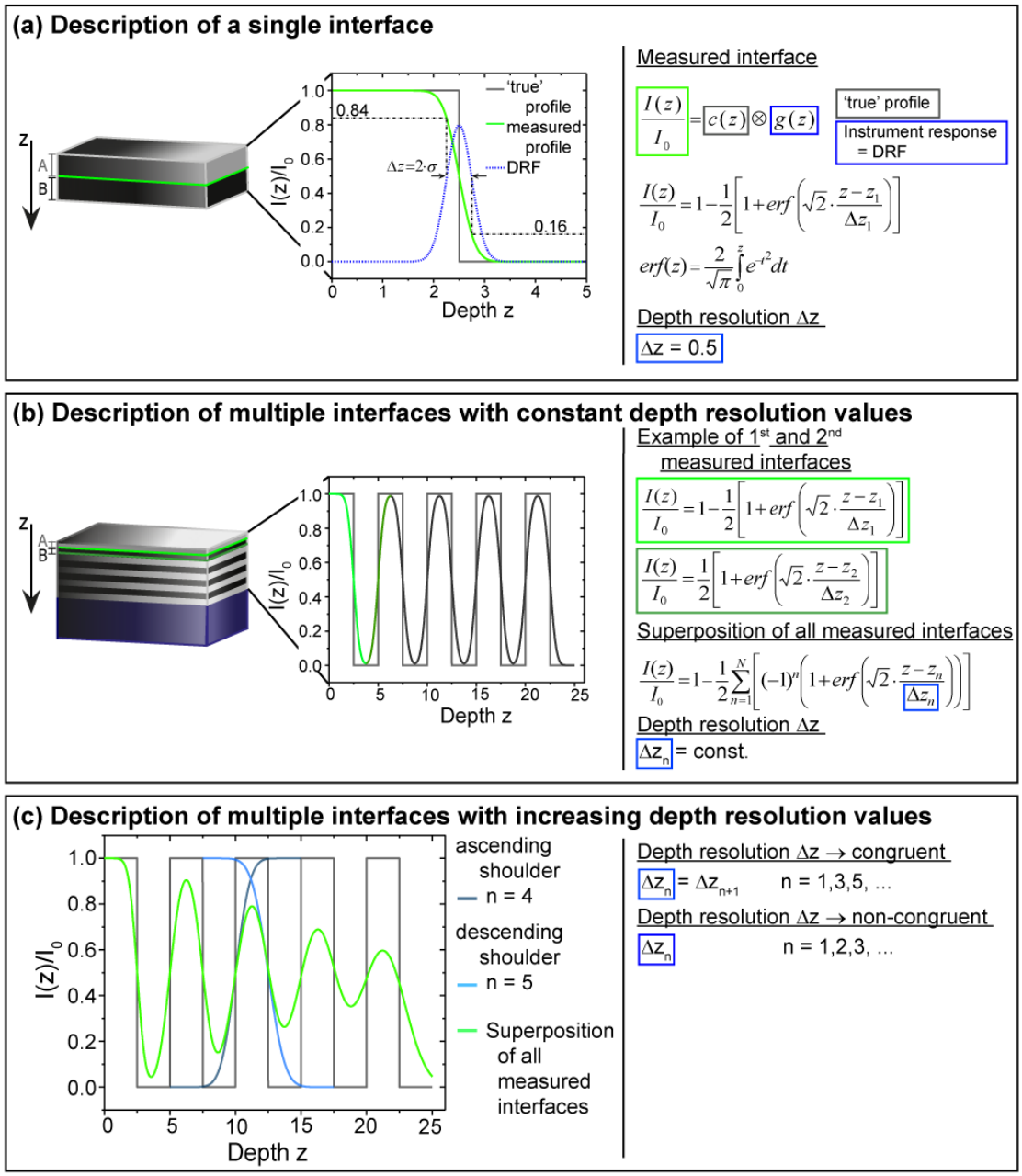

Figure III.8.1: (a) Theoretical description of the convolution of the 'true' profile and a Gaussian shaped DRF, adapted from Hofmann.[145] (a) Convolution of the 'true' profile and a Gaussian shaped DRF explained on a single interface. The 2σ of the DRF is defined as the depth resolution δz. In the case of a Gaussian shaped DRF, δz is equal to the intensity change from 16% to 84% of the full change between the respective plateau values.[145] (b) Representation of a multilayer film sample (which resembles the structure of the NIST SRM 2135c investigated). The 'true' profile of A is represented by a square wave-like function. The measured profile is described by the same DRF for each interface and hence a constant depth resolution value is present. (c) Representation of a depth profile for A with changing DRFs. The damping of the wave-like depth profile originates from an increasing depth resolution value with increasing depth.

Furthermore, if the sample structure shows higher complexity and for instance a multilayer film with alternating layers of A and B with equal thicknesses (e.g. NIST SRM 2135c with A = Cr and B = Ni) is analyzed, the description of the measured profiles for A and B gets more complicated. If we assume a Gaussian shaped DRF throughout all the interfaces between the different layers, the measured profile can be fitted by a superposition of the error-like functions, as described in Fig. III.8.1b. In the case of a constant depth resolution the measured depth profile of A for example shows a continuous wave-like profile. Nonetheless, many experimental results show a damped wave-like profile as indicated in Fig. III.8.1c. This profile is a result of increasing values for the depth resolution. Additionally, we can differentiate between congruent and non-congruent DRFs along one layer of A. For example, as shown in Fig. III.8.1c, the DRFs for the third layer of A could be non-congruent, hence $\Delta z_4(A_{ascendingshoulder}) < \Delta z_5(A_{descendingshoulder})$.
A comprehensive study of this mathematical description of a depth profile has been realized by Hofmann,[145] and is nowadays applied for various sputtering techniques, such as AES, XPS or SIMS.[202–207] However, many of these publications are dealing with the reconstruction of depth profiles and so more precise DRFs have been investigated.[199,208] Indeed, deviations from a simple Gaussian shaped DRF were examined and mainly attributed to different contributions from various factors, such as atomic mixing, the surface or interface roughness and the information depth. Correspondingly, also the depth profile measured by fs-LA-ICP-MS can be described by a convolution of a DRF and the 'true' profile. Recapitulating the important processes of the LA event, which influence the crater morphology and LA depth per LA pulse include:

1. The laser energy density on the sample surface. It dominates the LA up-take rates and determines the ablation depth per LA pulse.

2. The crater morphology induced by the laser intensity profile on the sample surface. Craters with steep walls and flat bottoms are required to reduce mixing of individual layers during the course of the analysis. Imperfections of the beam intensity profile can give rise to irregular crater forms and reduce the depth resolution.

3. Characteristic surface modifications as effect of fs-LA.[190,209] These modifications

introduce roughness to the crater bottom and/ or walls and tend to grow with increasing number of LA pulses.

4. In addition, secondary mechanisms by aerosol intermixing due to plasma etching on the crater walls can occur.[210] The plasma formation during the LA process in He can lead to additional material removal from top-layers and lead to so-called cross-removal.

To this list, one can add heat diffusion[1], residual melting, etc. The interplay of all these processes determines the real DRF, which in return causes a profile degradation. In this chapter we focused on a Gaussian shaped DRF for the description of the depth resolution and the original formalism described in Figure III.8.1 was applied. Error functions as convolution products of the Gaussian DRF and the step functions of the samples investigated were fitted to the measured profiles in order to gain the depth resolution information per interface, as described in Figure III.8.1. Constrains of this formalism regarding a Gaussian DRF were explored and further limitations resulting from different sample types were investigated.

8.2 Experimental

The fs-LA-ICP-MS set-up was realized by coupling a Ti:sapphire fs-Laser to either an ICP-qMS instrument (Elan DRC II, Perkin-Elmer Sciex, Canada) or a prototype ICP-TOFMS.[10] The laser pulses were guided through a beam shaping system (see part III, chapter 7) to convert the initial Gaussian-like beam into a beam with uniform intensity profile at the image plane of the objective lens. The LA and subsequent transportation of the generated aerosol was carried out in helium (99.999% purity, PanGas AG, Dagmersellen, Switzerland) in a LA cell of cylindrical geometry (V=20 cm^3). A laminar flow adapter[211] was used to add argon as sample gas (99.996% purity, PanGas AG, Dagmarsellen, Switzerland) before the aerosol was injected into the plasma and analyzed by

[1]Even though it has been shown that the use of fs-lasers compared to ns-lasers for LA leads to a reduced heat diffusion, which has triggered the recent interest for their application in LA studies, this effect does not completely disappear. (S. Nolte, C. Momma, H. Jacobs, A. Tunnermann, B.N. Chichkov, B. Wellegehausen and H. Welling, Ablation of metals by ultrafast laser pulses, J. Opt. Soc. Am B 14(10), 1997, 2716-2722.[78])

the respective MS system. The capabilities of this system for depth profiling were explored by measuring different samples. The detailed parameters for the fs-LA-ICP-MS analyses and the different materials can be found in Table III.8.1.

Table III.8.1: Typical operating parameters for fs-LA-ICP-TOFMS and material properties of the test targets. The targets coloured in light blue indicate two samples with a single layer of Cr on different substrates. The targets colours in gray indicate two samples with different alternating multilayer structures.

LA parameters		
Laser wavelength	0.4 μm	
Laser energy density	0.5-2 J/cm^2	
Pinhole diameter	400 μm	
Objective lens	f = 100mm	
Laser-spot diameter	25 μm	
Ablation frequency	1 Hz	
ICP-MS parameters	**ICP-TOFMS**	**ICP-qMS**
Plasma Power	1400 W	1460 W
Auxiliary gas flow (Ar)	0.75 L/min	
Cooling gas flow (Ar)	18 L/min	17 L/min
Sample gas flow (Ar)	0.6 L/min	0.8 - 0.9 L/min
Carrier gas flow (He)	0.6 L/min	0.55 - 0.6 L/min
TOF time resolution	25 ms	–
Dwell time	–	10 ms
Material		
Standard Reference Material (Kocour sample 1, Kocour, Chicago, IL, USA) *	Cr layer (500 nm) on Ni	
Standard Reference Material (Kocour sample 2, Kocour, Chicago, IL, USA) *	Cr layer (5000 nm) on Brass	
Standard Reference Material (NIST SRM 2135c) **	Alternating Cr/Ni layers (5 x 57 nm Cr / 4 x 56 nm Ni)	
Al / Cu on SiO_2 **, ***	Alternating Al/Cu layers (5 x 100 nm Cu / 5 x 100 nm Al)	

* Measured by ICP-qMS.

** Measured by ICP-TOFMS.

*** Sample provided by M. Horisberger, PSI Villigen, Switzerland.
The layers were produced by DC magnetron sputtering (Leybold Z600 Sputtering unit)
and their thicknesses were confirmed by RBS measurements provided
by Max Döbeli, ETH Zurich, Switzerland (see Appendix A).

8.2.1 Data Acquisition and processing

By careful adjustment of the helium aerosol carrier gas flow rate and positioning of the sample as close to the outlet of the LA cell as possible, we obtained washout times below 500 ms. Hence, to ensure baseline separation between LA pulses and therefore avoid pulse to pulse mixing, a LA frequency of 1 Hz was used. The energy densities were adjusted for each sample. The measured transient signals are presented in Figure III.8.2.

For the two single layer samples 31, respectively 138 LA pulses were needed to drill through the Cr layer until the bulk material were reached (see Figure III.8.2(a) and (b)). This number of LA pulses was dependent on the layer thickness and the energy density applied on the sample surface. In case (a) the substrate material was Ni, while in case (b) a brass substrate was present. Due to the composition of brass, in the latter case, Cu was measured as indication for the substrate.

In Figure III.8.2(c) and (d) for the trained eye alternating local maxima and minima can be identified for the two elements of the alternating multilayer structures (Cr and Ni / Al and Cu) until the different substrates were reached. However, the alternating pattern may be challenging to distinguish due to different elemental sensitivities as well as biased by small energy density changes. Indeed, because of the low laser energy density very close to the LA threshold small energy density variations can have a large impact on the LA up-take rate.[77] In order to minimize the uncertainty caused by this effect, the average signal from 5 independent measurements was calculated in case (a), (c) and (d). A further positive effect of this averaging was the improved signal to noise ratio, which especially improved the signal of ^{28}Si and ^{29}Si.

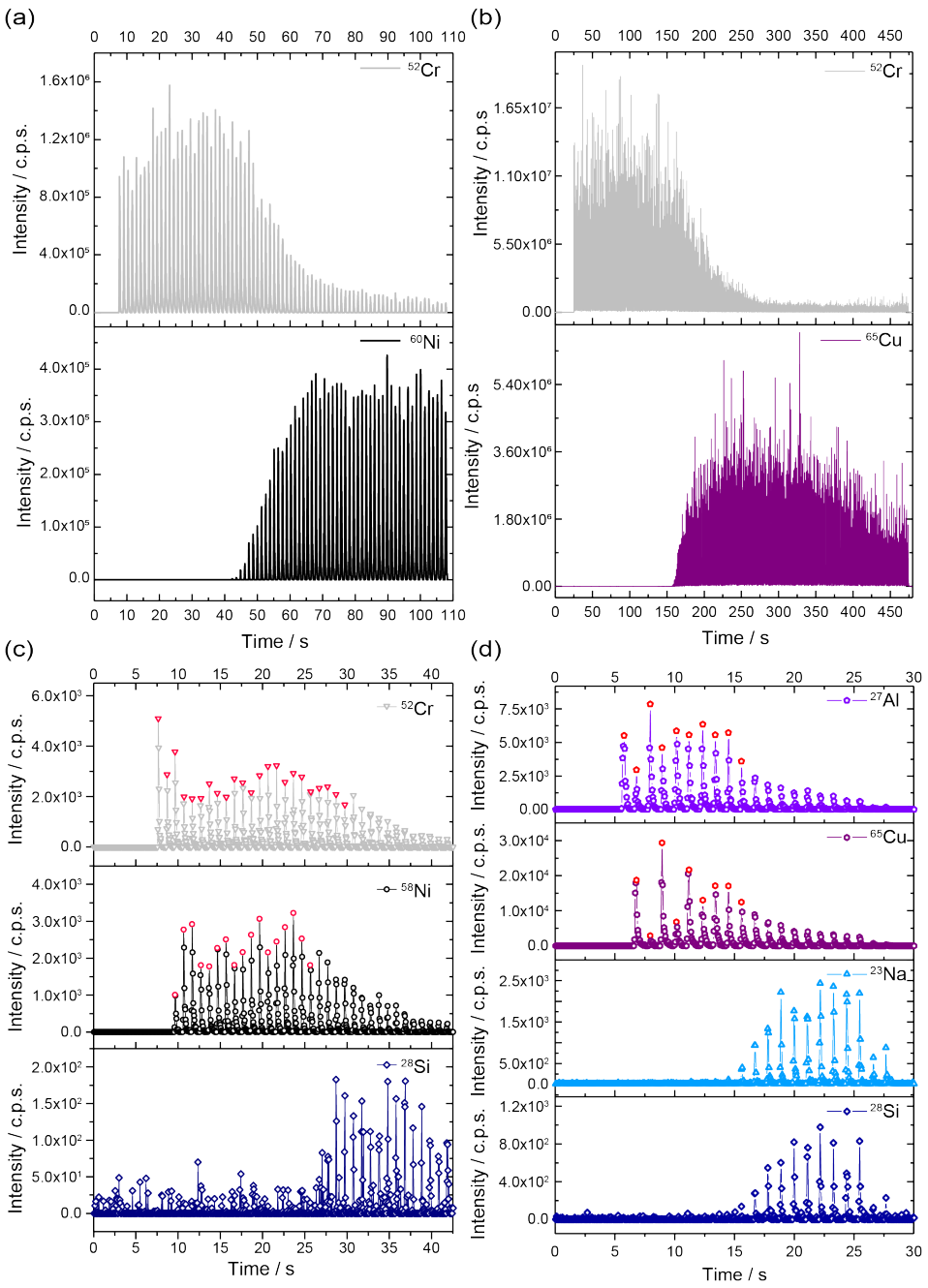

Figure III.8.2: Transient signals over (a) five individual measurements of the Kocour sample 1 and (b) a single measurement of the Kocour sample 2. Averaged transient signal over 5 individual measurements of (c) the NIST SRM 2135c and (d) the Al/Cu multilayer samples. The red marked data points represent the peak maximum of the respective mass channel for each LA pulse. They help to follow the local maxima and minima for Cr/Ni and Al/Cu, respectively. The other panels indicate the transient signal of the substrates. In case (c) it was a Si wafer, while in case (d) an SiO_2 substrate was present. Due to the composition of the SiO_2, also Na could be used as indication for the substrate.

To obtain the depth profile the respective (averaged) MS signals for each LA pulse were integrated by the trapezoidal rule after applying a threshold to evaluate the peak beginning and ending for each element of interest. Then each integrated LA pulse was background corrected and abundance normalized. Subsequently the integrated data were normalized per element, by their respective sensitivity factors, resulting in the patterns shown in Figure III.8.3. Due to the well defined structure of the samples, no external calibration was needed to determine the sensitivity factors. They were directly calculated from the total signal per element divided by its total mass ablated. In order to determine the total mass ablated, the total volume ablated was calculated from an assumed cylindrical crater and further multiplied with the bulk density for each element. Considering the different layers of the different samples, the total volume ablated could be determined by the respective layer thickness multiplied by the spot size. For the different substrates, the total ablated depths were calculated by the number of LA pulses, drilled into the substrates, multiplied by the LA up-take rates. The latter were approximated by the LA up-take rates from the different layers. The LODs were calculated according to the approach proposed by Longerich *et al.*,[99] as described in part II, chapter 2. Finally, the depth profiles were determined by the composition of each LA pulse based on the individual normalized patterns of the elements of interest, while values below the LODs were not taken into account.
All ICP-qMS and ICP-TOFMS data reduction and elemental analysis were carried out using Matlab R2016b (MathWorks, Massachusetts, USA). Mathematical fittings and descriptions were performed in OriginPro 8.6 (OriginLab Corporation, Northampton, England) and the processed data were plotted with OriginPro 8.6. All compiled figures were assembled in Adobe Illustrator (Adobe Systems, California, USA).

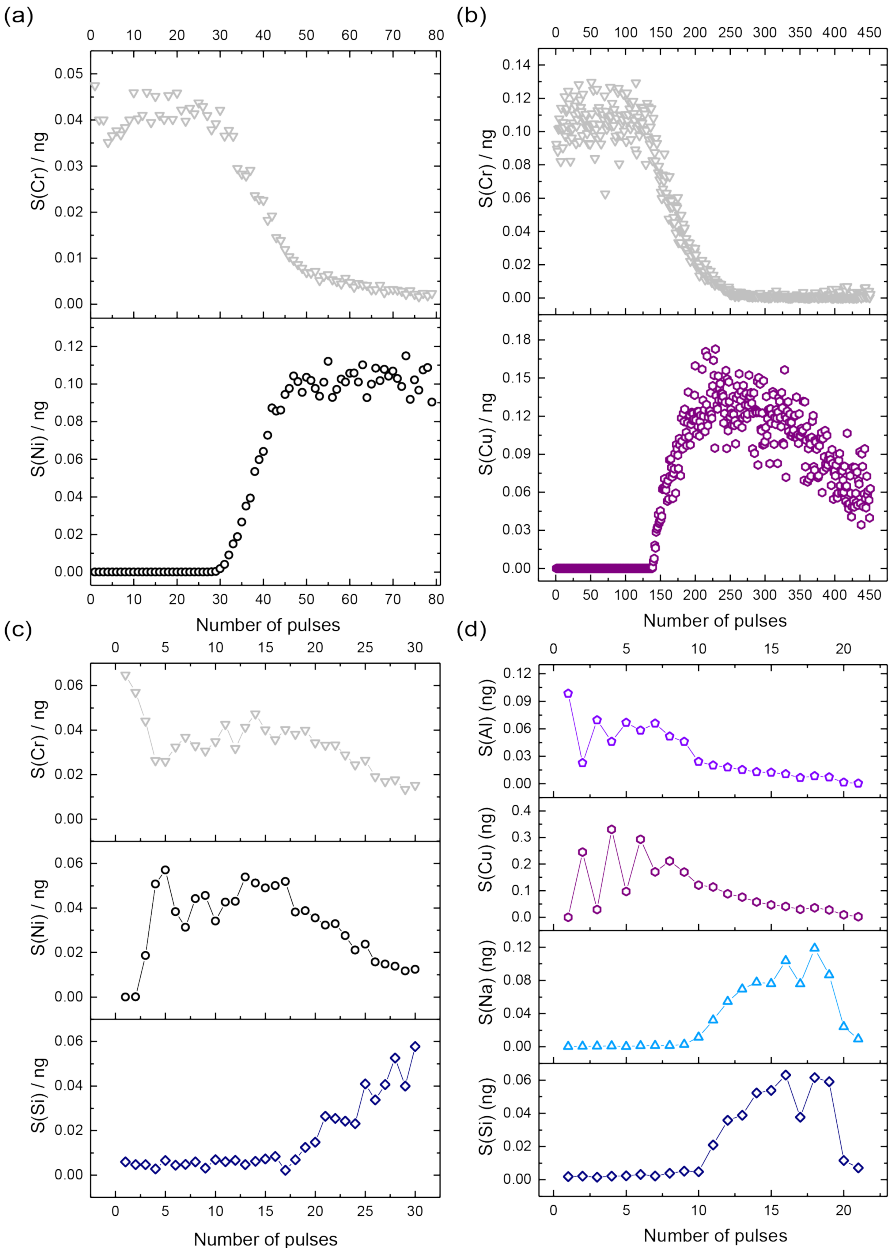

Figure III.8.3: Each data point shows the mass of the respective element per laser pulse. They were calculated by integration over each laser pulse, further abundance normalized and divided by the sensitivity factor for each element. The LODs were calculated to be 0.008 ng and 0.009 ng for Cr and Ni, respectively in case (a), 0.005 ng and 0.0002 ng for Cr and Cu, respectively in case (b), 0.06 ng, 0.004 ng and 0.004 ng for Si, Cr and Ni, respectively in case (c) and 0.008 ng, 0.009 ng, 0.009 ng and 0.009 ng for Al, Cu, Si and Na, respectively in case (d).

8.3 Results and discussion

In this section four different samples will be discussed. In the first part, two samples (Kocour sample 1 and 2) consisting of a single Cr thin layer on a substrate were explored – In one case the layer was 500 nm thick, while in the second case a layer thickness of 5000 nm was present. Since both layers consisted of Cr, material dependent LA processed could be neglected and the aim was to evaluate the applicability of the error-like function to describe the measured profile and hence the Gaussian DRF as instrumental response. In the second part, the lower limitation concerning the depth resolution and the material dependence thereof were examined. In addition, the importance of the sample positions was highlighted. For this study two complex sample types (i.e. multilayer samples, with alternating layers of Cr/Ni (NIST SRM 2135c) and Al/Cu) were examined.

8.3.1 Single layer samples

Kocour sample 1

In Figure III.8.4a the measured depth profile of the Kocour sample 1 is shown. The top layer consisted of Cr and was 500 nm thick and its substrate was Ni. The applied energy density was ≈ 0.5 J/cm^2 and resulted in an average LA up-take rate of 17 nm/LA pulse. It was approximated by the number of LA pulses needed to drill through the Cr layer until the substrate was reached (500 nm / 30 LA pulses). The depth resolution was calculated according to the formalism discussed in Figure III.8.1a. This way a resolution in units of number of LA pulses was extracted. In order to transform the number of LA pulses into a depth in units of nm, the LA up-take rate was used. This way a depth resolution in the range of $\Delta z = 160 \pm 5$ nm was obtained.

The deviation from the step-like function of the measured depth profile in Figure III.8.4a can be attributed to different LA-ICP-MS measurement characteristics. In this context, aforementioned LA up-take rates, crater morphology, LA induced surface roughness and secondary mechanisms directly influence the DRF and therefore highly affect the depth resolution. Yet, the LA up-take rate is the ultimate depth resolution and hence minimal LA up-take rates are desired. In case of a perfect cylindrical ablation the depth profile would always follow a step-like function. However, in here a deviation thereof was ob-

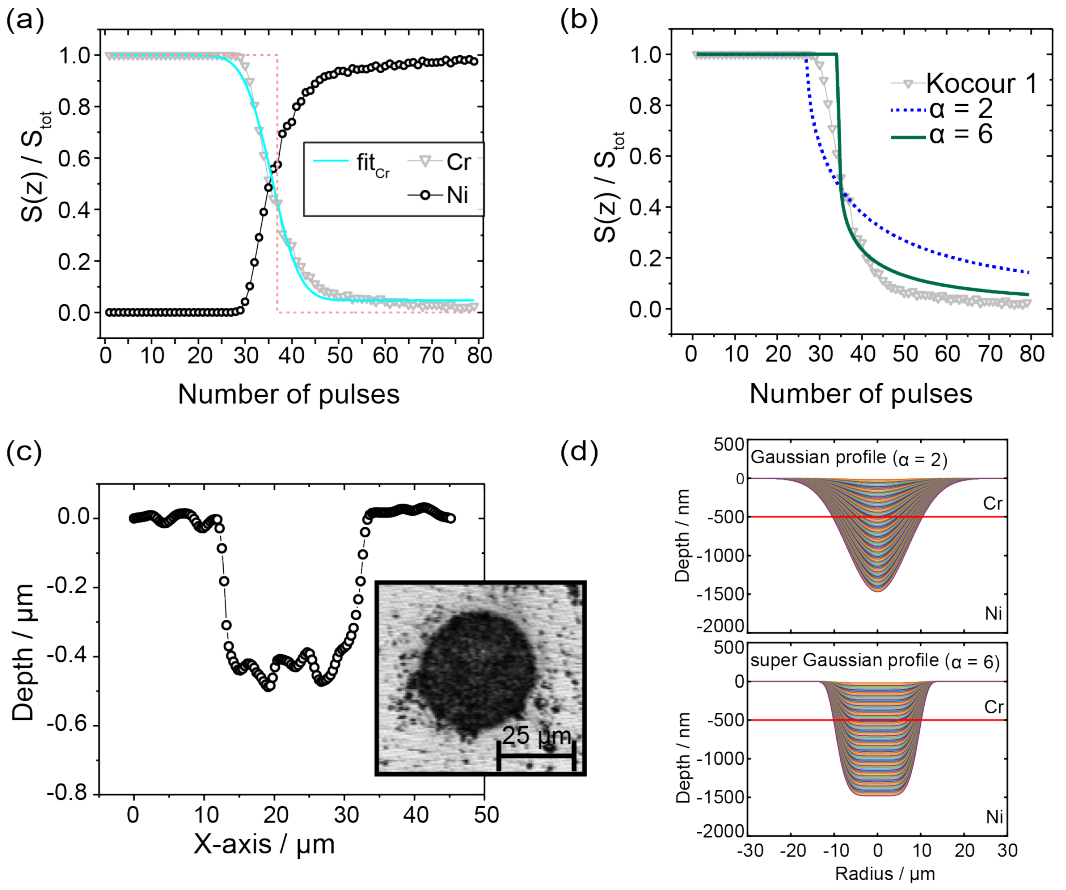

Figure III.8.4: (a) Depth profile of the Kocour sample 1 with 500 nm Cr on Ni. An experimental fit using an error function as described in the infographic III.8.1a was applied. The adjusted R^2 values was 0.997. (b) Simulation of the depth profile in case of a Gaussian ($\alpha = 2$) and Super-Gaussian ($\alpha = 6$) crater profile. (c) Measured crater profile after 25 LA pulses on the Kocour sample 1 by CM. The crater depths was determined to be in the range of 400 nm. (d) Simulated crater profile, in case of a (top) Gaussian ($\alpha = 2$) and (bottom) Super-Gaussian ($\alpha = 6$) energy density profile.

tained and hence a low LA up-take can result in a significant broadening of the signal, due to higher number of LA pulses used to drill through the interface region.[170] Another important parameter to influence the broadening of the obtained interface was the energy density distribution, as described in part III, chapter 6. In Figure III.8.4b, the result of a Gaussian ($\alpha = 2$) and a Super-Gaussian energy density distribution ($\alpha = 6$) on the depth profile were simulated. [2] The basic idea was adapted from St-Onge[170] and based

[2] More details on the energy density distribution are described in part III, chapter 6, equation (6.7), (6.8), and (6.9)

on the percentage of ablated volume of the top layer to the total ablated volume per LA pulse. [3] As indicated in Figure III.8.4d, the change in crater profiles per laser pulse were approximated by the successive addition of the energy density distribution, depending on the LA up-take rate (see equation (6.7)). Due to the aspect ratio of $r/R_0 = 0.04$ in this experiment the change in surface morphology per laser pulse and hence the influence of it on the absorption, were neglected (see part III, chapter 6). The simulation could be reduced to a two dimensional problem, due to its symmetry and hence the simulated profiles were approximated by the percentage of area. The LA up-take rates were adjusted, so the decrease to 50% of the layer were reached after the same number of LA pulses compared to the experimental results ($\simeq$ 35 LA pulses). In doing so, the simulated profile for a Super-Gaussian revealed a $\approx$ 15% lower LA up-take rate. The slower decrease of the profile concerning the measurement could be explained by the measured structure of the crater profile (see Figure III.8.4c). Indeed, a CM measurement after 25 LA pulses revealed irregularities in the range of 20% on the crater bottom (i.e. difference between highest and lowest values on the bottom compared to the total depth of the crater). The origin thereof is not clear – they could be due to remaining heterogeneities in the laser beam profile (see part III, chapter 7, Figure III.7.4) or due to the LA process itself – however, their appearance could lead to a broadening of the sharp interface. Nevertheless, once the interface region is passed ($S(Cr) \leq 50\%$), the measured profile follows the trend of the simulated curve for $\alpha = 6$. By comparing the measurement with the simulated profile for $\alpha = 2$, the bulk material would be reached already after 26 LA pulses, in case of a Gaussian energy density distribution. This could be explained by higher peak energies in the central part of a Gaussian energy density distribution resulting in higher LA up-take rates. However, if we assume a Gaussian energy density distribution for the measurement, the LA up-take rates would have to be the same and hence, the simulated curve would be shifted slightly to the right. In this case, the curve would even decrease slower. [170] In conclusion of this simulations we could show that the measured profile did not follow the simulated curve for $\alpha = 2$ but rather the simulated curve for $\alpha = 6$. Finally, due to the found crater profile, and in addition residual melting and/or heat diffusion, a broadening

[3] In an ideal case, the volume would be multplied by the respective densities of the ablated materials, however in the case of Cr and Ni, the densities are very close and therefore this transformation was neglected, in order to be able to reduce the problem to a 2 dimensional calculation.

of the sharp interface was already revealed before the Cr signal decreased to 50% of its initial value. Hence assuming an error like profile as described in the infographic III.8.1a and hence a symmetric DRF, where such effects are summarized, resulted in a good approximation to determine the depth resolution.

Kocour sample 2

In Figure III.8.5a the measured depth profile of the Kocour sample 2 is shown. The top layer consisted of Cr and was 5000 nm thick and its substrate was brass. In comparison to the Kocour sample 1, the applied energy density was ≈ 1 J/cm^2 and hence twice the value applied for the thinner layer. This resulted in an average LA up-take rate of 36.2 nm/LA pulse (5000 nm / 140 LA pulses). Applying again the formalism described in the infographic (Figure III.8.1a), a depth resolution of $\Delta z = 1530 \pm 40$ nm was obtained and hence an almost 10 times higher value compared to the Kocour sample 1.

Comparing the different craters obtained close to the interface region in both cases, similar morphologies were found (see Figure III.8.4c and III.8.5b). Indeed, also for the Kocour sample 2 irregularities on the crater bottom became apparent. They were in the range of 12% and hence could contribute to the discussed broadening of a sharp interface. However, considering the measured depth profile in Figure III.8.5a, a sharp decrease seemed to be apparent. Due to the higher LA up-take rate combined with the lower percentage of irregularities on the crater bottom a better depth resolution would be expected, which would be reflected in the measured depth profile as steep decrease. However, if the depth profile of the Kocour sample 2 and 1 are directly compared and their interface regions were adjusted relatively in order to overlay the start of the substrate materials, a clear broadening of the interface became apparent for the Kocour sample 2 (see Figure III.8.5c). Even though the slope in the beginning overlap very nicely, a much slower decrease for the Kocour sample 2 was revealed. Indeed, this slow decrease could be a result of the thickness of the layer. While for the Kocour sample 1, the aspect ratio (r/R_0) was below 0.2, in here it was in the range of 0.4, and hence ten times higher than for the Kocour sample 1. In case of such high aspect ratios (i.e. 0.4), the impact of the crater on the absorption of the laser energy became important,[170] and may have resulted in more conical shaped

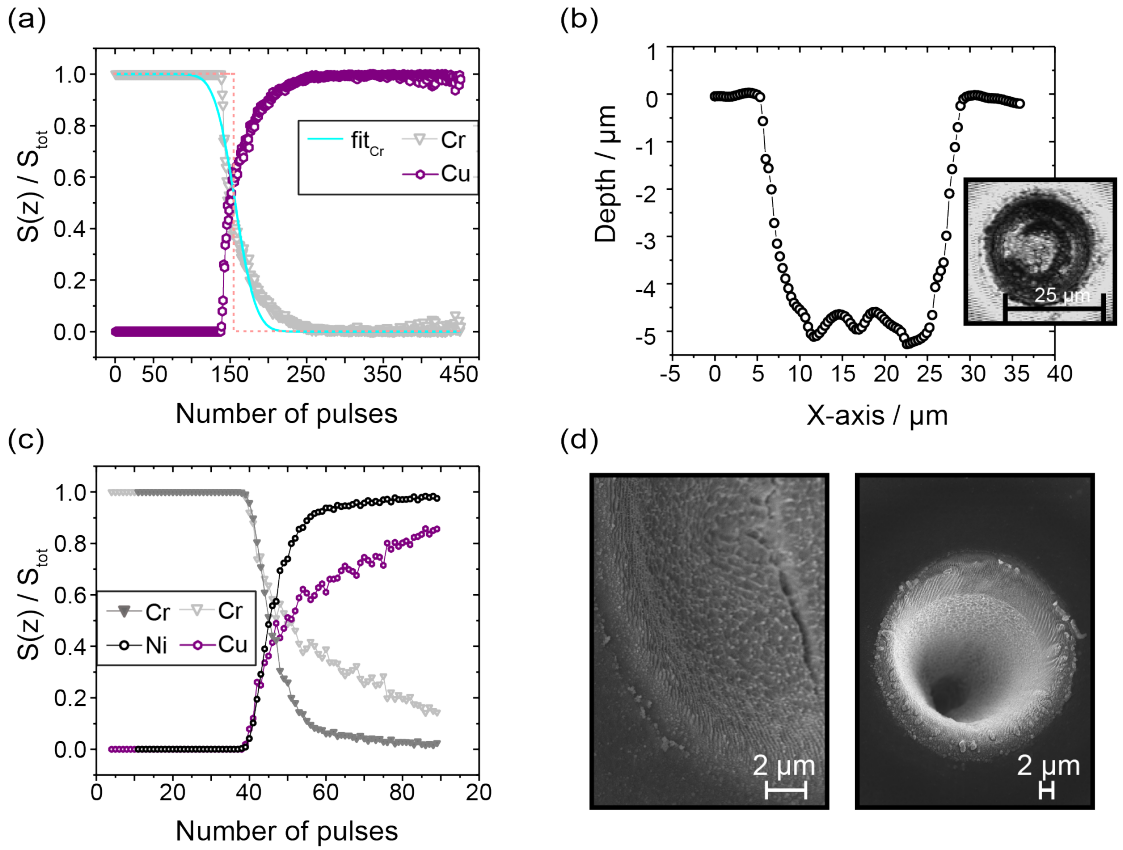

Figure III.8.5: Depth profile of the Kocour sample 2 with 5000 nm Cr on brass and applying an experimental fit using an error function as described in the infographic III.8.1a. The adjusted R^2 value was 0.99. (b) Measured crater profile after 25 LA pulses by CM. The crater depth was determined to be in the range of 5000 nm, after $\sim$ 140 LA pulses. (c) Comparison of the depth profile of the two Kocour samples 1 (dark gray Cr and black Ni) and 2 (light gray Cr and purple Cu). The number of LA pulses indicate relative values. They were adjusted to overlay the start of the two bulk materials. (d) SEM micrographs of the crater after (left) 20 and (right) 450 LA pulses.

crater after 450 LA pulses. This assumption was supported by the SEM micrograph after 450 LA pulses (see Figure III.8.5d). At this point, a limitation of the symmetric Gaussian DRF was reached. Indeed, the profile revealed an asymmetric curve. The effects of the crater bottom at the interface may have been lower compared to the contributions from the energy density profile on the crater walls and/or secondary effects (i.e. plasma etching). While the irregularities of the crater bottom did only result in a minimal contribution to S(Cr) after the interface was drilled through, the energy density profile and plasma etching may have still resulted in significant ablation of the crater wall and hence have

contributed to S(Cr). Finally, the investigation of sharp interfaces or other features further down within a sample may be possible, however their analysis are more challenging. Possible workarounds may include a successive decrease of the spot size and readjusting of the image plane. This way the plasma etching may be reduced and cumulative effects of the Super-Gaussian energy density distribution with deep craters and high aspect ratios may be reduced.

8.3.2 Multilayer samples

NIST SRM 2135c

Figure III.8.6 shows the measured depth profile of NIST SRM 2135c, at two different sample positions. In here an energy density of $\simeq 0.6$ J/cm^2 was applied. In Figure III.8.6a the alternating pattern of the thin film could be extracted until the last layer of Cr, before the Si-substrate started to appear and hence, all 9 interfaces were revealed. On the other side, in Figure III.8.6b, only the first 4 layers (i.e. two layers of Cr and two layers of Ni) were resolved. At this point, it could assumed that in case (a) the sample surface was in-line with the image plane of the objective lens, while in case (b) the sample was moved 40 μm out of this plane. Indeed, the position of the sample with respect to the image plane of the objective lens was very critical in order to be able to resolve the 9 alternating layers of the sample.

Concerning Figure III.8.6a, where all 9 interfaces were revealed, the depth resolution for each interface was determined (see Figure III.8.7). To do so, the formula from the infographic (Fig. III.8.1b) was applied, assuming a noncongruent depth resolution (see Fig. III.8.1c). This time, for each element of the thin film (i.e. Ni and Cr) a linear superposition of the error functions was fitted to the measured depth profile. The distances between the interfaces (i.e. $z - n_n$) were set according to the number of LA pulses in between. Indeed, according to the pattern observed, 3.5 pulses are required to drill through the top Cr layer and to reach the first interface, whereas for all further interfaces we assumed a distance of 2 LA pulses. According to this the LA up-take rate seemed to be constant for all layers after the top Cr layer, where the LA up-take rate appeared to be almost twice as small. A possible explanation for this observation could be a change in absorbance after the first LA pulse, according to the literature.[212] Due to the surface roughness induced

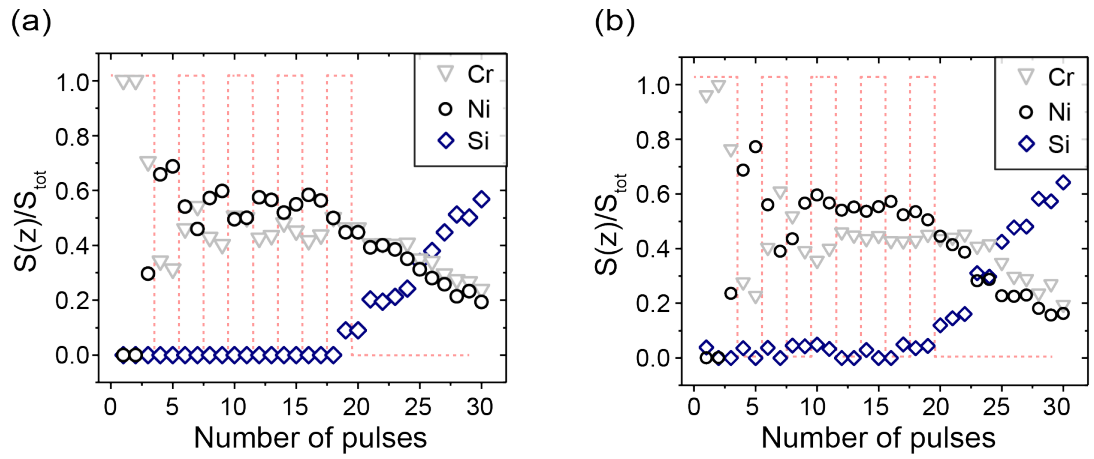

Figure III.8.6: Measured depth profile of the NIST SRM 2135c sample at two different sample positions. **(a) Image plane:** The nine layers of Cr and Ni are revealed. **(b)** $40\,\mu m$ **out of image plane:** The Cr data points do not follow the ideal pattern which is indicated by the dashed red line. The alternating pattern can only be interpreted until the fourth layer of the thin film. Layer number 5 to 9 are nomore seperated.

after the first LA pulse, the ablation behaviour changes for all subsequent LA pulses. It was shown that depending on the laser energy density, the first few LA pulses may only have a minimal ablation depth while a constant LA up-take rate for the subsequent LA pulses was apparent.[212] The difference in LA up-take rate for the top layer might be attributed to this pulse-to-pulse ablation behaviour.

Within the next step, the depth resolution per interface and element (Fig. III.8.7b) was calculated from the Δz values in units of number of LA pulses and again transformed to units of nm by the LA up-take rate. In this case, we assumed a constant LA up-take rate of 27 nm/LA pulse (509 nm/19 pulses $\approx$ 27 nm/LA pulse) and the aforementioned pulse-to-pulse effect only affecting the first LA pulse was neglected. The calculated depth resolutions ranged from 47 nm up to 152 nm. Here, a significant difference between ascending and descending shoulders per layer was observed. This observation can best be explained, when looking at e.g. the experimental fit for the measured Cr depth profile. In Fig. III.8.7c the single error functions per interface are shown in grey. Comparing these curves with the 'true' profile a higher degree of profile degradation for all descending shoulders compared to the ascending was shown. Hence, the depth resolution values were higher. This finding pointed towards different processes and/or effects within a layer and

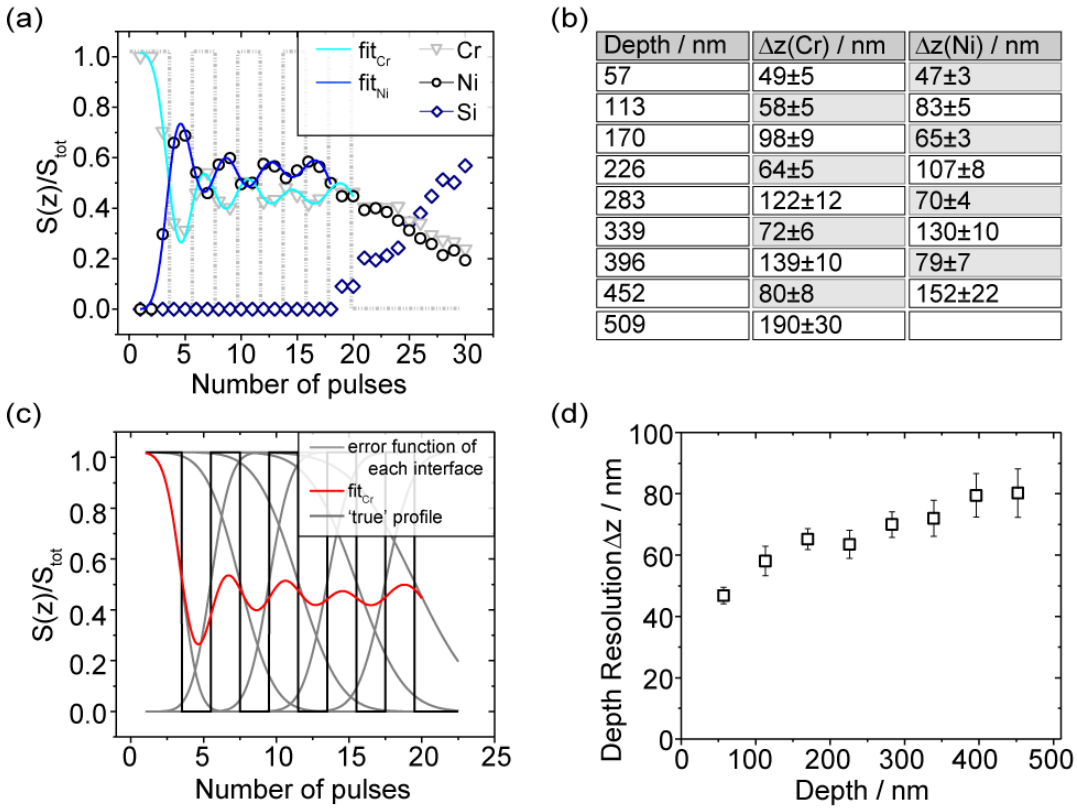

Depth / nm	Δz(Cr) / nm	Δz(Ni) / nm
57	49±5	47±3
113	58±5	83±5
170	98±9	65±3
226	64±5	107±8
283	122±12	70±4
339	72±6	130±10
396	139±10	79±7
452	80±8	152±22
509	190±30	

Figure III.8.7: (a) Experimental fits using a superposition of error-like functions for both elements to determined the depth resolution per interface. The number of LA pulses on the x-axis can be translated to the depth by the LA up-take rate. The adjusted R^2 values for both experimental fits were above 0.98, indicating adequate fit results. (b) Evaluated depth resolutions for each interface for both elements involved. Grey shaded values indicate the depth resolutions for the ascending shoulder of each interface. The last interface located at a depth of 509 nm corresponds to the transition of Cr to the Si substrate. (c) Representation of the experimental fit for Cr. The grey curves represent the error functions for each layer. They show a decreasing maximal slope with increasing depth (i.e. increasing number of LA pulses). A profile degradation overreaching the actual layer thickness can be observed starting from the second Cr layer. (d) Overview of the depth resolutions of the ascending shoulders (grey shaded values from subplot (b)) showing increased values for the depth resolution.

its transition. However, if only the depth resolution values of the ascending shoulders per interface were extracted (see Fig. III.8.7d) a constant increase became visible and the depth resolution values varied from 47 nm for the first interface up to 80 nm for the last interface between Cr and Ni, respectively.

The damping wave-like pattern of the depth profile and the resulting increase of the depth

resolution could again be attributed to the irregularities on the crater bottom already found for the two Kocour samples 1 and 2. Indeed, they were also present in the case of NIST SRM 2135c (see also Figure III.7.10b). Yet these irregularities seemed to be more pronounced for higher number of LA pulses and hence may not influence the depth resolution inhere. However, in the case of such thin layers, the LA induced surface roughness, i.e. LIPSS, might play a major role. Already after 5 LA pulses such LIPSS were revealed on NIST SRM 2135c (see Figure III.7.10a). Concerning conductors, the dimensions of these LIPSS were found to be in the range of some 100 nm's (see part III, chapter 7). In case of lower energy density as applied in this study, the groves of the LIPSS tend to be less deep.[190] Nevertheless, they increase with increasing number of LA pulses and hence also increase the surface roughness.[190] As a result, many mechanisms related to the LA process highly influence the depth profile analysis by LA-ICP-MS and hence lead to the measured damping wave-like structure of the NIST SRM 2135c depth profile and directly affect the depth resolution as shown in Figure III.8.7.

Al/Cu multilayer sample

The last example investigated consisted of 10 alternating layers of Al and Cu, with each a thickness of 100 nm. Compared to the samples explored before different metals were present with lower melting points.

In Figure III.8.8a the obtained depth profile thereof is presented. While here, the different layers were difficult to identify the alternating pattern was clearly resolved, if the mass percentages were transformed to the mole percentages in Figure III.8.8b, due to the molar mass of Al compared to Cu. However, not all 10 layers were identified. Indeed, the last two layers were difficult to follow unambiguously. Also in this sample a damping wave like structure was encountered, which was attributed to the discussed fs-LA-ICP-MS characteristics.

Yet the most astonishing result within this sample was the impossibility to have more than one LA pulse per layer. In fact only at energy densities in the range of 1.4 J/cm^2 the pattern could be resolved – while for higher energy densities significant heat diffusion started to occur, which made it impossible to resolve the layers in case of lower energy densities almost no significant LA occurred. In this sample we encountered with most

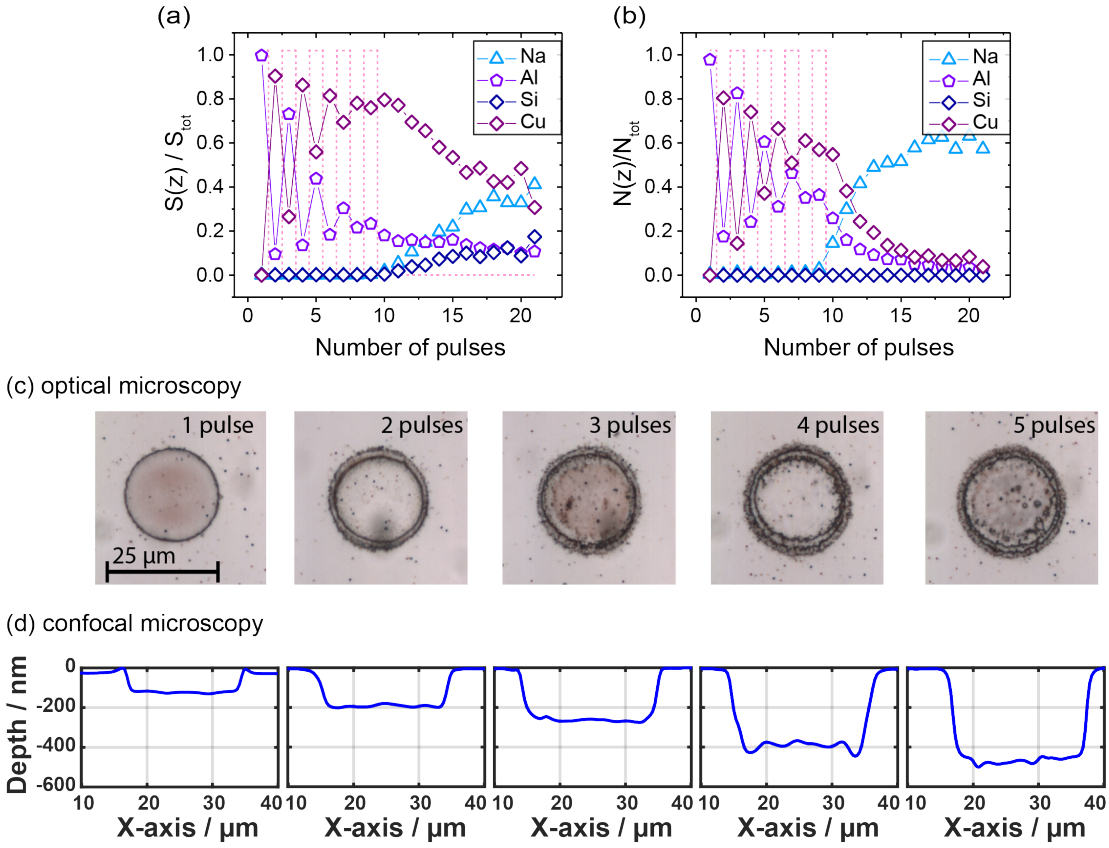

Figure III.8.8: Depth profile of the Al/Cu multilayer sample in (a) mass percentages per laser pulse per element and (b) mole percentages per laser pulse per element. (c) OM measurements of the crater after 1 to 5 LA pulses. (C) CM of the same craters, revealing a constant LA up-take rate of 100 nm / $LA\,pulse$.

excitement the importance of the LA threshold, residual melting and heat diffusion in case of fs-LA. Strong evidence for this single layer removal per LA pulse was also found within the crater morphologies. Indeed, the OM measurements reflected the copper colour after one LA pulse, while after the second LA pulse, it disappeared again, etc. (see Figure III.8.8c). Further positive correlation with the obtained depth profile resulted from the measurement of the crater profile by CM in Figure III.8.8d.

One reason for this single layer removal per LA pulse could be the electronic heat penetration depth and the related LA up-take rate. According to Nolte *et al.*,[78] if the energy density is above 0.5 J/cm^2 the electronic heat penetration depth becomes important and can be approximated by the following equation:

$$l \simeq a\left(\frac{M_i}{3 \cdot m_e}\right)^{1/2} \tag{8.1}$$

with a being the average inter-atomic distance, M_i and m_e the ion and electron masses, respectively. In the case of Cu, Nolte *et al.* calculated $l = 60 - 80$ nm.[78] Since Al^+ ions are lighter then Cu^+ ions and $a = 4\mathring{A}$ the heat penetration depth decreases slightly to $l \simeq 50$ nm. Yet, the specific electronic heat penetration depth do not vary much from the ones of Cr and Ni, however the energy density applied was higher. The higher LA thresholds found in this experiment were supported by a previous study,[213] and resulted in higher LA up-take rates. In addition, also the non-conducting glass substrate may have influenced the ablation behaviour of the thin film. Indeed, Kim *et al.* showed the effect of a glass substrate on the LA of a thin film.[214] Due to the non-conducting properties of such a substrate, thermal diffusion was blocked, resulting in greater hydrodynamic flow and recoil pressure within the thin film. The increased thermal conductivity of the Al/Cu thin film compared to the Cr/Ni thin film may have increased this effect. Hence higher energy densities resulted in increased redistribution and melting of the layers. Furthermore, the blocked thermal diffusion most likely played an important role concerning the last two layers. It may have resulted in increased heat effects and hence a redistribution within these two layers. Finally, the alternating pattern of Al/Cu in this thin film was resolved up until the last two layers and a depth resolution equal to the LA up-take rate of 100 nm may be assumed. The material dependence of the LA also in case of fs-lasers clearly demonstrated the limitations of fs-LA-ICP-MS for depth profile analysis.

8.4 Conclusion

For many years, a major limitation for high-resolution depth profile analysis by fs-LA-ICP-MS was the lack of a versatile and practically applicable homogenization unit for the laser beam, allowing a uniform sample removal per laser pulse. Hence, the implementation of the optical processing for a homogenized laser intensity profile at the sample surface was an important step towards high-resolution depth profiling. Indeed, we were able to resolve 9 alternating thin layers of Cr and Ni of approx. 60 nm thickness each. Challenges were encountered when different thin film systems were analysed. Indeed, in the case of a thin film, consisting of thin alternating layers of Al and Cu, limitations of the LA up-take rate and heat diffusion were obtained. The analysis of a single layer of Cr supported the formation of craters with steep walls as found in part III, chapter

7. The applicability of the formalism proposed by Hofmann,[145] and the assumption of a Gaussian shaped DRF was demonstrated. Indeed, through the application of this mathematical description of the measured depth profile the significant differences between the LA up-take rate and the depth resolution were identified. In addition, different effects (i.e. LA up-take rates, beam imperfections, ripple formation, as well as plasma etching), which have been discussed to limit the depth resolution, were summarized within this formalism. However, limitations of the symmetric DRF were encountered, when sharp interfaces further down within the sample were probed. The application of this convention offers a better comparison among different analytical techniques as well as within different LA-ICP-MS set-ups, especially when compared to the aforementioned concepts previously applied in LA-ICP-MS.[155,166,200] Additionally, it renders the possibility to reconstruct the 'true' depth profile for LA-ICP-MS and hence, it may reveal deeper insights into the 'true' depth profile of unknown samples. However, one should keep in mind, that LA is a highly material dependent process. The samples investigated in this study represent only a small range of samples. For example thin films composed of alloys, where preferential ablation could be a major challenge or thin films of non-metals where higher energy densities are required could introduce new challenges. Additionally, future research may assess possible workarounds to erase/minimize the formation of LIPSS.[215]

Finally, in light of this work we achieved a depth resolution down to 47 nm for a Cr/Ni thin film and so fs-LA-ICP-MS equipped with a homogenization unit for uniform LA could become an important and complementary analytical technique for fast and high-resolution depth profile analysis of thin metal layers.

Part IV

Summary and Outlook

"Don't worry. Eat curry."

Tuck-tuck - Stephan & Benito

Over the past decades the complexity of the LA process in combination with LA-ICP-MS has driven many research studies. The two key findings which have promoted the research efforts of this thesis were: (1) The development of a homogenized beam delivery set-up for nanosecond-LA systems and (2) the introduction of femtosecond-lasers in LA-ICP-MS. With respect to (1), this system has resulted in higher lateral and/or depth resolution through controllable LA up-take rates, lower elemental fractionation, higher reproducibility and, thus, enhanced analytical performance was achieved. Regarding point (2), due to minimized heat effects in case of fs-LA, reduced elemental fractionation especially for conducting materials was proposed and therefore triggered the possibility for non-matrix matched analysis.

Regarding the first point, which has channelled the capabilities of state-of-the-art LA-ICP-MS for 2D and 3D elemental imaging, enforced our study about elemental fractionation of matrix elements of silicate minerals (Na, Al, Si, Ca, Ti, Fe, Mn). It is the nature of many rock types to have multiple mineral phases and hence imaging thereof may entail the analysis of different phases. To simplify quantification procedures, the strategy of 100% mass normalization is typically employed and therefore, accurate quantification of geological important matrix elements is essential. In addition, the material dependency of the LA process requires a matrix-matched analysis as elemental fractionation may occur. This promoted the need for a variety of different reference materials. In this regard, researchers came up with the idea of producing pressed nano-powders as alternative reference materials to the once routinely used in glass phase. Due to this we evaluated the term matrix-matched analysis from a different point of view: the importance of the solid phase,

e.g. glassy or powder, rather than a miss-match in the overall compositions of sample and reference. In this thesis, we showcased the occurrence of elemental fractionation regarding Si in a variety of silicate reference materials present in different phases. To name some important findings regarding the Si fractionation, studies about the LA-generated aerosol morphology showed distinct Si enrichment in particles ≥ 10 μm for a reference material in glass phase. Furthermore, under wet plasma conditions the highest sensitivity gain of approximately a factor of 6 in case of Si in comparison to the other elements investigated was revealed. An extensive study of different mineral samples showed, that in some cases, even non-matrix matched analysis provided accurate determination for SiO_2. In conclusion, the accuracy was not dependent on matching absorption, concentrations, or matrix composition in general and even though a dependency on the phase of the external standard was revealed no clear assignment of when which of the aforementioned characteristics results in accurate quantification of Si to either of the two phases was possible.
When changing from ns-LA to fs-LA our results showed minimal improvement in accuracy, and indeed only in the case of matrix-matched analysis. Concerning the key point (2), however, the introduction of ultrashort (i.e. fs) laser pulses was expected to result in minimized elemental fractionation, which was at this point not observed in the case of Si. One could speculate that it might be the combination of the two key points, which could unravel the obtained elemental fractionation of Si. If fs-LA with a homogenized beam profile would be applied, higher accuracy might be obtained, due to the shorter pulse duration in combination with a mono-modal particle size distribution, as a result of the homogenized beam profile.[31]

To this regard the homogenization of fs-laser beam profile by pinhole imaging in the second part of this thesis was addressed. This strategy allowed for homogeneous LA by fs-lasers and well-defined craters on both non-conducting and conducting materials with diameters of 25 μm were achieved. Due to the promising characteristics of fs-LA, such as minimal heat effects and LA up-take rates, the applicability of fs-LA-ICP-MS for depth profile analysis of thin metal layers was further investigated. TO do so, single layers of chromium (Cr) deposited on different substrates were analysed. By comparison of the measured to simulated depth profiles for which either a Gaussian or a Super-Gaussian beam profile was

assumed, evidence for the latter was obtained. In order to evaluate the achieved depth resolution, the obtained depth profiles were further analysed by a formalism proposed by Hofmann[145] and in agreement with the ISO guidelines. In addition to the single layer Cr samples, multilayer thin film samples were used as ideal targets to determine the depth dependent depth resolution. Indeed, our results suggested a depth resolution of 50 nm for near-surface transitions to 100 nm further in the sample. Finally, the goal of any depth profile analysis is to measure the true concentration profile of elements as a function of sampling depth. Given the nature of LA being highly material dependent, makes the estimation of ablated material volume, i.e. crater depth, very challenging. Hence, on-line monitoring of crater depths and diameters would allow calculating ablated volumes and, thus, render absolute quantification possible.

During the final steps of this thesis, we have performed first proof of principle experiments to study the feasibilities of Fourier domain low coherence interferometry (FD-LCI) to monitor the depths of craters in conducting materials using ultrashort bursts of white light. A Fresnel double-mirror set-up[216] served as proxy for crater rim and bottom to first split, delay and reflect, and then reassemble individual pulses for interference along an optical grating (see Figure IV.8.9). Preliminary results showed accuracies for depth measurements, i.e. mirror displacements, to range from several micrometers to less than 100 nm, depending on whether the interference patterns were processed by discrete Fourier transform or by non-linear least square regression, respectively. For future studies, the applicability of such FD-LCI for on-line monitoring of the crater depth of obtained craters after fs-LA need to be investigated.

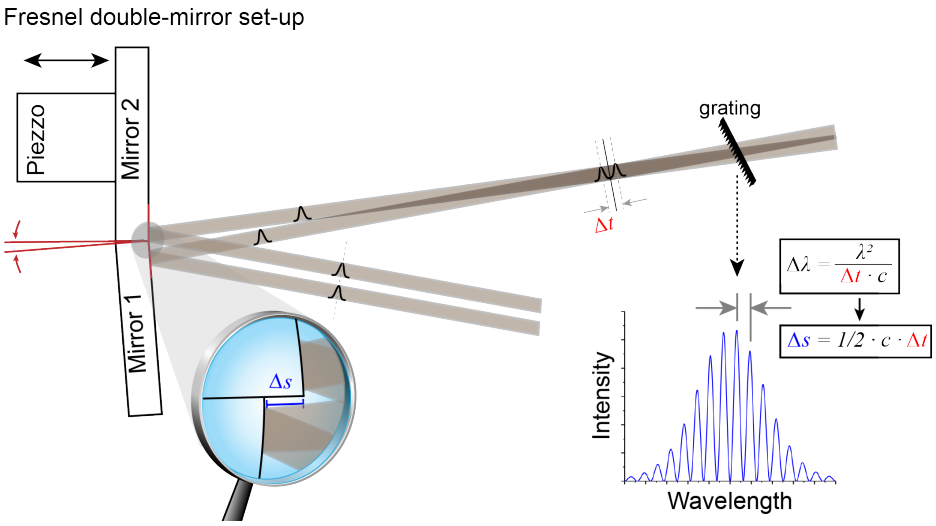

Figure IV.8.9: Schematic representation of Fourier domain low coherence interferometry (FD-LCI) for on-line crater depth measurements. Proof of principle study was performed, using two mirrors as proxy for crater rim and bottom, as indicated in the magnification. Due to the various distance, between crater bottom and rim to the optical grating, pulses originating from the same light pulse, arrive at a specific time difference (Δt) at the optical grating. In case of spatial overlapping of two pulses arriving at the optical grating, an interference pattern will be obtained. According to the distance between the fringes in the interference pattern ($\Delta\lambda$), the time difference (Δt) can be evaluated. The speed of light (c) can then be used to transform Δt into the distance between crater rim and bottom (Δs).

Finally, the line of arguments and visions throughout this thesis promote further studies about the effect of the homogenized laser beam profile for fs-laser systems on the analytical outcome for silicate samples with respect to the obtained Si fractionation. Moreover, the depth resolution achieved by fs-LA using the proposed set-up not only provides a promising complementary analytical technique for fast and high-resolution depth profile analysis of thin metal layers but may also push 3D elemental imaging by fs-LA-ICP-MS further.

Chapter A

Appendix - part III

A.1 Two-temperature diffusion model for ultrashort laser pulses

The fallowing section summarizes the characteristic interaction of ultrashort laser pulses with metal targets according to Nolte *et. al.*[78]

In the case of metals, the energy of an incoming ultrashort laser pulse is absorbed by free electrons. This concept is based on the inverse Bremsstrahlung. The absorbed laser energy leads to thermalization of the electronic subsystems and subsequently to an energy transfer to the lattice, meanwhile energy loss due to electron heat transport into the target occurs. Assuming the thermalization of the electronic subsystem to be much faster than the energy transfer to the lattice, the temperature of each subsystem is characterized individually (T_e and T_i) and the energy transfer into the metal is calculated by a one-dimensional, two-temperature diffusion model.

$$C_e \frac{\partial T_e}{\partial t} = -\frac{\partial Q(z)}{\partial z} - \gamma\big(T_e - T_i\big) + S \tag{A.1}$$

$$C_i \frac{\partial T_i}{\partial t} = -\gamma\big(T_e - T_i\big) \tag{A.2}$$

$$Q(z) = -k_e \frac{\partial T_e}{\partial z} \tag{A.3}$$

$$S = I(t)A\alpha e^{\alpha z} \tag{A.4}$$

With C_i and C_e the heat capacities of the electron and the lattice subsystems, respectively, γ the parameter characterizing the electron-lattice coupling, z the direction perpendicular to the surface, Q(z) the heat flux, k_e the electron thermal conductivity, S the laser heating source term, and I(t) the laser intensity, $A = 1 - R$ the surface transmissivity and α the material absorption coefficient.

According to Nolte *et. al.* the heat capacity C_e, the thermal conductivity k_e and the electron thermal diffusivity $D = \frac{k_e}{C_e}$ are assumed to be constant during the laser pulse.[78] This leads to the following equations (A.5) and (A.6) describing the evolution of the electron and the ion temperatures, respectively for short-pulse laser ablation.

$$\frac{\partial T_e}{\partial t} = -\frac{\partial D}{\partial z}\frac{\partial T_e}{z} - \frac{T_e - T_i}{\tau_e} + \frac{IA\alpha}{C_e}e^{-\alpha z} \tag{A.5}$$

$$\frac{\partial T_i}{\partial t} = -\frac{T_e - T_i}{\tau_i} \tag{A.6}$$

The three characteristic time scales can be attributed to: $\tau_e = \frac{C_e}{\gamma}$, describing the electron cooling time, $\tau_i = \frac{C_i}{\gamma}$, the lattice heating time and τ_L, the duration of the laser pulse, with $\tau_L \ll \tau_e \ll \tau_i$. Important for the solution of these equations are the assumptions of two different penetration depths (the optical penetration depth α^{-1} and the heat penetration depth $\beta^{-1} = \left(D\tau_{eff}\right)^{1/2}$, with $\tau_{eff} = \frac{(\tau_e\tau_L)}{\tau_e+\tau_L}$) and the linear correlation between the lattice temperature and the electron temperature. If the laser pulse is now switched off, the electron and ion temperatures still follow the equations (A.5) and (A.6) with $I = 0$. To further allow electron thermal diffusion after the laser pulse, the effective time interval τ_{eff} is expanded by the time interval the system takes to equilibrate τ_{eq} to give the time interval for the laser ablation τ_a. With this correction and because $\tau_e \ll \tau_i$ for ultrashort laser pulses, the spatial ion temperature profile at the end of the thermal relaxation between the electron and ion subsystem can be described by the following equation (A.7)

$$T_i \cong \frac{F_\alpha}{C_i} \cdot \frac{1}{l^2 - \delta^2} \cdot \left[l \cdot exp\left(-\frac{z}{l}\right) - \delta \cdot exp\left(-\frac{z}{\delta}\right)\right] \tag{A.7}$$

With $F_a = I_0 A\tau_L$ the absorbed laser fluence, $l = (D\tau_a)^{\frac{1}{2}}$ the thermal and $\delta = \frac{1}{\alpha}$ the optical contribution to the penetration depth.

At this point two cases can be distinguished; when the optical penetration depth is much

larger or much smaller than the heat penetration depth. Eventually, significant evaporation only occurs when the energy of the lattice $T_i \cdot C_i$ becomes larger than the heat of evaporation $\rho \cdot \Omega$, according to the evaporation kinetics. As a result, the corresponding ablation depth per pulse can be calculated by the following equations (A.8) and (A.9).

$$L_\delta = z = \delta \cdot ln\big(\frac{F_\alpha}{F_{th}{}^{\delta}}\big) \qquad \rightarrow \qquad \big(\delta \gg l\big) \tag{A.8}$$

$$L_l = z = l \cdot ln\big(\frac{F_\alpha}{F_{th}{}^{l}}\big) \qquad \rightarrow \qquad \big(\delta \ll l\big) \tag{A.9}$$

With $F_{th}{}^{\delta} = \rho \cdot \Omega \cdot \delta$ and $F_{th}{}^{l} = \rho \cdot \Omega \cdot l$ the corresponding thresholds for the absorbed laser fluences. According to Nolte et. al., if the laser fluences are below 0.5 J/cm^2, the density of hot electrons is too low and the ablation depth behaves as predicted by equation (A.8). Though for higher pulse energies the influence of the electronic heat conduction becomes important and the second ablation regime described by equation (A.9) appears.
Nolte et. al. finally calculated the effective electronic heat penetration depth $l = \big(D\tau_a\big)^{1/2}$ of copper to be 60-80 nm, where they estimated the time which is necessary for the electron energy transfer to the ions to be $\tau_a = \tau \cdot \frac{M_{ion}}{m_e} = 22 - 30\,ps$.

A.2 Temporal characterization of the fs-laser pulse using transient-grating frequency-resolved optical gating

The fs laser pulse of the Ti:Sapphire fs laser system (Mira Legend, Coherent Inc., Santa Clara, CA, USA) used for all measurements in part III, were temporally characterized using **T**ransient-**G**rating **F**requency-**R**esolved **O**ptical **G**ating (TG-FROG). For the purpose of this thesis, only a short description of the TG-FROG will be given here. For further details see ref.[217,218]

The typical set-up for a FROG measurement is similar to that of an intensity autocorrelator. Inhere, however, the photo-detector is replaced with a spectrometer. Within a FROG measurement a specific number of spectra, using different settings, the arrival time differences between two laser pulses are recorded. According to such FROG traces, the pulse shape can be reconstructed, using sophisticated algorithms. In TG-FROG two beams are overlapping in a medium, generating a non-linear refractive index grating. A third pulse with a variable delay as the probe is diffracted at the grating generated by the other two beams. The spectrum of the signal is then recorded as a function of the delay of one of the input pulses.[217] Overall, preliminary analyses showed that even though the reconstruction is not perfect yet, the determined time duration of 170±20% fs agreed with the cross correlation from the FROG measurement and gave a good estimation of the actual pulse duration.

A.3 RBS measurement of Al/Cu sample - part III chapter 7

In this project provided by Max Döbeli from ETH Zurich, Switzerland, measurements with initial He energies of 2 and 5 MeV were performed and a Si PIN diode detector was placed under an angle of 168° to the incident beam direction.

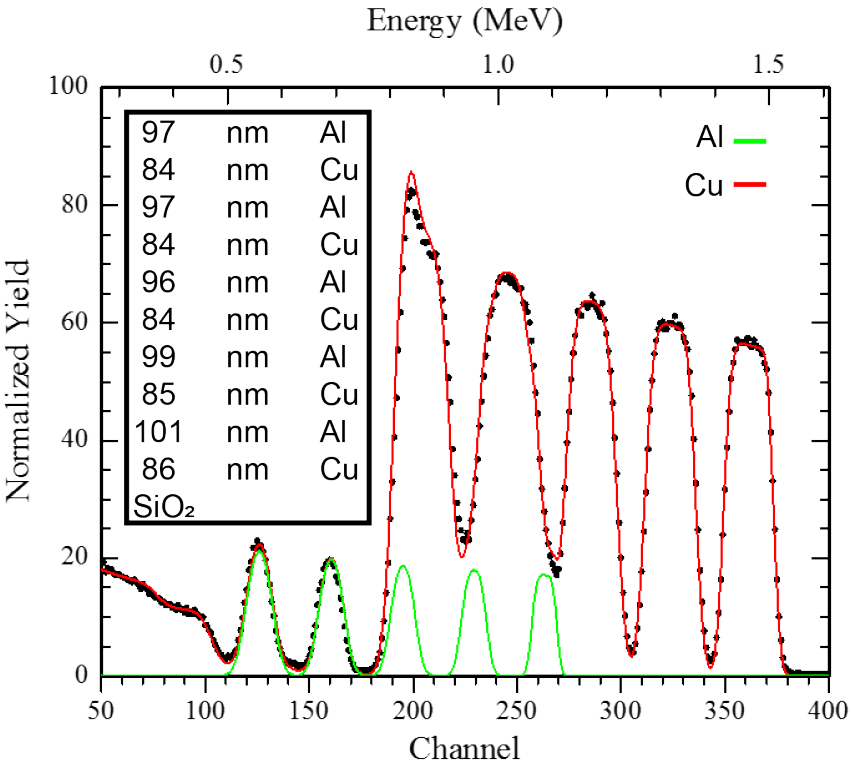

Figure IV.1.1: RBS energy spectrum of an Al/Cu multilayer sample measured with a 2 MeV He^+ beam and a Si PIN diode detector placed under 168°. The spectrum can be interpreted as an overlay of the Cu and Al concentration depth profiles with the depth scale running from right to left. The red curve represents a RUMP simulation [219] which was fitted to the measured spectrum. For clarity, the green curve shows the simulated spectrum for Al. The accuracy of layer thicknesses is approximately 4%

Chapter B

List of Abbreviations

AC	Alternating current	AES	Auger electron spectroscopy
AFM	Atomic Force Microscopy	CM	Confocal Microscopy
DC	Direct Current	DOFMS	Distance of Flight Mass Spectrometry
EDX	Energy Dispersive X-ray Spectroscopy	EPMA	Electron Probe Microanalysis
ESA	Electrostatic Analyzer	FC	Faraday Cup
fs	Femtosecond	GD-MS	Glow Discharge Mass Spectrometry
HSFL	High Spatial Frequency Laser-Induced Periodic Surface Structures	ICP	Inductively Coupled Plasma
IS	Internal Standard	ISO	International Organization for standardization

LA	Laser Ablation	LA-ICP-MS	Laser Ablation – Inductively Coupled Plasma – Mass Spectrometry
Laser	Laser Light Amplification by Stimulated emission of radiation	LIPPS	Laser-Induced Periodic Surface Structures
LOD	Limit of Detection	LSFL	Low Spatial Frequency Laser-Induced Periodic Surface Structures
m/z	mass-to-charge ratio	MCP	Multichannel Plates
MS	Mass Spectrometer	NIST	National institute of standards and technology
ns	Nanosecond	OM	Optical Microscopy
OPC	Optical Particle Counter	PSD	Particle Size Distribution
qMS	quadrupole Mass Spectrometry	R	Resolution
RBS	Rutherford Backscattering Spectroscopy	REE	Rare Earth Elements
RF	Radiofrequency	S/N	Signal to Noise ratio
SEM	Scanning Electron Microscopy	SEM	Secondary Electron Multiplier
SEM-EDX	Scanning Electron Microscopy – Energy Dispersive X-ray Spectroscopy	sfMS	sectorfield Mass Spectrometry
SIMS	Secondary Ion Mass Spectrometry	SN	Solution Nebulization

SRM	Standard Reference Material	TEM	Transmission Electron Microscopy
TG-FROG	Transient-grating frequency-resolved optical gating	TOFMS	Time of Flight spectroscopy
AC	Alternating current	AES	Auger electron Mass Spectrometry
USGS	U.S. geological survey	WDX	Wavelength Dispersive X-Ray Spectroscopy
XPS	X-ray Photoelectron Spectroscopy	XRF	X-ray Fluorescence Spectroscopy

Bibliography

[1] Cammann, K. Analytical Chemistry — today's definition and interpretation. *Fresenius' Journal of Analytical Chemistry* **1992**, *343*, 812–813.

[2] Gross, J. H. In *Mass Spectrometry: A Textbook*; Gross, J. H., Ed.; Springer Berlin Heidelberg, 2011; pp 1–20.

[3] Jakubowski, N.; Prohaska, T.; Rottmann, L.; Vanhaecke, F. Inductively coupled plasma- and glow discharge plasma-sector field mass spectrometry Part I. Tutorial: Fundamentals and instrumentation. *Journal of Analytical Atomic Spectrometry* **2011**, *26*, 693–726.

[4] Jakubowski, N.; Moens, L.; Vanhaecke, F. Sector field mass spectrometers in ICP-MS. *Spectrochimica Acta Part B: Atomic Spectroscopy* **1998**, *53*, 1739–1763.

[5] Thomson, J. J. Bakerian Lecture: 2014; Rays of positive electricity. *Proceedings of the Royal Society of London. Series A, Containing Papers of a Mathematical and Physical Character* **1913**, *89*, 1–20.

[6] Gray, A. L. Solid sample introduction by laser ablation for inductively coupled plasma source mass spectrometry. *Analyst* **1985**, *110*, 551–556.

[7] Audétat, A.; Günther, D.; Heinrich, C. A. Formation of a Magmatic-Hydrothermal Ore Deposit: Insights with LA-ICP-MS Analysis of Fluid Inclusions. *Science* **1998**, *279*, 2091.

[8] Günther, D. UV-Laser ablation - In combination with ICP mass spectrometry. *Nachrichten Aus Chemie Technik Und Laboratorium* **1997**, *45*, 784–788.

[9] Wang, H. A. O.; Grolimund, D.; Giesen, C.; Borca, C. N.; Shaw-Stewart, J. R. H.; Bodenmiller, B.; Günther, D. Fast Chemical Imaging at High Spatial Resolution by Laser Ablation Inductively Coupled Plasma Mass Spectrometry. *Analytical Chemistry* **2013**, *85*, 10107–10116.

[10] Borovinskaya, O.; Hattendorf, B.; Tanner, M.; Gschwind, S.; Günther, D. A prototype of a new inductively coupled plasma time-of-flight mass spectrometer providing temporally resolved, multi-element detection of short signals generated by single particles and droplets. *Journal of Analytical Atomic Spectrometry* **2013**, *28*, 226–233.

[11] Gundlach-Graham, A.; Günther, D. Toward faster and higher resolution LA–ICPMS imaging: on the co-evolution of LA cell design and ICPMS instrumentation. *Analytical and Bioanalytical Chemistry* **2016**, *408*, 2687–2695.

[12] Van Malderen, S. J. M.; Managh, A. J.; Sharp, B. L.; Vanhaecke, F. Recent developments in the design of rapid response cells for laser ablation-inductively coupled plasma-mass spectrometry and their impact on bioimaging applications. *Journal of Analytical Atomic Spectrometry* **2016**, *31*, 423–439.

[13] Haglund, R. F. In *Laser Ablation*; Fogarassy, E., Geohegan, D., Stuke, M., Eds.; Elsevier: Oxford, 1996; pp 1–13.

[14] Chichkov, B. N.; Momma, C.; Nolte, S.; vonAlvensleben, F.; Tunnermann, A. Femtosecond, picosecond and nanosecond laser ablation of solids. *Applied Physics a-Materials Science & Processing* **1996**, *63*, 109–115.

[15] Paschotta, Non-radiative Transitions. https://www.rp-photonics.com/non-radiative-transitions.html/ (accessed January 2019).

[16] Wälle, M.; Koch, J.; Tabersky, D.; Hametner, K.; Zhigadlo, N. D.; Katrych, S.; Karpinski, J.; Günther, D. Analyses of lithium-doped and pure magnesium diboride using ultraviolet nano- and femtosecond laser ablation inductively coupled plasma mass spectrometry. *Journal of Analytical Atomic Spectrometry* **2010**, *25*, 193–195.

[17] Koch, J.; Schlamp, S.; Rösgen, T.; Fliegel, D.; Günther, D. Visualization of aerosol particles generated by near infrared nano- and femtosecond laser ablation. *Spectrochimica Acta Part B: Atomic Spectroscopy* **2007**, *62*, 20–29.

[18] Hattendorf, B.; Günther, D. In *Handbook of Spectroscopy*; Gauglitz, G., Moore, D. S., Eds.; Wiley-VCH Verlag GmbH & Co. KGaA: Hoboken, USA, 2014; pp 647–698.

[19] Koch, J.; von Bohlen, A.; Hergenröder, R.; Niemax, K. Particle size distributions and compositions of aerosols produced by near-IR femto- and nanosecond laser ablation of brass. *Journal of Analytical Atomic Spectrometry* **2004**, *19*, 267–272.

[20] E. Jeffries, T.; E. Jackson, S.; P. Longerich, H. Application of a frequency quintupled Nd:YAG source (=213 nm) for laser ablation inductively coupled plasma mass spectrometric analysis of minerals. *Journal of Analytical Atomic Spectrometry* **1998**, *13*, 935–940.

[21] Günther, D.; A. Heinrich, C. Comparison of the ablation behaviour of 266 nm Nd:YAG and 193 nm ArF excimer lasers for LA-ICP-MS analysis. *Journal of Analytical Atomic Spectrometry* **1999**, *14*, 1369–1374.

[22] Horn, I.; Guillong, M.; Günther, D. Wavelength dependant ablation rates for metals and silicate glasses using homogenized laser beam profiles — implications for LA-ICP-MS. *Applied Surface Science* **2001**, *182*, 91–102.

[23] Figg, D.; Kahr, M. S. Elemental Fractionation of Glass Using Laser Ablation Inductively Coupled Plasma Mass Spectrometry. *Applied Spectroscopy* **1997**, *51*, 1185–1192.

[24] Garcia, C. C.; Lindner, H.; von Bohlen, A.; Vadla, C.; Niemax, K. Elemental fractionation and stoichiometric sampling in femtosecond laser ablation. *Journal of Analytical Atomic Spectrometry* **2008**, *23*, 470–478.

[25] Günther, D.; Frischknecht, R.; Heinrich, C. A.; Kahlert, H. J. Capabilities of an Argon Fluoride 193 nm excimer laser for laser ablation inductively coupled plasma mass spectrometry microanalysis of geological materials. *Journal of Analytical Atomic Spectrometry* **1997**, *12*, 939–944.

[26] Diwakar, P. K.; Gonzalez, J. J.; Harilal, S. S.; Russo, R. E.; Hassanein, A. Ultrafast laser ablation ICP-MS: role of spot size, laser fluence, and repetition rate in signal intensity and elemental fractionation. *Journal of Analytical Atomic Spectrometry* **2014**, *29*, 339–346.

[27] Pécheyran, C.; Cany, S.; Chabassier, P.; Mottay, E.; Donard, O. F. X. High repetition rate and low energy femtosecond laser ablation coupled to ICPMS detection: a new analytical approach for trace element determination in solid samples. *Journal of Physics: Conference Series* **2007**, *59*, 112–117.

[28] Yokoyama, T. D.; Suzuki, T.; Kon, Y.; Hirata, T. Determinations of Rare Earth Element Abundance and U-Pb Age of Zircons Using Multispot Laser Ablation-Inductively Coupled Plasma Mass Spectrometry. *Analytical Chemistry* **2011**, *83*, 8892–8899.

[29] Eggins, S. M.; Kinsley, L. P. J.; Shelley, J. M. *G Appl. Surf. Sci.* **1998**, *127*, 86.

[30] Pisonero, J.; Koch, J.; Wälle, M.; Hartung, W.; Spencer, N. D.; Günther, D. Capabilities of Femtosecond Laser Ablation Inductively Coupled Plasma Mass Spectrometry for Depth Profiling of Thin Metal Coatings. *Analytical Chemistry* **2007**, *79*, 2325–2333.

[31] Menéndez-Manjón, A.; Barcikowski, S.; Shafeev, G. A.; Mazhukin, V. I.; Chichkov, B. N. Influence of beam intensity profile on the aerodynamic particle size distributions generated by femtosecond laser ablation. *Laser and Particle Beams* **2010**, *28*, 45–52.

[32] Glaus, R.; Kaegi, R.; Krumeich, F.; Günther, D. Phenomenological studies on structure and elemental composition of nanosecond and femtosecond laser-generated aerosols with implications on laser ablation inductively coupled plasma mass spectrometry. *Spectrochimica Acta Part B: Atomic Spectroscopy* **2010**, *65*, 812–822.

[33] D'Abzac, F.-X.; Seydoux-Guillaume, A.-M.; Chmeleff, J.; Datas, L.; Poitrasson, F. In situ characterization of infra red femtosecond laser ablation in geological samples. Part B: the laser induced particles. *Journal of Analytical Atomic Spectrometry* **2012**, *27*, 108–119.

[34] Pisonero, J.; Günther, D. Femtosecond Laser Ablation Inductively Coupled Plasma Mass Spectrometry: Fundamentals and Capabilities for Depth Profiling Analysis. *Mass Spectrometry Reviews* **2008**, *27*, 609–623.

[35] Perkins, W. T.; Fuge, R.; Pearce, N. J. G. Quantitative analysis of trace elements in carbonates using laser ablation inductively coupled plasma mass spectrometry. *Journal of Analytical Atomic Spectrometry* **1991**, *6*, 445–449.

[36] Garbe-Schönberg, C.-D.; McMurtry, G. M. In-situ micro-analysis of platinum and rare earths in ferromanganese crusts by laser ablation-ICP-MS (LAICPMS). *Fresenius' Journal of Analytical Chemistry* **1994**, *350*, 264–271.

[37] Jochum, K. P.; Scholz, D.; Stoll, B.; Weis, U.; Wilson, S. A.; Yang, Q.; Schwalb, A.; Börner, N.; Jacob, D. E.; Andreae, M. O. Accurate trace element analysis of speleothems and biogenic calcium carbonates by LA-ICP-MS. *Chemical Geology* **2012**, *318-319*, 31–44.

[38] Reed, T. B. Induction-Coupled Plasma Torch. *Journal of Applied Physics* **1961**, *32*, 821–824.

[39] Niu, H.; Houk, R. S. Fundamental aspects of ion extraction in inductively coupled plasma mass spectrometry. *Spectrochimica Acta Part B: Atomic Spectroscopy* **1996**, *51*, 779–815.

[40] Greenfield, S.; Jones, I. L.; Berry, C. T. High-pressure plasmas as spectroscopic emission sources. *Analyst* **1964**, *89*, 713–720.

[41] Wendt, R. H.; Fassel, V. A. Induction-Coupled Plasma Spectrometric Excitation Source. *Analytical Chemistry* **1965**, *37*, 920–922.

[42] Houk, R. S.; Fassel, V. A.; Flesch, G. D.; Svec, H. J.; Gray, A. L.; Taylor, C. E. Inductively coupled argon plasma as an ion source for mass spectrometric determination of trace elements. *Analytical Chemistry* **1980**, *52*, 2283–2289.

[43] Houk, R. S. Mass spectrometry of inductively coupled plasmas. *Analytical Chemistry* **1986**, *58*, 97A–105A.

[44] Tanner, S. D. Space charge in ICP-MS: calculation and implications. *Spectrochimica Acta Part B: Atomic Spectroscopy* **1992**, *47*, 809–823.

[45] De Hoffmann, E.; Stroobant, V. *Mass spectrometry principles and applications*, 3rd ed.; Wiley: Hoboken, N.J., 2007; p 489 S.

[46] Graham, A. W. G.; Ray, S. J.; Enke, C. G.; Felton, J. A.; Carado, A. J.; Barinaga, C. J.; Koppenaal, D. W.; Hieftje, G. M. Resolution and Mass Range Performance in Distance-of-Flight Mass Spectrometry with a Multichannel Focal-Plane Camera Detector. *Analytical Chemistry* **2011**, *83*, 8552–8559.

[47] March, R.; Todd, J. *Practical Aspects of Trapped Ion Mass Spectrometry*; CRC Press: Boca Raton, 2010; Vol. IV.

[48] Becker, J. S.; Dietze, H.-J. gDouble-focusing Sector Field Inductively Coupled Plasma Mass Spectrometry for Highly Sensitive Multi-element and Isotopic Analysis. *Journal of Analytical Atomic Spectrometry* **1997**, *12*, 881–889.

[49] Wieser, M. E.; Schwieters, J. B. The development of multiple collector mass spectrometry for isotope ratio measurements. *International Journal of Mass Spectrometry* **2005**, *242*, 97–115.

[50] Gundlach-Graham, A.; Burger, M.; Allner, S.; Schwarz, G.; Wang, H. A. O.; Gyr, L.; Grolimund, D.; Hattendorf, B.; Günther, D. High-Speed, High-Resolution, Multielemental Laser Ablation-Inductively Coupled Plasma-Time-of-Flight Mass Spectrometry Imaging: Part I. Instrumentation and Two-Dimensional Imaging of Geological Samples. *Analytical Chemistry* **2015**, *87*, 8250–8258.

[51] Burger, M.; Gundlach-Graham, A.; Allner, S.; Schwarz, G.; Wang, H. A. O.; Gyr, L.; Burgener, S.; Hattendorf, B.; Grolimund, D.; Günther, D. High-Speed, High-Resolution, Multielemental LA-ICP-TOFMS Imaging: Part II. Critical Evaluation of Quantitative Three-Dimensional Imaging of Major, Minor, and Trace Elements in Geological Samples. *Analytical Chemistry* **2015**, *87*, 8259–8267.

[52] Koppenaal, D. W.; Barinaga, C. J.; Denton, M. B.; Sperline, R. P.; Hieftje, G. M.; Schilling, G. D.; Andrade, F. J.; Barnes, J. H.; Iv, I. V. MS Detectors. *Analytical Chemistry* **2005**, *77*, 418 A–427 A.

[53] Käser, D.; Hendriks, L.; Koch, J.; Günther, D. Depth profile analyses with sub 100-nm depth resolution of a metal thin film by femtosecond - laser ablation - inductively coupled plasma - time-of-flight mass spectrometry. *Spectrochimica Acta Part B: Atomic Spectroscopy* **2018**, *149*, 176–183.

[54] Käser, D.; Hendriks, L.; Koch, J.; Günther, D. Corrigendum to "Depth profile analyses with sub 100-nm depth resolution of a metal thin film by femtosecond - laser ablation - inductively coupled plasma - time-of-flight mass spectrometry" Spectrochimica Acta Part B: Atomic Spectroscopy 149 (2018) 176–183. *Spectrochimica Acta Part B: Atomic Spectroscopy* **2018**, *149*, 322.

[55] Rudnick, R. L.; Gao, S. In *Treatise on Geochemistry*; Turekian, K. K., Ed.; Pergamon: Oxford, 2003; pp 1–64.

[56] Fryer, B. J.; Jackson, S. E.; Longerich, H. P. The design, operation and role of the laser-ablation microprobe coupled with an inductively coupled plasma; mass spectrometer (LAM-ICP-MS) in the earth sciences. *The Canadian Mineralogist* **1995**, *33*, 303–312.

[57] Bogaerts, A.; Chen, Z.; Gijbels, R.; Vertes, A. Laser ablation for analytical sampling: what can we learn from modeling? *Spectrochimica Acta Part B: Atomic Spectroscopy* **2003**, *58*, 1867–1893.

[58] Kuhn, H. R.; Günther, D. *Anal. Chem.* **2003**, *75*, 53.

[59] Kroslakova, I.; Günther, D. Elemental fractionation in laser ablation-inductively coupled plasma-mass spectrometry: evidence for mass load induced matrix effects in the ICP during ablation of a silicate glass. *Journal of Analytical Atomic Spectrometry* **2007**, *22*, 51–62.

[60] Shaheen, M. E.; Fryer, B. J. Femtosecond laser ablation of brass: A study of surface morphology and ablation rate. *Laser and Particle Beams* **2012**, *30*, 473–479.

[61] Jochum, K. P.; Stoll, B.; Weis, U.; Jacob, D. E.; Mertz-Kraus, R.; Andreae, M. O. Non-Matrix-Matched Calibration for the Multi-Element Analysis of Geological and Environmental Samples Using 200 nm Femtosecond LA-ICP-MS: A Comparison with Nanosecond Lasers. *Geostandards and Geoanalytical Research* **2014**, *38*, 265–292.

[62] Guillong, M.; Hametner, K.; Reusser, E.; Wilson, S. A.; Günther, D. Preliminary Characterisation of New Glass Reference Materials (GSA-1G, GSC-1G, GSD-1G

and GSE-1G) by Laser Ablation-Inductively Coupled Plasma-Mass Spectrometry Using 193 nm, 213 nm and 266 nm Wavelengths. *Geostandards and Geoanalytical Research* **2005**, *29*, 315–331.

[63] Kane, J. S. An Assessment of the Suitability of NIST Glass SRM Literature Data for the Derivation of Reference Values. *Geostandards Newsletter* **1998**, *22*, 15–31.

[64] Kane, J. S. A History of the Development and Certification of NIST Glass SRMs 610-617. *Geostandards Newsletter* **1998**, *22*, 7–13.

[65] Kane, J. S. Fitness-for-Purpose of Reference Material Reference Values in Relation to Traceability of Measurement, as Illustrated by USGS BCR-1, NIST SRM 610 and IAEA NBS28. *Geostandards Newsletter* **2002**, *26*, 7–29.

[66] Pearce, N. J.; Perkins, W. T.; Westgate, J. A.; Gorton, M. P.; Jackson, S. E.; Neal, C. R.; Chenery, S. P. A Compilation of New and Published Major and Trace Element Data for NIST SRM 610 and NIST SRM 612 Glass Reference Materials. *Geostandards Newsletter* **1997**, *21*, 115–144.

[67] Hinton, R. W. NIST SRM 610, 611 and SRM 612, 613 Multi-Element Glasses: Constraints from Element Abundance Ratios Measured by Microprobe Techniques. *Geostandards Newsletter* **1999**, *23*, 197–207.

[68] Jochum, K. P.; Weis, U.; Stoll, B.; Kuzmin, D.; Yang, Q.; Raczek, I.; Jacob, D. E.; Stracke, A.; Birbaum, K.; Frick, D. A.; Günther, D.; Enzweiler, J. Determination of Reference Values for NIST SRM 610–617 Glasses Following ISO Guidelines. *Geostandards and Geoanalytical Research* **2011**, *35*, 397–429.

[69] Rocholl, A. B.; Simon, K.; Jochum, K. P.; Bruhn, F.; Gehann, R.; Kramar, U.; Luecke, W.; Molzahn, M.; Pernicka, E.; Seufert, M.; Spettel, B.; Stummeier, J. Chemical Characterisation of NIST Silicate Glass Certified Reference Material SRM 610 by ICP-MS, TIMS, LIMS, SSMS, INAA, AAS and PIXE. *Geostandards Newsletter* **1997**, *21*, 101–114.

[70] Yang, Q.-C.; Jochum, K. P.; Stoll, B.; Weis, U.; Kuzmin, D.; Wiedenbeck, M.; Traub, H.; Andreae, M. O. BAM-S005 Type A and B: New Silicate Reference Glasses for Microanalysis. *Geostandards and Geoanalytical Research* **2012**, *36*, 301–313.

[71] Ødegård, M.; Mansfeld, J.; Dundas, S. H. Preparation of calibration materials for microanalysis of Ti minerals by direct fusion of synthetic and natural materials: Experience with LA–ICP–MS analysis of some important minor and trace elements in ilmenite and rutile. *Fresenius' Journal of Analytical Chemistry* **2001**, *370*, 819–827.

[72] Wolf, R. E.; Wilson, S. A. *USGS Reference Materials Program: Serving the Needs of the Global Analytical Community*; Report 2007-3056, 2007.

[73] Wohlgemuth-Ueberwasser, C. C.; Ballhaus, C.; Berndt, J.; Stotter née Paliulionyte, V.; Meisel, T. Synthesis of PGE sulfide standards for laser ablation inductively coupled plasma mass spectrometry (LA-ICP-MS). *Contributions to Mineralogy and Petrology* **2007**, *154*, 607–617.

[74] Garbe-Schönberg, D.; Müller, S. Nano-particulate pressed powder tablets for LA-ICP-MS. *Journal of Analytical Atomic Spectrometry* **2014**, *29*, 990–1000.

[75] Tabersky, D.; Luechinger, N. A.; Rossier, M.; Reusser, E.; Hametner, K.; Aeschlimann, B.; Frick, D. A.; Halim, S. C.; Thompson, J.; Danyushevsky, L.; Günther, D. Development and characterization of custom-engineered and compacted nanoparticles as calibration materials for quantification using LA-ICP-MS. *Journal of Analytical Atomic Spectrometry* **2014**, *29*, 955–962.

[76] Hergenröder, R. Hydrodynamic sputtering as a possible source for fractionation in LA-ICP-MS. *Journal of Analytical Atomic Spectrometry* **2006**, *21*, 517–524.

[77] Margetic, V.; Ban, T.; Leis, F.; Niemax, K.; Hergenröder, R. Hydrodynamic expansion of a femtosecond laser produced plasma. *Spectrochimica Acta - Part B Atomic Spectroscopy* **2003**, *58*, 415–425.

[78] Nolte, S.; Momma, C.; Jacobs, H.; Tunnermann, A.; Chichkov, B. N.; Wellegehausen, B.; Welling, H. Ablation of metals by ultrashort laser pulses. *Journal of the Optical Society of America B-Optical Physics* **1997**, *14*, 2716–2722.

[79] Miotello, A.; Kelly, R. Laser-induced phase explosion: new physical problems when a condensed phase approaches the thermodynamic critical temperature. *Applied Physics A* **1999**, *69*, S67–S73.

[80] Miotello, A.; Kelly, R. Critical assessment of thermal models for laser sputtering at high fluences. *Applied Physics Letters* **1995**, *67*, 3535–3537.

[81] Martynyuk, M. M. Phase explosion of a metastable fluid. *Combustion, Explosion and Shock Waves* **1977**, *13*, 178–191.

[82] Bulgakova, N. M.; Stoian, R.; Rosenfeld, A.; Hertel, I. V.; Campbell, E. E. B. Electronic transport and consequences for material removal in ultrafast pulsed laser ablation of materials. *Physical Review B* **2004**, *69*, 054102.

[83] Arnold, N.; Gruber, J.; Heitz, J. Spherical expansion of the vapor plume into ambient gas: an analytical model. *Applied Physics A* **1999**, *69*, S87–S93.

[84] Bäuerle, D. *Laser Processing and Chemistry*; Springer Berlin Heidelberg: Berlin, Heidelberg, 2011; pp 201–235.

[85] Guillong, M.; Horn, I.; Günther, D. A comparison of 266 nm, 213 nm and 193 nm produced from a single solid state Nd:YAG laser for laser ablation ICP-MS. *Journal of Analytical Atomic Spectrometry* **2003**, *18*, 1224–1230.

[86] Zeng, X.; Mao, X.; Greif, R.; Russo, R. Experimental investigation of ablation efficiency and plasma expansion during femtosecond and nanosecond laser ablation of silicon. *Applied Physics A* **2005**, *80*, 237–241.

[87] Bleiner, D.; Bogaerts, A. Multiplicity and contiguity of ablation mechanisms in laser-assisted analytical micro-sampling. *Spectrochimica Acta Part B: Atomic Spectroscopy* **2006**, *61*, 421–432.

[88] Koch, J.; Günther, D. Femtosecond laser ablation inductively coupled plasma mass spectrometry: achievements and remaining problems. *Analytical and Bioanalytical Chemistry* **2007**, *387*, 149–153.

[89] Garcia, C. C.; Lindner, H.; Niemax, K. Laser ablation inductively coupled plasma mass spectrometry—current shortcomings, practical suggestions for improving performance, and experiments to guide future development. *Journal of Analytical Atomic Spectrometry* **2009**, *24*, 14–26.

[90] Hu, Z.; Liu, Y.; Gao, S.; Hu, S.; Dietiker, R.; Günther, D. A local aerosol extraction strategy for the determination of the aerosol composition in laser ablation inductively coupled plasma mass spectrometry. *Journal of Analytical Atomic Spectrometry* **2008**, *23*, 1192–1203.

[91] Horn, I.; Günther, D. The influence of ablation carrier gasses Ar, He and Ne on the particle size distribution and transport efficiencies of laser ablation-induced aerosols: implications for LA–ICP–MS. *Applied Surface Science* **2003**, *207*, 144–157.

[92] Koch, J.; Günther, D. Review of the State-of-the-Art of Laser Ablation Inductively Coupled Plasma Mass Spectrometry. *Applied Spectroscopy* **2011**, *65*, 155A–162A.

[93] Guillong, M.; Günther, D. Effect of particle size distribution on ICP-induced elemental fractionation in laser ablation-inductively coupled plasma-mass spectrometry. *Journal of Analytical Atomic Spectrometry* **2002**, *17*, 831–837.

[94] Guillong, M.; Kuhn, H.-R.; Günther, D. Application of a particle separation device to reduce inductively coupled plasma-enhanced elemental fractionation in laser ablation-inductively coupled plasma-mass spectrometry. *Spectrochimica Acta Part B: Atomic Spectroscopy* **2003**, *58*, 211–220.

[95] Aeschliman, D. B.; Bajic, S. J.; Baldwin, D. P.; Houk, R. S. High-speed digital photographic study of an inductively coupled plasma during laser ablation: comparison of dried solution aerosols from a microconcentric nebulizer and solid particles from laser ablation. *Journal of Analytical Atomic Spectrometry* **2003**, *18*, 1008–1014.

[96] Flamigni, L.; Koch, J.; Günther, D. Experimental and theoretical investigations about the vaporization of laser-produced aerosols and individual particles inside inductively-coupled plasmas — Implications for the extraction efficiency of ions prior to mass spectrometry. *Spectrochimica Acta Part B: Atomic Spectroscopy* **2012**, *76*, 70–76.

[97] Niemax, K. Considerations about the detection efficiency in inductively coupled plasma mass spectrometry. *Spectrochimica Acta Part B: Atomic Spectroscopy* **2012**, *76*, 65–69.

[98] Kuhn, H.-R.; Günther, D. Laser ablation-ICP-MS: particle size dependent elemental composition studies on filter-collected and online measured aerosols from glass. *Journal of Analytical Atomic Spectrometry* **2004**, *19*, 1158–1164.

[99] Longerich, H. P.; Jackson, S. E.; Günther, D. Inter-laboratory note. Laser ablation inductively coupled plasma mass spectrometric transient signal data acquisition and analyte concentration calculation. *Journal of Analytical Atomic Spectrometry* **1996**, *11*, 899–904.

[100] Liu, Y.; Hu, Z.; Gao, S.; Günther, D.; Xu, J.; Gao, C.; Chen, H. In situ analysis of major and trace elements of anhydrous minerals by LA-ICP-MS without applying an internal standard. *Chemical Geology* **2008**, *257*, 34–43.

[101] Bian, Q.; Garcia, C. C.; Koch, J.; Niemax, K. Non-matrix matched calibration of major and minor concentrations of Zn and Cu in brass, aluminium and silicate glass using NIR femtosecond laser ablation inductively coupled plasma mass spectrometry. *Journal of Analytical Atomic Spectrometry* **2006**, *21*, 187–191.

[102] El Korh, A. Ablation behaviour of allanites during U–Th–Pb dating using a quadrupole ICP-MS coupled to a 193nm excimer laser. *Chemical Geology* **2014**, *371*, 46–59.

[103] Pisonero, J.; Fernandez, B.; Günther, D. Critical revision of GD-MS, LA-ICP-MS and SIMS as inorganic mass spectrometric techniques for direct solid analysis. *Journal of Analytical Atomic Spectrometry* **2009**, *24*, 1145–1160.

[104] Luo, T.; Ni, Q.; Hu, Z.; Zhang, W.; Shi, Q.; Günther, D.; Liu, Y.; Zong, K.; Hu, S. Comparison of signal intensities and elemental fractionation in 257 nm femtosecond LA-ICP-MS using He and Ar as carrier gases. *Journal of Analytical Atomic Spectrometry* **2017**, *32*, 2217–2225.

[105] Jackson, S. E. *CHAPTER 11: CALIBRATION STRATEGIES FOR ELEMENTAL ANALYSIS BY LA-ICP-MS*; Québec : Mineralogical Association of Canada, 2008.

[106] Jackson, S.; Longerich, H.; Dunning, G.; Fryer, B. J. The application of laser ablation microprobe–inductively coupled plasma–mass spectrometry (LAM–ICP–MS) to in situ trace element determinations in minerals. *Can. Mineral.* **1992**, *30*, 1049–1064.

[107] Klemme, S.; Prowatke, S.; Münker, C.; Magee, C. W.; Lahaye, Y.; Zack, T.; Kasemann, S. A.; Cabato, E. J. A.; Kaeser, B. Synthesis and Preliminary Characterisation of New Silicate, Phosphate and Titanite Reference Glasses. *Geostandards and Geoanalytical Research* **2008**, *32*, 39–54.

[108] Ødegård, M. Preparation of Synthetic Calibration Materials for Use in the Microanalysis of Oxide Minerals by Direct Fusion in High-Purity Graphite Electrodes: Preliminary Results for Quartz and Rutile. *Geostandards Newsletter: The Journal of Geostandards and Geoanalysis* **1999**, *23*, 173–186.

[109] Ødegård, M.; Skår, y.; Schiellerup, H.; Pearson, N. J. Preparation of a Synthetic Titanite Glass Calibration Material for In Situ Microanalysis by Direct Fusion in Graphite Electrodes: A Preliminary Characterisation by EPMA and LA-ICP-MS. *Geostandards and Geoanalytical Research* **2005**, *29*, 197–209.

[110] Jochum, K. P.; Nohl, U. Reference materials in geochemistry and environmental research and the GeoReM database. *Chemical Geology* **2008**, *253*, 50–53.

[111] Tanner, M.; Günther, D. Short transient signals, a challenge for inductively coupled plasma mass spectrometry, a review. *Analytica Chimica Acta* **2009**, *633*, 19–28.

[112] Halicz, L.; Günther, D. Quantitative analysis of silicates using LA-ICP-MS with liquid calibration. *Journal of Analytical Atomic Spectrometry* **2004**, *19*, 1539–1545.

[113] Leach, A. M.; Hieftje, G. M. Methods for shot-to-shot normalization in laser ablation with an inductively coupled plasma time-of-flight mass spectrometer. *Journal of Analytical Atomic Spectrometry* **2000**, *15*, 1121–1124.

[114] Chen, L.; Liu, Y.; Hu, Z.; Gao, S.; Zong, K.; Chen, H. Accurate determinations of fifty-four major and trace elements in carbonate by LA-ICP-MS using normalization strategy of bulk components as 100**2011**, *284*, 283–295.

[115] Gundlach-Graham, A.; Garofalo, P. S.; Schwarz, G.; Redi, D.; Günther, D. High-resolution, Quantitative Element Imaging of an Upper Crust, Low-angle Cataclasite (Zuccale Fault, Northern Apennines) by Laser Ablation ICP Time-of-Flight Mass Spectrometry. *Geostandards and Geoanalytical Research* **2018**, *42*, 559–574.

[116] Li, Z.; Hu, Z.; Liu, Y.; Gao, S.; Li, M.; Zong, K.; Chen, H.; Hu, S. Accurate determination of elements in silicate glass by nanosecond and femtosecond laser ablation ICP-MS at high spatial resolution. *Chemical Geology* **2015**, *400*, 11–23.

[117] GOVINDARAJU, K. 1994 COMPILATION OF WORKING VALUES AND SAMPLE DESCRIPTION FOR 383 GEOSTANDARDS. *Geostandards Newsletter* **1994**, *18*, 1–158.

[118] Jochum, K. P.; Willbold, M.; Raczek, I.; Stoll, B.; Herwig, K. Chemical Characterisation of the USGS Reference Glasses GSA-1G, GSC-1G, GSD-1G, GSE-1G, BCR-2G, BHVO-2G and BIR-1G Using EPMA, ID-TIMS, ID-ICP-MS and LA-ICP-MS. *Geostandards and Geoanalytical Research* **2005**, *29*, 285–302.

[119] O' Connor, C.; Sharp, B. L.; Evans, P. On-line additions of aqueous standards for calibration of laser ablation inductively coupled plasma mass spectrometry: theory and comparison of wet and dry plasma conditions. *Journal of Analytical Atomic Spectrometry* **2006**, *21*, 556–565.

[120] Wälle, M.; Koch, J.; Günther, D. Analysis of brass and silicate glass by femtosecond laser ablation inductively coupled plasma mass spectrometry using liquid standard calibration. *Journal of Analytical Atomic Spectrometry* **2008**, *23*, 1285–1289.

[121] Flamigni, L.; Koch, J.; Günther, D. The effect of carrier gas humidity on the vaporization of laser-produced aerosols in inductively coupled plasmas. *Journal of Analytical Atomic Spectrometry* **2014**, *29*, 280–286.

[122] Flamigni, L. A. Fundamental studies on the vaporization behavior of laser-generated aerosols in an inductively-coupled plasma used for mass spectrometry. Thesis, 2014.

[123] Fricker, M. B.; Kutscher, D.; Aeschlimann, B.; Frommer, J.; Dietiker, R.; Bettmer, J.; Günther, D. High spatial resolution trace element analysis by LA-ICP-MS using a novel ablation cell for multiple or large samples. *International Journal of Mass Spectrometry* **2011**, *307*, 39–45.

[124] Ebdon, L.; Goodall, P. Slurry atomization using hydrogen-modified inductively coupled plasmas. *Journal of Analytical Atomic Spectrometry* **1992**, *7*, 1111–1116.

[125] Guillong, M.; Heinrich, C. A. Sensitivity enhancement in laser ablation ICP-MS using small amounts of hydrogen in the carrier gas. *Journal of Analytical Atomic Spectrometry* **2007**, *22*, 1488–1494.

[126] Evensen, N. M.; Hamilton, P. J.; O'Nions, R. K. Rare-earth abundances in chondritic meteorites. *Geochimica et Cosmochimica Acta* **1978**, *42*, 1199–1212.

[127] *Field Guide to Meteors and Meteorites*; Springer London: London, 2008; pp 113–133.

[128] Vogel, W.; Kuipers, G. A pre-calibrated program for geological applications, Phillips New Developments. *X-Ray Spectrometry.* **1987**, *11*, 2–8.

[129] Stoll, B.; Jochum, K. P.; Herwig, K.; Amini, M.; Flanz, M.; Kreuzburg, B.; Kuzmin, D.; Willbold, M.; Enzweiler, J. An Automated Iridium-Strip Heater for LA-ICP-MS Bulk Analysis of Geological Samples. *Geostandards and Geoanalytical Research* **2008**, *32*, 5–26.

[130] WEBMINERALS. www.webminerals.com/ (accessed January 2019).

[131] Hou, T.-H.; Su, C.-H.; Liu, W.-L. Parameters optimization of a nano-particle wet milling process using the Taguchi method, response surface method and genetic algorithm. *Powder Technology* **2007**, *173*, 153–162.

[132] Tsujimoto, Y.; Matsushita, Y.; Yu, S.; Yamaura, K.; Uchikoshi, T. Size dependence of structural, magnetic, and electrical properties in corundum-type Ti2O3 nanoparticles showing insulator–metal transition. *Journal of Asian Ceramic Societies* **2015**, *3*, 325–333.

[133] Günster, J.; Görke, R.; Heinrich, J. G.; Souda, R. Pulsed laser ablation of dense sintered AlN and AlN powder samples studied by time-of-flight mass spectroscopy. *Applied Surface Science* **2001**, *173*, 76–83.

[134] Kuhn, H.-R.; Günther, D. The agglomeration state of nanosecond laser-generated aerosol particles entering the ICP. *Analytical and Bioanalytical Chemistry* **2005**, *383*, 434–441.

[135] J. G. Mank, A.; R. D. Mason, P. A critical assessment of laser ablation ICP-MS as an analytical tool for depth analysis in silica-based glass samples. *Journal of Analytical Atomic Spectrometry* **1999**, *14*, 1143–1153.

[136] Hu, Z.; Liu, Y.; Chen, L.; Zhou, L.; Li, M.; Zong, K.; Zhu, L.; Gao, S. Contrasting matrix induced elemental fractionation in NIST SRM and rock glasses during laser ablation ICP-MS analysis at high spatial resolution. *Journal of Analytical Atomic Spectrometry* **2011**, *26*, 425–430.

[137] Rumble, J. R. *CRC Handbook of Chemistry and Physics*; Press/Taylor & Francis: Boca Raton, FL, Internet Version 2018.

[138] McDonough, W.; Sun, S. s. *The composition of the Earth*; 1995; Vol. 120; pp 223–253.

[139] Koch, J.; Wälle, M.; Pisonero, J.; Günther, D. Performance characteristics of ultraviolet femtosecond laser ablation inductively coupled plasma mass spectrometry at [similar]265 and [similar]200 nm. *Journal of Analytical Atomic Spectrometry* **2006**, *21*, 932–940.

[140] Koch, J.; Lindner, H.; von Bohlen, A.; Hergenröder, R.; Niemax, K. Elemental fractionation of dielectric aerosols produced by near-infrared femtosecond laser ablation of silicate glasses. *Journal of Analytical Atomic Spectrometry* **2005**, *20*, 901–906.

[141] Stoian, R.; Rosenfeld, A.; Ashkenasi, D.; Hertel, I. V.; Bulgakova, N. M.; Campbell, E. E. B. Surface Charging and Impulsive Ion Ejection during Ultrashort Pulsed Laser Ablation. *Physical Review Letters* **2002**, *88*, 097603.

[142] Yuan, J.-H.; Zhan, X.-C.; Sun, D.-Y.; Zhao, L.-H.; Fan, C.-Z.; Kuai, L.-J.; Hu, M.-Y. Investigation on Matrix Effects in Silicate Minerals by Laser Ablation-Inductively Coupled Plasma-Mass Spectrometry. *Chinese Journal of Analytical Chemistry* **2011**, *39*, 1582–1587.

[143] Machida, M.; Sato, A.; Kijima, T.; Inoue, H.; Eguchi, K.; Arai, H. Catalytic properties and surface modification of hexaaluminate microcrystals for combustion catalyst. *Catalysis Today* **1995**, *26*, 239–245.

[144] Banger, K. K.; Yamashita, Y.; Mori, K.; Peterson, R. L.; Leedham, T.; Rickard, J.; Sirringhaus, H. Low-temperature, high-performance solution-processed metal oxide thin-film transistors formed by a 'sol–gel on chip' process. *Nature Materials* **2010**, *10*, 45.

[145] Hofmann, S. Determination of depth resolution from measured sputtering profiles of multilayer structures: Equations and approximations. *Surface and Interface Analysis* **1986**, *8*, 87–89.

[146] Hoffmann, V.; Klemm, D.; Brackmann, V.; Venzago, C.; Rockett, A. A.; Wirth, T.; Nunney, T.; Kaufmann, C. A.; Caballero, R.; Cojocaru-Mirédin, O. *Advanced Characterization Techniques for Thin Film Solar Cells*; Wiley-VCH Verlag GmbH & Co. KGaA, 2016; pp 523–567.

[147] Goh, K. H.; Haseeb, A. S. M. A.; Wong, Y. H. Structural characteristics of samarium oxynitride on silicon substrate. *Journal of Alloys and Compounds* **2017**, *722*, 729–739.

[148] Pawbake, A.; Waman, V.; Waykar, R.; Jadhavar, A.; Bhorde, A.; Kulkarni, R.; Funde, A.; Parmar, J.; Bhattacharyya, S.; Date, A.; Devan, R.; Sharma, V.; Lonkar, G.; Jadkar, S. Hot wire chemical vapor deposited multiphase silicon carbide (SiC) thin films at various filament temperatures. *Journal of Materials Science: Materials in Electronics* **2016**, *27*, 12340–12350.

[149] Das, D.; Kar, D. Structural studies of n-type nc-Si–QD thin films for nc-Si solar cells. *Journal of Physics and Chemistry of Solids* **2017**, *111*, 115–122.

[150] Vogel, U.; Oswald, S.; Eckert, J. Interface and stability analysis of Tantalum- and Titanium nitride thin films onto Lithiumniobate. *Applied Surface Science* **2017**, *425*, 254–260.

[151] Abou-Ras, D.; Nichterwitz, M.; Romero, M. J.; Schmidt, S. S. *Advanced Characterization Techniques for Thin Film Solar Cells*; Wiley-VCH Verlag GmbH & Co. KGaA, 2016; pp 371–420.

[152] Pisonero, J.; Bordel, N.; Gonzalez de Vega, C.; Fernández, B.; Pereiro, R.; Sanz-Medel, A. Critical evaluation of the potential of radiofrequency pulsed glow

discharge–time-of-flight mass spectrometry for depth-profile analysis of innovative materials. *Analytical and Bioanalytical Chemistry* **2013**, *405*, 5655–5662.

[153] Liu, Y.; Hofmann, S.; Wang, J. Y.; Chakraborty, B. R. Quantitative reconstruction of Ta/Si multilayer depth profiles obtained by Time-of-Flight-Secondary-Ion-Mass-Spectrometry (ToF-SIMS) using Cs+ ion sputtering. *Thin Solid Films* **2015**, *591*, 60–65.

[154] Gonzalez-Gago, C.; Pisonero, J.; Bordel, N.; Sanz-Medel, A.; Tibbetts, N. J.; Smentkowski, V. S. Radiofrequency pulsed glow discharge-ToFMS depth profiling of a CdTe solar cell: A comparative study versus time of flight secondary ion mass spectrometry. *Journal of Vacuum Science & Technology A: Vacuum, Surfaces, and Films* **2013**, *31*, 06F106.

[155] Grimaudo, V.; Moreno-García, P.; Riedo, A.; Neuland, M. B.; Tulej, M.; Broekmann, P.; Wurz, P. High-Resolution Chemical Depth Profiling of Solid Material Using a Miniature Laser Ablation/Ionization Mass Spectrometer. *Analytical Chemistry* **2015**, *87*, 2037–2041.

[156] Aréna, H.; Godon, N.; Rébiscoul, D.; Podor, R.; Garcès, E.; Cabie, M.; Mestre, J. P. Impact of Zn, Mg, Ni and Co elements on glass alteration: Additive effects. *Journal of Nuclear Materials* **2016**, *470*, 55–67.

[157] Popovych, V. D.; Böttger, R.; Heller, R.; Zhou, S.; Bester, M.; Cieniek, B.; Mroczka, R.; Lopucki, R.; Sagan, P.; Kuzma, M. Heavy doping of CdTe single crystals by Cr ion implantation. *Nuclear Instruments and Methods in Physics Research Section B: Beam Interactions with Materials and Atoms* **2018**, *419*, 26–31.

[158] Escobar Galindo, R.; Gago, R.; Albella, J. M.; Escobar Galindo, R.; Gago, R.; Lousa, A. Comparative depth-profiling analysis of nanometer-metal multilayers by ion-probing techniques. *TrAC Trends in Analytical Chemistry* **2009**, *28*, 494–505.

[159] Pisonero, J.; Fernández, B.; Pereiro, R.; Bordel, N.; Sanz-Medel, A. Glow-discharge spectrometry for direct analysis of thin and ultra-thin solid films. *TrAC Trends in Analytical Chemistry* **2006**, *25*, 11–18.

[160] Watts, J.; Wolstenholme, J. *An introduction to surface analysis by XPS and AES*; John Wiley & Sons Ltd, 2003.

[161] Grasserbauer, M.; Zacherl, M. *Progress in Materials Analysis*; Springer, 2014.

[162] Ratner, B. D. In *Biomaterials Science (Third Edition)*; Ratner, B. D., Hoffman, A. S., Schoen, F. J., Lemons, J. E., Eds.; Academic Press, 2013; pp 34–55.

[163] Nastasi, M.; Mayer, J.; Wang, Y. *Ion Beam Analysis: Fundamentals and Applications*; CRC Press, 2014.

[164] King, F. L.; Harrison, W. W. In *Glow Discharge Spectroscopies*; Marcus, R. K., Ed.; Springer US: Boston, MA, 1993; pp 175–214.

[165] Winchester, M. R.; Payling, R. Radio-frequency glow discharge spectrometry: A critical review. *Spectrochimica Acta - Part B Atomic Spectroscopy* **2004**, *59*, 607–666.

[166] Gutierrez-Gonzalez, A.; Gonzalez-Gago, C.; Pisonero, J.; Tibbetts, N.; Menendez, A.; Velez, M.; Bordel, N. Capabilities and limitations of LA-ICP-MS for depth resolved analysis of CdTe photovoltaic devices. *Journal of Analytical Atomic Spectrometry* **2015**, *30*, 191–197.

[167] LaHaye, N. L.; Kurian, J.; Diwakar, P. K.; Alff, L.; Harilal, S. S. Femtosecond laser ablation-based mass spectrometry: An ideal tool for stoichiometric analysis of thin films. *Scientific Reports* **2015**, *5*, 13121.

[168] Cheng, X.; Li, W.; Hang, W.; Huang, B. Depth profiling of nanometer thin layers by pulsed micro-discharge with inductively coupled plasma mass spectrometry. *Spectrochimica Acta Part B: Atomic Spectroscopy* **2015**, *111*, 52–56.

[169] Leach, A. M.; Hieftje, G. M. Factors Affecting the Production of Fast Transient Signals in Single Shot Laser Ablation Inductively Coupled Plasma Mass Spectrometry. *Applied Spectroscopy* **2002**, *56*, 62–69.

[170] St-Onge, L. A mathematical framework for modeling the compositional depth profiles obtained by pulsed laser ablation. *Journal of Analytical Atomic Spectrometry* **2002**, *17*, 1083–1089.

[171] Semerok, A.; SallÉ, B.; Wagner, J. F.; Petite, G. *Femtosecond, picosecond, and nanosecond laser microablation: Laser plasma and crater investigation*; 2002; Vol. 20; pp 67–72.

[172] Shirk, M. D.; Molian, P. A. A review of ultrashort pulsed laser ablation of materials. *Journal of Laser Applications* **1998**, *10*, 18–28.

[173] Gamaly, E. G.; Rode, A. V.; Luther-Davies, B.; Tikhonchuk, V. T. Ablation of solids by femtosecond lasers: Ablation mechanism and ablation thresholds for metals and dielectrics. *Physics of Plasmas* **2002**, *9*, 949–957.

[174] Du, D.; Liu, X.; Korn, G.; Squier, J.; Mourou, G. Laser-induced breakdown by impact ionization in SiO2 with pulse widths from 7 ns to 150 fs. *Applied Physics Letters* **1994**, *64*, 3071–3073.

[175] Liu, X.; Du, D.; Mourou, G. Laser ablation and micromachining with ultrashort laser pulses. *IEEE Journal of Quantum Electronics* **1997**, *33*, 1706–1716.

[176] Stuart, B. C.; Feit, M. D.; Herman, S.; Rubenchik, A. M.; Shore, B. W.; Perry, M. D. Nanosecond-to-femtosecond laser-induced breakdown in dielectrics. *Physical Review B* **1996**, *53*, 1749–1761.

[177] Quéré, F.; Guizard, S.; Martin, P. Time-resolved study of laser-induced breakdown in dielectrics. *Europhysics Letters (EPL)* **2001**, *56*, 138–144.

[178] Rethfeld, B. Unified Model for the Free-Electron Avalanche in Laser-Irradiated Dielectrics. *Physical Review Letters* **2004**, *92*, 187401.

[179] Jupé, M.; Jensen, L.; Melninkaitis, A.; Sirutkaitis, V.; Ristau, D. Calculations and experimental demonstration of multi-photon absorption governing fs laser-induced damage in titania. *Optics Express* **2009**, *17*, 12269–12278.

[180] F. M., D.; S. C., H. *Laser Beam Shaping - Theory and Technique*; CRC Press, 2000; p 428.

[181] Momma, C.; Nolte, S.; Kamlage, G.; von Alvensleben, F.; Tünnermann, A. Beam delivery of femtosecond laser radiation by diffractive optical elements. *Applied Physics A* **1998**, *67*, 517–520.

[182] Bor, Z. Distortion of Femtosecond Laser Pulses in Lenses and Lens Systems. *Journal of Modern Optics* **1988**, *35*, 1907–1918.

[183] Bor, Z. Distortion of femtosecond laser pulses in lenses. *Optics Letters* **1989**, *14*, 119–121.

[184] Goodman, J. *Introduction to Fourier Optics*; W. H. Freeman, 1968.

[185] Amelinckx, S.; van Dyck, D.; van Landuyt, J.; van Tendeloo, G. In *Handbook of Microscopy*; Amelinckx, S., van Dyck, D., van Landuyt, J., van Tendeloo, G., Eds.; 2008.

[186] Paddock, S. W.; Eliceiri, K. W. In *Confocal Microscopy: Methods and Protocols*; Paddock, S. W., Ed.; Springer New York: New York, NY, 2014; pp 9–47.

[187] Haugstad, G. In *Atomic Force Microscopy*; Haugstad, G., Ed.; John Wiley & Sons, Inc., 2012; Chapter Overview of AFM.

[188] Goldstein, J. I.; Newbury, D. E.; Michael, J. R.; Ritchie, N. W. M.; Scott, J. H. J.; Joy, D. C. In *Scanning Electron Microscopy and X-Ray Microanalysis*; Goldstein, J. I., Newbury, D. E., Michael, J. R., Ritchie, N. W. M., Scott, J. H. J., Joy, D. C., Eds.; Springer New York: New York, NY, 2018; pp 65–91.

[189] Nečas, D.; Klapetek, P. Gwyddion: an open-source software for SPM data analysis. *Central European Journal of Physics* **2012**, *10*, 181–188.

[190] Bonse, J.; Krüger, J.; Höhm, S.; Rosenfeld, A. Femtosecond laser-induced periodic surface structures. *Journal of Laser Applications* **2012**, *24*, 042006.

[191] Emmony, D. C.; Howson, R. P.; Willis, L. J.; J., G. A.; H., G. A. Laser mirror damage in germanium at 10.6 m. *Applied Physics Letters* **1973**, *23*, 598–600.

[192] Soileau, M. Ripple structures associated with ordered surface defects in dielectrics. *IEEE Journal of Quantum Electronics* **1984**, *20*, 464–467.

[193] Dufft, D.; Rosenfeld, A.; Das, S. K.; Grunwald, R.; Bonse, J. Femtosecond laser-induced periodic surface structures revisited: A comparative study on ZnO. *Journal of Applied Physics* **2009**, *105*, 034908.

[194] Reif, J.; Costache, F.; Henyk, M.; Pandelov, S. V. Ripples revisited: non-classical morphology at the bottom of femtosecond laser ablation craters in transparent dielectrics. *Applied Surface Science* **2002**, *197-198*, 891–895.

[195] Borowiec, A.; Haugen, H. K. Subwavelength ripple formation on the surfaces of compound semiconductors irradiated with femtosecond laser pulses. *Applied Physics Letters* **2003**, *82*, 4462–4464.

[196] Martsinovskiĭ, G. A.; Shandybina, G. D.; Smirnov, D. S.; Zabotnov, S. V.; Golovan', L. A.; Timoshenko, V. Y.; Kashkarov, P. K. Ultrashort excitations of surface polaritons and waveguide modes in semiconductors. *Optics and Spectroscopy* **2008**, *105*, 67–72.

[197] Miyaji, G.; Miyazaki, K. Origin of periodicity in nanostructuring on thin film surfaces ablated with femtosecond laser pulses. *Optics Express* **2008**, *16*, 16265–16271.

[198] Wu, Q.; Ma, Y.; Fang, R.; Liao, Y.; Yu, Q.; Chen, X.; Wang, K. Femtosecond laser-induced periodic surface structure on diamond film. *Applied Physics Letters* **2003**, *82*, 1703–1705.

[199] Hofmann, S. From depth resolution to depth resolution function: refinement of the concept for delta layers, single layers and multilayers. *Surface and Interface Analysis* **1999**, *27*, 825–834.

[200] Plotnikov, A.; Vogt, C.; Hoffmann, V.; Taschner, C.; Wetzig, K. Application of laser ablation inductively coupled plasma quadrupole mass spectrometry (LA-ICP-QMS) for depth profile analysis. *Journal of Analytical Atomic Spectrometry* **2001**, *16*, 1290–1295.

[201] ISO14606:2015(en), *Surface chemical analysis - Sputter depth profiling - Optimization using layered systems as reference materials - Part 2: terms and definitions*; 2015.

[202] Dowsett, M. G.; Barlow, R. D. Characterization of Sharp Interfaces and Delta-Doped Layers in Semiconductors Using Secondary-Ion Mass-Spectrometry. *Analytica Chimica Acta* **1994**, *297*, 253–275.

[203] Dowsett, M. G.; Barlow, R. D.; Allen, P. N. Secondary-Ion Mass-Spectrometry Analysis of Ultrathin Impurity Layers in Semiconductors and Their Use in Quantification, Instrumental Assessment, and Fundamental Measurements. *Journal of Vacuum Science & Technology B* **1994**, *12*, 186–198.

[204] Dowsett, M. G.; Rowlands, G.; Allen, P. N.; Barlow, R. D. An Analytic Form for the Sims Response Function Measured from Ultra-Thin Impurity Layers. *Surface and Interface Analysis* **1994**, *21*, 310–315.

[205] Hofmann, S. Compositional depth profiling by sputtering. *Progress in Surface Science* **1991**, *36*, 35–87.

[206] Hofmann, S. Cascade Mixing Limitations in Sputter Profiling. *Journal of Vacuum Science & Technology B* **1992**, *10*, 316–322.

[207] Hofmann, S. Atomic Mixing, Surface-Roughness and Information Depth in High-Resolution Aes Depth Profiling of a Gaas/Alas Superlattice Structure. *Surface and Interface Analysis* **1994**, *21*, 673–678.

[208] Hofmann, S.; Liu, Y.; Wang, J. Y.; Kovac, J. Analytical and numerical depth resolution functions in sputter profiling. *Applied Surface Science* **2014**, *314*, 942–955.

[209] Sipe, J. E.; Young, J. F.; Preston, J. S.; van Driel, H. M. Laser-induced periodic surface structure. I. Theory. *Physical Review B* **1983**, *27*, 1141–1154.

[210] Kamlage, G.; Bauer, T.; Ostendorf, A.; Chichkov, B. Deep drilling of metals by femtosecond laser pulses. *Applied Physics A* **2003**, *77*, 307–310.

[211] Lindner, H.; Autrique, D.; Garcia, C. C.; Niemax, K.; Bogaerts, A. Optimized Transport Setup for High Repetition Rate Pulse-Separated Analysis in Laser AblationInductively Coupled Plasma Mass Spectrometry. *Analytical Chemistry* **2009**, *81*, 4241–4248.

[212] Tani, S.; Kobayashi, Y. Pulse-by-pulse depth profile measurement of femtosecond laser ablation on copper. *Applied Physics A* **2018**, *124*, 265.

[213] Min, K. K.; Takao, T.; Oki, Y.; Maeda, M. Thin-Layer Ablation of Metals and Silicon by Femtosecond Laser Pulses for Application to Surface Analysis. *Japanese Journal of Applied Physics* **2000**, *39*, 6277.

[214] Kim, J.; Na, S. Metal thin film ablation with femtosecond pulsed laser. *Optics & Laser Technology* **2007**, *39*, 1443–1448.

[215] Lou, K.; Qian, J.; Shen, D.; Wang, H.; Ding, T.; Wang, G.; Dai, Y.; Zhao, Q.-Z. Recording, erasing, and rewriting of ripples on metal surfaces by ultrashort laser pulses. *Optics Letters* **2018**, *43*, 1778–1781.

[216] Demtröder, W. In *Experimentalphysik 2: Elektrizität und Optik*; Demtröder, W., Ed.; Springer Berlin Heidelberg: Berlin, Heidelberg, 2013; pp 299–345.

[217] Sweetser, J. N.; Fittinghoff, D. N.; Trebino, R. Transient-grating frequency-resolved optical gating. *Optics Letters* **1997**, *22*, 519–521.

[218] Trebino, R. *Frequency-Resolved Optical Gating: The Measurement of Ultrashort Laser Pulses*; Springer US, 2012.

[219] Doolittle, L. R. A semiautomatic algorithm for rutherford backscattering analysis. *Nuclear Instruments and Methods in Physics Research Section B: Beam Interactions with Materials and Atoms* **1986**, *15*, 227–231.